

# ADVANCED STEEL CONSTRUCTION

*An International Journal*

Volume 11 Number 2

June 2015

CONTENTS

## Technical Papers

Flexural Performance of Circular Concrete Filled CFRP-Steel Tubes

*Q.L. Wang and Y.B. Shao*

Residual Stress Study on Welded Section of High Strength Q460 Steel after Fire Exposure

*W.Y. Wang, G.Q. Li and Y. Ge*

Design Strength of Concrete-Filled Steel Columns

*W.-H. Kang, B. Uy, Z. Tao and S. Hicks*

Load-Carrying Capacity of Single-Row Steel Scaffolds with Various Setups

*Jui-Lin Peng, Chung-Ming Ho, Chen-Chung Lin and Wai-Fah Chen*

Evaluation for Earthquake-Resistant Capability of Un-Landing Steel Arch

*Qinghua Han, Yan Lu and QiuHong Zhao*

Novel Non-Linear Elastic Structural Analysis with Generalised Transverse Element Loads using a Refined Finite Element

*C.K. Iu and M.A. Bradford*

Announcement by IJASC :

*Announcement for ICASS'2015*

*Announcement for ICSCS15 and ASEM 2015*

Copyright © 2015 by :

The Hong Kong Institute of Steel Construction

Website: <http://www.hkisc.org>

ISSN 1816-112X

Science Citation Index Expanded, Materials Science Citation Index and ISI Alerting

Cover: Scene of London with aesthetic steel buildings

e-copy of IJASC is free to download at "[www.ascjournal.com](http://www.ascjournal.com)" in internet and mobile apps.

ADVANCED STEEL CONSTRUCTION

VOL.11, NO.2 (2015)

# ADVANCED STEEL CONSTRUCTION

*an International Journal*

ISSN 1816-112X

Volume 11 Number 2

June 2015



## Editors-in-Chief

**S.L. Chan**, The Hong Kong Polytechnic University, Hong Kong

**W.F. Chen**, University of Hawaii at Manoa, USA

**R. Zandonini**, Trento University, Italy



ISSN 1816-112X

Science Citation Index Expanded,  
Materials Science Citation Index  
and ISI Alerting

#### EDITORS-IN-CHIEF

##### Asian Pacific, African and organizing Editor

S.L. Chan  
The Hong Kong Poly. Univ.,  
Hong Kong

##### American Editor

W.F. Chen  
Univ. of Hawaii at Manoa, USA

##### European Editor

R. Zandonini  
Trento Univ., Italy

#### INTERNATIONAL EDITORIAL BOARD

F.G. Albermani  
The Univ. of Queensland, Australia

I. Burgess  
Univ. of Sheffield, UK

F.S.K. Bijlaard  
Delft Univ. of Technology, The Netherlands

R. Bjorhovde  
The Bjorhovde Group, USA

M.A. Bradford  
The Univ. of New South Wales, Australia

D. Camotim  
Technical Univ. of Lisbon, Portugal

C.M. Chan  
Hong Kong Univ. of Science & Technology, Hong Kong

T.H.T. Chan  
Queensland Univ. of Technology, Australia

S.P. Chiew  
Nanyang Technological Univ., Singapore

W.K. Chow  
The Hong Kong Poly. Univ., Hong Kong

G.G. Deierlein  
Stanford Univ., California, USA

L. Dezi  
Univ. of Ancona, Italy

D. Dubina  
The Politehnica Univ. of Timisoara, Romania

R. Greiner  
Technical Univ. of Graz, Austria

L. Gardner  
Imperial College of Science, Technology and Medicine, UK

L.H. Han  
Tsinghua Univ. China

S. Herion  
University of Karlsruhe, Germany

G.W.M. Ho  
Ove Arup & Partners Hong Kong Ltd., Hong Kong

B.A. Izzuddin  
Imperial College of Science, Technology and  
Medicine, UK

J.P. Jaspart  
Univ. of Liege, Belgium

S. A. Jayachandran  
IIT Madras, Chennai, India

S.E. Kim  
Sejong Univ., South Korea

S. Kitipornchai  
The Univ., of Queensland, Australia

D. Lam  
Univ. of Bradford, UK

L.J. Leu  
National Taiwan Univ., Taiwan

G.Q. Li  
Tongji Univ., China

J.Y.R. Liew  
National Univ. of Singapore, Singapore

E.M. Lui  
Syracuse Univ., USA

Y.L. Mo  
Univ. of Houston, USA

J.P. Muzeau  
CUST, Clermont Ferrand, France

D.A. Nethercot  
Imperial College of Science, Technology and  
Medicine, UK

Y.Q. Ni  
The Hong Kong Poly. Univ., Hong Kong

D.J. Oehlers  
The Univ. of Adelaide, Australia

J.L. Peng  
Yunlin Univ. of Science & Technology, Taiwan

K. Rasmussen  
The Univ. of Sydney, Australia

J.M. Rotter  
The Univ. of Edinburgh, UK

C. Scawthorn  
Scawthorn Porter Associates, USA

P. Schaumann  
Univ. of Hannover, Germany

G.P. Shu  
Southeast Univ. China

L. Simões da Silva  
Department of Civil Engineering, University of  
Coimbra, Portugal

J.G. Teng  
The Hong Kong Poly. Univ., Hong Kong

G.S. Tong  
Zhejiang Univ., China

K.C. Tsai  
National Taiwan Univ., Taiwan

C.M. Uang  
Univ. of California, USA

B. Uy  
The University of New South Wales, Australia

M. Veljkovic  
Univ. of Lulea, Sweden

F. Wald  
Czech Technical Univ. in Prague, Czech

Y.C. Wang  
The Univ. of Manchester, UK

Y.L. Xu  
The Hong Kong Poly. Univ., Hong Kong

D. White  
Georgia Institute of Technology, USA

E. Yamaguchi  
Kyushu Institute of Technology, Japan

Y.B. Yang  
Chongqing University, China

Y.B. Yang  
National Taiwan Univ., Taiwan

Y.Y. Yang  
China Academy of Building Research, Beijing, China

B. Young  
The Univ. of Hong Kong, Hong Kong

X.L. Zhao  
Monash Univ., Australia

X.H. Zhou,  
Chongqing University, China

Z.H. Zhou  
Alpha Consultant Ltd., Hong Kong

R.D. Ziemian  
Bucknell University, USA

Cover: Scene of London with aesthetic steel buildings

e-copy of IJASC is free to download at "www.ascjournal.com" in internet and mobile apps.

## General Information

### *Advanced Steel Construction, an international journal*

#### **Aims and scope**

The International Journal of Advanced Steel Construction provides a platform for the publication and rapid dissemination of original and up-to-date research and technological developments in steel construction, design and analysis. Scope of research papers published in this journal includes but is not limited to theoretical and experimental research on elements, assemblages, systems, material, design philosophy and codification, standards, fabrication, projects of innovative nature and computer techniques. The journal is specifically tailored to channel the exchange of technological know-how between researchers and practitioners. Contributions from all aspects related to the recent developments of advanced steel construction are welcome.

#### **Instructions to authors**

**Submission of the manuscript.** Authors may submit double-spaced manuscripts preferably in MS Word by emailing to one of the chief editors as follows for arrangement of review. Alternatively papers can be submitted on a diskette to one of the chief editors.

Asian Pacific, African and organizing editor : Professor S.L. Chan, Email: [ceslchan@polyu.edu.hk](mailto:ceslchan@polyu.edu.hk)

American editor : Professor W.F. Chen, Email: [waifah@hawaii.edu](mailto:waifah@hawaii.edu)

European editor : Professor R. Zandonini, Email: [riccardo\\_zandonini@ing.unitn.it](mailto:riccardo_zandonini@ing.unitn.it)

All manuscripts submitted to the journal are recommended to accompany with a list of four potential reviewers suggested by the author(s). This list should include the complete name, address, telephone and fax numbers, email address, and at least five keywords that identify the expertise of each reviewer. This scheme will improve the process of review.

#### **Style of manuscript**

**General.** Author(s) should provide full postal and email addresses and fax number for correspondence. The manuscript including abstract, keywords, references, figures and tables should be in English with pages numbered and typed with double line spacing on single side of A4 or letter-sized paper. The front page of the article should contain:

- a) a short title (reflecting the content of the paper);
- b) all the name(s) and postal and email addresses of author(s) specifying the author to whom correspondence and proofs should be sent;
- c) an abstract of 100-200 words; and
- d) 5 to 8 keywords.

The paper must contain an introduction and a conclusion. The length of paper should not exceed 25 journal pages (approximately 15,000 words equivalents).

**Tables and figures.** Tables and figures including photographs should be typed, numbered consecutively in Arabic numerals and with short titles. They should be referred in the text as Figure 1, Table 2, etc. Originally drawn figures and photographs should be provided in a form suitable for photographic reproduction and reduction in the journal.

**Mathematical expressions and units.** The Systeme Internationale (SI) should be followed whenever possible. The numbers identifying the displayed mathematical expression should be referred to in the text as Eq. (1), Eq. (2).

**References.** References to published literature should be referred in the text, in the order of citation with Arabic numerals, by the last name(s) of the author(s) (e.g. Zandonini and Zanon [3]) or if more than three authors (e.g. Zandonini et al. [4]). References should be in English with occasional allowance of 1-2 exceptional references in local languages and reflect the current state-of-technology. Journal titles should be abbreviated in the style of the Word List of Scientific Periodicals. References should be cited in the following style [1, 2, 3].

Journal: [1] Chen, W.F. and Kishi, N., "Semi-rigid Steel Beam-to-column Connections, Data Base and Modelling", Journal of Structural Engineering, ASCE, 1989, Vol. 115, No. 1, pp. 105-119.

Book: [2] Chan, S.L. and Chui, P.P.T., "Non-linear Static and Cyclic Analysis of Semi-rigid Steel Frames", Elsevier Science, 2000.

Proceedings: [3] Zandonini, R. and Zanon, P., "Experimental Analysis of Steel Beams with Semi-rigid Joints", Proceedings of International Conference on Advances in Steel Structures, Hong Kong, 1996, Vol. 1, pp. 356-364.

**Proofs.** Proof will be sent to the corresponding author to correct any typesetting errors. Alternations to the original manuscript at this stage will not be accepted. Proofs should be returned within 48 hours of receipt by Express Mail, Fax or Email.

**Copyright.** Submission of an article to "Advanced Steel Construction" implies that it presents the original and unpublished work, and not under consideration for publication nor published elsewhere. On acceptance of a manuscript submitted, the copyright thereof is transferred to the publisher by the Transfer of Copyright Agreement and upon the acceptance of publication for the papers, the corresponding author must sign the form for Transfer of Copyright.

**Permission.** Quoting from this journal is granted provided that the customary acknowledgement is given to the source.

**Page charge and Reprints.** There will be no page charges if the length of paper is within the limit of 25 journal pages. A total of 30 free offprints will be supplied free of charge to the corresponding author. Purchasing orders for additional offprints can be made on order forms which will be sent to the authors. These instructions can be obtained at the Hong Kong Institute of Steel Construction, Journal website: <http://www.hkisc.org>

The International Journal of Advanced Steel Construction is published quarterly by learnt society, The Hong Kong Institute of Steel Construction, c/o Department of Civil & Environmental Engineering, The Hong Kong Polytechnic University, Hung Hom, Kowloon, Hong Kong.

**Disclaimer.** No responsibility is assumed for any injury and / or damage to persons or property as a matter of products liability, negligence or otherwise, or from any use or operation of any methods, products, instructions or ideas contained in the material herein.

**Subscription inquiries and change of address.** Address all subscription inquiries and correspondence to Member Records, IJASC. Notify an address change as soon as possible. All communications should include both old and new addresses with zip codes and be accompanied by a mailing label from a recent issue. Allow six weeks for all changes to become effective.

#### **The Hong Kong Institute of Steel Construction**

HKISC

c/o Department of Civil and Environmental Engineering,

The Hong Kong Polytechnic University,

Hung Hom, Kowloon, Hong Kong, China.

Tel: 852- 2766 6047 Fax: 852- 2334 6389

Email: [ceslchan@polyu.edu.hk](mailto:ceslchan@polyu.edu.hk) Website: <http://www.hkisc.org/>

ISSN 1816-112X

Science Citation Index Expanded, Materials Science Citation Index and ISI Alerting

Copyright © 2015 by:

The Hong Kong Institute of Steel Construction.



ISSN 1816-112X

Science Citation Index Expanded,  
Materials Science Citation Index and  
ISI Alerting

## EDITORS-IN-CHIEF

### Asian Pacific, African and organizing Editor

S.L. Chan  
*The Hong Kong Polyt. Univ.,  
Hong Kong*  
Email: [ceslchan@polyu.edu.hk](mailto:ceslchan@polyu.edu.hk)

### American Editor

W.F. Chen  
*Univ. of Hawaii at Manoa, USA*  
Email: [waifah@hawaii.edu](mailto:waifah@hawaii.edu)

### European Editor

R. Zandonini  
*Trento Univ., Italy*  
Email: [riccardo.zandonini@ing.unitn.it](mailto:riccardo.zandonini@ing.unitn.it)

# Advanced Steel Construction

*an international journal*

VOLUME 11 NUMBER 2

JUNE 2015

## Technical Papers

- |   |     |
|---|-----|
| Flexural Performance of Circular Concrete Filled CFRP-Steel Tubes<br><i>Q.L. Wang and Y.B. Shao</i>   | 127 |
| Residual Stress Study on Welded Section of High Strength Q460 Steel after Fire Exposure<br><i>W.Y. Wang, G.Q. Li and Y. Ge</i>                            | 150 |
| Design Strength of Concrete-Filled Steel Columns<br><i>W.-H. Kang, B. Uy, Z. Tao and S. Hicks</i>   | 165 |
| Load-Carrying Capacity of Single-Row Steel Scaffolds with Various Setups<br><i>Jui-Lin Peng, Chung-Ming Ho, Chen-Chung Lin and Wai-Fah Chen</i>           | 185 |
| Evaluation for Earthquake-Resistant Capability of Un-Landing Steel Arch<br><i>Qinghua Han, Yan Lu and Qiuhong Zhao</i>                                    | 211 |
| Novel Non-Linear Elastic Structural Analysis with Generalised Transverse Element Loads using a Refined Finite Element<br><i>C.K. Iu and M.A. Bradford</i> | 223 |

## Announcement by IJASC :

Announcement for ICASS'2015

Announcement for ICSCS15 and ASEM 2015



# FLEXURAL PERFORMANCE OF CIRCULAR CONCRETE FILLED CFRP-STEEL TUBES

Q. L. Wang<sup>1,\*</sup> and Y. B. Shao<sup>2</sup>

<sup>1</sup> Professor, School of Civil Engineering, Shenyang Jianzhu University, Shenyang, P. R. China

<sup>2</sup> Professor, School of Civil Engineering, Yantai University, Yantai, P. R. China

\*(Corresponding author: E-mail: ceqlwang@sjzu.edu.cn)

*Received: 26 September 2012; Revised: 15 January 2014; Accepted: 26 February 2014*

**ABSTRACT:** Sixteen circular concrete filled CFRP-steel tubular (C-CF-CFRP-ST) flexural members were tested. The test results indicate that the moment versus curvature curve at mid-span of C-CF-CFRP-ST members without longitudinal CFRP reinforcement is similar to such relationship of corresponding un-reinforced circular concrete filled steel tubular (C-CFST) flexural members. The moment versus curvature curve at mid-span for members with longitudinal CFRP reinforcement can be divided into following stages: elastic stage, elasto-plastic stage and softening stage. The longitudinal CFRP can enhance the stiffness of the specimens significantly. The steel tube and the CFRP tube could cooperate both in the transverse and in the longitudinal directions. The steel tube in the region under longitudinal tension has no confinement effect on the core concrete in the same tensile region because the concrete is in a state of contraction in transverse direction. The longitudinal strain distribution over depth of the specimens' cross-section satisfies the plane section assumption approximately. Finite element model is built and ABAQUS is used to analyze both the moment versus curvature curves at mid-span and the deformation of the C-CF-CFRP-ST flexural members. The finite element results are found to agree well with experimental results. Interaction forces exist both in the tensile region and in the compressive region between the outer tube and the concrete. However, there is essential difference between the interaction forces in the tensile region and in the compressive region respectively. Finally, flexural load carrying capacity of the C-CF-CFRP-ST is defined, and parametric equations for calculating it are presented. The accuracy and the reliability of the proposed equations are verified.

**Keywords:** Circular CFRP-steel tube, In-filled concrete, Beams, Flexural performances, Interaction force, Flexural load carrying capacity

## 1. INTRODUCTION

Concrete Filled Tubular structure (denoted by CFT structure, as shown in Figure 1) has aroused wide applications and deep studies all over the world for its advantage of high strength of tri-axially compressed concrete. Concrete Filled Steel Tubular structure (denoted by CFST structure, as shown in Figure 1 (a)) is a very typical CFT structure and it is used widely in civil engineering. The research work in this field has been studied systematically in the literature, such as the investigations on the static behavior (Han [1]; Tao et al. [2]; Georgios and Lam [3]; Uy [4]), the hysteretic behavior (Han and Yang [5]; Han and Li [6]) of the components and the connections, and fire and corrosion resistance (Han, Wang and Yu [7]; Han, Hou and Wang [8]). Nevertheless, Carbon Fiber Reinforced Polymer (denoted by CFRP) has been used in more and more engineering structures due to its advantages of high strength/weight ratio, good corrosion resistance, ease of installation, cheaper cost and so on. Concrete Filled CFRP Tubular structure (denoted by CF-CFRP-T structure, as shown in Figure 1 (b)) is a typical example of CFRP structures (Wang and Restrepo [9]; Teng et al. [10]). However, the failure mode of CF-CFRP-T structure has brittle characteristics in most cases, and the load carrying capacity in the transverse direction for this structure is weak. There is also a new type of CFT structures, i.e., Concrete Filled CFRP-Steel Tubular structure (denoted by CF-CFRP-ST structure, as shown in Figure 1 (c)). CFRP can enhance load carrying capacity of the CFST structure and reduce local buckling of the steel tubes. It can also improve the structural durability. Comparing with CF-CFRP-T, CF-CFRP-ST has better ductility and shearing load carrying capacity. Additionally, CF-CFRP-ST can also provide a new approach to

repair existing CFST with some slight damages (fire or corrosion) or with requirement to sustain more additional loads.

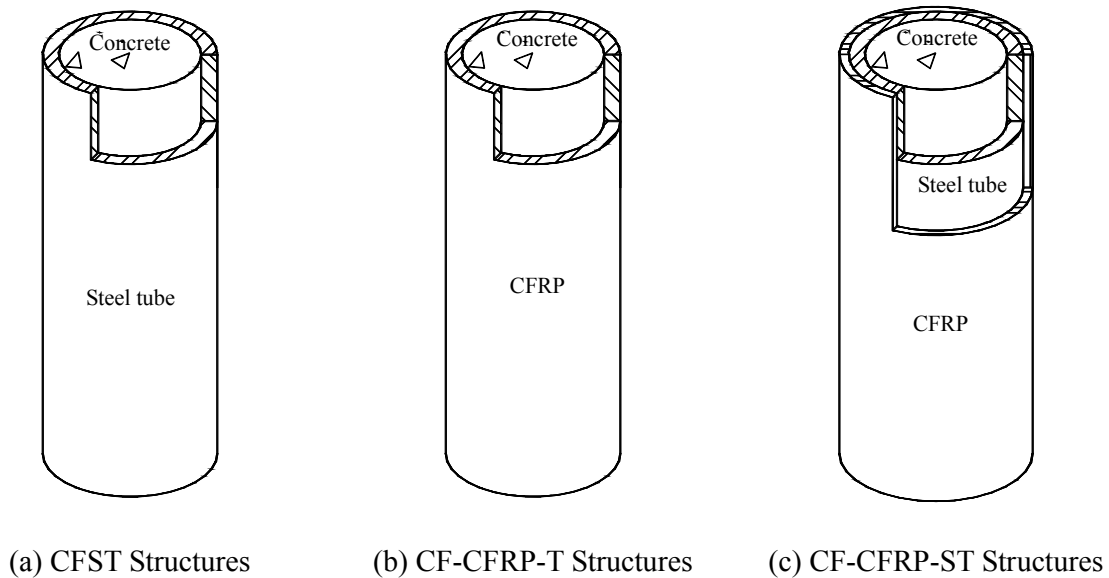


Figure 1. CFT Structures

It is pointed out here that most resin as the matrix of CFRP composites has a poor fire-resistant capacity, and how to resolve the fire resistance of CFRP in engineering practice is still the primary concern. It is better to use CF-CFRP-ST in an environment with less fire but with severe corrosion, such as bridge engineering, offshore and ocean engineering and so on. From reported experiments under fire condition in the literature (Han, Tao and Wang [11]), it seems that CF-CFRP-ST has demonstrated satisfactory fire endurance under external loading when supplemental insulation to the CFRP composites has been used. Actually, the composite CFRP-metal tanks or tubes have been used in many fields, for example, gas tank used in motor vehicle, pipeline system for transporting high pressure gas or liquid used in municipal engineering or chemical engineering. Sometimes, steel petroleum pipeline system after corrosion is also reinforced with CFRP, which can save much cost compared to the measure of replacing the corroded tube with new one. Based on the above introduction, it is believed that the use of CF-CFRP-ST in civil engineering is quite reasonable and potential.

Some research studies in this field have been reported in the literature. Research work of using CFRP to repair CFST stub columns including circular specimens and square specimens after exposed to fire was conducted (Tao, Han and Wang [12]). A new CFST column system with circular cross-section, where CFRP materials were used as additional confinement to the potential plastic hinge regions of the composite column, was proposed (Xiao, He and Choi [13]), and a simplified analytical solution in association with a numerical computer program of the CF-CFRP-ST column was developed (Choi and Xiao [14]). Additionally, a systematic study on Circular CF-CFRP-ST (denoted by C-CF-CFRP-ST) stub columns has been carried out (Che, Wang and Shao [15]). The constitutive relationship of concrete confined by circular CFRP-steel tube under compression as well as the index of load carrying capacity of the axially compressed C-CF-CFRP-ST stub columns was presented. However, the performance of the C-CF-CFRP-ST flexural members or beam-columns is scarcely reported, although using CFRP wrapped in transverse direction to repair circular CFST (denoted by C-CFST) flexural members after exposed to fire was investigated (Tao, Han and Wang [12]). For the members carrying large bending

moment, it is found that CFRP wrapped in transverse direction does not have remarkable efficiency, and in this situation CFRP is only necessary to be wrapped mainly in longitudinal direction. Furthermore, theoretical analysis on C-CF-CFRP-ST flexural members is also scarce.

In order to do some further studies and to understand the reinforcing efficiency of longitudinal CFRP, 16 C-CF-CFRP-ST flexural members with both transverse and longitudinal CFRPs are tested. Moment ( $M$ ) versus curvature ( $\phi$ ) curves at mid-span, cooperation between the steel tube and the CFRP, plane section assumption and stiffness of the composite members are all analyzed and discussed. Furthermore, the finite element software ABAQUS is used to simulate the deforming shape and the  $M - \phi$  curves of the C-CF-CFRP-ST flexural members. The distributions of longitudinal stress and strain on the cross-section at mid-span, effect of the strengthening factor of the longitudinal CFRP ( $\eta$ ), and interaction force ( $p$ ) between core concrete and outer tube are also analyzed. Finally, the flexural load carrying capacity is defined, and a corresponding theoretical equation is presented.

## 2. EXPERIMENTAL PROGRAM

### 2.1 Specimen Geometry

In overall, sixteen C-CF-CFRP-ST flexural specimens were conducted, and the parameters include the number of longitudinal CFRP layer(s) ( $m'$ ) and the outer diameter of the steel tube ( $D_s$ ) respectively. Specimen details are provided in Table 1.

Table 1. Specimen Labels and Member Capacities

No.	Specimens label	$D_s$ (mm)	$t_s$ (mm)	$L$ (mm)	$L_0$ (mm)	$m'$ (layer (s))	$m$ (layer)	$M_u^t$ ( $\text{kN} \cdot \text{m}$ )	$K_{ie}$ ( $\text{kN} \cdot \text{m}^2$ )	$K_{se}$ ( $\text{kN} \cdot \text{m}^2$ )	$\varepsilon_{cfr}^t$ ( $\mu\epsilon$ )
1	CB A-0	89	4.5	1400	1200	0	1	12.5	225	221	-
2	CB A-1	89	4.5	1400	1200	1	1	14.2	231	226	12367
3	CB A-2	89	4.5	1400	1200	2	1	15.4	255	250	8581
4	CB A-3	89	4.5	1400	1200	3	1	17.5	277	259	-
5	CB B-0	108	4.5	1400	1200	0	1	18.5	457	465	-
6	CB B-1	108	4.5	1400	1200	1	1	19.9	505	474	9652
7	CB B-2	108	4.5	1400	1200	2	1	21.6	569	501	8795
8	CB B-3	108	4.5	1400	1200	3	1	24.2	853	509	9721
9	CB C-0	133	4.5	1400	1200	0	1	32.7	909	744	-
10	CB C-1	133	4.5	1400	1200	1	1	37.4	960	843	9913
11	CB C-2	133	4.5	1400	1200	2	1	37.4	992	860	8706
12	CB C-3	133	4.5	1400	1200	3	1	40.2	1009	898	9758
13	CB D-0	159	4.5	1400	1200	0	1	51.5	1721	1443	-
14	CB D-1	159	4.5	1400	1200	1	1	53.5	1715	1459	9603
15	CB D-2	159	4.5	1400	1200	2	1	59.6	1746	1542	9211
16	CB D-3	159	4.5	1400	1200	3	1	64.2	1757	1627	12041

In Table 1, “CB” in the specimen’s label refers to Circular Beam, and the third letter can be anyone among letters “A”, “B”, “C” or “D” which denotes different  $D_s$  with its value equal to 89mm, 108mm, 133mm or 159mm respectively. The number in the specimen label with “0”, “1”, “2” or “3” refers to the value of  $m'$ . For other parameters,  $t_s$  is wall thickness of the steel tube,  $L$  is length of the specimens,  $L_0$  is net span of the specimens, and  $m$  is number of the transverse CFRP layer.

## 2.2 Specimen Preparations

Fabrication of C-CFST specimens can be found in reported reference (Han [1]). Carbon fiber sheets are applied using a hand lay-up method. The longitudinal CFRP is glued firstly, and the transverse CFRP is then placed sequentially. The final end of a sheet is overlapped the initial end by 150 mm. Some specimens before testing are shown in Figure 2.

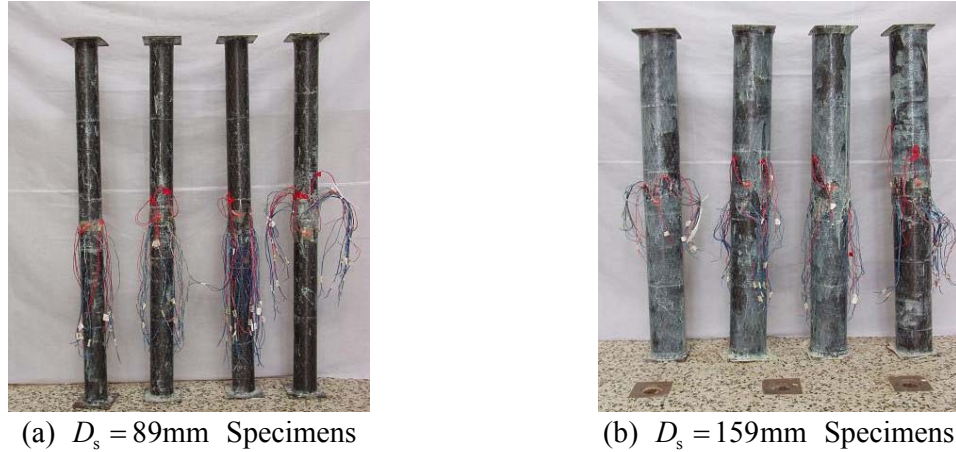


Figure 2. Several Specimens before Testing

## 2.3 Material Properties

Tensile tests on steel coupons cut from the original seamless steel tubes are conducted to measure the material properties. The tested results are given in Table 2, where  $E_s$ ,  $f_y$ ,  $\nu_s$  and  $f_u$  are elastic modulus, yield stress, Poisson's ratio and ultimate stress of the steel tube respectively.

Table 2. Material Properties of Steel Tube

$D_s$ (mm)	$E_s$ (GPa)	$f_y$ (MPa)	$\nu_s$	$f_u$ (MPa)
89	216	304	0.26	465
108	216	269	0.25	434
133	216	333	0.27	474
159	217	333	0.31	474

All the specimens were cast with same concrete. In the concrete mixture, Portland cement was used, and fine aggregate was silica-based sand. The coarse aggregate was limestone with the largest size of 20mm, and 1% (in weight) water reducing agent was added. The mixture proportion of the concrete is summarized in Table 3.

Table 3. Mixture Proportions of Concrete ( $\text{kg} \cdot \text{m}^{-3}$ )

Cement	Water	Fine aggregate	Course aggregate
485	150	703	1062

To determine the compressive strength of the concrete, six 150mm cubic specimens were cast and cured in conditions similar to that of the tested specimens. The average cubic strength ( $f_{cu}$ ) at 28 days was 48.8 MPa. At the time of tests (six months later due to the delay of the test program), the cubic strength of 60.7 MPa was achieved and this strength is used in following FE simulation and

calculation of flexural load carrying capacity. Elastic modulus of the concrete ( $E_c$ ) was 35.9GPa.

The used carbon fiber sheet is made in EPO Company, Germany, which is a kind of one-way sheet. The material properties of the CFRP in tension, determined from tensile tests of six flat coupons (as shown in Figure 3), are given in Table 4, where  $f_{cf}'$ ,  $E_{cf}$ ,  $\delta_{cf}$  and  $w_{cf}$  are tensile strength, elastic modulus, elongation percentage and density of the carbon fiber sheet respectively, and  $t_{cf}$  is thickness of one layer carbon fiber sheet.

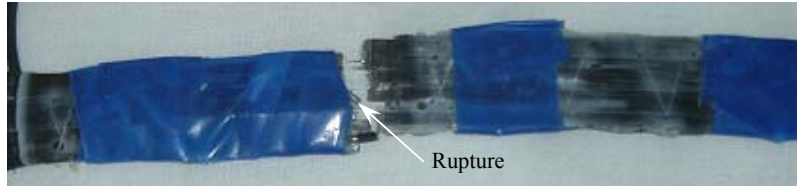


Figure 3. Typical Failed CFRP Coupon

Table 4. Main Technical Properties of Carbon Fiber Sheets

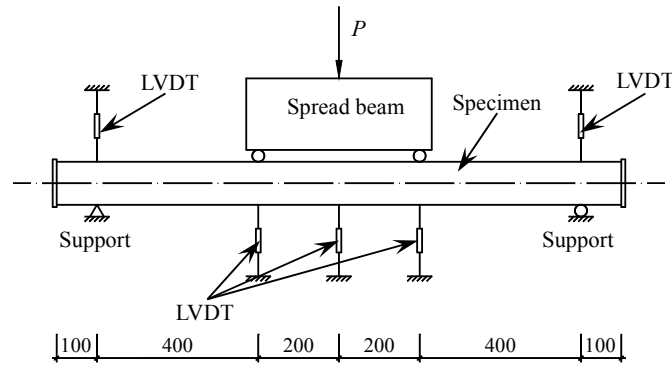
Model number	$f_{cf}'$ (GPa)	$E_{cf}$ (GPa)	$\delta_{cf}$ (%)	$w_{cf}$ (g·m <sup>-2</sup> )	$t_{cf}$ (mm)
C300/300	4.83	230	2.1	300	0.167

JGN-C, a kind of epoxy resin used for building structures produced by Building Science Research Institute of Liaoning Province, P. R. China, was used for adhering the CFRP to the steel tube. Another epoxy resin, JGN-P, was also used for gluing CFRPs together.

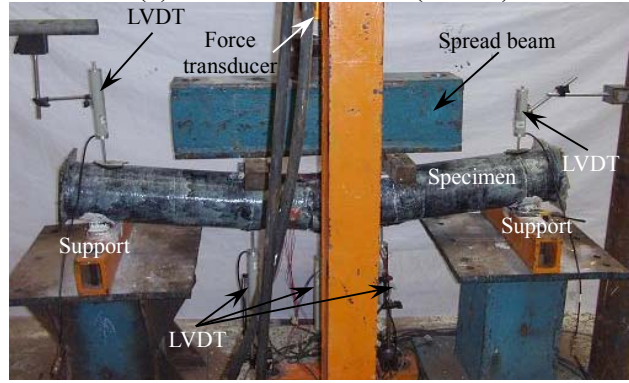
## 2.4 Test Setup and Instrumentation

The experimental test was carried out in the Structural Engineering Laboratory of Shenyang Jianzhu University, P. R. China. As shown in Figure 4, the specimen is simply supported at both ends. A jack which is located at the mid-span of the specimen is used to apply lateral load ( $P$ ), and the load is transferred by a spread beam with enough stiffness to the two tri-span points of the specimen. The load is applied in several steps. In the elastic stage, each loading step is 5.0 kN. When the applied load is about 60% of the estimated flexural load carrying capacity, the magnitude of the loading step reduces. The estimated flexural load carrying capacity is obtained by the following method: the transverse and the longitudinal CFRPs are transferred to equivalent steel tube, and then the flexural load carrying capacity can be calculated by using corresponding equations of C-CFST flexural members (Han [16]). However, the equivalent steel tube besides longitudinal CFRP is not considered in calculating the confinement factor of the steel tube ( $\xi_s$ ) (Han [17]). After the deflection at the mid-span exceeds  $L_0/50$ , displacement control is used till failure.

A force transducer with a capacity of 600kN was used to measure the loading magnitude. Three Linear Variable Differential Transformers (LVDTs) were placed to measure the deflection of the specimens. At the two supporting points, two LVDTs were also used to measure the settlements. Overall 11 strain gauges were glued on the surfaces of each steel tube and the CFRP around cross-section at mid-span of the specimens respectively, as shown in Figure 5, where points 1-7 were the locations for measuring longitudinal strains and points 1, 3, 5 and 8 were the locations for measuring transverse strain.



(a) General Placement (in mm)



(b) Test Figure

Figure 4. Test Arrangement

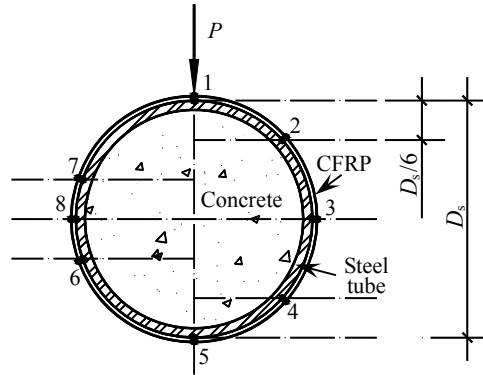


Figure 5. The Location of Strain Gauges

The data was captured and saved by data acquisition system U-CAM-70A, and the load ( $P$ ) versus deflection ( $u_m$ ) at mid-span curve was obtained simultaneously.

## 2.5 Test Observations and Failure Modes

For the specimens only reinforced with transverse CFRP, the failure process is gradual. During the initial loading stage, in general, the bending load presents an approximately proportional relationship to  $u_m$ . There are no obvious damages in the appearance of the specimens. New cracks between carbon fibers and extensions of existing cracks are observed during further loading. At the end of the tests, through-cracks are observed on the CFRP jackets in the pure-bending region and large deformation of the specimen appears. Finally, the transverse CFRP located at longitudinally compressed region begins to rupture as shown in Figure 6 (a).



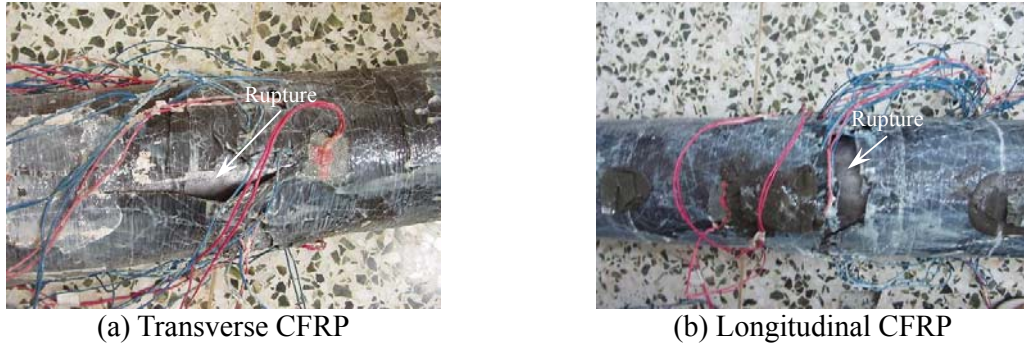


Figure 6. Rupture of CFRPs

For those specimens reinforced with longitudinal CFRP, longitudinal CFRP begins to rupture when the strain at the extreme fiber of the tensile region reaches about  $10000\mu\epsilon$ , which can be seen in Figure 6 (b). At this time, the flexural load carrying capacity of the beam decreases suddenly. The transverse CFRP located at longitudinally compressive region begins to rupture when the deformation of the specimen becomes larger in the later loading stage. The final failure modes of several specimens are shown in Fig. 7.

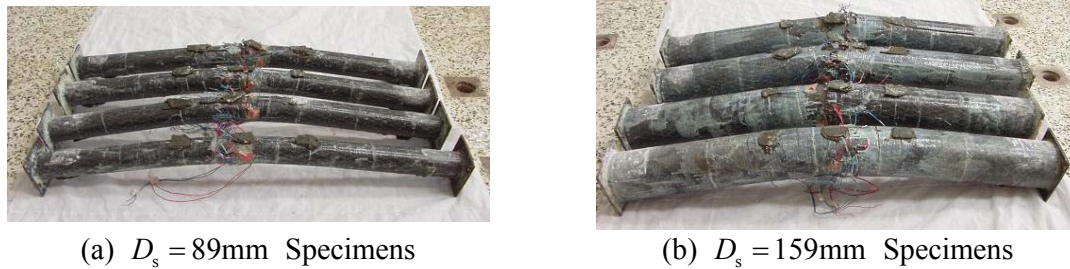


Figure 7. Typical Deformation of Several Specimens

The specimens are cut into two halves after the tests, as shown in Figure 8, to find that the concrete can be divided into both tensile and compressive regions. It can be seen that the concrete in longitudinally tensile region has some cracks while it is crushed in the region under longitudinal compression.

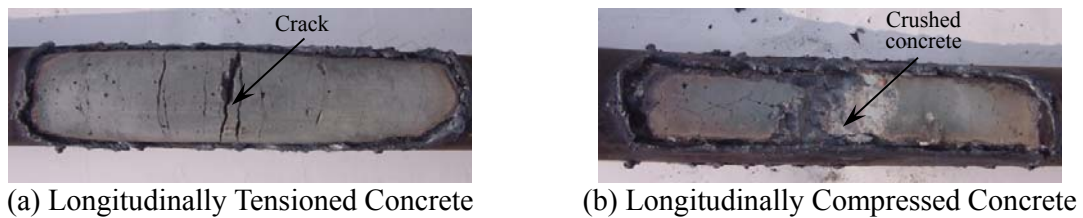


Figure 8. Failure Modes of Concrete

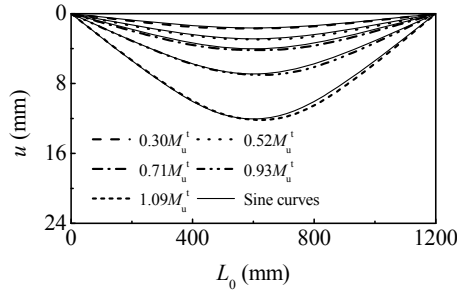


## 2.6 Test Results and Analysis

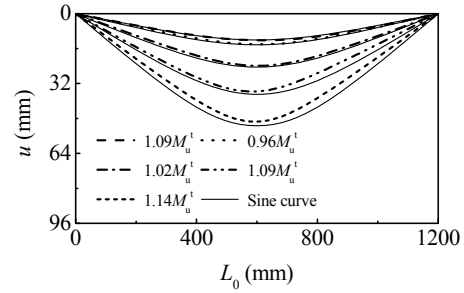
### 2.6.1 Tested $M$ - $\phi$ curves

Figure 9 shows the deflection ( $u$ ) curves of specimen CB D-3, where  $M_u^t$  is tested value of the flexural load carrying capacity ( $M_u$ ). All values of  $M_u^t$  are listed in Table 1. From Figure 9, it is found that the deflection of each specimen is very close to half sinusoidal curve. Therefore,  $\phi$  can be calculated from  $u_m$  approximately according to the following equation (Han, Yao and Zhao [18])

$$\phi = \pi^2 u_m / L_0^2 \quad (1)$$



(a) Before Rupture of Longitudinal CFRP

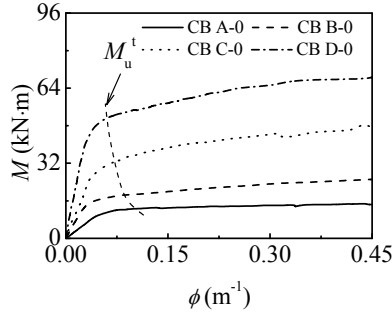


(b) After Rupture of Longitudinal CFRP

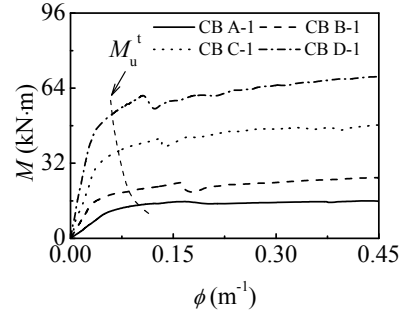
Figure 9. Deflection Curves of Specimen CB D-3

Figure 10 shows the  $M$  -  $\phi$  curves at mid-span of the specimens, where

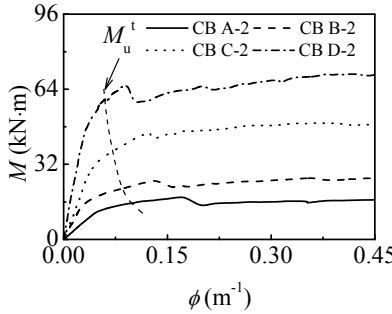
$$M = PL_0/6 \quad (2)$$



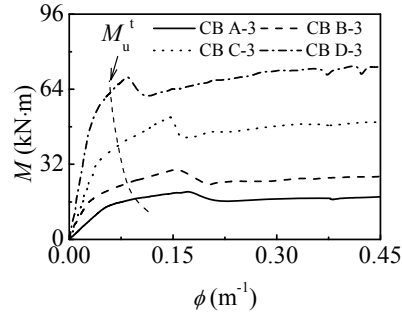
(a)  $m'=0$



(b)  $m'=1$



(c)  $m'=2$



(d)  $m'=3$

Figure 10. Tested  $M$  -  $\phi$  Curves

It is found that parameter  $m'$  has a remarkable effect on the curve shape of the C-CF-CFRP-ST flexural members. For specimens with  $m'=0$ , their curves are similar to those of the corresponding C-CFST flexural members (Han [16]). While for specimens with  $m' \neq 0$ , both the load and the deflection are smaller during the initial loading stage, and the relationship between them is approximately linear. This stage belongs to elastic stage. As load increases continuously, the deflection increases much more rapidly than before, and this stage belongs to elasto-plastic stage. The curve falls in softening stage after the longitudinal CFRP is ruptured, and the rest of the curves are similar to those of the corresponding C-CFST flexural members. For the specimens with  $m' \neq 0$ , their failure seems to be brittle. However, due to the existence of the steel tube, the specimens could still keep high flexural load carrying capacity even they are suffered from a large deformation.

### 2.6.2 Stiffness

According to the  $M-\phi$  curves shown in Figure 10, the initial flexural stiffness ( $K_{ie}$ ) and the service flexural stiffness ( $K_{se}$ ) (Verma et al. [19]) are defined. The relationship of  $K_{ie}-m'$  and  $K_{se}-m'$  is illustrated in Figure 11.  $K_{ie}$  and  $K_{se}$  are also listed in Table 1. As show in Figure 11,  $K_{ie}$  and  $K_{se}$  are both enhanced by the increase of  $m'$ . It is clear that the longitudinal CFRP can enhance the stiffness of the specimens significantly.

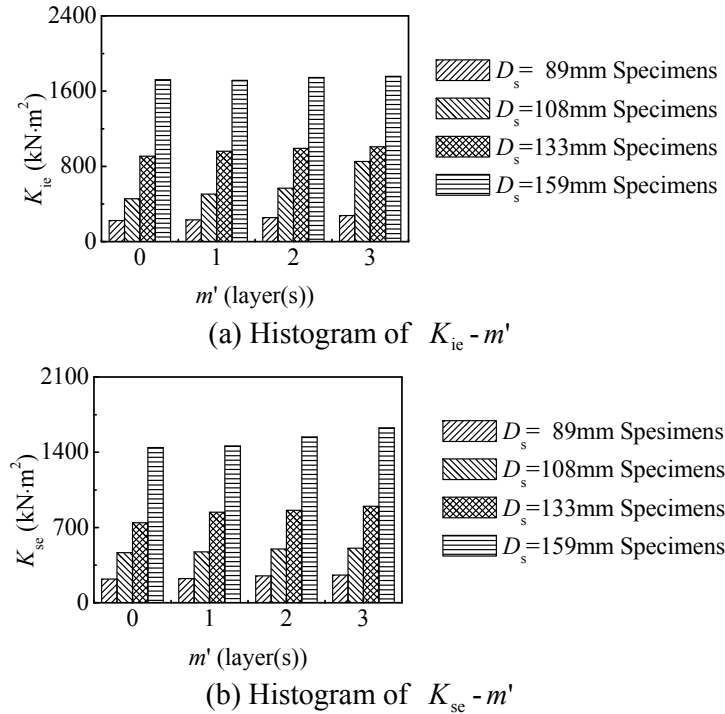


Figure 11. Stiffness versus  $m'$  Relationship

### 2.6.3 Cooperation between Steel Tube and CFRP

Figure 12 shows the comparison of strains between the steel tube and the CFRP, where  $\varepsilon_l$  and  $\varepsilon_t$  are longitudinal and transverse strains respectively. Similarly,  $\varepsilon_{sl}$  and  $\varepsilon_{cfl}$  are longitudinal strains of the steel tube and the CFRP respectively, and  $\varepsilon_{st}$  and  $\varepsilon_{cft}$  are transverse strains of the steel tube and the CFRP respectively. As shown in Figure 12,  $\varepsilon_{sl}$  and  $\varepsilon_{cfl}$  are basically the same, and

so is the relationship between  $\varepsilon_{st}$  and  $\varepsilon_{cft}$ . Additionally, from the observation of the cut CFRP-steel tubes after the experiment, it is found that the adherence between the CFRP and the steel tube is still intact except in the region where CFRP is ruptured. All above results indicate that steel tubes and CFRP can cooperate well in both longitudinal and transverse directions. Otherwise, as shown in Figure 12 (b), the distribution of transverse strains around the cross-section is not uniform: largest transversely tensile and compressive strains are located at point 5 and at point 1 respectively. Actually, the outer tube can be divided into a tensile region and a compressive region in transverse direction. Such classification depends on the fact that the outer tube is under tension or under compression in longitudinal direction. As the specimen is subjected to bending moment, part of the cross-section of the outer tube is under compression in longitudinal direction, which causes this part of the cross-section under tension in transverse direction. Accordingly, the other part of the cross-section of the outer tube is under tension in longitudinal direction, which causes this part of the cross-section under compression in transverse direction. This phenomenon has been proved from experimental measurement. Due to the above reason, the outer tube compressed transversely does not provide confinement effect for the concrete.

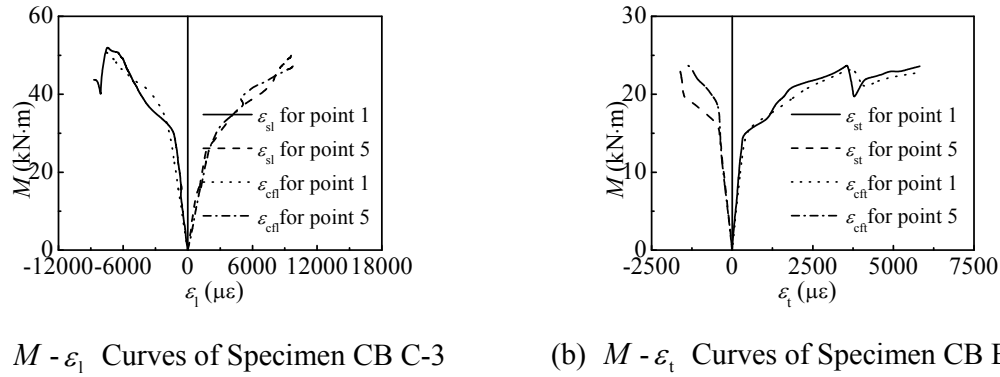
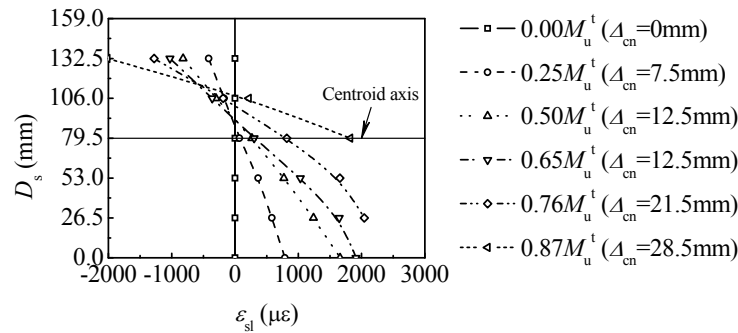


Figure 12. Comparisons of Strains between Steel Tube and CFRP

#### 2.6.4 Plane Section Assumption

Figure 13 shows the distribution of  $\varepsilon_{sl}$  over depth of the cross-section of the specimen with  $D_s = 133\text{mm}$ , where  $\Delta_{cn}$  is the distance measured from the neutral axis to the centroid axis. The distribution of  $\varepsilon_{sl}$  is basically in accordance with the plane section assumption. The neutral axis moves toward the compression region gradually as the moment increases.



(a) Specimen CB D-0

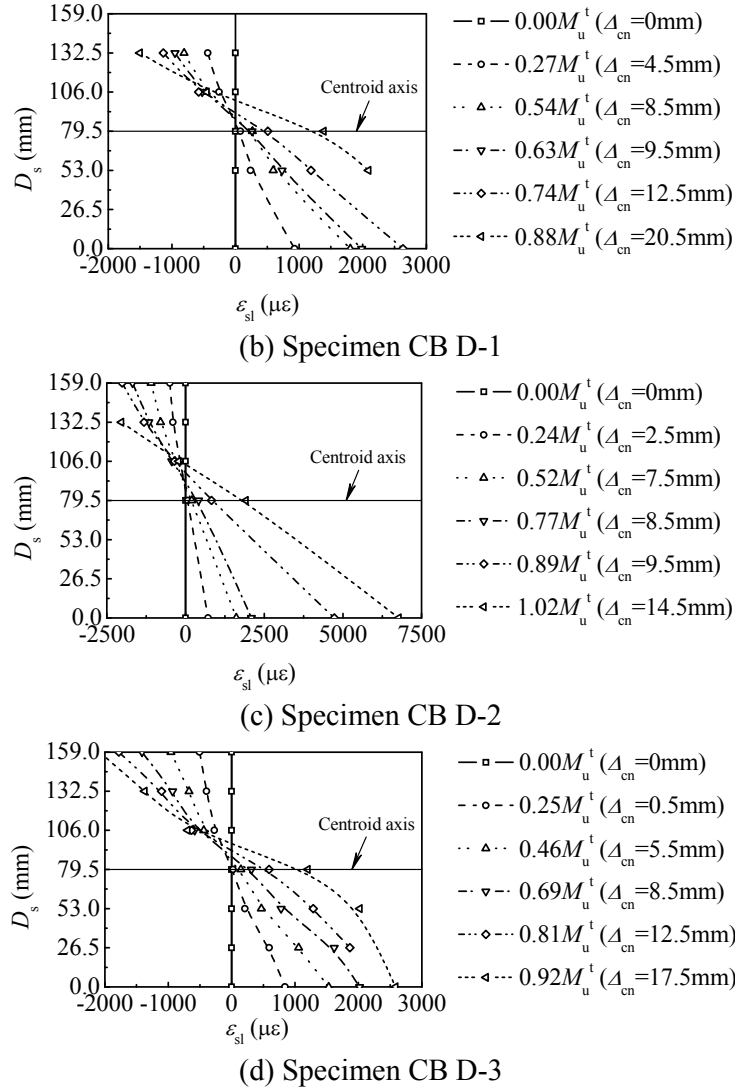


Figure 13. Distribution of  $\varepsilon_{sl}$  over Depth on Cross-Section of Specimens with  $D_s = 133\text{mm}$

### 3. FE SIMULATION

#### 3.1 Stress-Strain Relationship of Materials

A 5-stage stress-strain relationship of steel material (Han, Yao and Tao [20]) is used here. This stress-strain curve includes 5 segments: linear and elastic stage, nonlinear but elastic stage, plastic flowing stage, hardening stage and softening stage. The constitutive relationship of concrete confined by CFRP-steel tube under compression as well as under tension (Che, Wang and Shao [15]) is adopted. CFRP is assumed to be only able to sustain tension. Before fracture, the stress-strain relationship of CFRP is in accordance with Hooke's Law as follow

$$\sigma_{cf} = E_{cf} \varepsilon_{cf} \quad (3)$$

where  $\sigma_{cf}$  and  $\varepsilon_{cf}$  are the stress and strain of CFRP respectively.

When longitudinal CFRP reaches its rupture strain ( $\varepsilon_{\text{cflr}} = 10000 \mu\epsilon$ ). Rupture strain of the longitudinal CFRP for each specimen measured from experimental test ( $\varepsilon_{\text{cflr}}'$ ) is tabulated in Table 1. The value of  $\varepsilon_{\text{cflr}}$  is determined from the average value of all measured  $\varepsilon_{\text{cflr}}'$ , it loses longitudinal strengthening effect to the members. However, when transverse CFRP reaches its rupture strain ( $\varepsilon_{\text{cft}} = 5500 \mu\epsilon$ ) (Che, Wang and Shao [15]), it loses transverse confinement to the steel tube.

An interesting point is stressed here that CFRP has three rupture strains, i. e., for the transverse CFRP,  $\varepsilon_{\text{cft}} = 5500 \mu\epsilon$ ,  $\phi = 12.5 - 22.5 \text{ m}^{-1}$ ; for the longitudinal CFRP,  $\varepsilon_{\text{cflr}} = 10000 \mu\epsilon$ ,  $\phi = 0.1 - 0.2 \text{ m}^{-1}$ ; while for the CFRP coupon,  $\delta_{\text{cf}} = 2.1\% = 21000 \mu\epsilon$ ,  $\phi = 0$ . This means the rupture strain may decrease with a bigger curvature. Similar conclusion can be found from the reported research work (Yu et al. [21]). The above defined rupture strains of the CFRPs in longitudinal and in transverse directions are used in finite element simulation.

In the research work on CFST (Han [17]), the confinement of steel tube to concrete is represented by a confinement factor of the steel tube ( $\xi_s$ ). Similarly, the confinement of the transverse CFRP can be also represented by a confinement factor of the transverse CFRP ( $\xi_{\text{cf}}$ ) (Che, Wang and Shao [15]), and the strengthening efficiency of longitudinal CFRP may be represented by a strengthening factor of the longitudinal CFRP ( $\eta$ ). The definitions of all the confinement or strengthening factors are listed as follows:

$$\xi_s = A_s f_y / (A_c f_{\text{ck}}) \quad (4)$$

$$f_{\text{ck}} = 0.67 f_{\text{cu}} \quad (5)$$

$$\xi_{\text{cf}} = A_{\text{cft}} f_{\text{cft}} / (A_c f_{\text{ck}}) \quad (6)$$

$$f_{\text{cft}} = E_{\text{cf}} \varepsilon_{\text{cft}} = 1260 \text{ MPa} \quad (7)$$

$$\eta = A_{\text{cfl}} f_{\text{cfl}} / (A_s f_y) \quad (8)$$

$$f_{\text{cfl}} = E_{\text{cf}} \varepsilon_{\text{cflr}} = 2300 \text{ MPa} \quad (9)$$

where  $A_s$  is cross-sectional area of the steel tube;  $A_c$  and  $f_{\text{ck}}$  are cross-sectional area and characteristic axial compressive strength of the concrete respectively;  $A_{\text{cft}}$  and  $f_{\text{cft}}$  are cross-sectional area and ultimate tensile strength of the transverse CFRP respectively;  $A_{\text{cfl}}$  and  $f_{\text{cfl}}$  are cross-sectional area and ultimate tensile strength of the longitudinal CFRP respectively.

## 3.2 FE Model

### 3.2.1 Element type selection

Shell element S4 with full integration is selected for discretizing the steel tube in finite element model. Simpson integration with 9 integrating points in the shell thickness direction is used. For the core concrete, 3-D brick elements C3D8R with reduced integration are used. Membrane element

M3D4 with 4-nodes is used for modelling CFRP.

### 3.2.2 Mesh discretization

The convergent analysis is carried out by using refined mesh in finite element analysis, and the details can be referred to relative research (Che, Wang and Shao [15]). Figure 14 shows the FE mesh of a typical model.

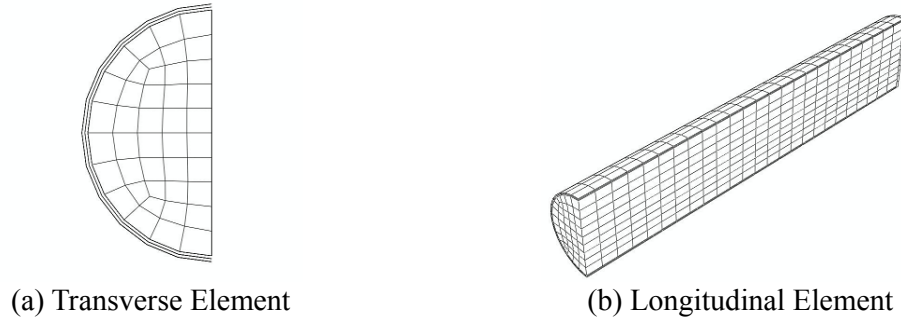


Figure 14. Mesh Discretization

### 3.2.3 Interface model

Hard contact is used for defining contact interface between steel tube and concrete, i.e., the pressure perpendicular to the contact surfaces ( $p$ ) can be transferred completely between the two surfaces (Han, Liu and Yang [22]). The tangential force between the steel tube and the concrete surface is simulated by using Coulumb model, i.e., shear force can be transferred between surfaces (Han, Liu and Yang [22]). In the experimental tests, CFRP is bound to the steel tube, and it is assumed that no slip exists between CFRP and the steel tube. Same nodal freedoms are used for the contact elements between CFRP and the steel tube. In the tangential direction of the contact surfaces between the end plate and the concrete, there is also no slipping, and hard contact assumption is used in normal direction of the contact surfaces.

### 3.2.4 Boundary conditions

Boundary conditions are shown in Figure 15, which are in accordance with experimental process. According to the symmetry of both the geometry and the boundary condition, 1/4 model is selected for FE analysis. On the symmetrical plane of the model, symmetrical constraints are applied. The displacement in  $y$ -direction at the supporting points is constrained.

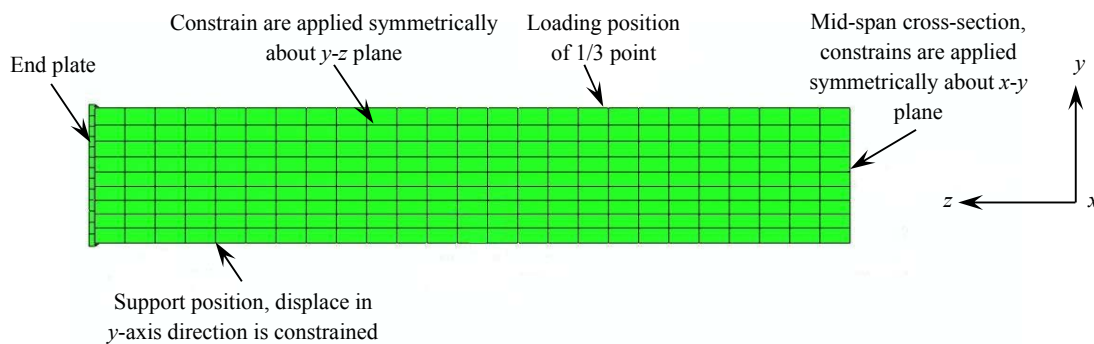


Figure 15. Boundary Conditions

### 3.3 FE Results

#### 3.3.1 Failure modes

To verify the reliability of the above presented FE method, overall 16 C-CF-CFRP-ST flexural specimens are analyzed by using ABAQUS software. Figure 16 shows the deformation obtained from experimental test and FE simulation. From Figure 16, it can be found that the FE predicted deformation of the specimen is quite similar to the experimental observation.

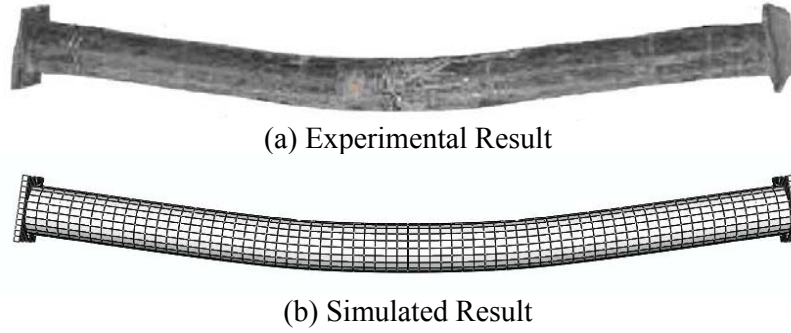
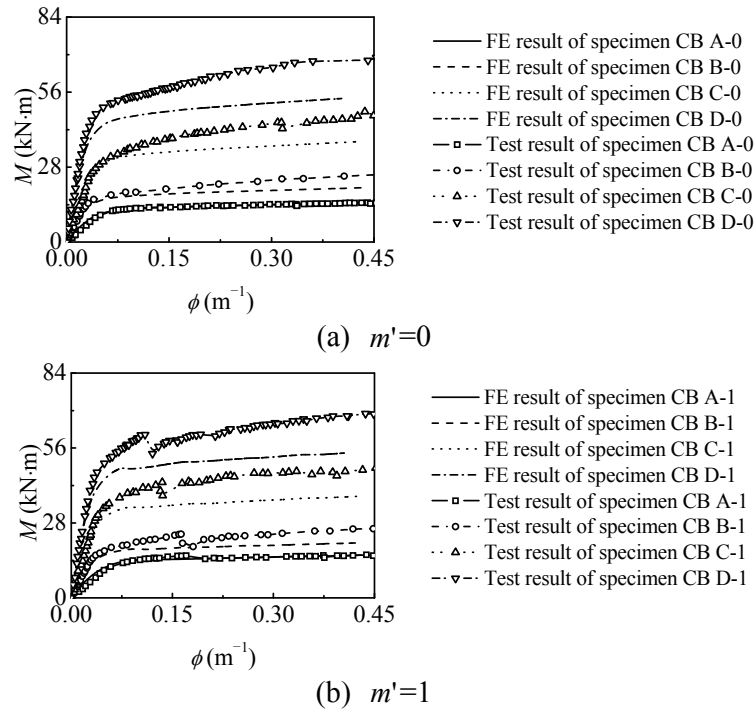


Figure 16. Comparison of Deformations

#### 3.3.2 $M$ - $\phi$ curves

The FE  $M$ - $\phi$  curves together with the experimentally measured results are plotted in Figure 17. In the FE simulation, the deflection of the specimens can be obtained from FE analysis, and the curvature is then calculated from Eq. (1). It can be found from Figure 17 that the FE results are reasonable compared with the experimental results although the FE predictions seem to be a little lower.





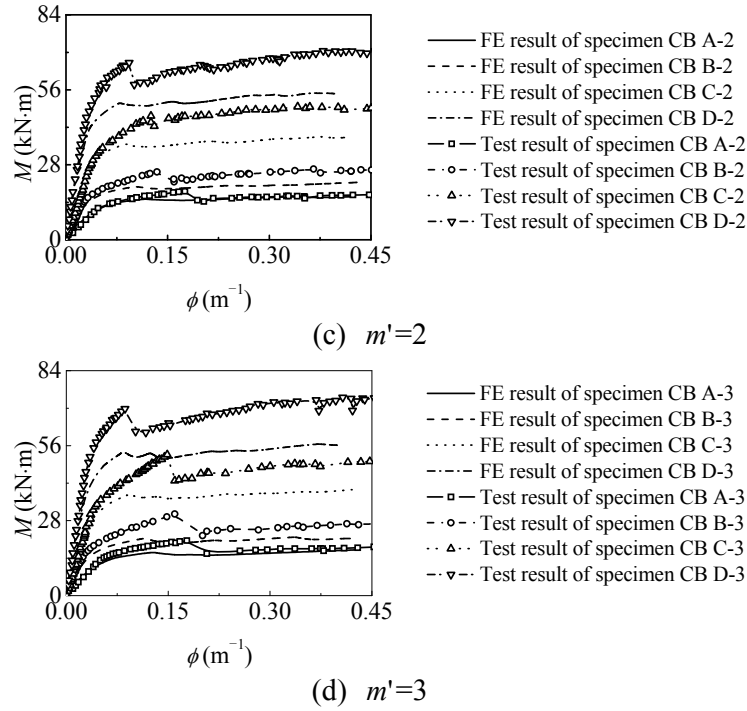


Figure 17. Comparison of  $M - \phi$  Curves between FE Result and Experimental Result

#### 4. THEORETICAL ANALYSIS

Three typical points, as shown in Figure 18, are selected for discussion: at point 1, the tensile extreme fiber of the steel tube reaches its proportional limit; at point 2, longitudinal CFRP is fractured; and at point 3, the deflection at the mid-span is about  $L_0/25$ .

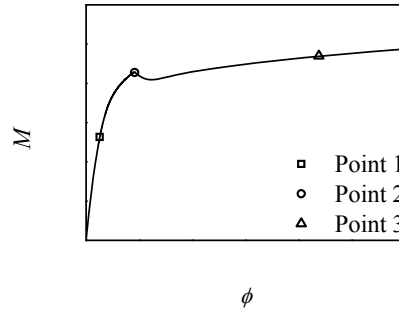


Figure 18. Typical Points in  $M - \phi$  Curve

##### 4.1 Longitudinal Stress and Strain of Concrete on Cross-Section at Mid-Span

Figures 19 and 20 show the distributions of the longitudinal strain and the longitudinal stress of concrete on the cross-section at mid-span respectively ( $D_s = 400\text{mm}$ ,  $t_s = 9.31\text{mm}$ ,  $L_0 = 4000\text{mm}$ ,  $f_y = 345\text{MPa}$ ,  $f_{cu} = 60\text{MPa}$ ,  $\xi_{cf} = 0.115$ ,  $\eta = 0.13$ ,  $E_s = 206\text{GPa}$ ,  $\nu_s = 0.3$ ,  $E_c = 4700\sqrt{f'_c}\text{MPa}$ , (where  $f'_c$  is strength of the cylinder concrete specimens, and  $f'_c \approx 0.8f_{cu}$ ), Poisson's ratio of the concrete ( $\nu_c$ ) was 0.2).

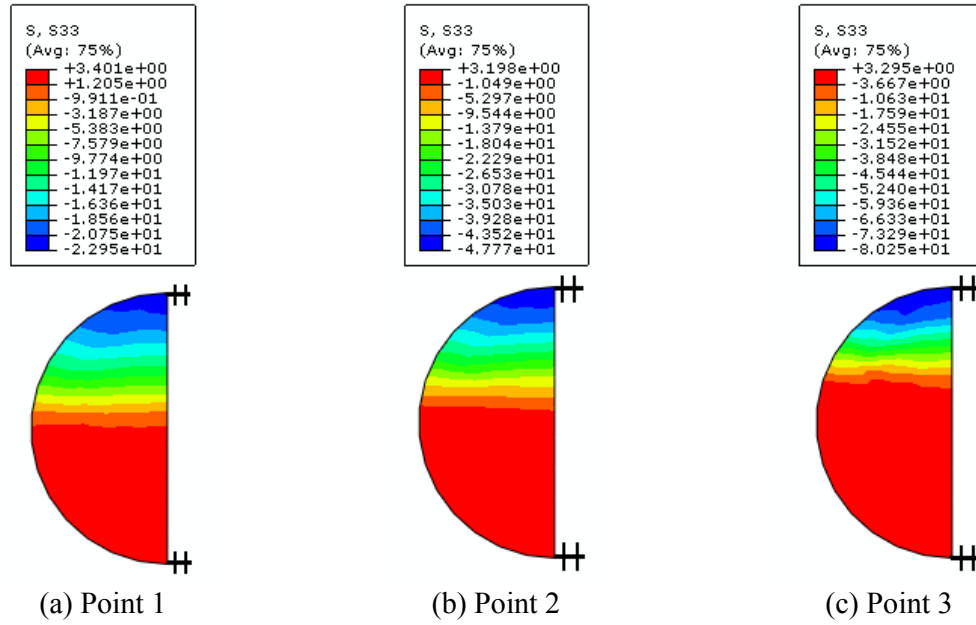


Figure 19. Longitudinal Stress Distribution of Concrete on Cross-Section at Mid-span

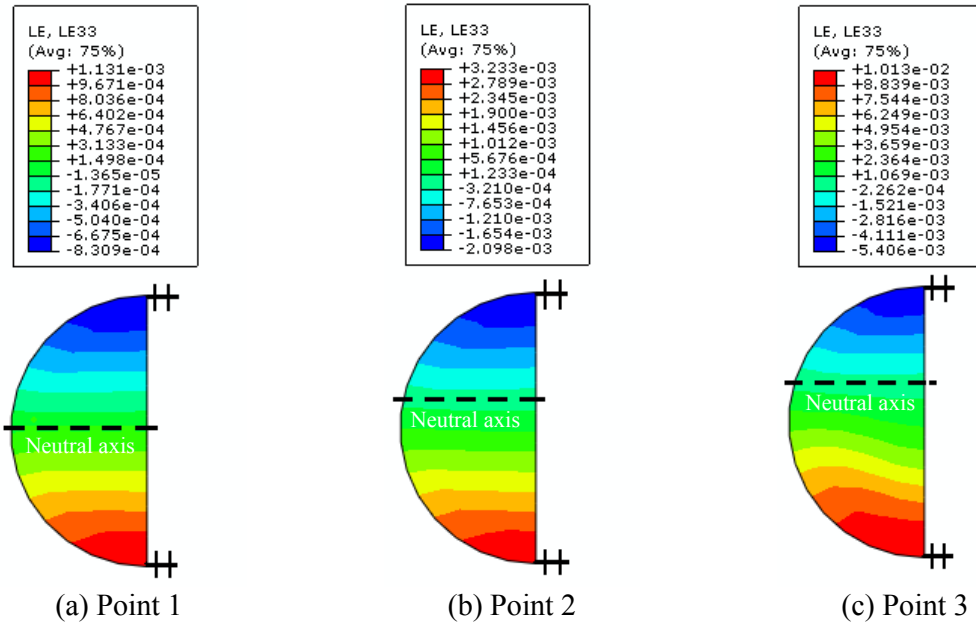


Figure 20. Longitudinal Strain Distribution of Concrete on Cross-Section at Mid-span

It is found that the neutral axis moves toward the compressive region gradually with the increase of the curvature at the mid-span, and this is in accordance with experimental results as shown in Figure 13. In elastic stage (before point 1), the neutral axis is very close to the centroid of the cross-section, and the steel tube and CFRP are both in elastic stage and the maximum longitudinal stress of the compressive concrete is less than  $f_c'$ . In the elasto-plastic stage (between point 1 and point 2), plastic region forms. In this stage, the longitudinal CFRP is not fractured, and it can still restrict the deformation of the flexural member. At point 2, strain of the longitudinal CFRP reaches

about 1000µε and the longitudinal CFRP begins to fracture. The maximum longitudinal stress of the concrete in the compressive region is close to  $f'_c$ . In the stage between point 2 and point 3, the longitudinal stress of the steel tube increases continuously with the development of the deflection. The area of the tensile concrete region increases. At point 3, the maximum longitudinal stress of the compressive concrete exceeds  $f'_c$ .

The longitudinal stress distribution of the concrete in axial direction is shown in Figure 21. The longitudinal stress in pure-bending segment of the member distributes uniformly in axial direction. The maximum longitudinal stress is located at the extreme fiber of the specimen.

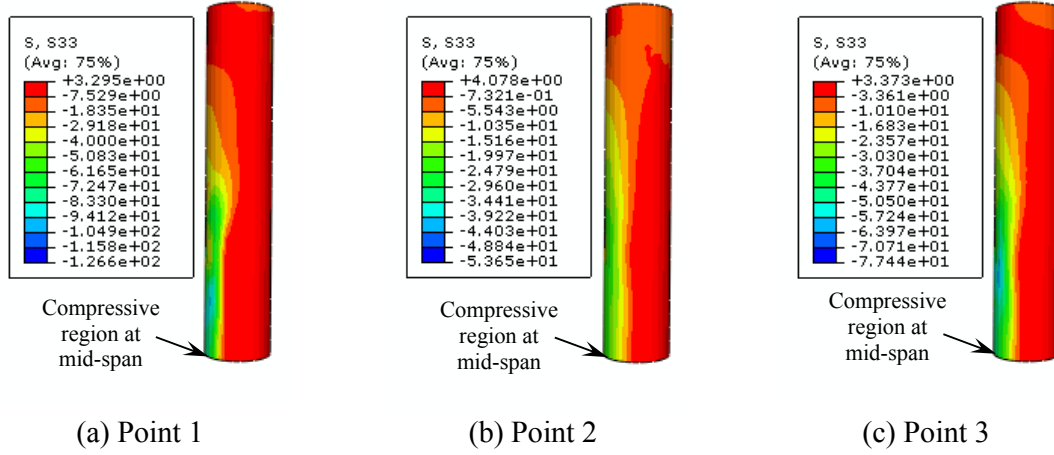


Figure 21. Distribution of Longitudinal Stress of Concrete along Axial Direction

#### 4.2 Influence of $\eta$

Figure 22 shows the influence of  $\eta$  on the position of the neutral axis on the cross-section at mid-span during elasto-plastic stage ( $D_s = 160\text{mm}$ ,  $t_s = 4.5\text{mm}$ ,  $f_y = 345\text{MPa}$ ,  $f_{cu} = 60\text{MPa}$ ,  $L_0 = 1400\text{mm}$ ,  $\xi_{cf} = 0.1$ ,  $\eta = 0 - 0.4$ ,  $E_s = 206\text{GPa}$ ,  $\nu_s = 0.3$ ,  $E_c = 4700\sqrt{f'_c}\text{MPa}$ , and  $\nu_c = 0.2$ ). The neutral axis has a little offset toward the tensile region of the concrete.

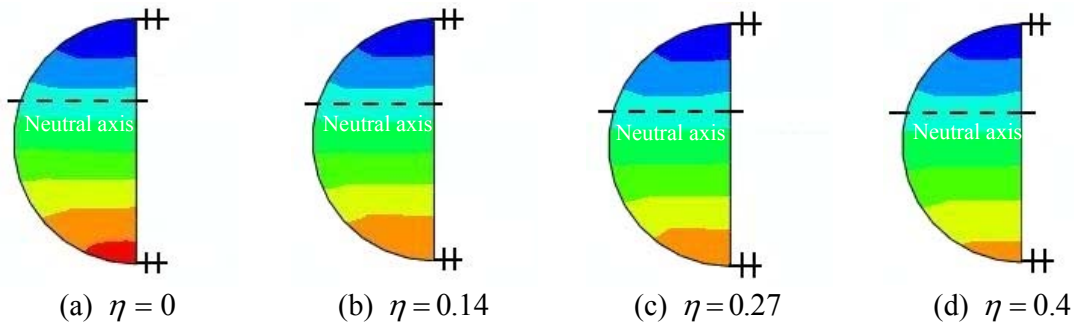


Figure 22. Influence of  $\eta$  on Position of Neutral Axis

Figure 23 shows the effect of  $\eta$  on the longitudinal stress distribution on the cross-section at mid-span. It is clear that the longitudinal compressive stress of the concrete increases a little as  $\eta$  increases.

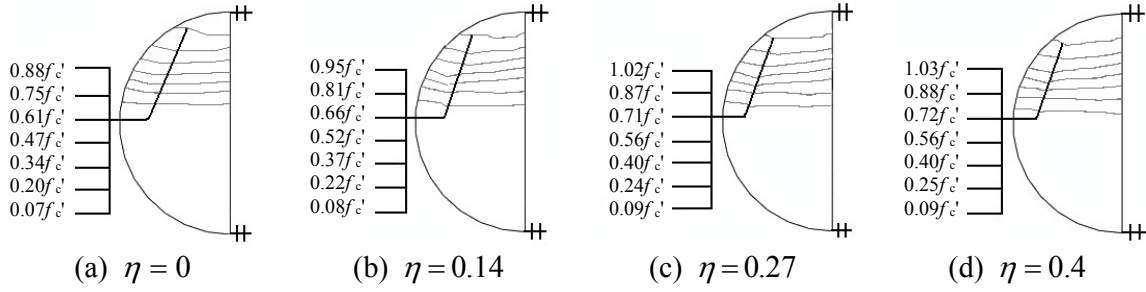


Figure 23. Influence of  $\eta$  on Distribution of Longitudinal Stress of Concrete

### 4.3 Interaction Force between Concrete and Steel Tube

Figure 24 shows the interaction forces ( $p$ ) between the concrete and the outer tube on the cross-section at mid-span ( $D_s = 160\text{mm}$ ,  $t_s = 4.5\text{mm}$ ,  $f_y = 345\text{MPa}$ ,  $f_{cu} = 60\text{MPa}$ ,  $L_0 = 1400\text{mm}$ ,  $\xi_{cf} = 0.0976$ ,  $\eta = 0.169$ ,  $E_s = 206\text{GPa}$ ,  $\nu_s = 0.3$ ,  $E_c = 4700\sqrt{f'_c}\text{MPa}$ , and  $\nu_c = 0.2$ ). Interaction force with a large magnitude also exists between the tensile steel tube and the concrete. However, it is different in essence for the interaction forces in the compressive region and in the tensile region of the concrete. In the compressive region, steel tube restricts the expansion of concrete, which produces confinement force. While in the tensile region, the steel tube is under tension in longitudinal direction but under contraction in transverse direction. Concrete also contracts in transverse direction. However, the transverse deformation of the concrete is much smaller than that of the steel tube (especially after the cracking of the concrete). Thus, the transverse deformation of the steel tube is restrained by the concrete, and the reaction force between steel tube and concrete then initiates. However, this interaction force is not the confinement force.

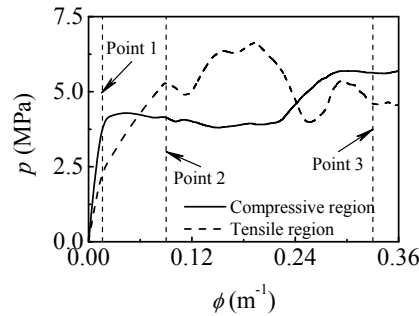


Figure 24. Interaction Force between Outer Tube and Concrete on Cross-Section at Mid-Span

## 5. FLEXURAL LOAD CARRYING CAPACITY

### 5.1 Definition of Flexural Load Carrying Capacity

The calculated results of the FE models ( $f_y = 235\text{--}390\text{MPa}$ ,  $f_{cu} = 30\text{--}120\text{MPa}$ ,  $\xi_s = 0.2\text{--}4$ ,  $\xi_{cf} = 0\text{--}0.6$ ,  $\eta = 0\text{--}0.9$ ,  $E_s = 206\text{GPa}$ ,  $\nu_s = 0.3$ ,  $E_c = 4700\sqrt{f'_c}\text{MPa}$ , and  $\nu_c = 0.2$ ) show that the bending moment corresponding to the tensile strains at the extreme fiber reaching  $\varepsilon_{\max}$  is the flexural load carrying capacity ( $M_u$ ), and  $\varepsilon_{\max}$  is defined in this study as follow:

$$\varepsilon_{\max} = 2837 + 166800/D_s \quad (10)$$

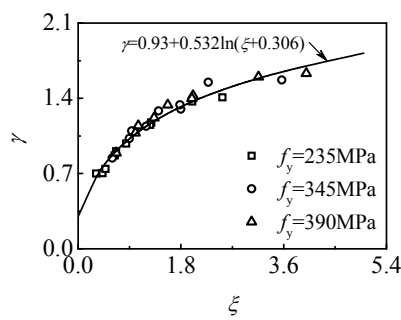
where  $D_s$  is in mm.

Eq. (10) is obtained using regression analysis based on a parametric study on the calculated FE models. In Eq. (10), the bending moment at this time ( $\varepsilon_{\max}$ ) is larger than the elastic limit value but less than the plastic ultimate moment. Partial section of the steel tube is already in yielding state, and the deflection at this time is about  $L_0/100$ .

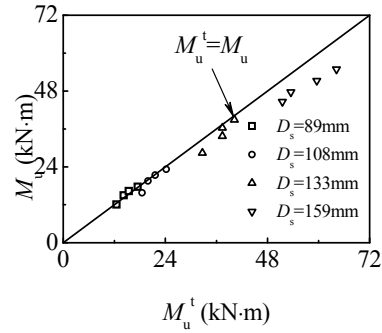
It is clarified here that  $M_u^t$  shown in Figure 10 is actually determined by  $\varepsilon_{\max}$ . In Eq. (10),  $\varepsilon_{\max}$  of each specimen can be firstly calculated. The bending moment corresponding to  $\varepsilon_{\max}$  is then defined as  $M_u^t$ .

## 5.2 Parametric Equation of Load Carrying Capacity

The flexural load carrying capacity of the member with only transverse CFRP ( $M_0$ ) is determined firstly.  $M_0$  is mainly related to the flexural modulus ( $W_{cfscm} = \pi D_s^3/32$ ), the total confinement coefficient ( $\xi$ ) (Che, Wang and Shao [15]) and the index of axial compressive load carrying capacity ( $f_{cfscy}$ ) (Che, Wang and Shao [15]) of C-CF-CFRP-ST stub columns. Based on a parametric study on amount of FE models, the relationship between  $\gamma = M_0/(W_{cfscm}f_{cfscy})$  and  $\xi$  is obtained, and it is shown in Figure 25 (a).



(a)  $\gamma$ - $\xi$  Relationship



(b) Comparison between  $M_u$  and  $M_u^t$

Figure 25. Flexural Load Carrying Capacity

The relationship between  $\gamma$  and  $\xi$  can also be presented as well and it is listed as follow:

$$\gamma = 0.93 + 0.532 \ln(\xi + 0.306) \quad (11)$$

$$\xi = \xi_s + \xi_{cf} \quad (12)$$

Hence

$$M_0 = \gamma W_{cfscm} f_{cfscy} \quad (13)$$

where

$$f_{cfscy} = [1.14 + 1.02(\xi_s + 3\xi_{cf})]f_{ck} \quad (14)$$

When the member has both transverse and longitudinal CFRPs, the relationship between  $\gamma_m = M_u / (W_{cfscm} f_{cfscy})$  and  $\eta$  can be obtained as follow

$$\gamma_m = \gamma + (0.3 + 0.2\xi)\eta \quad (15)$$

Thus, the flexural load carrying capacity of the C-CF-CFRP-ST members ( $M_u$ ) is given as follow:

$$M_u = \gamma_m W_{cfscm} f_{cfscy} \quad (16)$$

### 5.3 Validation of Equation

Figure 25 (b) displays comparison between the calculated flexural load carrying capacity  $M_u$  and the tested value  $M_u^t$ . The average value of  $M_u / M_u^t$  is 0.96, and the mean square error is 0.07. That means the two results agree well.

## 6. CONCLUSIONS

Based on the experimental study, the finite element simulation, and the theoretical analysis, the following conclusions can be drawn: (1) The  $M-\phi$  curves at mid-span of circular concrete filled CFRP-steel tubular flexural specimens without longitudinal CFRP reinforcement are similar to those of the corresponding circular concrete filled steel tubular flexural members, while  $M-\phi$  curves at mid-span of C-CF-CFRP-ST flexural specimens with longitudinal CFRP reinforcement can be defined as elastic stage, elasto-plastic stage and softening stage. Thereafter, the rest of the curves are similar to those of the corresponding C-CFST flexural members. The stiffness of the specimen can be enhanced by the longitudinal CFRP. (2) The steel tube and the CFRP tube can cooperate well both in transverse and in longitudinal directions. The distribution of the longitudinal strain of the specimens over the depth of the cross-section meets the plane section assumption approximately. The shape of the deflection-curve is basically similar to half sinusoidal curves. (3) The finite element simulation results of the deformation and  $M-\phi$  curves of C-CF-CFRP-ST flexural members agree well with experimental results. (4) Interaction forces between the outer tube and the core concrete exist not only in the compressive region but also in the tensile region. However, the mechanisms of the interaction forces in the two regions are essentially different. (5) The flexural load carrying capacity of C-CF-CFRP-ST is defined, and the calculating equation of the flexural load carrying capacity is given.

## ACKNOWLEDGEMENTS

The research reported in the paper is part of the Project 51378320 supported by Natural Science Foundation of China (NSFC) and the Project 2013003004 supported by Public Welfare Foundation of Liaoning Province, P R China. Their financial supports are highly appreciated.

## NOMENCLATURE

$A_c$	: Cross-sectional area of concrete
$A_{cfl}$	: Cross-sectional area of longitudinal CFRP
$A_{cft}$	: Cross-sectional area of transverse CFRP
$A_s$	: Cross-sectional area of steel tube
C-CF-CFRP-ST	: Circular concrete filled CFRP-steel tubes
C-CFST	: Circular concrete filled steel tubes
CF-CFRP-ST	: Concrete filled CFRP steel tubes
CF-CFRP-T	: Concrete filled CFRP tubes
CFRP	: Carbon fiber reinforced polymer
CFST	: Concrete-filled steel tubes
CFT	: Concrete-filled tubes
$D_s$	: Outer diameter of steel tube
$E_c$	: Elastic modulus of concrete
$E_{cf}$	: Elastic modulus of carbon fiber sheets
$E_s$	: Elastic modulus of steel tube
$f_{cfscy}$	: Load carrying capacity index of axial compressive strength of circular concrete filled CFRP-steel tubular (C-CF-CFRP-ST) stub columns
$f_{cfl}$	: Ultimate tensile strength of longitudinal CFRP
$f_{cft}$	: Ultimate tensile strength of transverse CFRP
$f_{ck}$	: Characteristic axial compressive strength of concrete
$f_{cu}$	: Cubic strength of concrete
$f_u$	: Ultimate strength of steel tube
$f_y$	: Yield strength of steel tube
$f'_c$	: Compressive strength of cylinder concrete specimens
$f'_{cf}$	: Tension strength of carbon fiber sheet
$K_{ie}$	: Initial flexural stiffness
$K_{se}$	: Service flexural stiffness
$L$	: Length of specimens
$L_0$	: Net span of specimens
$M$	: Moment at mid-span
$M_0$	: Flexural load carrying capacity of circular concrete filled CFRP-steel tubular (C-CF-CFRP-ST) member with only transverse CFRP
$M_u$	: Flexural load carrying capacity of circular concrete filled CFRP-steel tubular (C-CF-CFRP-ST) member with both transverse CFRP and longitudinal CFRP
$M_u^t$	: Tested value of $M_u$
$m$	: Number of transverse CFRP layer
$m'$	: Number of longitudinal CFRP layer(s)
$P$	: Lateral load
$p$	: Interaction force between concrete and outer tube
$t_{cf}$	: Thickness of one layer carbon fiber sheet
$t_s$	: Wall thickness of steel tube



$u$	: Deflection
$u_m$	: Deflection at mid-span
$\nu_c$	: Poisson's ratio of concrete
$\nu_s$	: Poisson's ratio of steel tube
$W_{cfscm}$	: Flexural modulus
$w_{cf}$	: Density of carbon fiber sheet
$\delta_{cf}$	: Elongation percentage of carbon fiber sheet
$\Delta_{cn}$	: Distance measured from neutral axis to centroid axis
$\varepsilon_{cf}$	: Strain of CFRP
$\varepsilon_{cfl}$	: Strain of longitudinal CFRP
$\varepsilon_{cft}$	: Strain of transverse CFRP
$\varepsilon_{cflr}$	: Rupture strain of longitudinal CFRP
$\varepsilon_{cflr}'$	: Rupture strain of longitudinal CFRP for each specimen measured from test
$\varepsilon_{cfr}$	: Rupture strain of transverse CFRP
$\varepsilon_l$	: Longitudinal strain
$\varepsilon_{max}$	: Tensile strain at extreme fiber of specimens corresponding to $M_u$
$\varepsilon_{sl}$	: Longitudinal strain of steel tube
$\varepsilon_{st}$	: Transverse strain of steel tube
$\varepsilon_t$	: Transverse strain
$\phi$	: Curvature at mid-span
$\gamma$	: Coefficient, $= M_0 / (W_{cfscm} f_{cfscy})$
$\gamma_m$	: Coefficient, $= M_u / (W_{cfscm} f_{cfscy})$
$\eta$	: Strengthening factor of longitudinal CFRP
$\sigma_{cf}$	: Stress of CFRP
$\xi$	: Total confinement factor
$\xi_{cf}$	: Confinement factor of CFRP
$\xi_s$	: Confinement factor of steel tube

## REFERENCES

- [1] Han, L. H., "Tests on Concrete Filled Steel Tubular Columns with High Slenderness Ratio", *Advances in Structural Engineering*, 2000, Vol. 3, No. 4, pp. 337-344.
- [2] Tao, Z., Uy, B., Han, L. H. and Wang, Z. B., "Analysis and Design of Concrete-filled Stiffened Thin-walled Steel Tubular Columns under Axial Compression", *Thin-Walled Structures*, 2009, Vol. 47, No. 12, pp. 1544-1556.
- [3] Georgios, G. and Lam, D., "Axial Capacity of Circular Concrete-filled Tube Columns", *Journal of Constructional Steel Research*, 2004, Vol. 60, No. 7, pp. 1049-1068.
- [4] Uy, B., "Strength of Short Concrete Filled High Strength Steel Box Columns", *Journal of Constructional Steel Research*, 2001, Vol. 57, No. 2, pp. 113-134.
- [5] Han, L. H. and Yang, Y. F., "Cyclic Performance of Concrete-filled Steel CHS Columns under Flexural Loading", *Journal of Constructional Steel Research*, 2005, Vol. 61, No. 4, pp. 423-452.

- [6] Han, L. H. and Li, W., "Seismic Performance of CFST Column to Steel Beam Joint with RC Slab: Experiments", *Journal of Constructional Steel Research*, 2010, Vol. 66, No. 11, PP. 1374-1386.
- [7] Han, L. H., Wang, W. H. and Yu, H. X., "Experimental Behaviour of Reinforced Concrete (RC) Beam to Concrete-filled Steel Tubular (CFST) Column Frames Subjected to ISO-834 Standard Fire", *Engineering Structures*, 2010, Vol. 32, No. 10, pp. 3130-3144.
- [8] Han, L. H., Hou, C. and Wang, Q. L., "Square Concrete Filled Steel Tubular (CFST) Members under Loading and Chloride Corrosion: Experiments", *Journal of Constructional Steel Research*, 2012, Vol. 71, No. 1, pp. 11-25.
- [9] Wang, Y. C. and Restrepo, J. I., "Investigation of Concentrically Loaded Reinforced Columns Confined with Glass Fiber-reinforced Polymer Jackets", *Structure Journal*, 2001, Vol. 98, No. 3, pp. 377-385.
- [10] Teng, J. G., Chen, J. F., Smith, S. T. and Lam, L., "FRP Strengthened RC Structures", John Wiley & Sons Ltd., 2002.
- [11] Han, L. H., Tao, Z. and Wang, W. D., "Advanced Composite and Mixed Structures-Testing, Theory and Design Approach", China Science Press, 2009. (in Chinese)
- [12] Tao, Z., Han, L. H. and Wang, L. L., "Compressive and Flexural Behaviour of CFRP Repaired Concrete-filled Steel Tubes after Exposure to Fire", *Journal of Constructional Steel Research*, 2007, Vol. 63, No. 8, pp. 1116-1126.
- [13] Xiao, Y., He, W. H. and Choi, K. K., "Confined Concrete-filled Tubular Columns." *Journal of Structural Engineering*, 2005, Vol. 131, No. 3, pp. 488-497.
- [14] Choi, K. K. and Xiao, Y., "Analytical Model of Circular CFRP Confined Concrete-Filled Steel Tubular Columns under Axial Compression", *Journal of Composites for Construction*, 2010, Vol. 14, No. 1, pp. 125-133.
- [15] Che, Y., Wang, Q. L. and Shao, Y. B., "Compressive Performances of the Concrete Filled Circular CFRP-steel Tube (C-CFRP-CFST)", *International Journal of Advanced Steel Construction*, 2012, Vol. 8, No. 4, pp. 311-338.
- [16] Han, L. H., "Flexural Behaviour of Concrete Filled Steel Tubes", *Journal of Constructional Steel Research*, 2004, Vol. 60, No. 2, pp. 313-337.
- [17] Han, L. H., "Fire Resistance of Concrete Filled Steel Tubular Columns", *Advances in Structural Engineering*, 1998, Vol. 2, No. 1, pp. 35-39.
- [18] Han, L. H., Yao, G. H. and Zhao, X. L., "Behavior and Calculation on Concrete-filled Steel CHS (Circular Hollow Section) Beam-columns", *Steel and Composite Structures*, 2004, Vol. 4, No. 3, pp. 169-188.
- [19] Verma, A. H., Ricles, J. M., Sause, R. and Lu, L. W., "Seismic Behaviour and Modeling of High-strength Composite Concrete-filled Steel Tube (CFT) Beam-columns", *Journal of Constructional Steel Research*, 2002, Vol. 58, No. 5-8, pp. 725-758.
- [20] Han, L. H., Zhao, X. L. and Tao, Z., "Tests and Mechanics Model of Concrete-filled SHS Stub Columns, Columns and Beam-columns", *Steel and Composite Structures*, 2001, Vol. 1, No. 1, pp. 51-74.
- [21] Yu, T., Wong, Y. L., Teng, J. G., Dong, S. L. and Lam, E.S.S., "Flexural Behavior of Hybrid FRP-concrete-steel Double-skin Tubular Members", *Journal of Composites for Construction*, 2006, Vol. 10, No. 5, pp. 443-452.
- [22] Han, L. H., Liu, W. and Yang, Y. F., "Behaviour of Concrete-filled Steel Tubular Stub Columns Subjected to Axially Local Compression", *Journal of Constructional Steel Research*, 2008, Vol. 64, No. 4, pp. 377-387.

# RESIDUAL STRESS STUDY ON WELDED SECTION OF HIGH STRENGTH Q460 STEEL AFTER FIRE EXPOSURE

W.Y. Wang<sup>1,\*</sup>, G. Q. Li<sup>2</sup> and Y. Ge<sup>3</sup>

<sup>1</sup> Associate Professor, School of Civil Engineering, Chongqing University, Chongqing, China;

<sup>2</sup> Professor, State Key Laboratory for Disaster Reduction in Civil Engineering, Tongji University, Shanghai, China

<sup>3</sup> Assistant Engineer, Architecture design institute for civil air defense of Shandong province, Jinan, China

\*(Corresponding author: E-mail: wywang@cqu.edu.cn)

Received: 2 September 2013; Revised: 3 July 2014; Accepted: 29 September 2014

**ABSTRACT:** The residual stress magnitude and distribution of mild carbon steel sections at room temperature has been widely studied. Little investigation has been performed on residual stress of high strength steel sections, especially at elevated temperatures and after fire exposure. The fire exposure and elevated temperature have great influence on the residual stress distribution. This paper presents the experimental study of residual stress of welded high strength steel H-shaped section after fire exposure. The residual stress at room temperature was compared with that after fire exposure both for mild steel and high strength steel. The residual stress of welded high strength Q460 steel section was also simulated by finite element analysis and the validated finite element model was employed to analysis the residual stress of high strength steel section at elevated temperatures. It is found that the residual stress of high strength steel section after fire exposure decreases significantly and the residual stress variation should be considered on fire resistance design of high strength steel structures.

**Keywords:** Residual stress; high strength steel; elevated temperature; finite element analysis

## 1. INTRODUCTION

High strength steel (HSS, yield strength  $\geq 460$  MPa) has been widely used in many buildings, spatial structures and bridges by providing benefits when compared with regular strength steel, such as reducing structural dead load and dimensions of members, saving material and space [1]. It is well known that residual stresses exist in most structural steel members induced by welding, flame cutting, uneven cooling or cold forming during processes of manufacture and fabrication. Although the internal equilibrium residual stresses are not detrimental to the resistance of cross section for steel members, the presence of residual stress will significantly influence the stiffness of compression members and shorten the fatigue life of steel members under periodical load or dynamic load [2].

In order to understand the effect of residual stress on the structural behavior of steel structures, the magnitudes and distributions of regular strength steel sections have been extensively investigated in the past decades [3]. In recent years, the residual stress in stainless steel section and high strength steel section has also been studied. An experimental program to quantify the residual stresses in stainless steel sections from three different production routes has been carried out by Gardner et al [4] and comprehensive residual stress distributions was obtained for three hot rolled angles, eight press braked angles and seven cold rolled box sections. The residual stress of high strength Q460 steel in box section was experimental investigated by Li et al. [5] by adopting both sectioning and hole-drilling methods and the corresponding simplified residual stress pattern was proposed. However, the research work on residual stresses of Q460 welded sections after fire exposure or at elevated temperatures is very limited. It is expected that the residual stresses of Q460 members at elevated temperature are rather different from that at room temperature, since the stress-strain curves and high-temperature material properties of Q460 are different from that at room temperature [6]. For this reason, the influence of residual stress on ultimate bearing capacities of compressed HSS members at elevated temperatures will be different from that at room temperature.

For the fire safety design of HSS members in civil engineering structures, especially for compressed steel members, it is important to evaluate the magnitudes and patterns of residual stress distribution for HSS members at elevated temperatures.

In the present paper, residual stress magnitude and distribution for welded high strength Q460 steel of H-shaped section was tested at room temperature and after fire exposure by utilizing sectioning method technique, which is a destructive method and was widely adopted in residual stress measuring. To compare the decrease of residual stress of high strength steel with mild steel, mild steel Q235 was also tested at room temperature and after fire exposure. The residual stress of high strength steel section after fire exposure was also simulated by finite element analysis and the validated finite element model was employed to analysis the residual stress of high strength steel section at elevated temperatures. In the previous fire resistance design of steel columns, the assumption of residual stress keeping constant was adopted due to lack of data of residual stress at elevated temperatures. Therefore, the residual stress variation at elevated temperatures of high strength steel sections is very helpful to determine the load bearing capacity of high strength steel columns in fire condition.

## 2. MATERIAL PROPERTIES

In the testing specimen, high strength Q460 steel is used. The mechanical properties of this steel at room temperature are obtained by coupon test and the yield strength is  $f_y = 585$  MPa, ultimate strength is  $f_u = 660$  MPa and the elastic modulus is  $E = 2.12 \times 10^5$  MPa. At elevated temperatures, the mechanical properties are referred to literatures [6-7]. In the finite element analysis, in addition to mechanical properties, the thermal properties including conductivity, specific heat, thermal expansion coefficient and enthalpy, are used and the values of them are adopted by EC3 [8]. The material properties are plotted in Figure 1.

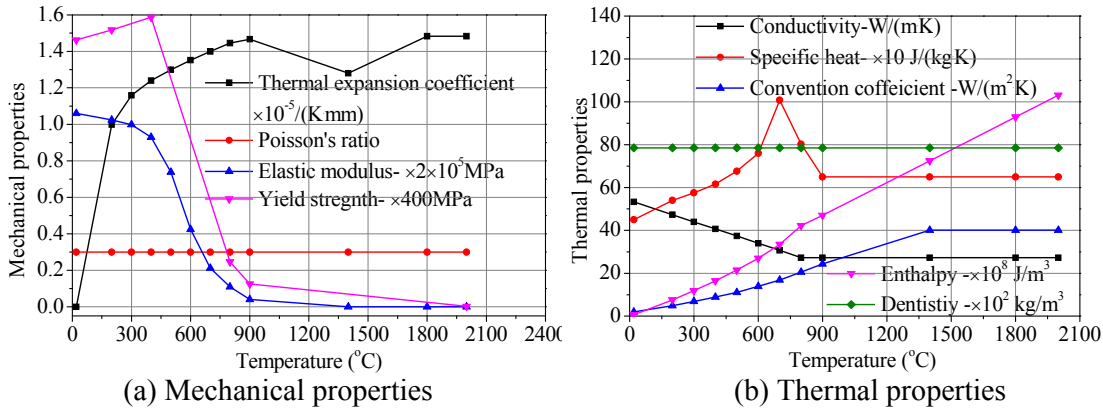


Figure1. Properties of High Strength Q460 Steel

The enthalpy is computed by

$$\Delta H(T) = \int_0^T \rho c dT \quad (1)$$

where,  $\Delta H(T)$  is increment of enthalpy at temperature  $T$ ;  $\rho$  is mass of steel and  $c$  is specific heat.

### 3. EXPERIMENTAL PROGRAM

#### 3.1 Experimental Technique

Techniques to measure residual stresses may be classified as either destructive or non-destructive. Non-destructive methods include X-ray, neutron or electron diffraction, ultrasonic methods and magnetic methods. Destructive methods rely on the measurement of deformations due to the release of residual stresses upon removal of material from the specimen. Sectioning is the principal destructive technique used to measure residual stresses in structural members. This method has been used extensively to analyze residual stresses in structural carbon steel, aluminum and stainless steel sections and is adopted in this study. Its advantages of adequate, accurate and economical have been proven with requirement of proper care in the preparation of the specimen and the measurement procedures [9]. A comprehensive description of the different techniques and their potential for measuring residual stresses has been presented in literature [10].

#### 3.2 Specimen and Instruments

The testing specimen of H-shaped section is fabricated with welded high strength Q460 steel plate of 8 mm in thickness and the dimension of cross section is H200×195×8×8 (height × width × flange thickness × web thickness). One 2.32 m column in length was welded and it was cut into two parts at the middle section. One is used to prepare specimen for measuring residual stress at room temperature and another one is used for measuring residual stress after fire exposure. In order to reduce the influence of flame cutting ends on the measured results of residual stress, the columns were cutting into three segments (testing segment is the middle one) by using Wire cut Electrical Discharge Machining. The testing segment is 300 mm in length and the two others segments are 430 mm in length, which is longer than required length (1.5~2.0 times of section height). Previous experimental researches have shown that, the distance of test section from the member end must be far enough in order to reduce the influence of end, and a distance of 1.5 to 2.0 times the lateral dimensions is required [9]. The strips are about 10 mm in width and 300 mm in length, with two gauge holes at two ends, and the distance between the two gauge holes is 250 mm. The cutting order of segments and strips dimension is shown in Figure 2.

The instruments used in the strips preparation include Wire-cut Electrical Discharge Machine, Electric Hole-drilling Machine and Hand-hold Strain Gauge. The cutting lines and centers of gauge holes are marked on the sectioning regions. Corresponding to center markers, through thickness holes are drilled by the drilling machine. In order to reduce the variation of gauge length, gauge holes are centrally located by using a punch. By using this method, strain measurements can be taken over a 250 mm gauge length using the hand-hold strain gauge. The minimum scale value of strain gauge is 0.001 mm. The original gauge lengths were measured and recorded. Three sets of measurements for each gauge length were taken if measurement variation does not exceeds 0.005 mm. Temperature changes during readings are practically eliminated by using a reference bar at the first and last of each measurement set. The sectioning segment is cut out with Wire cut Electrical Discharge Machining. Then, the sectioning proceeds are performed on a milling machine as shown in Figure 3. The influence of released heat from mechanical milling can be suppressed by supplying fluid coolant. The middle strips of specimen on flange and web are 10 mm and 13 mm in width, other strips are about 14 or 15 mm in width before released from specimens. Strips sectioned from the same specimen are put together in orders, as shown in Figure 4. Iron filings and grease need to be cleaned from the sectioned strips, especial around gauge holes. Three sets of gauge length are measured again following the procedure recommended in Ref. [9]. The released strains can be computed from the measured strains and temperature compensations.

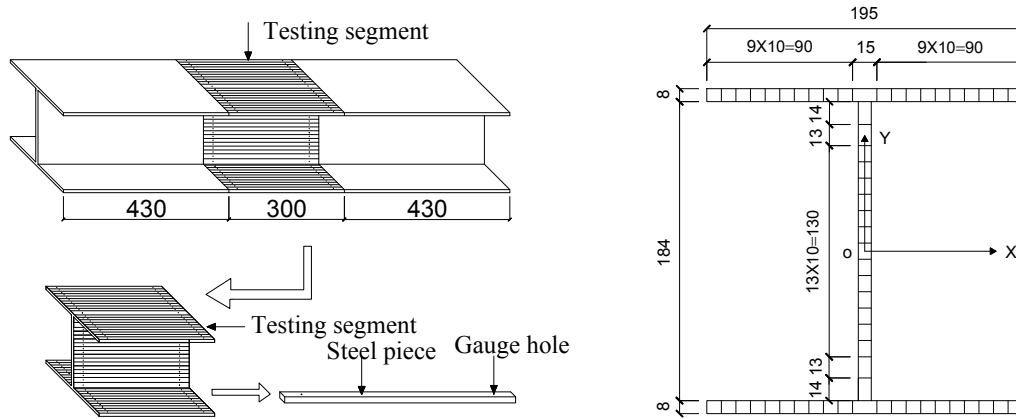


Figure 2. Cutting Order and Trip Dimensions (mm)



Figure 3. Sectioning Procedure of H-shaped Section



Figure 4. Sectioned Strips

In order to investigate the effect of fire exposure on the residual stress of mild steel, testing is also conducted on Q235 steel specimen. The preparation and process of Q235 steel specimen is same to the high strength Q460 steel except that the Q235 steel is hot-rolling H-shaped section and the dimension of cross section is  $H194 \times 150 \times 9 \times 6$  (height  $\times$  width  $\times$  flange thickness  $\times$  web thickness). The measured yield strength of mild Q235 steel used in the specimen is 280 MPa.

For the specimens used to measure residual stress after fire exposure, the steel columns are put into a furnace and the furnace is started to follow ISO-834 standard temperature curve for a period until the temperature of steel reaches  $600^\circ\text{C}$ . The cooling phase of furnace is obtained by natural cooling. After the temperature of column approaches room temperature, the trips begin to prepare and the procedures are same as those for measuring residual stress before fire exposure. The temperature of furnace and steel specimen during heating and cooling is shown in Figure 5. It can be observed that the temperature of steel columns increases slowly than the furnace even though the length of columns is only 1.16 meters in length. This is due to the temperature increase of steel member in high temperature has great relation with shape of cross section instead of length of specimen.

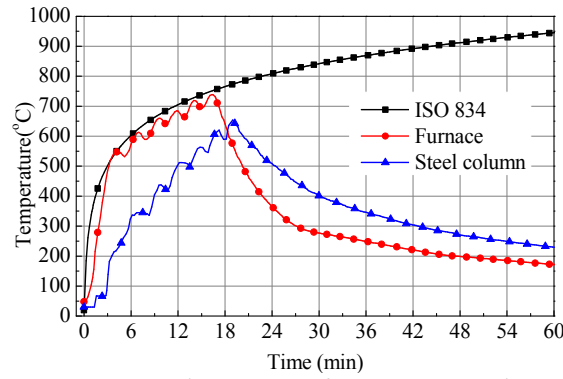


Figure 5. Temperature-time Curve for Furnace and Steel Column

### 3.3 Testing Procedures

The testing procedure comprises the following steps:

#### (1) Drilling holes

Before drilling gauge holes, it is necessary to clean the rust on the surface of steel by polishing. Then the cutting lines are drawn on the surface to mark the boundary of strips and then a sign is marked on each trip. In order to compensate the influence of temperature variation on the measured strain, a reference bar is fabricated to consider the temperature strain. Finally, the gauge holes are drilled on the sectioned segment with a strain gauge length of 250 mm. The diameter of gauge hole is 0.5 mm.

#### (2) Measuring gauge length

After cleaning the dust in the gauge holes, the length of standard strips, temperature compensating strips and the distance between gauge holes are measured for three times. According to the difference of standard trip and temperature compensating segment and sectioned strips, the length of temperature compensating segment and gauge holes can be calculated. If the difference of the three results exceeds 0.015 mm, the results are abandoned and measured again. Otherwise, the average value of three results is represented as gauge length of temperature compensating segment ( $L_{T1}$ ) and sectioned trips ( $L_1$ ).

#### (3) Cutting strips

Along the lines on the surface of columns, the column is cut into three segments and then the sectioning segment is cut into many strips. Finally, the coolant on the surface and gauge holes of strips is cleaned.

#### (4) Measuring gauge length after sectioning

Similar to the step (2), the distance between two gauge holes on each strip and the length of temperature compensating segment are measured again to obtain the new length after the residual stress releases and the temperature changes. The average value of three results is represented as gauge length of temperature compensating segment ( $L_{T2}$ ) and sectioned trips ( $L_2$ ).



#### (5) Computing the residual stress

Based on the measured results in step (2) and (4), the strain of temperature compensating segment can be obtained by  $\varepsilon_T = (L_{T2} - L_{T1}) / L_{T1}$ ; and the strain of strip can be calculated with  $\varepsilon = (L_2 - L_1) / L_1$ . The bending deformation of strip needs to be modified by [9]

$$\bar{\varepsilon} = \varepsilon + (f/l)^2 / (6(f/l)^4 + 1) \quad (2)$$

where  $f$  is deflection of strips at mid-span and  $l$  is the length of strip.

The strain generated by residual stress release can be obtained by subtracting temperature compensating strain from the total strain of strip, that is  $\varepsilon_r = \varepsilon - \varepsilon_T$ . According to Hooke's law, the residual stress on each trip can be obtained as  $\sigma_r = E\varepsilon_r$ .

## 4. EXPERIMENTAL RESULTS AND DISCUSSION

### 4.1 Experimental results

The residual stress distribution for the whole section is shown in Figure 6 and Figure 7 for high strength Q460 steel and mild Q235 steel, respectively. Using the measured residual stress before fire exposure, the equilibrium condition for the cross section is checked. Theoretically, since no external forces exist, equilibrium requires that the integration of the force over the whole section must be zero. For this particular case, a difference of 0.75 kN and 1.8 kN in tension is computed. This small difference may be attributed to the effect of saw cutting and accumulated experimental errors [9].

From the Figure 6, one can find that the maximum residual stress of high strength Q460 steel is about 300 MPa, which is approximate 50% of the yield strength. After fire exposure, the residual stress reduces significantly due to the reduction of yield strength and creep behavior of steel at high temperature, which results in the elastic deformation changing to plastic deformation. The maximum value of residual stress after fire exposure is about 70 MPa, which is only 12% of yield strength. For mild Q235 steel (as shown in Figure 7), similar trend can be observed and maximum residual stress before and after fire exposure are 180 MPa and 85 MPa, which are 65% and 30% of yield strength, respectively.

### 4.2 Discussion

The comparison of residual stress distribution before and after fire exposure for high strength Q460 steel is shown in Figure 8. As can be seen from the figure, the residual stress distribution mode both on flange and web before fire exposure is similar to that after fire exposure. The distribution mode looks like a “W” on the flange and “U” on the web. However, the maximum value after fire exposure decreases obviously. For the residual stress at the middle of flange, the reduction factor after fire exposure is 0.23. For the residual stress at middle of web, the residual stress almost disappears after fire exposure.

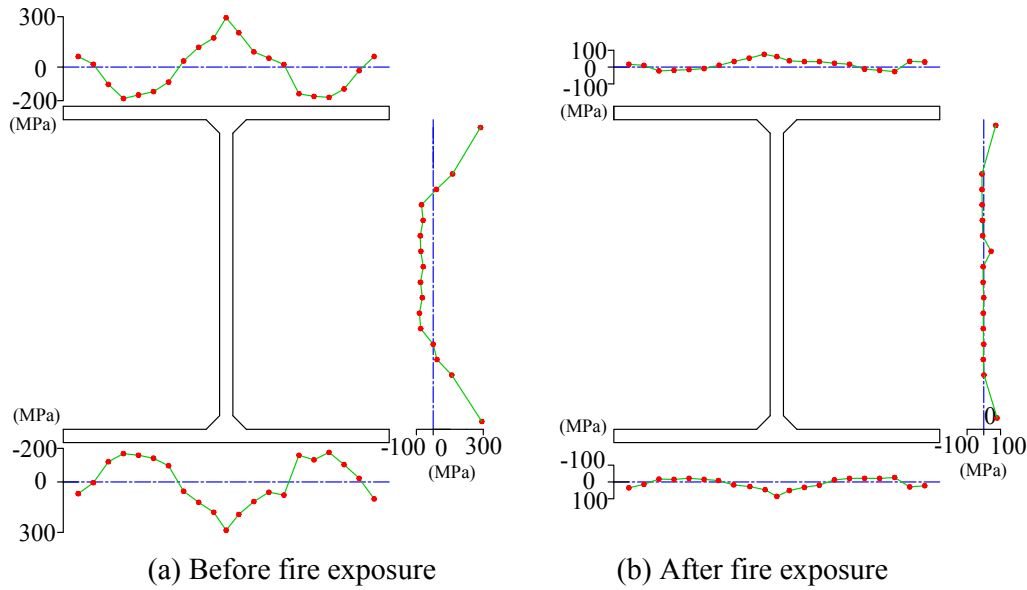


Figure 6. Residual Stress Distribution in High Strength Q460 Steel Section

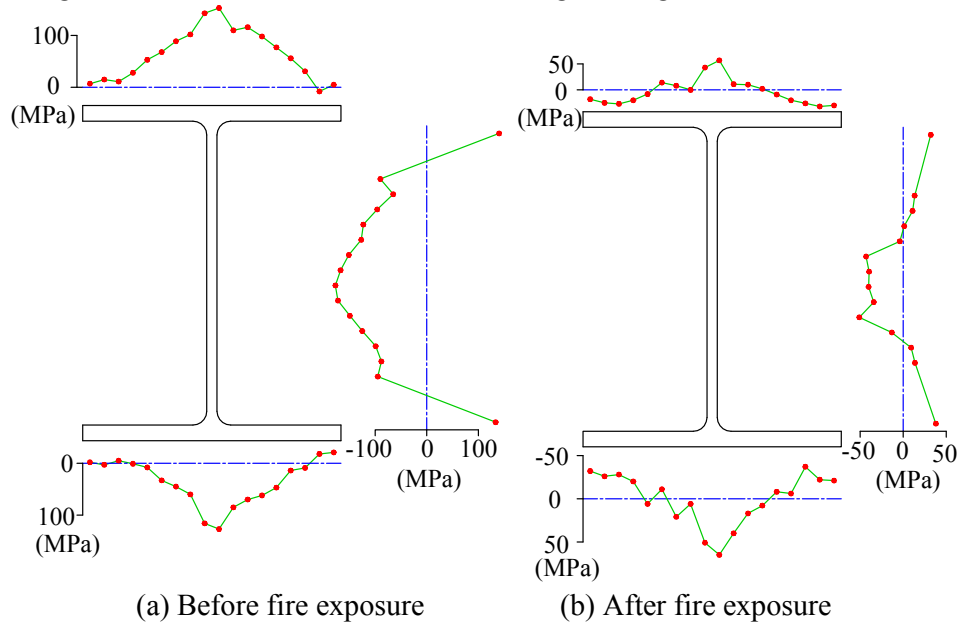


Figure 7. Residual Stress Distribution in Mild Q235 Steel Section

The comparison of residual stress distribution before and after fire exposure for mild Q235 steel is shown in Figure 9. It can be seen that on the flange, the distribution mode looks like an inverse “V”. The distribution mode on the web is similar to that for high strength Q460 steel. After fire exposure, the maximum value of residual stress on the flange reduces significantly but not as much as that of high strength Q460 steel and there is still 40% residual stress left compared to that before fire exposure. For the web, the reduction is obvious and 25% left, which is almost same as that of high strength Q460 steel.

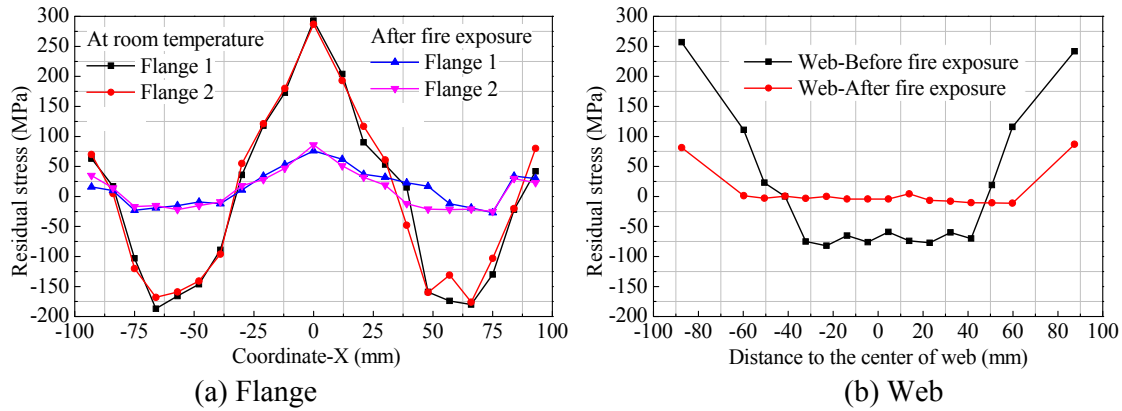


Figure 8. Comparison of Residual Stress of High Strength Q460 Steel before and after Fire Exposure

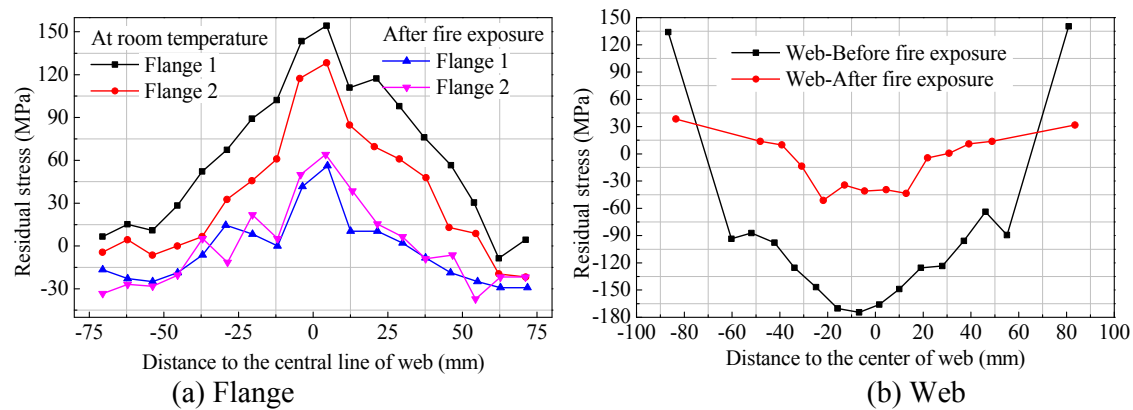


Figure 9. Comparison of Residual Stress of Mild Q235 Steel before and after Fire Exposure

The distribution mode between high strength Q460 steel and mild steel are different due to the difference of fabrication method. For the high strength Q460 steel, the plate is obtained by flame cutting and the section is compositing by welding; and for the mild Q235 steel, the plate and section is hot rolled. From the testing results of residual stress after fire exposure, it can be found that, the residual stress generated by welding is relative easy to reduce by tempering.

## 5. FINITE ELEMENT ANALYSIS

As to now, there is no proper method to measure the residual stress distribution at high temperature and the residual stress must be reducing at high temperature based on the intuitive judgment. Finite element method is very powerful and proved to be capable to analysis welding residual stress. In order to quantify the residual stress of high strength Q460 steel welded H-shaped section at high temperature, finite element analysis was performed by employing ANSYS soft package.

### 5.1 Finite element model

Two models are established to obtain the residual stress generated by flame cutting and welding, namely thermal model and structural model.

### 5.1.1 Thermal model

The thermal model in ANSYS is created using two types of elements, namely SOLID70 and SOLID90. SOLID90 is a higher order version of the element SOLID70. Only at the transition zone, SOLID90 is used and at the other zone, SOLID70 is used. SOLID70 element has eight nodes with a single degree of freedom, temperature, at each node. The element is applicable to a three-dimensional, steady-state or transient thermal analysis.

For the flame cutting simulation, a defined high temperature is applied on the edge of flange (4 mm width from the boundary of flange) and the temperature for all the other area keeps ambient. Then transient thermal analysis is performed until the temperature reduces to room temperature. Based on the literatures [11] and [12], 600°C is adopted to apply thermal boundary on the 4 mm width of the two edges of flange. For simulation of welding, a mobile heat source generated internally is adopted to simulate the heat input during welding on the element of weld [13], and the temperature for all the other elements keeps ambient. The heat generation per time unit can be obtained by

$$Q = \eta UI \quad (3)$$

where  $Q$  is heat generation in per time unit;  $\eta$  is heat efficiency of welding, can be adopted as 0.65~0.9 [14], in this paper  $\eta=0.85$ ;  $U$  is voltage of welding and it is 24 V;  $I$  is electric current of welding and it is 180 A.

The heat generation rate can be obtained by

$$q = Q/V \quad (4)$$

where  $V$  is welding volume per time unit, can be computed with welding speed (6mm/s) and thickness of weld leg (8mm).

When applying heat generation rate of weld mobile heat source on element, “birth and death” function of element is used. Before welding simulation starts, all welding elements are killed (death). When applying heat generation rate on a welding element, this element is activated (birth). After the heat source moves away, the activated elements are killed again. In this way, the temperature distribution during welding can be simulated.

### 5.1.2 Structural model

In the structural analysis, SOLID185 and SOLID186 are used. Corresponding to thermal model, SOLID186 only is used for transition zone. SOLID185 element is defined by eight nodes having three degrees of freedom at each node. The element has plasticity, hyperelasticity, stress stiffening, creep, large deflection, and large strain capabilities. In order to improve analysis efficiency, only half of column (600 mm) is established. Figure 10 shows the dimension and discretized of H-shaped welded column. At the flame cutting zone and welding part, the temperature varies rapidly and the mesh is discretized densely.

After performing thermal analysis, the temperature distribution is saved and read into structural analysis to obtain the residual stress distribution. In the structural analysis, the boundary condition of the column is set up according to the realistic condition during welding. All the nodes on one end of column are restrained in three directions and for the nodes on another end are restrained in two directions except the axial direction. Therefore, the columns can expand freely along the axial direction.

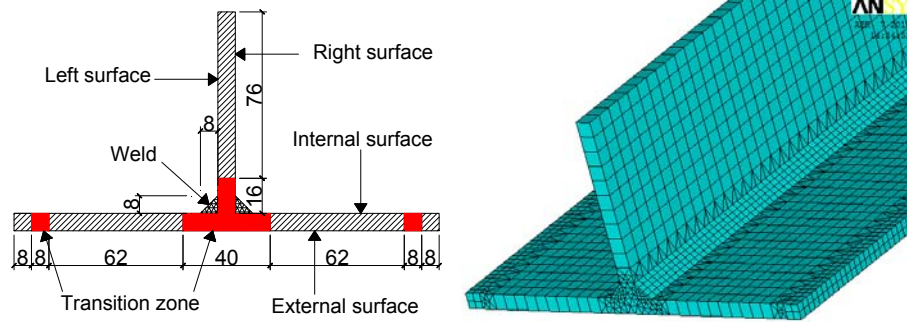


Figure 10. Finite Element Model

## 5.2 Temperature Distribution

The temperature distribution after cutting on flange is shown in Figure 11. Due to high thermal conductivity of steel, the heat on the edge is transferred quickly to the middle of plate and to the atmosphere. As can be seen from Figure 11, One minute and forty seconds later, the maximum temperature is about 80 °C and ten thousand seconds (approximate 2.8 hours) later, the temperature is close to room temperature (27 °C).

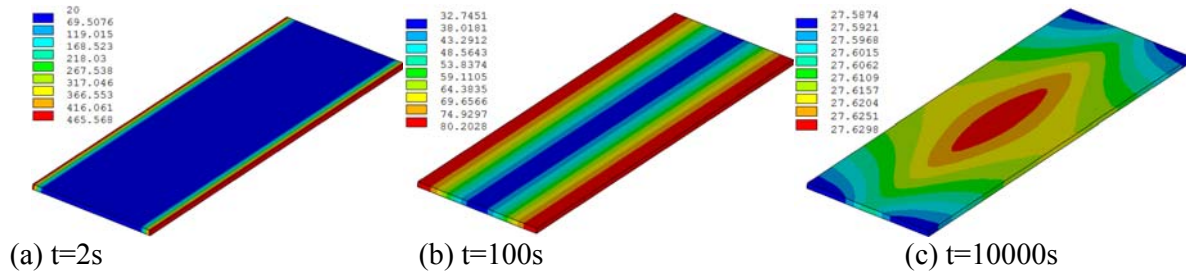


Figure 11. Temperature Distribution of Flame Cutting

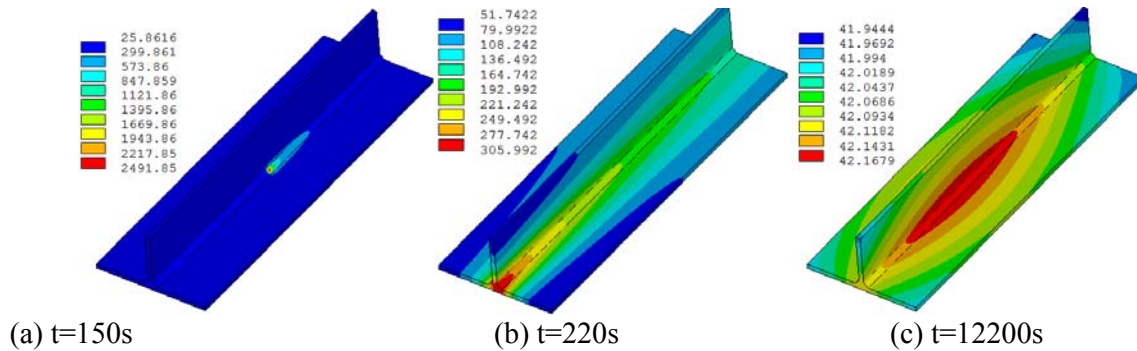


Figure 12. Temperature Distribution of Steel Column during Welding

The temperature distribution of welding simulation is shown in Figure 12. The column is 600 mm in length and the welding speed is 6 mm per second. Therefore the welding time for the two filled weld may last for 200 seconds. As is shown in Figure 12, during the welding, the temperature is very high at the welding location and the maximum temperature reaches to 2500 °C. Twenty seconds later after finishing welding, the maximum temperature reduces to about 306 °C and 12000 seconds (3 hours and twenty minutes) later; the temperature reduces to room temperature. The temperature-time curves for two welding element at middle and quarter span are shown in Figure 13. It is shown that when welding the rear welding element, the temperature of the welding element increases and reaches about 250 °C; and when the welding reaches the welding element, the temperature increases sharply and reaches 2500 °C in few seconds.

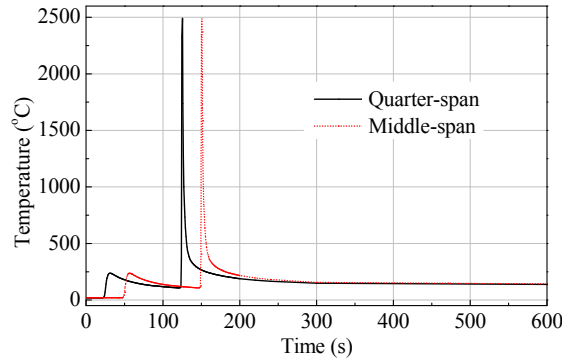


Figure 13. Temperature-time Curves for Two Welding Elements during Welding

### 5.3 Stress Distribution before Fire Exposure

The residual stress distribution on the whole section after flame cutting and welding are shown in Figure 14. For the right surface of web, the values of residual stress at the ends of web are irregular and omitted. From the Figure 14, it can be seen that at the area of flame cutting welding, the residual stress is very significant tension stress and reaches to 60% of yield strength. The residual stress in these two areas mainly generated due to non-uniform cooling of cutting and welding. At the other portion of section, the compressive residual stresses in flange or web are much lower compared to tension stress. This is caused by the greater tensile residual stresses in the same section, which are balanced by compressive stresses to maintain internal equilibrium.

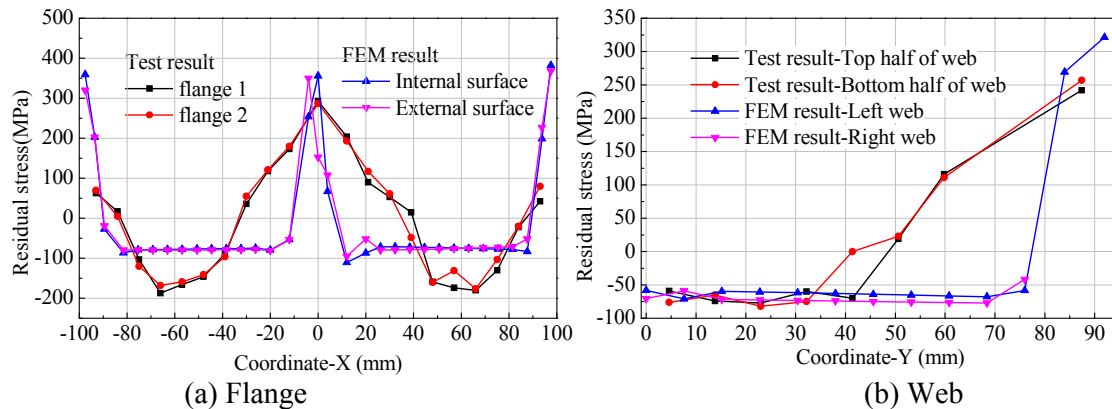


Figure 14. Comparison of Residual Stress between Test and FEM before Fire Exposure

## 5.4 Comparison and Discussion

The comparison between experimental and analyzed results is also shown in Figure 14. As can be seen from the figure, the maximum values of residual stress at the middle of flange, half and ends of web are agreeable. At the middle of flange, the difference between them is 63 MPa (account for 20% of experimental result). At the end of web, the difference between them is 64 MPa (account for 20% of experimental result). However, at the flange cutting area, the difference is significant. It may be attributed to two reasons. One is that the simplified approach was used to simulate the temperature distribution at this portion and the temperature decrease too quickly, which results in the results of FEM is higher than test. Another reason is that the experimental results in one segment is average value of the whole width of segment and it is much lower than the real maximum value. In addition, the residual stress curves obtained by experiment are smoother than that of analyzed results. This may be attributed to that in the finite element model, only residual stress produced by welding and flange cutting is considered and the residual stress generated by rolling is neglect. In the experiment, the section is welded by three steel plates, which have residual stress when hot-rolling before welding. In general, the analyzed results agree with experimental data with an acceptable range.

## 5.5 Post-fire Residual Stress Distribution

After obtaining the residual stress distribution by simulating the flame cutting and welding, post-fire residual stress distribution is simulated by thermal analysis and structural analysis. The fire scenario is ISO-834 standard fire. The comparison of temperature-time curve for the columns obtained by finite element analysis and experiment is shown in Figure 15. It can be seen that the analyzed temperature during heating and cooling agree well with test data.

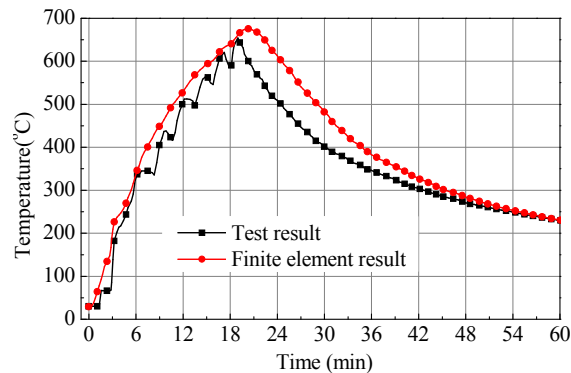


Figure 15. Comparison of Temperature between Finite Element Analysis Results and Test Results

The residual stress generated by flame cutting and welding is imported to the structural model as well as the temperature distribution during heating and cooling, the post-fire residual stress can be obtained. The analyzed results of post-fire residual stress and the comparison of the results with test data are shown in Figure 16. Generally, the residual stress reduces significantly after fire exposure. At the two ends and middle of flange, there is a big difference between analyzed results and test data due to the following possible reasons. Firstly, in the finite element model, the residual stress produced by hot-rolling is not considered to simplify the analysis procedure. Secondly, the element dimension is not small enough in order to improve the computing efficiency. Even though, the trend of residual stress variation is agreeable and the method and model can be employed to analysis the residual stress distribution at high temperatures.

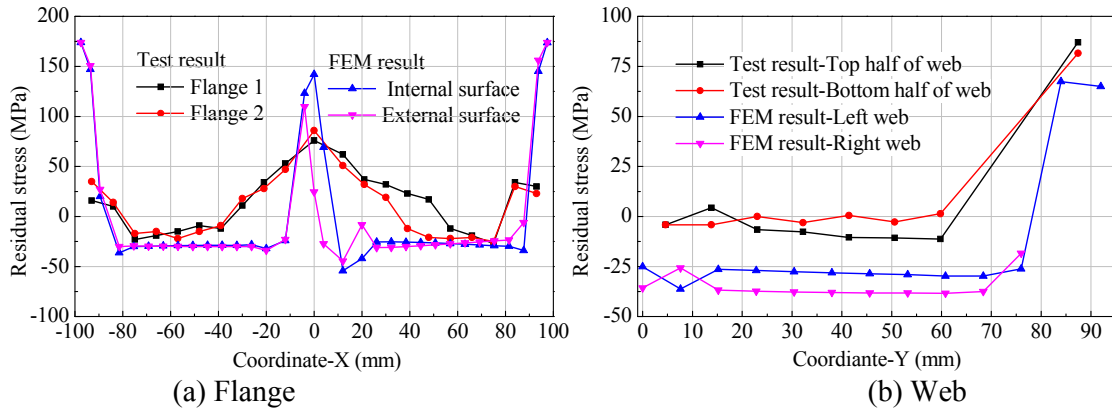


Figure 16. Comparison of Residual Stress between Test and FEM after Fire Exposure

### 5.6 Residual Stress Distribution at High Temperatures

The residual stress distribution at temperatures 100 °C~800 °C was analyzed and the reduction factor of maximum values at end of the flange, one fourth width of the flange, half width of the flange, end of the web and half of the web with the elevation of temperature are shown in Figure 17. As can be seen from Figure 17, the maximum values of residual stress decrease with the increase of temperature except at the position of middle of web. When the temperature is lower than 400 °C, the maximum values of residual stress at edge of the flange, half width of the flange and end of the web almost keep constant and then decrease sharply with the elevation of temperature. This can be attributed to that when the temperature exceeds 400 °C, the thermoplastic deformation will arise and the deformation will results in the redistribution of residual stress. For the position of middle of web, the residual stress increase within the temperature of 600 °C may be attributed to the complex redistribution of residual stress, including the variation of width of tension or compression areas. The further study will be investigated in the following research.

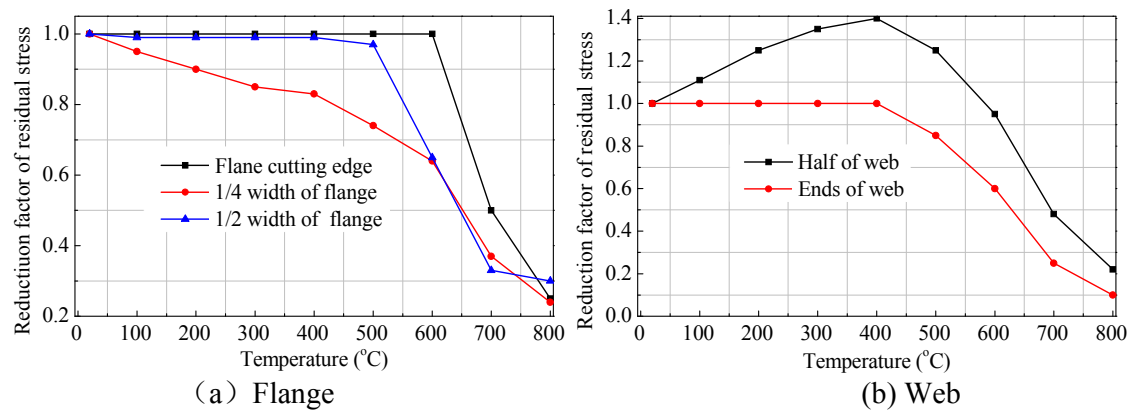


Figure 17. Reduction Factor of Residual Stress of High Strength Q460 Steel at High Temperatures



## 6. CONCLUSIONS

Based on the results presented in this paper, the following conclusions can be drawn:

- (1) After fire exposure, the residual stress reduces significantly for welded H-shaped section fabricated with high strength Q460 steel.
- (2) At high temperature, the maximum value of residual stress varied and should be put into consideration in fire resistance design of high strength steel structures.
- (3) The finite element can be used to simulate the residual stress distribution at high temperature and after fire exposure with an acceptable accuracy.

In addition, the test data presented in this paper can be used to provide validation to other researchers as well as provide a reference for fire resistance design of high strength Q460 steel.

## NOTATIONS

The following symbols are used in this paper:

$f_y$ —	yield strength of steel;
$f_u$ —	ultimate strength of steel;
$E$ —	elastic modulus of steel;
$\Delta H(T)$ —	is increment of enthalpy at temperature $T$ ;
$\rho$ —	mass of steel;
$c$ —	specific heat of steel;
$L_T$ —	gage length of temperature compensate segment ; .
$L$ —	gage length of sectioned trips;
$\varepsilon_T$ —	strain of temperature compensate segment;
$\varepsilon$ —	strain of strip;
$f$ —	deflection of strips at mid-span;
$\varepsilon_r$ —	strain generated by residual stress release;
$\sigma_r$ —	residual stress;
$Q$ —	heat generation in per time unit;
$\eta$ —	heat efficiency of welding;
$U$ —	voltage of welding;
$I$ —	electric current of welding;
$V$ —	welding volume per time unit.

## ACKNOWLEDGMENT

The authors wish to acknowledge the support from the Fundamental Research Funds for the Central Universities (Grant No.: CDJZR12200004 and 106112013CDJZR200006), China Postdoctoral Science Foundation (Grant No.:20110490811 and 2012T50765) and Funding Plan or Young Teachers in Universities of Chongqing. The support from State Key Lab for Disaster Reduction in Civil Engineering of Tongji University in China is also greatly appreciated. Any opinions, findings, and conclusions or recommendations expressed in this paper are those of the authors and do not necessarily reflect the views of the sponsors.

## REFERENCE

- [1]. Shi, G, Shi, Y.J. and Wang, Y.Q., “Engineering Application of Ultra-High Strength Steel Structures”, *Progress in Steel Building Structures*, 2008, Vol. 10, No. 4, pp. 32-38. (In Chinese)
- [2]. Beedle, L.S., “Stability of Metal Structures- A World View”, 2<sup>nd</sup> Ed. Structural Stability Research Council, 1991.
- [3]. Tebedge, N. and Tall, L., “Residual Stress in Structural Steel Shapes - A Summary of Measured Values”, Fritz Laboratory Report; February 1973.
- [4]. Cruise, R.B. and Gardner, L., “Residual Stress Analysis of Structural Stainless Steel Sections”, *Journal of Constructional Steel Research*, 2008, Vol. 64, pp. 352–66.
- [5]. Wang, Y.B., Li, G.Q. and Chen, S.W., “The Assessment of Residual Stress in Welded High Strength Steel Box Sections”, *Journal of Constructional Steel Research*, 2012, Vol. 76, pp.93-99.
- [6]. Wang, W.Y., Liu, B. and Kodur, V.K.R., “Effect of Temperature on Strength and Elastic Modulus of High Strength Steel”, *Journal of Materials in Civil Engineering-ASCE*, 2013, Vol. 25, No. 2, pp. 174-182.
- [7]. Qiang, X., Bijlaard, F.S.K. and Kolstein, H., “Deterioration of Mechanical Properties of High Strength Structural Steel S460N under Steady State Fire Condition”, *Materials and Design*, 2012, Vol. 36, No. 1, pp. 438-442.
- [8]. European Committee for Standardization, ENV 1993-1-2, “Eurocode 3, Design of Steel Structures, Part 1.2: General Rules-Structural Fire Design”, 2001.
- [9]. Tebedge, N., Alpsten, G. and Tall, L., “Residual-stress Measurement by the Sectioning Method”, *Experimental Mechanics*, 1973, Vol. 13, pp. 88–96.
- [10]. Withers, P.J. and Bhadeshia, H.K.D.H., “Residual Stress: Part 1 — Measurement Techniques”, *Materials Science and Technology*, 2001, Vol. 17, No. 4, pp. 355–65.
- [11]. Chen, J., “GJ Measurement and Analysis on Residual Stress in Welded I-shaped Cross-sectional Member”, Master’s degree thesis, Chongqing University, Chongqing, 2010.
- [12]. Huang, H., “Research on Residual Stress of Plate Oxygen Cutting based on Numerical Simulation and Experiment”, Master’s degree thesis, Dalian University of Technology, Dalian, 2010.
- [13]. Wang, J.F., “Heat Source Model Study on Weld Temperature Field and Stress Field”, Master’s Degree Thesis, Yanshan University, Qinghuadao, 2006.
- [14]. Cheng, S.L., “Numerical Analysis on Weld Residual Stress based on Temperature and Stress Field”, Master’s Degree Thesis, Nanchang University, Nanchang, 2007.

# DESIGN STRENGTH OF CONCRETE-FILLED STEEL COLUMNS

W.-H. Kang<sup>1,\*</sup>, B. Uy<sup>2</sup>, Z. Tao<sup>1</sup> and S. Hicks<sup>3</sup>

<sup>1</sup> *Institute for Infrastructure Engineering, University of Western Sydney, Penrith, NSW 2751, Australia*

<sup>2</sup> *Centre for Infrastructure Engineering & Safety, The University of New South Wales, Sydney, NSW 2052, Australia*

<sup>3</sup> *Heavy Engineering Research Association, Manukau, Auckland City, New Zealand*

*\*(Corresponding author: E-mail: w.kang@uws.edu.au)*

*Received: 18 March 2013; Revised: 17 June 2014; Accepted: 24 June 2014*

---

**ABSTRACT:** The purpose of this paper is to recalibrate the capacity reduction factors, estimate the reliability of current equations, and investigate the effect of these factors in AS 5100.6, the Australian Bridge Standard for concrete-filled steel tubular columns. This work has important ramifications for other international codes of practice as the Australian code has the identical or similar underlying design philosophy with Eurocode 4, AISC and the code of practice in Hong Kong. The method developed by Johnson and Huang is extensively applied to the Australian code format to recalibrate the capacity factors in AS 5100 for a target reliability of  $\beta = 3.04$  based on an extensive database of 1,583 test results covering a wide range of input parameter values. In addition, an inverse analysis procedure based on Johnson and Huang's method is proposed to estimate the reliability of design equations with known capacity factors. The analysis results show that the interaction between the concrete and steel needs to be considered for the current capacity factors in AS 5100. The results also show that the current capacity factors provide greater reliability than the target reliability suggested in AS 5104:2005/ISO 2394:1998, but after considering the additional uncertainties created due to the application of multiple capacity factors, the reliability was almost the same as the recommended value. In conclusion, the current capacity factor values in AS 5100 are adequate with regards to safety and can be maintained, but better optimised values would be preferable to improve the cost-safety balance.

**Keywords:** Capacity factors, Composite structures, Concrete-filled steel columns, Design strength, Safety factor calibration

---

## 1. INTRODUCTION

Concrete-filled steel tubular (CFST) members have been used in many structural applications including high-rise buildings, bridges, and offshore structures, due to their outstanding mechanical performance: such as high axial load capacity, good ductility performance, large energy absorption capacity, and low strength degradation [1],[2]. In the structural design of these composite members, it is desirable to achieve the most optimised balance between the cost and the safety of the members in the context of the safety of the whole structure. The safety factors regarding the ultimate structural member resistance in the existing design code provisions need to be promptly checked as more experimental data becomes available and improved statistical techniques are developed. In addition, these factors should be determined based on the statistical rationale provided by a reliability analysis. In this context, this paper aims to recalibrate the capacity factors for the design of CFST members, to estimate the reliability of the current bridge design Standard in AS 5100 [3] and to investigate the optimal cost-safety balance of the current design codes. The proposed work in this paper has important ramifications for other international codes of practice as the Australian code has the identical or similar underlying design philosophy with Eurocode 4 (EC 4) [4], AISC [5], and the code of practice in Hong Kong [6].

In this paper, first a brief summary of the current code provisions of AS 5100: Australian Standard for Bridges for CFST columns is provided, and the database employed for the reliability based capacity recalibration analysis is introduced. An extensive database of failure tests of CFST members developed by Tao et al. [7] is used, which merged two available test databases established by Goode [8] and Wu [9]. Although this database includes the test results of six structural CFST member types (circular and rectangular columns, beam-columns, and beams) with a total of 2,194 test results, we herein limit our attention to CFST columns and use a total of 1,583 test results. Although more experimental studies have recently been carried on the axial load bearing capacity of CFST columns such as Gupta et. al. [10], Lue et al. [11], Tao et al. [12], Yu et al. [13], Yang and Han [14], and Chang et al. [15], they are not considered in this study as the number of test results in the Tao et al.'s database is already statistically sufficient. Based on this information, we conduct the following three types of reliability-based analyses: firstly, we recalibrate the capacity factors in AS 5100 using the statistical method proposed by Johnson and Huang [16]. This method is selected because: it can calibrate multiple factors at once; it assumes a lognormal distribution which is realistic for member strength with non-negative values; and it utilises the data only for member resistance, neglecting the load effect and its uncertainties. Secondly, we estimate the reliability of the design equations in AS 5100 with the existing specified capacity factors (0.9 for steel and 0.6 for concrete), by proposing a calculation procedure that is inverse of the method proposed by Johnson and Huang. Thirdly, the reliability estimation for the design codes and the capacity factors in AS 5100 is repeated, considering the effect of the applied capacity factors on the accuracy of the equations. Based on these calibration and reliability estimation results, discussions and recommendations are provided regarding useful in-sights into and supporting information for the current design code provisions.

## 2. AUSTRALIAN CODE PROVISIONS FOR CFST MEMBERS

### 2.1 Ultimate Section Capacity

In the Australian bridge standard, AS 5100 [3], the ultimate section capacity ( $N_{us}$ ) for a rectangular CFST stub column under axial compression is calculated as follows:

$$N_{us} = \phi A_s f_y + \phi_c A_c f'_c \quad (1)$$

where  $A_s$  and  $A_c$  = the areas of the steel and concrete sections, respectively;  $f_y$  = the nominal yield strength of the steel;  $f'_c$  = the characteristic compressive strength of the concrete; and  $\phi$  and  $\phi_c$  = the capacity reduction factors for steel and concrete, respectively (with the existing values given as 0.9 and 0.6). In this equation, the contribution of the reinforcement is not considered, because no test data in this study included this variable.

Eq. 1 can also be used for a circular CFST stub column. However, if the relative slenderness ( $\lambda_r$ ) is not greater than 0.5 and the eccentricity of loading under the greatest design bending moment is not greater than  $d_o/10$  (where  $d_o$  is the diameter of a circular section), the additional increase in concrete strength due to the confinement effect should be considered. When the confinement effect is considered, the ultimate section capacity is as follows:

$$N_{us} = \phi A_s \eta_2 f_y + \phi_c A_c f'_c \left( 1 + \frac{\eta_1 f_y}{d_o f'_c} \right) \quad (2)$$

where  $\eta_1$  and  $\eta_2$  = the coefficients for reflecting the confinement effect.  $\eta_1$  represents the concrete strength increase, and  $\eta_2$  represents the steel strength reduction, due to the confinement effect. The calculation procedure for these coefficients is given in Clause 10.6.2.2 of AS 5100. 6 [3].

## 2.2 Ultimate Member Capacity

To estimate the ultimate member capacity ( $N_{uc}$ ), a slenderness effect represented by a slenderness reduction factor,  $\alpha_c$ , should be considered. For a stub column defined by  $L_e/d_o$  or  $L_e/b \leq 4$  (where  $L_e$  = the effective length of a column, and  $b$  = the section width of a rectangular tube), this slenderness effect can be ignored. Considering this slenderness reduction factor, the ultimate member capacity of a CFST column is calculated as follows:

$$N_{uc} = \alpha_c N_{us} \leq N_{us} \quad (3)$$

where  $N_{us}$  is calculated either from Eq. 1 or 2. The slenderness reduction factor,  $\alpha_c$ , is calculated using the following equation:

$$\alpha_c = \xi \left[ 1 - \sqrt{1 - \left( \frac{90}{\xi \lambda} \right)^2} \right] \quad (4)$$

where  $\xi$  is the compression member factor and  $\lambda$  is a factor defined as a function of the relative slenderness ( $\lambda_r$ ).  $\lambda_r$  is defined by  $\sqrt{N_{us} / N_{cr}}$ , where  $N_{us}$  is calculated from either Eq. (1) or (2) but the capacity factors  $\phi$  and  $\phi_c$  are taken as unity;  $N_{cr}$  is calculated as follows:

$$N_{cr} = \frac{\pi^2 (EI)_e}{L_e^2} \quad (5)$$

$$(EI)_e = \phi EI_s + \phi_c E_c I_c \quad (6)$$

where  $I_s$  and  $I_c$  are the second moment of the areas of the steel sections and uncracked concrete sections, respectively, and  $\phi$  and  $\phi_c$  are the capacity factors.

In this paper, we aim to calibrate the capacity reduction factors  $\phi$  and  $\phi_c$  in Eqs. 1 and 2 and investigate their effect on the reliability of the design equations, based on the extensive database developed by Tao et al. [7], introduced in the following section.

## 3. DATABASE FOR CFST STUB COLUMNS

Safety factors in the existing design code provisions may not provide the most optimal balance between cost and safety if they were developed based only on a limited number of test results. In this case, the factors need to be updated based on the latest collection from a database with a sufficient number of test results covering a wide range of input parameter values. For this purpose, we use the extensive database developed by Tao et al. [7], which covers the test results over the last few decades by merging two available test databases established by Goode [8] and Wu [9]. Goode's database contains 1,792 test results from 92 references, and Wu's database contains 1,514 test results from 104 references. In Tao et al.'s database, 1,575 test results from Goode's database were included (918 for circular members and 657 for rectangular members), discarding irrelevant datasets, and 619 test results from Wu's database were included that had not been included in Goode's database. A total of 2,194 test results (1,232 for circular members and 962 for rectangular members) from 130 references are included in Tao et al.'s database. In this paper, we limit our attention to column members and use a reduced database with 1,583 test results (445 for rectangular stub columns, 234 for long rectangular columns, 484 for circular stub columns, and 420 for circular long columns). Here, a stub column is defined as a short column member with  $L_e/d_o \leq 4$  (for circular members) or  $L_e/b \leq 4$  (for rectangular members), where  $L_e$  is the effective length of a

column,  $d_o$  is the diameter of a circular section, and  $b$  is the section width of a rectangular section. For a stub column, the slenderness effect is not considered.

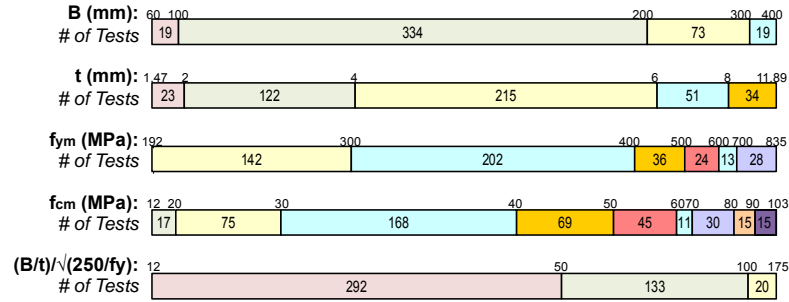
In Tao et al.'s database, some references do not provide the mean measured compressive strength of concrete ( $f_{cm}$ ) values. They report the compressive strength values of 150 mm cubes ( $f_{cu}$ ) instead. In this case, the conversion table given by Yu et al. [17] representing the approximate relationship between cylinder strength ( $f_{cm}$ ) and cube strength ( $f_{cu}$ ) was used to obtain the equivalent compressive strength. This table was developed based on Chen et al.'s work [18], which determined the equivalent compressive strength of high-strength concrete.

Figure 1 shows an overview of the distributions of the key parameters in Tao et al.'s [7] database: the diameters ( $d_o$ ) or the longer side lengths ( $B$ ) of the steel tubes, the tube thicknesses ( $t$ ), the mean measured yield strength of the steel ( $f_{ym}$ ), the mean measured compressive strength of the concrete ( $f_{cm}$ ), the column lengths for long columns, and the width-to-thickness ratio or diameter-to-thickness ratio with the effect of yield strength ( $(B/t)/\sqrt{(250/f_y)}$ ) or  $((D/t)/(250/f_y))$ . In this figure, the parameter ranges for the four section/member types (rectangular stub columns, circular stub columns, long rectangular columns, and long circular columns) are separately presented in Figures 1 (a), (b), (c), and (d).

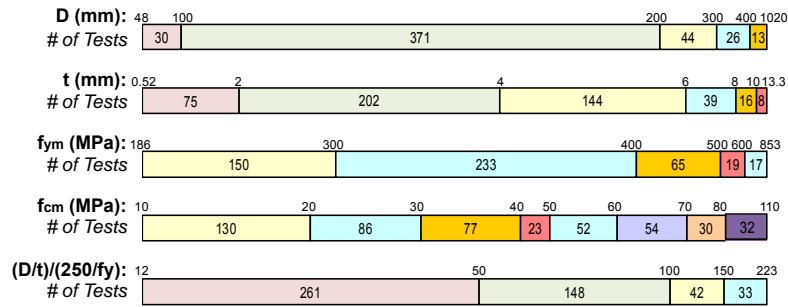
In Figure 1 (a), for rectangular stub columns, most members have longer side lengths between 100 and 200 mm, while some members have values outside of this range. Note that the longer to shorter side length ratio ( $B/B_{short}$ ) is between 1.00 and 2.00. The thickness is mostly distributed between 1.47 and 8 mm, while some members have values outside of this range. The mean measured yield strength of the steel ( $f_{ym}$ ) is uniformly distributed between 192 and 400 MPa (N/mm<sup>2</sup>), while a few members' yield strengths is 835 MPa (N/mm<sup>2</sup>). The mean measured compressive strength of the concrete ( $f_{cm}$ ) is almost uniformly distributed between 12 and 103 MPa (N/mm<sup>2</sup>). The width-to-thickness ratio with the effect of yield strength ( $(B/t)/\sqrt{(250/f_y)}$ ) is mostly distributed between 12 and 100, while some members' values are outside of this range.

For circular stub columns, a similar distribution is observed in Figure 1 (b). Most members have diameters between 100 and 200 mm, while several members have diameters up to 1,020 mm. The thickness is mostly distributed between 0.52 and 8 mm, while some members have values outside of this range. The mean measured yield strength of the steel ( $f_{ym}$ ) is uniformly distributed between 186 and 400 MPa (N/mm<sup>2</sup>), while a few members have a yield strength of 853 MPa (N/mm<sup>2</sup>). The mean measured compressive strength of the concrete ( $f_{cm}$ ) is uniformly distributed between 10 and 110 MPa (N/mm<sup>2</sup>). The diameter-to-thickness ratio with the effect of yield strength ( $(D/t)/(250/f_y)$ ) is mostly distributed between 12 and 150, but still many members' have their values between 150 and 223.

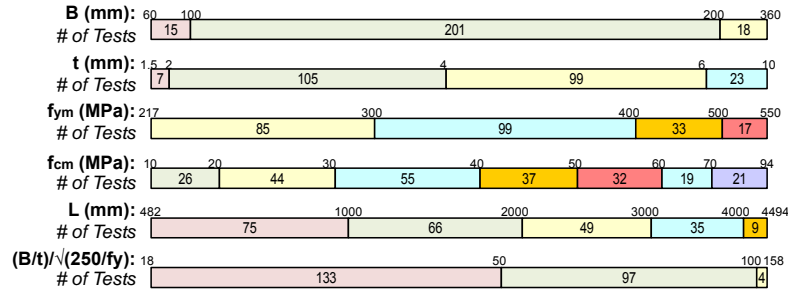
For long rectangular columns, as shown in Figure 1 (c), most members have longer side lengths between 100 and 200 mm. Note that the longer to shorter side length ratio ( $B/B_{short}$ ) is between 1.00 and 2.02. The thickness ranges between 1.5 and 6 mm, while some members have values outside of this range. The mean measured yield strength of the steel ( $f_{ym}$ ) is uniformly distributed between 217 and 500 MPa (N/mm<sup>2</sup>), while a few members' yield strength is 550 MPa (N/mm<sup>2</sup>). The mean measured compressive strength of the concrete ( $f_{cm}$ ) is almost uniformly distributed between 10 and 94 MPa (N/mm<sup>2</sup>). The length of the columns is also uniformly distributed between 482 and 4,000 mm, while some members' column lengths are up to 4,494 mm. The width-to-thickness ratio with the effect of yield strength ( $(B/t)/\sqrt{(250/f_y)}$ ) is mostly distributed between 18 and 100, and only few members' values are outside of this range.



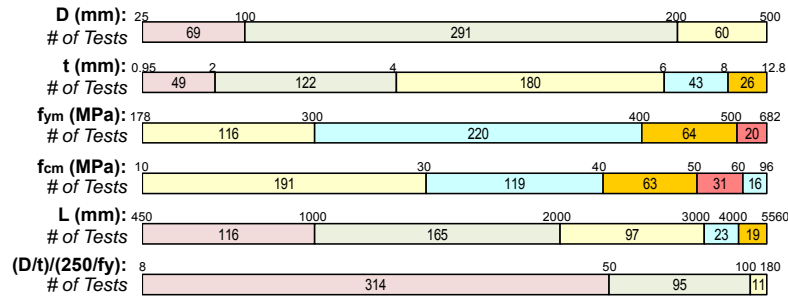
(a) Rectangular stub columns



(b) Circular stub columns



(c) Long rectangular columns



(d) Long circular columns

Figure 1. Distribution of Parameter Values in Tao et al.'s Database [7]

For long circular columns, as shown in Figure 1 (d), most members have longer side lengths between 100 and 200 mm, and the thickness ranging between 0.95 and 8 mm, while some members have values outside of this range. The mean measured yield strength of the steel ( $f_{ym}$ ) is uniformly distributed between 178 and 500 MPa (N/mm<sup>2</sup>), while a few members' yield strength is 682 MPa (N/mm<sup>2</sup>). The mean measured compressive strength of the concrete ( $f_{cm}$ ) is almost uniformly distributed between 10 and 96 MPa (N/mm<sup>2</sup>). The length of the columns is also uniformly distributed between 450 and 4,000 mm, while some members' column length is up to 5,560 mm. The diameter-to-thickness ratio with the effect of yield strength ( $(D/t)/(250/f_y)$ ) is mostly distributed between 8 and 100, and some values are outside of this range.

Because the experiments were conducted for research purposes, some cases may not represent the realistic conditions of existing structures. However, the comprehensiveness of the database enables us to cover a wide range of parameter values. The database lacks uniformity regarding some of the key parameters because it was randomly assembled from numerous test results in the literature. This should be carefully considered when the capacity factor calibration and reliability analysis results are used.

#### 4. CAPACITY FACTOR CALIBRATION METHOD

Based on the extensive database introduced in the previous section, we first adopt the statistical method proposed by Johnson and Huang [16] to calibrate the capacity factors in the resistance functions of CFST stub column members in AS 5100 [3]. Although this method was originally developed for the calibration of the partial safety factors of short and slender concrete-encased composite columns under combined axial compression and uni-axial bending, this method can be extensively applied to the calibration of the partial safety factors or capacity factors of any resistance function with multiple factors. In this study, this method is selected for the following three reasons: 1) This method can calibrate multiple capacity factors at the same time, which is required for the calibration of the two capacity factors for steel and concrete in CFST columns. 2) This method assumes that the CFST columns' strength follows a lognormal distribution with the lower limit at zero, instead of a normal distribution, and this corresponds to reality [19]. 3) This method considers the resistance of the CFST columns and neglects the load effect by using the First Order Reliability Method (FORM) sensitivity factor for resistance. Therefore, we can fully utilise the database introduced in the previous section, which does not have information about loading uncertainties. In this section, a summary of Johnson and Huang's method is provided. It includes a modification to allow its application to the Australian design code format, which has capacity factors  $\phi$  instead of partial safety factors  $\gamma_M$  (where  $\phi = 1/\gamma_M$ ).

##### 4.1 Capacity Factor Calibration Method

Let  $g_R(\mathbf{x})$  be a resistance function in an existing code provision, where  $\mathbf{x}$  is a vector of the input parameters. In this study,  $g_R(\mathbf{x})$  = the resistance functions in Eqs. 1 and 2, and  $\mathbf{x} = \{f_y, f'_c, d_o, B, L, \dots\}$ , where the values of  $f_y$  and  $f'_c$  are taken as those of  $f_{ym}$  and  $f_{cm}$  (mean-measured values).

The first step in capacity factor calibration is to make the resistance function unbiased. All the capacity factors inside the function are taken to be unity, and the intrinsic bias is corrected using the following bias correction term:

$$\bar{b} = \frac{1}{N} \sum_{i=1}^N \left( \frac{r_{ei}}{r_{ii}} \right) \quad (7)$$



where  $N$  = the number of test results in the database, e.g., in this study,  $N = 445, 234, 484$ , and  $420$  for rectangular stub columns, long rectangular columns, circular stub columns, and long circular columns, respectively;  $r_{ei}$  = the experimental resistance observed from the  $i$ -th test result; and  $r_{ti}$  = the theoretical resistance calculated from  $g_R(\mathbf{x}_i)$ , where  $\mathbf{x}_i$  is a set of mean-measured input parameters used in the  $i$ -th test. The intrinsic bias exists because the resistance function was not calibrated based on an extensive database. By multiplying this bias correction term with the resistance function, we can predict the unbiased resistance of  $g_R(\mathbf{x})$  as follows:

$$r = \bar{b} g_R(\mathbf{x}) \delta \quad (8)$$

where  $r$  = a predicted resistance for a given set of  $\mathbf{x}$  after bias correction and  $\delta$  is the error of the unbiased resistance function. The error term for each test result,  $\delta_i$ , is estimated as follows:

$$\delta_i = \frac{r_{ei}}{\bar{b} r_{ti}} \quad (9)$$

where  $r_{ei}$  = the experimental resistance observed from the  $i$ -th test result and  $r_{ti}$  = the theoretical resistance obtained from  $g_R(\mathbf{x}_i)$  using the mean measured input parameters. This error term represents the modelling uncertainty of the unbiased prediction model from all possible sources for prediction errors such as oversimplification in the design equations and the neglect of the size effect.

The variance of  $r$  in Eq. 8 is obtained from two sources: 1) the variance of the error term ( $\delta$ ) in Eq. 8, and 2) the variance of the resistance function  $g_R(\mathbf{x})$  based on the uncertainties in the input parameters  $\mathbf{x}$ . Assuming that  $r$  in Eq. 8 follows a lognormal distribution, the coefficient of variation of  $r$  in Eq. 8 is estimated as follows:

$$V_r \cong \sqrt{(V_\delta^2 + V_{rt}^2)} \quad (10)$$

where  $V_\delta$  = the coefficient of variation of the error term ( $\delta$ ); and  $V_{rt}$  = the coefficient of variation of  $g_R(\mathbf{x})$  due to the uncertainties in the input parameters  $\mathbf{x}$ .  $V_\delta$  can be statistically estimated from  $\delta_i$  ( $i=1, \dots, N$ ) in Eq. 9, and  $V_{rt}$  can be estimated for each test result using a Monte Carlo simulation or the first-order approximation of moments [20]. To calculate  $V_{rt}$ , we assume that the mean values of the input parameters  $\mathbf{x}$  are taken as the mean measured values in each test, and the coefficient of variation of the input parameters is obtained from Table 1. Note that the coefficient of variation (c.o.v.) of  $f'_c$  is not directly provided by AS 3600/ NZS 3104 [22],[23], but the values of  $f_{cm}$  according to those of  $f'_c$  are provided. Therefore, the c.o.v. of  $f'_c$  was inferred from the definition that  $f'_c$  is the lower 5% fractile of  $f_{cm}$ . The value for  $f_{cm}$  was chosen as the average of the  $f_{cm}$  values for the entire test dataset.

Table 1. Coefficient of Variation (c.o.v.) of Basic Variables

Variables	c.o.v.	References
Yield strength of steel ( $f_y$ )	0.07	[21]
Compressive strength of concrete ( $f'_c$ )	0.10	[22],[23]
All linear dimensions ( $d_o$ , $b$ , and $L$ )	0.01	[3],[24]
Tube thickness ( $t$ )	0.10	[24]

Because we assume that  $r$  in Eq. 8 follows a lognormal distribution, the standard deviation of  $\ln r$  ( $\sigma_{\ln r}$ ) is calculated as follows:

$$\sigma_{\ln r} = \sqrt{\ln(1 + V_r^2)} \quad (11)$$

This standard deviation is used to calculate the target design value of the resistance ( $r_d$ ) for a target reliability index  $\beta$  as follows:

$$r_d = \bar{b}g_R(\mathbf{x}) \exp(-k\sigma_{\ln r} - 0.5\sigma_{\ln r}^2) \quad (12)$$

where

$$k = \frac{(k_d V_\delta^2 + \beta V_{rt}^2)}{V_r^2} \quad (13)$$

and  $k_d$  = the fractile factor corresponding to  $\beta$  at the 75% confidence level, determined for a number of test data  $N$  from a non-central  $t$ -distribution. Note that the target reliability index  $\beta$  considers only the resistance, and ignores the effect of loads. In this case, AS 5104: 2005/ISO 2394:1998 [26],[27] recommends that  $\beta$  be empirically estimated as  $\alpha_R \times \beta_t$ , where  $\beta_t$  = the target reliability considering both resistance and load effects and  $\alpha_R$  = the First Order Reliability Method (FORM) sensitivity factor when resistance is taken as 0.8. Therefore, the design value for resistance corresponds to the product  $\alpha_R \beta = 0.8 \times 3.8 = 3.04$  (equivalent to the probability of the actual resistance falling below the design resistance of 1 in 845 = 0.0012).

## 4.2 Determination of Capacity Factors

This section provides the calculation steps of the statistical method proposed by Johnson and Huang [16] to estimate the multiple capacity factors for steel ( $\phi$ ) and concrete ( $\phi_c$ ). We assume that these capacity factors are defined by the product of a material independent model factor ( $\phi_m$ ), and material dependent factors  $\phi_{ms}$  for steel and  $\phi_{mc}$  for concrete. In other words,  $\phi = \phi_m \times \phi_{ms}$  for steel, and  $\phi_c = \phi_m \times \phi_{mc}$  for concrete.

First, we calculate the material dependent factors ( $\phi_{ms}$  and  $\phi_{mc}$ ) by using the ratio between the characteristic strength and the design strength of each material. For example, the characteristic strength of structural steel is defined as follows:

$$f_{yk} = \bar{f}_y \exp(-1.64\sigma_{\ln f_y} - 0.5\sigma_{\ln f_y}^2) \quad (14)$$

where

$$\sigma_{\ln f_y} = \sqrt{\ln(1 + V_{f_y}^2)} \quad (15)$$

and  $V_{f_y} = 0.07$  from Table 1. The design strength of steel for the target reliability index  $\beta$  is defined as follows:

$$f_{yd} = \bar{f}_y \exp(-\beta\sigma_{\ln f_y} - 0.5\sigma_{\ln f_y}^2) \quad (16)$$

Then, the material dependent factor for steel,  $\phi_{ms}$ , is obtained from the ratio of Eqs. 15 and 16 as follows:

$$\phi_{ms} = \frac{f_{yd}}{f_{yk}} = \frac{1}{\exp[(\beta - 1.64)\sigma_{\ln f_y}]} \quad (17)$$

The calculations in Eqs. 14-17 are repeated for concrete to calculate the material dependent factor  $\phi_{mc}$ , by replacing  $V_{f_y}$  with  $V_{f_c} = 0.015$ , as suggested in Table 1.

Next, we calculate the material independent model factor ( $\phi_m$ ) for the  $i$ -th test result as follows:

$$r_{di} = g_R(\Theta_i, \mathbf{x}_{ki}, \mathbf{x}_{ri}) \quad (18)$$

where  $r_{di}$  = the target design value obtained in Eq. 12 for each test result;  $\Theta_i$  = the capacity reduction factors  $\phi$  and  $\phi_c$  for the  $i$ -th test;  $\mathbf{x}_{ki}$  = the characteristic strength of the materials ( $f_y$  and  $f_c$ ) for the  $i$ -th test; and  $\mathbf{x}_{ri}$  = the input parameters, except  $\mathbf{x}_{ki}$ , for the  $i$ -th test. In this equation, for the  $i$ -th test, the only unknown term is the material independent factor  $\phi_{mi}$  inside  $\Theta_i$ . This term can easily be obtained using any numerical solver for non-linear programming. In this study, the Active-Set Optimisation algorithm [29] is used. We repeat this calculation for the entire test dataset and find the material dependent factor,  $\phi_m$  by averaging  $\phi_{mi}$  as follows:

$$\phi_m = \frac{1}{N} \sum_{i=1}^N \phi_{mi} \quad (19)$$

Finally, the capacity factors are calculated as follows:

$$\phi = \phi_m \times \phi_{ms} \quad (\text{for steel}) \quad \text{and} \quad \phi_c = \phi_m \times \phi_{mc} \quad (\text{for concrete}) \quad (20)$$

## 5. INVERSE ANALYSIS METHOD FOR THE RELIABILITY ESTIMATION OF EXISTING DESIGN EQUATIONS

In this section, an approach that is the inverse of the Johnson and Huang's method [16] for estimating the reliability of existing design codes for given capacity factors is proposed. It can be used when the capacity factors are known but the corresponding reliability index is unknown. This inverse approach is useful in quantifying the conservatism of the design equations with given capacity factors in terms of reliability.

This approach is based on inverting Johnson and Huang's method, which was introduced in the previous section. Let  $g_R(\Theta, \mathbf{x}_k, \mathbf{x}_r)$  be a resistance function, where  $\mathbf{x}_k$  = the characteristic strength of the materials;  $\mathbf{x}_r$  = the input parameters, except  $\mathbf{x}_k$ ; and  $\Theta$  = the capacity factors which are given. To calculate the reliability index of an equation with known capacity factors, the following equation can be derived by combining Eqs. 12 and 18 for each test datum:

$$\bar{b}g_R(\mathbf{x}_i) \exp(-k\sigma_{\ln r} - 0.5\sigma_{\ln r}^2) = g_R(\mathbf{x}_{ki}, \mathbf{x}_{ri}, \Theta) \quad (21)$$

where all the terms on the left-hand side ( $\bar{b}$ ,  $g_R(\mathbf{x}_i)$ ,  $k$ , and  $\sigma_{\ln r}$ ) can be calculated using Eqs. 7-13, except the target reliability index  $\beta$  in Eq. 13, which is also included in  $k_d$  in Eq. 13. This is the only unknown term in this equation, and it is calculated as  $\beta_i$  for each test result. The right-hand side of Eq. 21 is the design resistance, which is calculated from the design equation with the given capacity factors. Eq. 21 can be solved numerically for the only unknown term  $\beta_i$ . Again, the Active-Set Optimisation algorithm [29] is used as a numerical solver for this nonlinear equation. This solving for the term  $\beta_i$  in Eq. 21 is repeated for the complete test results, and the reliability of a design equation with given capacity factors is calculated as the average of the  $\beta_i$  values as follows:

$$\beta = \frac{1}{N} \sum_{i=1}^N \beta_i \quad (22)$$

where  $N$  = the number of test results.

## 6. RESULTS AND DISCUSSIONS

### 6.1 Capacity Factor Calibration using Johnson and Huang's Method

In this section, we first use Johnson and Huang's method summarised in Section 4 to calibrate the capacity reduction factors ( $\phi$  and  $\phi_c$ ) in Eqs. 1 and 2. The preliminary work of this analysis can be found in [25], in which Johnson and Huang's method was used to calibrate the factors for CFST stub columns according to the Eurocode format. For this calibration, we need to set the target reliability index  $\beta$  required in Eqs. 13 and 17. The target reliability index is related to the expected social and economic consequences of a design failure. According to AS 5104: 2005 [26] /ISO 2394:1998 [27], the suggested reliability index for ultimate limit-state design is  $\beta_t = 3.8$ , which corresponds to a case in which the consequences of failure are great (the highest level) and the relative costs of safety measures are moderate (Table 2). These are equivalent to 'Consequence Classes' in EN 1990, and 'Importance Levels' in AS/NZS 1170 [28]. As mentioned earlier, the procedure in Section 4 only considers resistance, ignoring the load effect, and the target reliability index  $\beta$  is calculated as  $0.8 \beta_t = 3.04$  by using a dominating resistance parameter,  $\alpha_R = 0.8$ , as recommended in AS 5104: 2005 [26] /ISO 2394:1998 [27].

Based on this target reliability index, the calculations in Eqs. 7-20 are conducted, and the capacity reduction factors for steel and concrete for rectangular and circular columns are calculated. The results are reported in Table 3, along with the results of the intermediate steps.

Table 3. Results Summary for Target Reliability Index  $\beta = 3.04$

Section types	Member types	$\bar{b}$ Eq. (7)	$V_r$ (mean) Eq. (10)	$\phi$	$\phi_c$
Rectangular	Stub columns	1.06	0.14	0.82	0.77
	Long columns	1.10	0.16	0.82	0.76
Circular	Stub columns	1.03	0.15	0.78	0.73
	Long columns	1.11	0.16	0.83	0.77

In this table, the constant bias term  $\bar{b}$  refers to the conservatism embedded in a design equation calculated using Eq. 7, and the average of the coefficient of variation of the resistance function  $V_r$  (mean) refers to the accuracy of a given design equation, considering the modelling and parameter uncertainties calculated using Eq. 10. Because  $\bar{b}$  is defined in terms of the ratio between the experimental resistance and the theoretical resistance, if the  $\bar{b}$  of a design equation is close to 1, the equation has almost no conservatism. In other words, the greater the capacity factor values are, the more embedded conservatism there is. A large  $V_r$  (mean) value indicates large uncertainties in a design equation. To achieve the same target reliability with a large value of  $V_r$  (mean), the capacity factors should be decreased to achieve more conservatism.

From the results reported in the table, long rectangular columns require slightly smaller capacity factors than long circular columns because they have a slightly smaller  $\bar{b}$  value with the same  $V_r$  (mean) values. Similarly, circular stub columns require the smallest capacity factors because they have the lowest  $\bar{b}$  value. The design equations for circular stub columns have almost no conservatism in itself as its  $\bar{b}$  value is 1.03, which is close to 1.

Based on the results of this table, the overall calibrated capacity reduction factors show values for steel and concrete that are closer together than the values suggested in AS 5100, i.e.,  $\phi = 0.9$ , and  $\phi_c = 0.6$ . The capacity reduction factor of steel shows a reduction, but that of concrete shows increases

for both rectangular and circular members. This difference can be explained by 1) the fact that the results in this paper were obtained based on an extensive up-to-date database with a large number of test results; and 2) the fact that the capacity reduction factors in AS 5100 were originally suggested for the separate use of steel and concrete, and they do not fully reflect the simultaneous behaviours of concrete and steel, such as the confinement effect of steel tubes. In Figure 2, the calibrated results of the capacity reduction factors in Eq. 20 are plotted for a range of target reliability values between 2.5 and 4.2 to demonstrate the sensitivity of the results. These plots show that the capacity reduction factors vary linearly according to the target reliability.

Based on these results, we cannot conclude that the current AS 5100 code should be immediately updated because we do not know how much conservatism is embedded in the capacity factors provided in AS 5100. However, the interaction between concrete and steel should be carefully considered when the capacity reduction factors are updated because the values of the capacity reduction factors are closer to one another than those in AS 5100 [3] for the overall range of reliability indices.

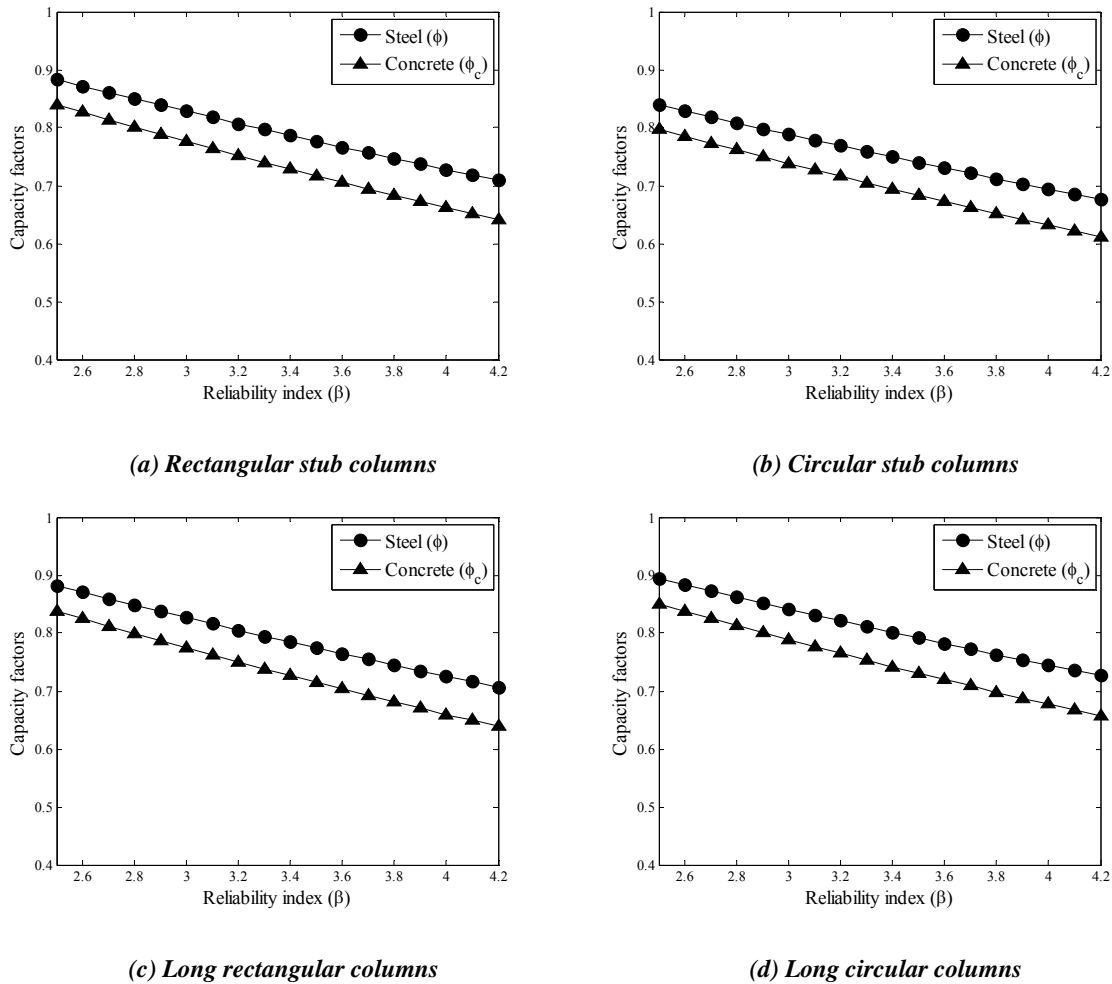


Figure 2. Capacity Factor Versus Reliability Index for Different Member Types

## 6.2 Inverse Analysis Results using the Proposed Inverse Analysis Method

To compare the effects of the capacity factor values calculated using Johnson and Huang's method [16] and those provided in AS 5100, regarding the design equations' reliability, the inverse analysis method proposed in Section 5 is utilised. For these two cases, inverse analyses have been performed, and the reliability for each section/member types has been calculated. The results are listed in Table 4. In this table, we can first confirm that, for all cases, the capacity factors obtained using Johnson and Huang's method provide reliability indices similar to the target reliability index,  $\beta = 3.04$ , as expected, while the capacity factors given by AS 5100 provide much higher reliability indices that are close to 3.40. Here, the slight fluctuations in the values around 3.04 for the capacity factors calculated from Johnson and Huang's method are caused by the error produced by the numerical solvers and the averaging procedures in Eqs. 19 and 22, where the scattering of the calculated values is neglected. These results are also illustrated in Figure 3 as a bar graph. In this graph, the dotted lines show the reliability index  $\beta = 3.04$ . Johnson and Huang's method's capacity factors provide reliability around this dotted line while the capacity factors provided in AS 5100 provide greater reliability around a value of 3.4, indicating greater conservatism. In addition, different section/member types of CFST columns provide different reliability indices based on type because the design equations themselves have different embedded conservatisms and accuracies for different column types.

The conservatism of the capacity factors provided by AS 5100 can also be clearly confirmed by the following analyses. Here, we calculate the optimal capacity factors for the target reliability index,  $\beta = 3.04$ , but we fix one of the capacity factors as the value provided in AS 5100 and calculate the other factor. For example, we fix the capacity factor for steel as 0.9 and calculate the remaining capacity factor for concrete, or we fix the capacity factor for concrete as 0.6 and calculate the remaining capacity factor for steel. From this analysis, we can confirm that the design equations are conservative if the calculated capacity factor has greater values than those in AS 5100 for the target reliability index,  $\beta = 3.04$ , and vice versa. For these analyses, all the calculations in Eqs. 7-13 are used in a same manner, but the remaining calculation steps in Eqs. 14-20 are modified so as to be simpler because we only estimate a single capacity factor. The calculation steps and assumptions used in Eqs. 14-17 are not needed in this analysis, because they are only needed for multiple capacity factor calculation, and in Eq. 18, the unknown term  $\phi_{mi}$  inside  $\Theta_i$  is replaced by  $\phi_i$  for steel or  $\phi_{ci}$  for concrete for the  $i$ -th test. Again, to solve for  $\phi_i$  or  $\phi_{ci}$ , any numerical solver designed for non-linear programming can be used, and in this study, the Active-Set Optimisation algorithm [29] is used.

Table 4. Calculated Reliability Indices from the Inverse Analysis

Section types	Member types	Capacity factors	Reliability index ( $\beta$ )
Rectangular	Stub columns	Johnson and Huang, $\phi = 0.82, \phi_c = 0.77$	3.06
		AS 5100, $\phi = 0.9, \phi_c = 0.6$	3.43
	Long columns	Johnson and Huang, $\phi = 0.82, \phi_c = 0.76$	3.02
		AS 5100, $\phi = 0.9, \phi_c = 0.6$	3.44
Circular	Stub columns	Johnson and Huang, $\phi = 0.78, \phi_c = 0.73$	2.97
		AS 5100, $\phi = 0.9, \phi_c = 0.6$	3.49
	Long columns	Johnson and Huang, $\phi = 0.83, \phi_c = 0.77$	3.00
		AS 5100, $\phi = 0.9, \phi_c = 0.6$	3.36

The analysis results are plotted in Figures 4 and 5, where one capacity factor is calculated for a

range of target reliability values between 2.5 and 4.2 when the other factor is fixed to the value provided in AS 5100. Figure 4 shows the results when the capacity factor for steel is fixed at 0.9 and the factor for concrete is calculated. Figure 5 shows the results when the capacity factor for concrete is fixed at 0.6 and the factor for steel is calculated. For all results in Figure 4, the calculated capacity factor for concrete is always greater than 0.6 for the target reliability index,  $\beta = 3.04$ . This means that the capacity factors given in AS 5100 provide higher reliability than the target reliability, implying more conservatism. This observation is also supported by Figure 5, and the calculated capacity factor for steel is always greater than that provided in AS 5100 for the target reliability index,  $\beta = 3.04$ . These results are consistent with the inverse reliability analysis results in Table 4 and Figure 3.

Table 5. Conservatism and Uncertainties after applying Capacity Factors

Section types	Member types	Capacity factors	$\bar{b}$ Eq. (7)	$V_r$ (mean) Eq. (10) (before applying capacity factors)	$V_r$ (mean) Eq. (10)
Rectangular	Stub columns	Johnson and Huang, $\phi = 0.82, \phi_c = 0.77$	1.33	0.14	0.14
		AS 5100, $\phi = 0.9, \phi_c = 0.6$	1.40		0.16
	Long columns	Johnson and Huang, $\phi = 0.82, \phi_c = 0.76$	1.43	0.16	0.16
		AS 5100, $\phi = 0.9, \phi_c = 0.6$	1.54		0.18
Circular	Stub columns	Johnson and Huang, $\phi = 0.78, \phi_c = 0.73$	1.37	0.15	0.15
		AS 5100, $\phi = 0.9, \phi_c = 0.6$	1.50		0.15
	Long columns	Johnson and Huang, $\phi = 0.83, \phi_c = 0.77$	1.46	0.16	0.18
		AS 5100, $\phi = 0.9, \phi_c = 0.6$	1.54		0.18

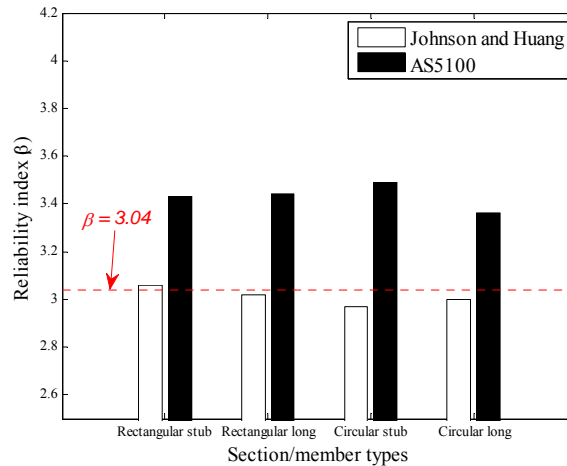


Figure 3. Comparison of Reliability Indices for Different Capacity Factors

To see the conservatism of the capacity factors for both steel and concrete in AS 5100, similar analyses have been performed by fixing the capacity factor for steel at 0.93, which is a slightly increased value from that in AS 5100. This value was chosen to confirm if the capacity factor for concrete is still greater than the value provided in AS 5100 when using this slightly increased value in the capacity factor for steel. The analysis results are plotted in Figure 6, and again, for all section/member types, the calculated capacity factor for concrete for the target reliability index,  $\beta = 3.04$  is still greater than 0.6, which is the value provided in AS 5100. These results imply that the capacity factors provided in AS 5100 are conservative compared to the target reliability suggesting both capacity factors can be slightly increased to create an optimal design.

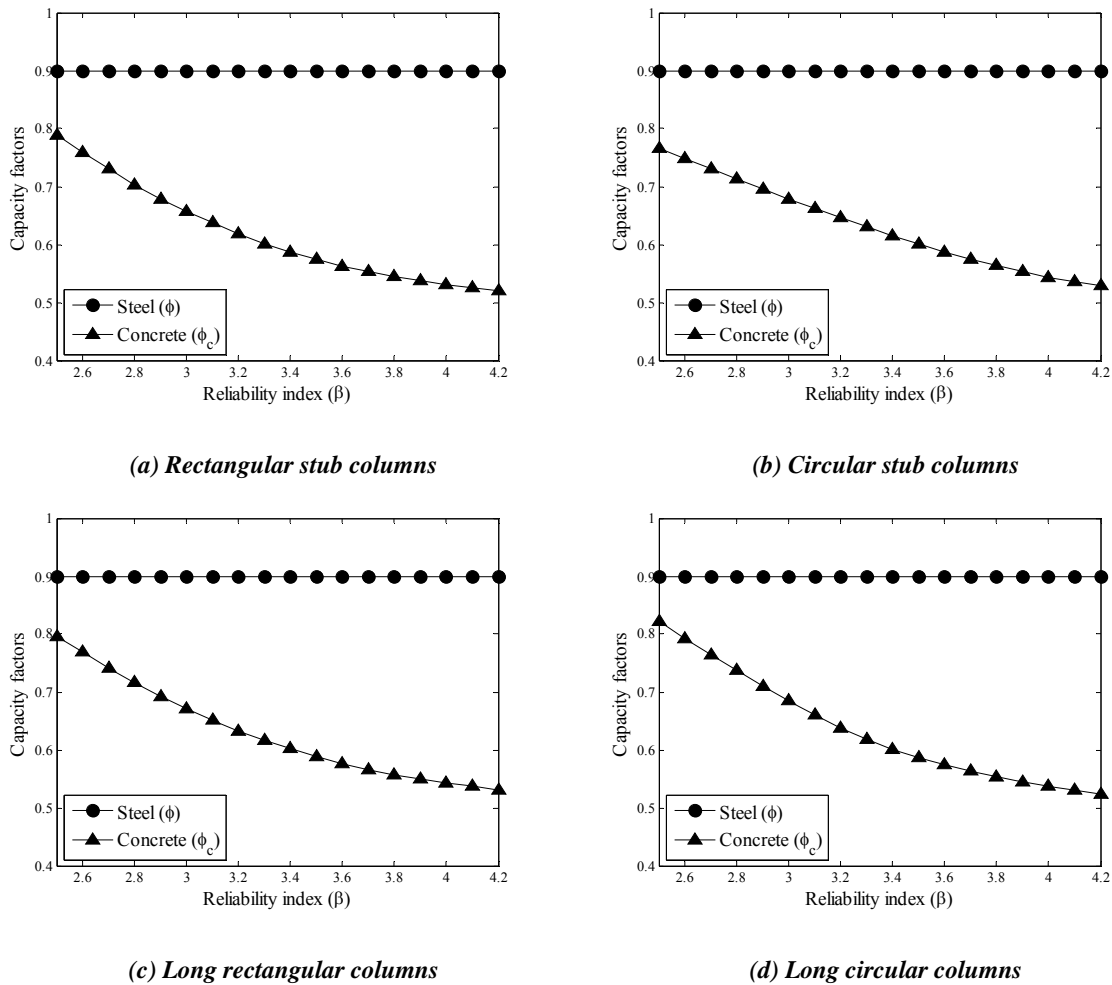
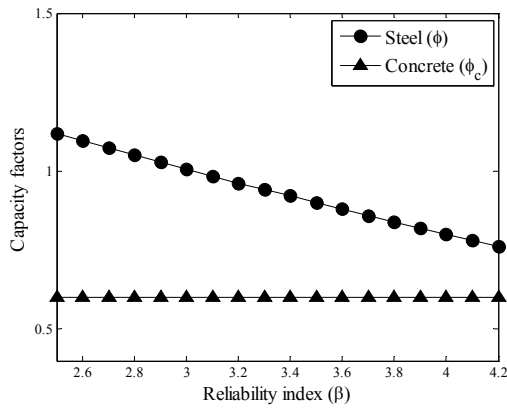
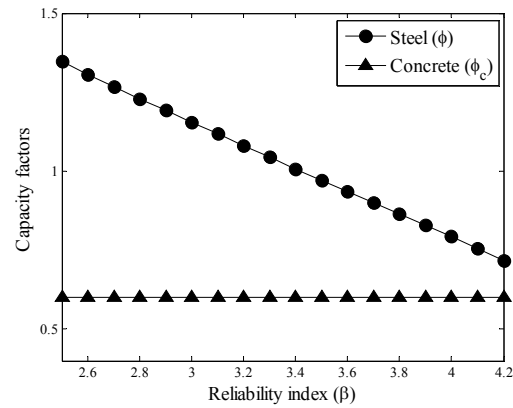


Figure 4. Capacity Factor Versus Reliability Index when the Capacity Factor for Steel is Fixed at 0.9.

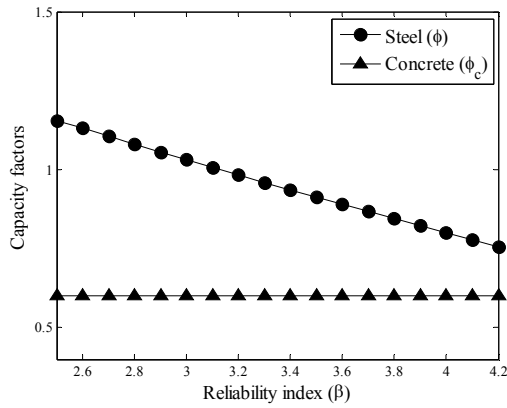




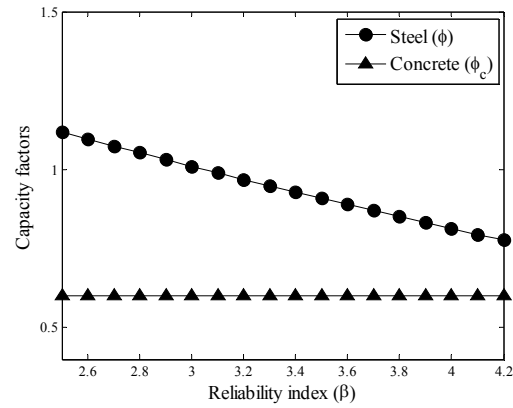
(a) Rectangular stub columns



(b) Circular stub columns



(c) Long rectangular columns



(d) Long circular columns

Figure 5. Capacity Factor Versus Reliability Index when the Capacity Factor for Concrete is Fixed at 0.6

### 6.3 The Effect of Multiple Unbalanced Capacity Factors

Johnson and Huang's method [16] and the inverse analyses in the previous sections assumed that the modelling and parameter uncertainties were same before and after the application of the capacity factors. However, they did not consider any additional uncertainties created after applying the capacity factors to the theoretical equations. In the original form of a theoretical equation, no capacity factors are considered, or it is assumed that all the capacity factors are equal to unity, and all the modelling and parameter uncertainties are estimated based on this form. However, if we apply different capacity factor values to different materials in a composite member, this will create an imbalance between the predicted strengths of these materials. This imbalance will create additional uncertainties because it will change the design equations' accuracies and propagate parameter uncertainties in a different manner. Therefore, in this study, we repeat the inverse analysis carried out in the previous section by recalculating the parameter and modelling uncertainties after applying the capacity factors. Because the application of imbalanced capacity factors for steel and concrete strengths will change the accuracy of the design equations, the uncertainties need to be updated accordingly.

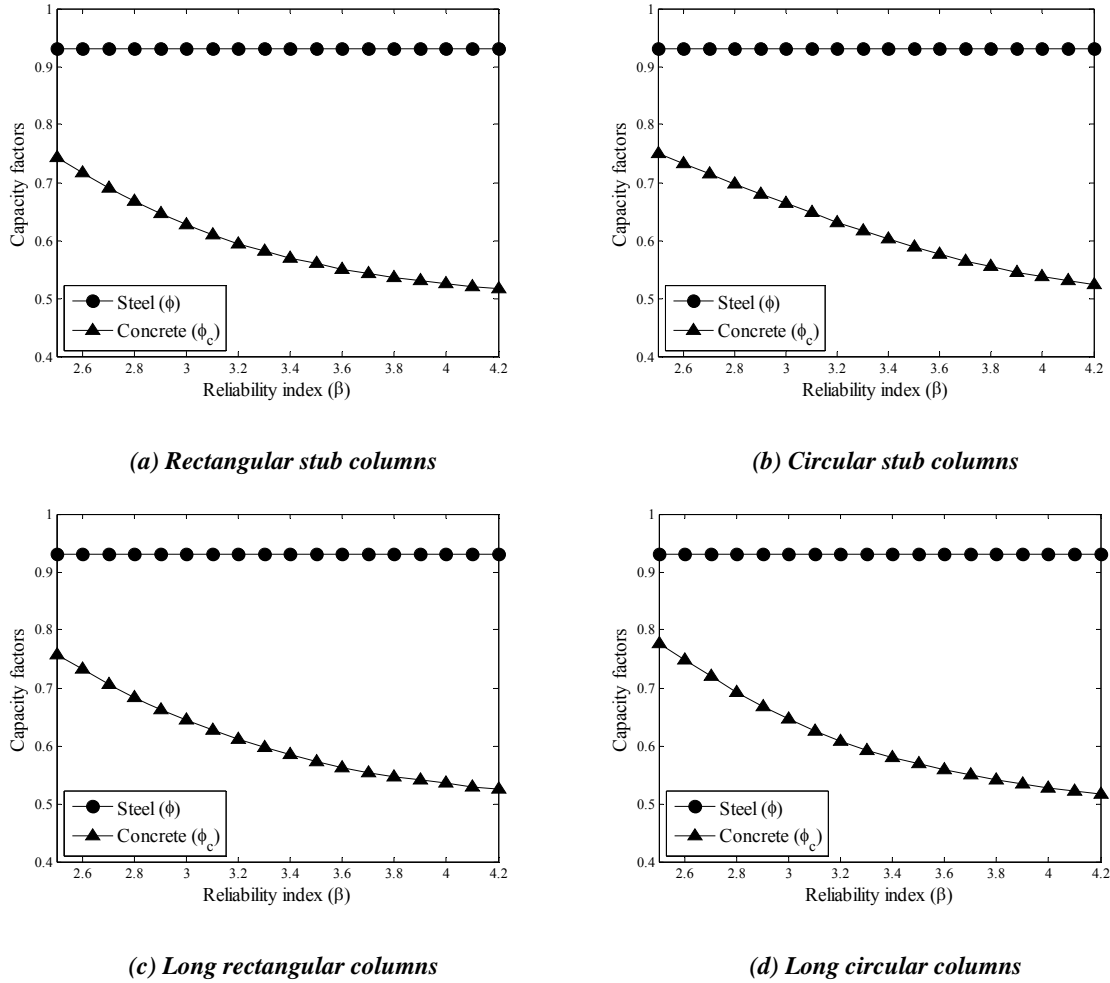


Figure 6. Capacity Factor Versus Reliability Index when the Capacity Factor for Steel is Fixed to be 0.93

To investigate the effect of these additional uncertainties created via the application of different capacity factors for different materials, the inverse analysis proposed in Section 5 has been repeated, but the resistance function  $g_R(\mathbf{x})$  in Eqs. 7-10 have been replaced by  $g_R(\mathbf{x}, \Theta)$ , where  $\mathbf{x}$  = the mean-measured input parameter values and  $\Theta$  = the applied capacity factors. Due to this change, the values of  $\bar{b}$  in Eq. 7 and  $V_r$  in Eq. 10 are updated as shown in Table 5. In this table, the constant bias term  $\bar{b}$  refers to the updated conservatism of a design equation, and  $V_r$  (mean) refers to the updated accuracy of a design equation. For all section/member types, the  $\bar{b}$  values are greater than those in the previous inverse analysis because the design equations now have more conservatism after applying capacity factors. The  $V_r$  (mean) values are increased or remain the same after applying the capacity factors, because the accuracy of the imbalanced equations has been changed due to the application of these factors.

After applying the capacity factors provided by AS 5100, the reliabilities for all section/member types have been reduced to values close to the target reliability index,  $\beta = 3.04$ , except for the equations for circular stub columns (Table 6). This exception occurred because the  $V_r$  (mean) value for the equations for circular stub columns did not increase after applying the capacity factors provided by AS 5100, while the  $V_r$  (mean) values for the other cases were increased. The increase

in the  $V_r$  (mean) values indicates an increase of modelling error or a decrease of accuracy, and this reduces the reliability of equations. The application of different constant values to the steel and concrete strength predictions in an unbalanced manner decreases the accuracy of the equations, except for those related to circular stub columns. It is also noted that the application of the capacity factors obtained from the Johnson and Huang's method decreases the accuracy of the equations for long circular columns and these values cannot achieve the target reliability index,  $\beta = 3.04$ , after considering the increased uncertainties caused by the application of the capacity factors obtained from Johnson and Huang's method. The reliability indices after applying the capacity factors are also represented as a bar graph in Figure 7.

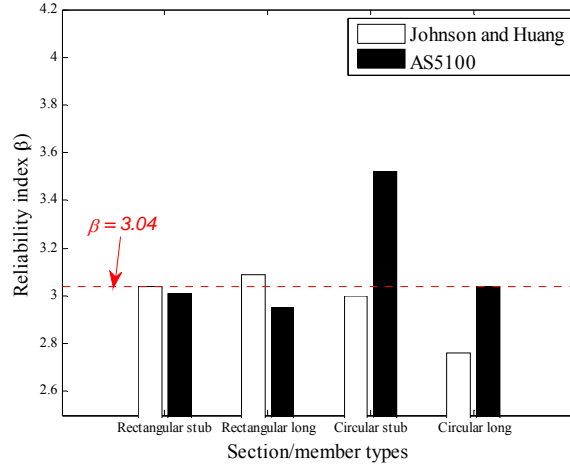


Figure 7. Comparison of Reliability Indices for Different Capacity Factors after applying Capacity Factors

It is observed that the capacity factors for composite columns in AS 5100 yield almost the same target reliability suggested in AS 5104: 2005 [26] /ISO 2394:1998 [27] after considering the additional uncertainties created via the application of the capacity factors. These results show that the current capacity factor values in AS 5100 for CFST columns need to be maintained. However, this is due to the significant reduction in the accuracy of the design equations that reduce the large conservatism embedded in these factors, which concludes that these factors are not optimally calibrated for cost-safety balanced design. In addition, the results in this paper and the parameter distributions shown in Figure 1 demonstrate that the existing design equations can be safely extended to cover a wider scope than is currently considered in either EC 4 or AISC, as follows:

- Rectangular hollow sections
  - $200 \text{ MPa} < f_{ym} < 460 \text{ MPa}$
  - $20 \text{ MPa} < f_{cm} < 100 \text{ MPa}$
  - Depth  $h$  to width  $B$  ratio of the composite cross section  $1.0 < h/D < 2.0$
  - $\text{Max } h/t = 125 \sqrt{\frac{250}{f_y}}$
- Circular hollow sections
  - $180 \text{ MPa} < f_{ym} < 680 \text{ MPa}$
  - $20 \text{ MPa} < f_{cm} < 100 \text{ MPa}$
  - $\text{Max } D/t = 225 \left( \frac{250}{f_y} \right)$

## 7. CONCLUSIONS

The aim of this paper was to attempt to improve the practical applications of CFST members by re-calibrating the capacity reduction factors in AS 5100 [3] and investigate the effect of these factors and the factors given by AS 5100. The factor calibration method developed by Johnson and Huang [16] was used to re-calibrate the capacity factors for CFST columns in AS 5100, based on the extensive database developed by Tao et al. [7], which contains 1,583 test results for CFST columns. In addition, an inverse analysis procedure based on Johnson and Huang's method was proposed in order to estimate the reliability of design equations with known capacity factors. Using these methods, first, the capacity factors for CFST columns in AS 5100 were calibrated, and the results showed that the values of the capacity reduction factors are closer to each other than those in AS 5100. Second, the proposed inverse analysis procedure was used to estimate the reliability of the equations in AS 5100, and the results showed that the current capacity factors given in AS 5100 provide more conservatism, represented by a higher reliability than the target reliability suggested in AS 5104: 2005 [26] /ISO 2394:1998 [27]. Lastly, the inverse analysis was repeated considering the additional uncertainties created from the application of the capacity factors. It was observed that the application of different constant values to the steel and concrete strength predictions in an unbalanced manner decreases the accuracy of the equations in most cases, and the capacity factors for composite columns in AS 5100 give almost the same target reliability as that suggested in AS 5104: 2005 [26] /ISO 2394:1998 [27]. After taking all the results into consideration, the current capacity factor values in AS 5100 for CFST columns are adequate with regards to safety and can be maintained to meet the target reliability suggested in the current design codes. However, it should also be noted that this is due to the significant reduction in the accuracy of the design equations that reduce the large conservatism embedded in these factors, which leads to the conclusion that they are not optimal for cost-safety balanced design. For future research, further development of the capacity factor calibration method would be advantageous in order to incorporate the uncertainties caused by the imbalance between the predicted strengths of these materials as observed from the analysis of the proposed inverse method for estimating the reliability of capacity prediction models. It should also be noted that although these studies have been carried out for the purposes of the Australian Standards, they have important ramifications for international codes of practice regarding structural composite members such as with EC 4 [4], AISC [5], and the code of practice in Hong Kong [6].

## ACKNOWLEDGMENTS

This work is supported by the Australian Research Council (ARC) under its Discovery project (Project No: DP120101944). The authors wish to thank Dr Douglas Goode, the University of Manchester, UK, and Professor Roberto T Leon, Virginia Tech, USA for providing the initial column databases.

## REFERENCES

- [1] Shams, M. and Saadeghvaziri, M.A., "State of the Art of Concrete-filled Steel Tubular Columns", *ACI Structural Journal*, 1997, Vol. 94, No.5, pp. 558-571.
- [2] Chitawadagi, M.V., Narasimhan, M.C. and Kulkarni, S., "Axial Capacity of Rectangular Concrete-filled Steel Tube Columns-DOE Approach", *Construction and Building Materials*, 2010, Vol. 24, No. 4, pp. 585-595.
- [3] Standards Australia International Ltd., "AS 5100.6:2004 Bridge Design, Part 6: Steel and Composite Construction", New South Wales, Australia, 2004.

- [4] British Standards Institution, "BS EN 1994-1-1:2005 Eurocode 4: Design of Composite Steel and Concrete Structures", Part 1-1. London, UK, 2005.
- [5] American Institute of Steel Construction, "Specification for Structural Steel Buildings. ANSI/AISC 360-10", Chicago, IL, USA, 2010.
- [6] Buildings Department of Hong Kong, "Code of Practice for Structural Use of Steel", Buildings Department, the HKSAR Government. Hong Kong, 2005.
- [7] Tao, Z., Uy, B., Han, L.H. and He, S.H., "Design of Concrete-filled Steel Tubular Members According to the Australian Standard AS 5100 Model and Calibration", Australian Journal of Structural Engineering, 2008, Vol. 8, No. 3, pp. 197-214.
- [8] Goode, C.D., "A Review and Analysis of over One Thousand Tests on Concrete Filled Steel Tube Columns", Proceedings of 8th International Conference on Steel-Concrete Composite and Hybrid Structures, Harbin, China, 2006, August 12-15.
- [9] Wu, F.Y., "Compressive Behaviour of Recycled Concrete-filled Steel Tubes", Masters Thesis, College of Civil Engineering, Fuzhou University, China, 2006. (in Chinese).
- [10] Gupta, P.K., Sarda, S.M. and Kumar, M.S., "Experimental and Computational Study of Concrete Filled Steel Tubular Columns under Axial Loads", Journal of Constructional Steel Research, 2007, Vol. 63, No. 2, pp. 182-193.
- [11] Lue, D.M., Liu, J.L. and Yen, T., "Experimental Study on Rectangular CFT Columns with High-Strength Concrete", Journal of Constructional Steel Research, 2007, Vol. 63, No. 1, pp. 37-44.
- [12] Tao, Z., Han, L.H. and Wang, D.Y., "Experimental Behaviour of Concrete-filled Stiffened Thin-walled Steel Tubular Columns", Thin-Walled Structures, 2007, Vol. 45, No. 5, pp. 517-527.
- [13] Yu, Z.W., Ding, F.X. and Cai, C.S., "Experimental Behavior of Circular Concrete-filled Steel Tube Stub Columns", Journal of Constructional Steel Research, 2007, Vol. 63, No. 2, pp. 165-174.
- [14] Yang, Y.F. and Han, L.H., "Concrete Filled Steel Tube (CFST) Columns Subjected to Concentrically Partial Compression", Thin-Walled Structures, 2012, Vol. 50, No. 1, pp. 147-156.
- [15] Chang, X., Fu, L., Zhao, H.B. and Zhang, Y.B., "Behaviors of Axially Loaded Circular Concrete-filled Steel Tube (CFT) Stub Columns with Notch in Steel Tubes", Thin-Walled Structures, 2013, Vol. 73, pp. 273-280.
- [16] Johnson, R.P. and Huang D., "Statistical Calibration of Safety Factors for Encased Composite Columns", Composite Construction in Steel and Concrete III, ASCE, New York, 1997, pp. 380-391.
- [17] Yu, Q., Tao, Z. and Wu, Y.X., "Experimental Behaviour of High Performance Concrete-filled Steel Tubular Columns", Thin-Walled Structures, 2008, Vol. 46, No. 4, pp. 362-370.
- [18] Chen, Z., Zhu, J. and Wu, P., "High Strength Concrete and its Application", Beijing, China, Tsinghua University Press, 1996. (in Chinese).
- [19] Gulvanessian, H. and Holicky, M., "Annex C – Calibration Procedure", Leonardo DaVinci Pilot Project CZ/02/B/F/PP-134007, Handbook 2-Reliability Backgrounds, 2005.
- [20] Ang, A.H.S. and Tang, W.H., "Probability Concepts in Engineering: Emphasis on Applications to Civil and Environmental Engineering", New York, John Wiley & Sons, 2007.
- [21] Joint Committee on Structural Safety, JCSS Probabilistic Model Code, <http://www.jcss.byg.dtu.dk/>, 2001.
- [22] Standards Australia International Ltd., "AS 3600:2009 Concrete Structures", New South Wales, Australia, 2009.
- [23] Standards New Zealand, "NZS 3104: 2003 Specification for Concrete Production", Wellington, New Zealand, 2003.

- [24] Standards Australia/Standards New Zealand, “AS/NZS 1163:2009 Cold-Formed Structural Steel Hollow Sections”, Sydney, Australia, 2009.
- [25] Kang, W.H., Uy, B., Tao, Z. and Hicks, S., “Statistical Safety Factor Calibration of Short Concrete-filled Steel Tubular Columns”, Proceedings of the 22nd Australasian Conference on the Mechanics of Structures and Materials, ACMSM 22, Sydney, Australia, 2012, December 11-14.
- [26] Standards Australia International Ltd., “AS 5104: 2005 General Principles on Reliability for Structures”, New South Wales, Australia, 2005.
- [27] International Organization for Standardization, “ISO 2394:1998 General Principles on Reliability for Structures”, Geneva, 1998.
- [28] Standards Australia International Ltd., “AS/NZS 1170.0: 2002 Structural Design Actions – General Principles”, New South Wales, Australia, 2002.
- [29] Nocedal, J and Wright, S., “Numerical Optimization. 2nd ed.”, Berlin, New York: Springer-Verlag, 2006, ISBN 978-0-387-30303-1.

# LOAD-CARRYING CAPACITY OF SINGLE-ROW STEEL SCAFFOLDS WITH VARIOUS SETUPS

Jui-Lin Peng<sup>1,\*</sup>, Chung-Ming Ho<sup>2</sup>, Chen-Chung Lin<sup>3</sup> and Wai-Fah Chen<sup>4</sup>

<sup>1</sup> Professor, Department of Construction Engineering,  
National Yunlin University of Science and Technology, Yunlin, Taiwan, ROC.

<sup>2</sup> Ph.D. Student, Graduate School of Engineering Science and Technology,  
National Yunlin University of Science and Technology, Yunlin, Taiwan, ROC.

<sup>3</sup> Associate Researcher, Institute of Occupational Safety and Health, Council of Labor Affairs,  
Executive Yuan, Taiwan, ROC.

<sup>4</sup> Professor, Department of Civil and Environmental Engineering, University of Hawaii at Manoa, Hawaii, USA.

\*(Corresponding author: E-mail: peng.jl@msa.hinet.net)

Received: 19 February 2014; Revised: 16 May 2014; Accepted: 30 June 2014

**ABSTRACT:** Factors such as high headroom and large spans explain why some areas of a reinforced concrete building, including the entrance lobby of a hospital or the stage area of an auditorium, often require large-scale isolated reinforced concrete beams to support the weight passed down from the slab. On a construction site, single-row steel scaffolds are often set up underneath these isolated beams to function as falsework. The setup method of these steel scaffolds is unique and design-related information is lacking. Single-row steel scaffolds are often set up on a construction site based on the construction experience of workers, explaining the occasional collapses of steel scaffolds underneath the isolated beams. Therefore, this study closely examines why single-row steel scaffolds collapse. Experimental results indicate that treating the variation of headroom under the isolated beams involves using single-row steel scaffolds with different setups. The load-carrying capacities of one-bay, two-story door-type steel scaffolds (2D) closely resemble those of one-bay, three-story door-type steel scaffolds (3D). When multi-bay setups are used, the load-carrying capacities of two-story door-type steel scaffolds (2D) increase with the number of bays. Similarly, when multi-bay setups are used, the load-carrying capacities of one-door, one-square, two-rectangle steel scaffolds (DS2R) also increase with the number of bays. Although the height of the DS2R setup exceeds that of the 2D setup, the load-carrying capacity of the DS2R setup is still higher than that of the 2D setup. This finding demonstrates that structural stiffness of the combined setup of steel scaffolds is higher than that of two-story door-type steel scaffolds. A more convenient design of the strength of steel scaffolds is possible by quickly estimating the load-carrying capacity of a single-row, multi-set steel scaffolds based on that of single-row, one-set steel scaffolds. By applying the second loading, this study also simulates the load-carrying capacity of the steel scaffolds using reusable materials in the worst condition in order to obtain the strength reduction factors of the reusable steel scaffolds. When designing the strength of single-row reusable steel scaffolds, designers may select proper strength reduction factors with different standard deviations based on project fund and safety requirements. Moreover, steel scaffolds with defects randomly selected from the construction site are evaluated. Test results indicate that the load-carrying capacities of the steel scaffolds with defects exceed those of the reusable steel scaffolds in the worst condition. This finding suggests that the strength of the steel scaffolds with defects is still reusable. The vertical displacements of various setups of steel scaffolds under maximum load provide a valuable reference for contractors in designing the isolated reinforced concrete beams when construction accuracy must be considered. The results of this study significantly contribute to efforts to determine related parameters in follow-up numerical analyses in the future.

**Keywords:** Load-carrying capacity, Scaffold, Single-row setup, Steel scaffold

## 1. INTRODUCTION

Owing to the internal layout of a building, large-scale reinforced concrete beams are often designed to bear the load from the top of the structure. Notable examples include beams at the entrance lobby of a hospital or an exhibition hall (Figure 1), beams above the stage area of an auditorium for hanging lighting devices, and beams used in the semi-prefabrication building adopted for building tech-factories or shopping malls that must be completed in a short period of time. Underneath these beams and in a longitudinal direction, contractors often set up single-row steel scaffolds with various setups to support the weight of the fresh concrete within the beams.



Figure 1. Setup of Single-row Steel Scaffolds Underneath the Beam of the Entrance Lobby of a Hospital during Construction

In a construction project, when steel scaffolds are frequently used as falsework to support the weight of the fresh reinforced concrete of beams and slabs on the construction site, steel scaffolds are usually set up as large-scale multi-row scaffolding systems. The contractor generally connects the multi-row steel scaffolds with horizontal stringers to function as a reinforcement in order to enhance the overall strength of the steel scaffolding structure.

Unlike the above-mentioned multi-row, single-type steel scaffolds reinforced with horizontal stringers, the steel scaffolds underneath an isolated beam are usually arranged as a single-row type of steel scaffolds with various setups. These single-row setups lead to structural behaviors that differ from those of multi-row steel scaffolds. If the designers fail to determine the variation of strength between single-row and multi-row steel scaffolds, the fault may lead to an extremely high collapse risk of the single-row steel scaffolds.

Figure 2 shows the collapse scene of single-row steel scaffolds underneath the beam of the entrance lobby of a new hospital during construction in central Taiwan. Figure 3 shows the collapse scene of single-row steel scaffolds underneath the beam of a shopping mall in a semi-prefabrication construction in central Taiwan. Figure 4 shows the collapse scene of single-row steel scaffolds underneath the beam of the auditorium of a university during construction in central Taiwan. The frequent occurrence of accidents involving the collapse of single-row steel scaffolds warrants an investigation of the load-carrying capacities and failure modes of single-row steel scaffolds.

The structural behaviors of falsework have been extensively studied. In terms of analytical study on steel scaffolds, Zhang and Rasmussen *et al.* (2010) analyzed the variability of parameters related to steel scaffolds, including joint stiffness, initial geometric imperfection, yield stress, and load eccentricity. That study also obtained the structural strength of the steel scaffolding structures based on Monte Carlo simulation. Zhang and Rasmussen *et al.* (2012) also investigated the failure modes of steel scaffolds, the effect of different random variables on structural strength and the reliability analysis of scaffolding structures. Chan *et al.* (2003) conducted nonlinear analyses on the shoring structures that did not assume an effective length. Based on stability functions, while adopting the notional disturbance force and considering the  $P-\delta$  and  $P-\Delta$  effects, the analytical method accurately estimates the load-carrying capacities of scaffolding structures with nonlinear analyses. Chan and Peng (2000) developed a computer method for stability analysis and design of slender scaffolding systems. The concept of system instability in place of the conventional method checking member buckling in K-factor was utilized. The new method carries a potential widely used by structural engineers for design of scaffolding systems.





Figure 2. Collapse Scene of Single-row Steel Scaffolds Underneath the Beam of the Entrance Lobby of Chayi Tzu-Chi Hospital during Construction in Chayi County, Taiwan



Figure 3. Collapse Scene of Single-row Steel Scaffolds of RT-mart Mall under Semi-prefabrication Construction in Zhanghua County, Taiwan



Figure 4. Collapse Scene of Single-row Steel Scaffolds Underneath the Beam of the Auditorium of Mingdao College of Management during Construction in Zhanghua County, Taiwan

While studying modular frame-type scaffolds, Weesner and Jones (2001) conducted load-carrying capacity tests on four modular frame-type scaffolds. That study also conducted eigenbuckling and geometrically nonlinear analyses of their load-carrying capacities by the analytical program ANSYS. Yu *et al.* (2004) examined the load-carrying capacities of multi-story modular door-type steel scaffolds through means of nonlinear analyses and loading tests. According to their results, boundary conditions of the U-shaped screw jacks and base screw jacks significantly affect the load-carrying capacity of the scaffolding structures. Huang *et al.* (2000) simplified the 2-D finite element analysis model of door-type steel scaffolds and, in doing so, obtained a closed-form solution of the simplified model. This closed-form solution is related to the number of stories, material properties, and section properties of the steel scaffolds.

Peng *et al.* (1996a) developed basic structure models of the “door-type steel scaffold system” and “steel scaffold system with wooden shores”. That study also explored the structural behaviors and failure modes of the unit setup of these two structure models with second order analyses. Peng *et al.* (1996b) examined the structural design guidelines of the “door-type steel scaffold system” and “steel scaffold system with wooden shores”. That study also explored the variation of load-carrying capacities and failure modes between these two structural systems. Peng *et al.* (2010) conducted loading tests on two-story systems with wooden shores or adjustable steel shores based on construction site setups in order to determine why these two-story systems collapse and propose suggestions on how to improve their load-carrying capacities.

Peng *et al.* (1997) explored how joint stiffnesses, boundary conditions, and initial eccentricities affect the load-carrying capacities of steel scaffolds through second-order elastic analyses with semi-rigid joints. That study also studied the variation of the load-carrying capacities between 2-D and 3-D structural analyses. In addition to developing a simplified analysis model for a steel scaffold system with wooden shores, Peng *et al.* (1998) obtained an analytical solution of the simplified model based on the stability theory. That study also explored how the leaning column effect influences the load-carrying capacities of steel scaffold systems. That study also established the relationship between first-order analysis and second-order analysis, as well as proposed design steps for the structural design of steel scaffolds.

Peng *et al.* (2001) developed an approximation method based on exact moment-curvature relations to analyze the strength of the steel tubes of the scaffolds under an axial load. Based on the deduced formula, that study also developed a load-deflection curve, which closely resembled the test results. Importantly, that study are conducive to confirming the quality of factory-fabricated steel scaffold components. Additionally, Peng *et al.* (2007) explored the load-carrying capacities of different setups of steel scaffold structural systems under different loads. While the setups of steel scaffolds included rectangular, *L*-shaped and *U*-shaped types, the second-order analysis was also performed on different loads, including uniform loads, various geometry-dependent loads, and time-dependent incremental loads.

While studying tube & coupler scaffolds, Liu *et al.* (2010a) and Liu *et al.* (2010b) conducted loading tests and ANSYS numerical analyses on full-size tube & coupler scaffolds with and without cross-brace respectively. This study explored the load-carrying capacities and failure modes of the tube & coupler scaffolds with different setups. While studying system scaffolds, Peng *et al.* (2009) conducted second-order analyses and loading tests on system scaffolds. That study also explored the load-carrying capacities and failure modes of the system scaffolds with different setups and under various situations such as number of stories, joint stiffnesses and boundary conditions.

Above falsework-related studies focus mainly on various scaffolding structures, including modular frame-type scaffolds, door-type steel scaffolds, tube & coupler scaffolds, and system scaffolds, with one-bay or multi-row setups. However, single-row steel scaffolds with different setups have seldom been studied. The results of those studies on steel scaffolds can only serve as a reference for estimating the load-carrying capacities of single-row steel scaffolds with various setups. Therefore, investigating the load-carrying capacities and failure modes of single-row steel scaffolds with various setups is of priority concern.

## **2. RESEARCH OBJECTIVE AND CONTENTS**

This study explores the structural behaviors of single-row steel scaffolds by conducting loading tests based on various scaffold setups commonly used in construction sites. In addition to providing the dimensions and elastic modulus of the steel scaffolds, test results of this study provide a valuable reference for determining related parameters in follow-up numerical analyses, including the bending moment stiffnesses of scaffold joints, U-shaped screw jacks and base screw jacks. Hopefully, results of this study can facilitate efforts to improve the structural design of single-row steel scaffolds with various setups, ultimately reducing the collapse risks of these scaffolding structures. In particular, this study focuses on the following objectives:

- determine the load-carrying capacities and failure modes of single-row, one-bay steel scaffolds with various setups to function as the basis for strength comparison;
- determine the load-carrying capacities and failure modes of single-row, multi-bay steel scaffolds with various setups;
- estimate the load-carrying capacities of single-row, multi-set scaffolds based on those of single-row, one-set scaffolds;
- determine the load-carrying capacities and failure modes of steel scaffolds with various setups in the worst quality condition on construction sites;
- determine the difference of load-carrying capacities between the steel scaffolds with defects and those in the worst quality condition on construction sites; and
- determine the vertical displacements of multi-bay steel scaffolds with various setups at failure to facilitate efforts to accurately control beam deformation.

## **3. TEST PLANNING**

This study attempts to accurately reflect the conditions on construction sites by using three setups of single-row steel scaffolds: one-bay (i.e., two-set) steel scaffolds, multi-bay steel scaffolds, and one-bay steel scaffolds with defects. Two loadings are applied to each setup of steel scaffolds in the test. The first loading is applied to obtain the load-carrying capacity of each setup of steel scaffolds. After unloading, each setup of steel scaffolds is reset and, then, the load-carrying capacity of the steel scaffolds in the worst condition on the construction site is determined using the second loading.

### **3.1 One-bay Steel Scaffolds**

In this study, tests are performed on one-bay steel scaffolds to provide a reference for tests on single-row steel scaffolds. These tests are conducted on various one-bay steel scaffolds with different heights to explore the correlation between the load-carrying capacity and change in the number of stories of steel scaffolds. The steel scaffolds used in the tests consist of a 170.00 cm high door scaffold (D), 91.30 cm high square scaffold (S), and 49.00 cm high rectangle scaffold (R) (Figure. 5).

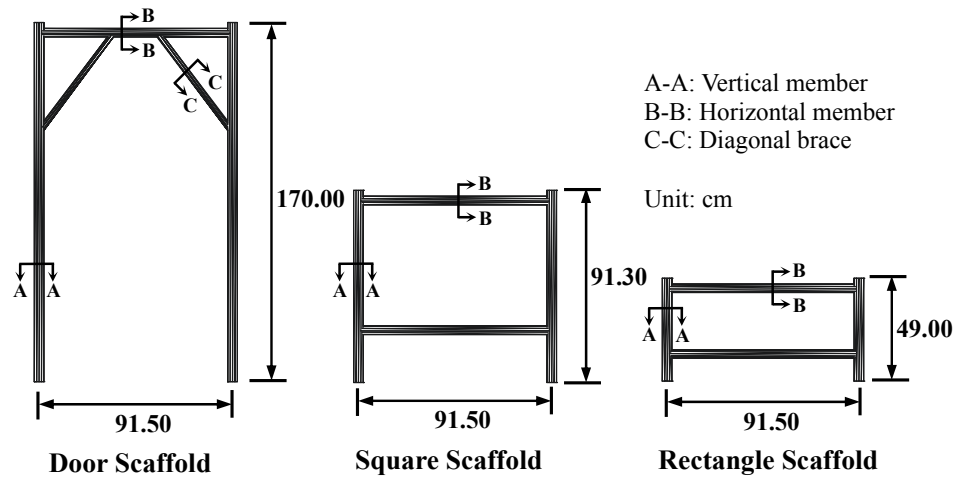


Figure 5. Dimensions of Members of Steel Scaffolds

Tests of one-bay, two-story door-type steel scaffolds (2D) are conducted on a setup consisting of two 170.00 cm high door-type steel scaffolds. The top and bottom of the scaffolding structure are attached with a 10.00 cm U-shaped screw jack and a base screw jack, respectively, and the 15.00 cm I-shaped steels are placed in the U-shaped screw jack. The scaffolding structure is reinforced with cross-brace on both sides of each story, and the total height of the scaffold system is 375.00 cm ( $=15.00+10.00+170.00+170.00+10.00$ ). Figure 6(A) shows the setup of the entire scaffold. Unless otherwise specified, the top and bottom arrangements as well as the cross-brace reinforcement for other one-bay steel scaffolds under test are the same. The total height of one-bay, three-story door-type steel scaffolds (3D) is 545.00 cm ( $=15.00+10.00+170.00+170.00+170.00+10.00$ ). Also, the setup of the three-story scaffolding structure is similar to that of the two-story door-type steel scaffolds, as shown in Figure 6(B). Figure 6 also shows the xyz coordinates to explain the deformation direction of the steel scaffolds, with y-z plane indicating “the in-plane” and x-z plane indicating “the out-of-plane.”

Figure 7(A) shows a combined setup of (bottom-up) one door, one square and one rectangle steel scaffolds (DSR) with a total height of 345.30 cm ( $=15.00+10.00+49.00+91.30+170.00+10.00$ ). Figure 7(B) shows a combined setup of (bottom-up) one door, one square and two rectangle steel scaffolds (DS2R) with a total height of 394.30 cm ( $=15.00+10.00+49.00+49.00+91.30+170.00+10.00$ ). Figure 7(C) shows a combined setup of (bottom-up) two door, one square and one rectangle steel scaffolds (2DSR) with a total height of 515.30 cm ( $=15.00+10.00+49.00+91.30+170.00+170.00+10.00$ ).

### 3.2 Multi-bay Steel Scaffolds

The setups of single-row, multi-bay steel scaffolds differ from each other, depending on the cross-section dimensions and the beam length. For a beam with smaller cross-sections and lengths, the multi-bay steel scaffolds can be set up with larger spans since the beam weight is light. As shown in Figure 8, span of the steel scaffolds is 183.00 cm. For a beam with larger cross-sections and lengths, multi-bay steel scaffolds can be set up with smaller spans and an overlap installation since the beam weight is heavy. As shown in Figure 9, span of the steel scaffolds is reduced to 91.50 cm.

Figures 10(A) to 10(C) show the setups of two-story, multi-bay steel scaffold systems with a total height of 375.00 cm ( $=15.00+10.00+170.00+170.00+10.00$ ). Figure 10(A) shows the setup of a two-story, two-bay steel scaffold system (2D-2B) with a total length of 366.00 cm (183.00 cm for

each span) ( $=2 \times 183.00$ ). The top and bottom of the scaffolding structure are attached with a 10.00 cm U-shaped screw jack and base screw jack, respectively; in addition, a 15.00 cm I-beam is placed in the U-shaped screw jack. The scaffolding structure is reinforced with a cross-brace on both sides of each story. A 6.00 m long, 20.00 cm high I-shaped steel is attached on the top of the 15.00 cm I-beams to connect the two-bay scaffolds. Unless otherwise specified, the setup arrangements for other multi-bay steel scaffolds under the test are the same. Figure 10(B) shows the setup of two-story, three-bay steel scaffold system (2D-3B) with a total length of 274.50 cm ( $=3 \times 91.50$ ) (91.50 cm for each span). Figure 10(C) shows the setup of a two-story, four-bay steel scaffold system (2D-4B) with a total length of 366.00 cm ( $=4 \times 91.50$ ) (91.50 cm for each span).

Figures 11(A) to 11(C) show the setups of (bottom-up) one-door, one-square, two-rectangle, multi-bay steel scaffold systems with a total height of 394.30 cm ( $=15.00+10.00+49.00+49.00+91.30+170.00+10.00$ ). Figure 11(A) shows the setup of a two-bay steel scaffold system (DS2R-2B) with a total length of 366.00 cm ( $=2 \times 183.00$ ) (183.00 cm for each span). Figure 11(B) shows the setup of a three-bay steel scaffold system (DS2R-3B) with a total length of 274.50 cm ( $=3 \times 91.50$ ) (91.50 cm for each span). Figure 11(C) shows the setup of a four-bay steel scaffold system (DS2R-4B) with a total length of 366.00 cm ( $=4 \times 91.50$ ) (91.50 cm for each span).

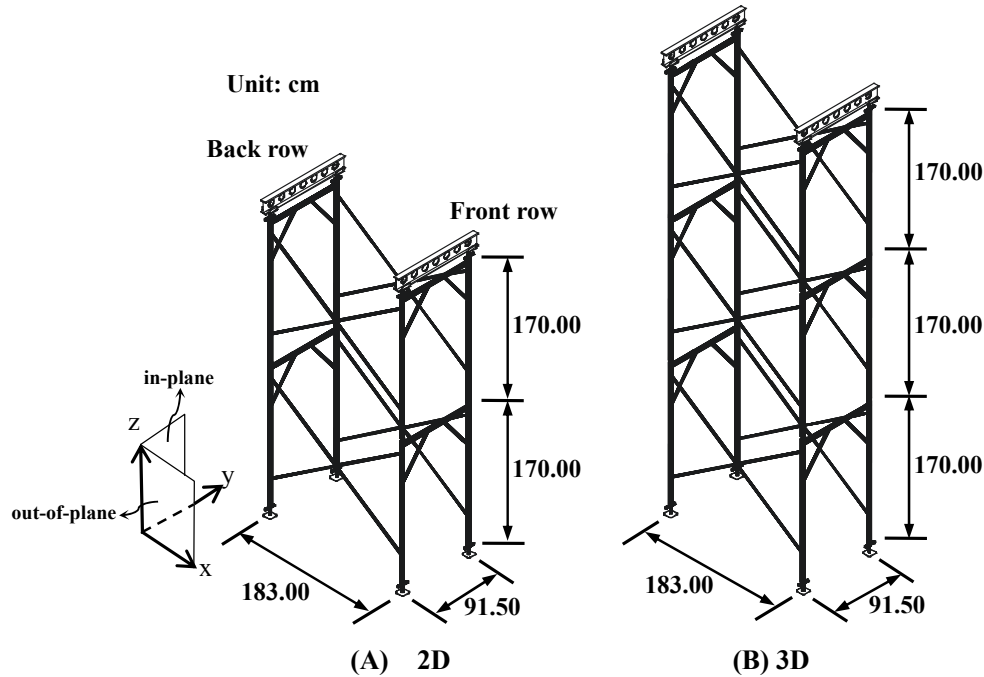


Figure 6. Setup of One-bay, Two-story Door-type (2D) and Three-story Door-type (3D) Scaffolds

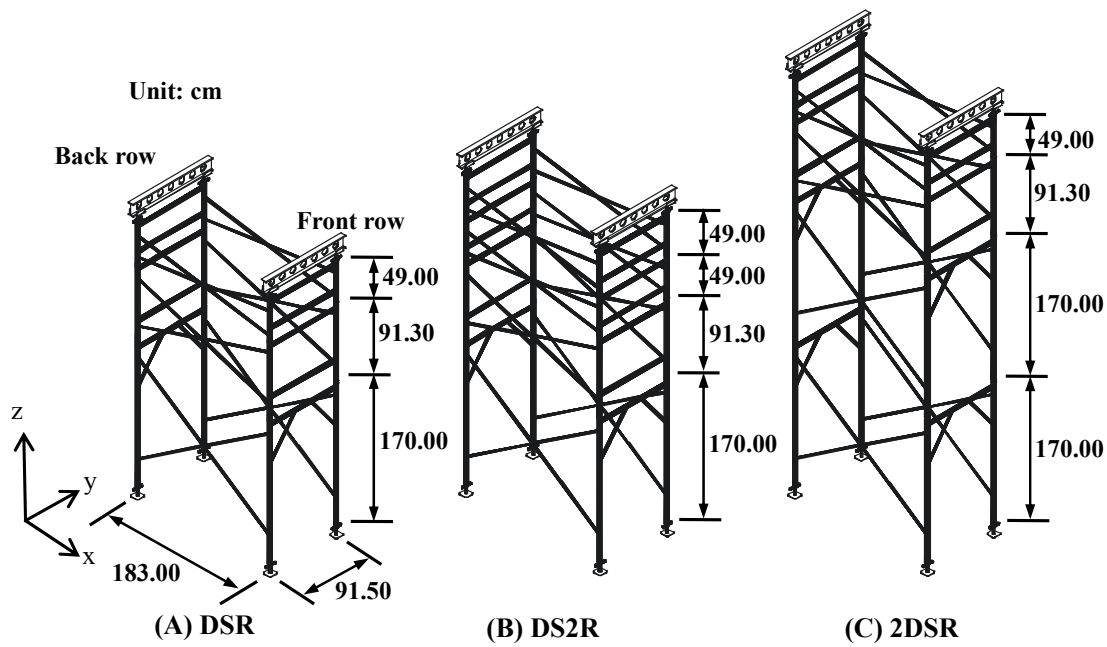


Figure 7. Setup of One-bay DSR, DS2R and 2DSR Scaffolds

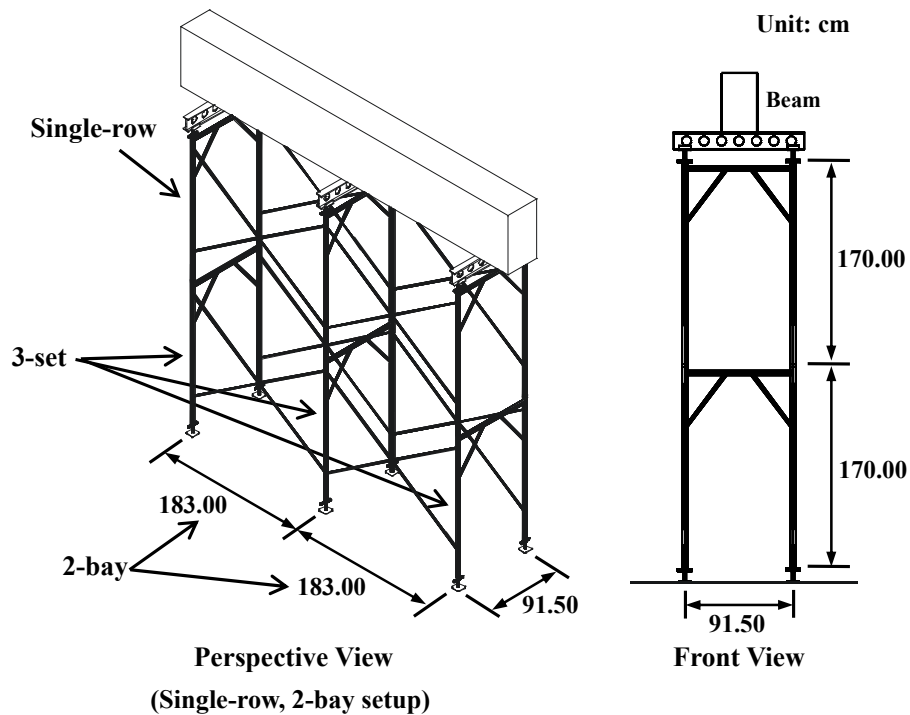


Figure 8. Setup of Scaffold System with Larger Spans under a Smaller Beam



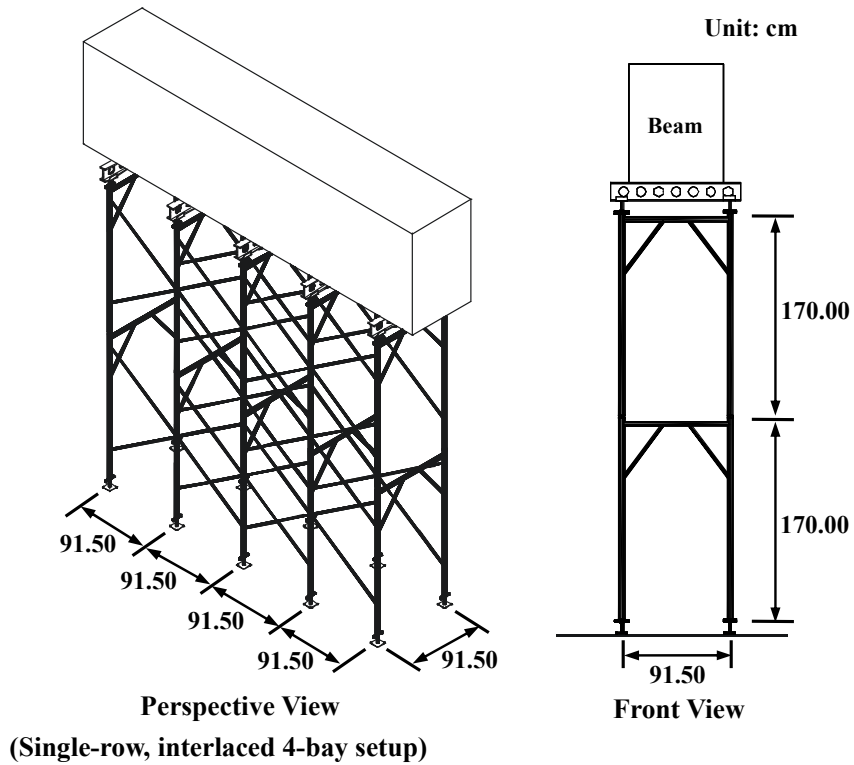


Figure 9. Setup of Scaffold System with Smaller Spans under a Larger Beam

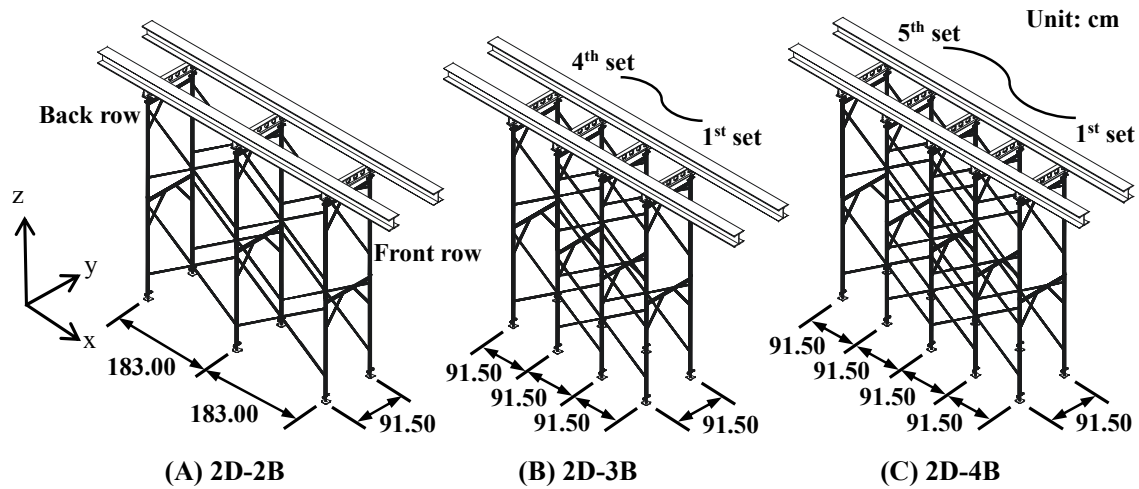


Figure 10. Setup of 2D-2B, 2D-3B, and 2D-4B scaffold systems

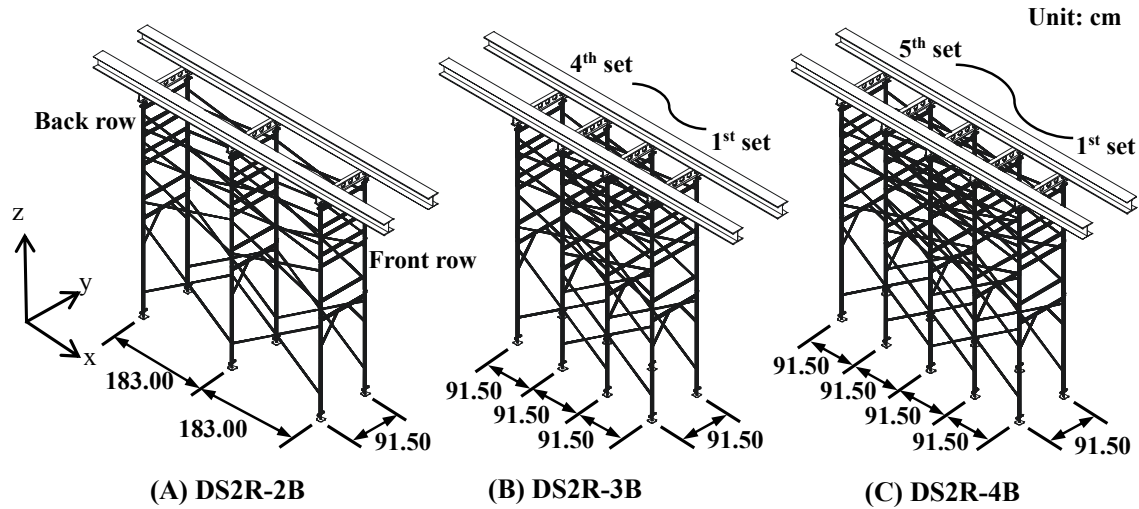


Figure 11. Setup of DS2R-2B, DS2R-3B and DS2R-4B Scaffold Systems

### 3.3 One-bay Steel Scaffolds with Defects

Steel scaffolds are often reused as temporary structures on a construction site. After construction, the contractor eliminates the seriously damaged steel scaffolds by examining them and refilling new ones for the next construction project. Steel scaffolds used on a construction site are generally set up with new and old materials. Since collision of steel scaffolds is unavoidable during construction, repeatedly used steel scaffolds tend to have deformations or indentations.

This study explores the effect of these deformations or indentations on the load-carrying capacities of steel scaffolding structures. The setups for the tests are the same as those shown in Figures 6(A), 6(B), 7(A) and 7(B). These test results can be compared with those on steel scaffolds without defects to determine how defects affect the load-carrying capacities of the steel scaffolds.

## 4. DIMENSIONS AND MATERIAL PROPERTIES

Section A-A of Figure 5 shows the vertical main tube of the steel scaffolds with  $D$  (external diameter) =  $48.26 \pm 0.30$  mm and  $t$  (thickness) =  $2.39 \pm 0.10$  mm. Section B-B shows the horizontal bar of the steel scaffolds with  $D$  (external diameter) =  $42.06 \pm 0.30$  mm and  $t$  (thickness) =  $2.10 \pm 0.10$  mm. Section C-C shows the diagonal bar of the steel scaffolds with  $D$  (external diameter) =  $26.89 \pm 0.30$  mm and  $t$  (thickness) =  $1.65 \pm 0.10$  mm. Additionally, the cross-brace used in the combined setup has an external diameter of  $21.27 \pm 0.30$  mm ( $D$ ) and a thickness of  $1.59 \pm 0.10$  mm ( $t$ ).

The elastic moduli of the material are obtained from tests on three randomly selected steel scaffolds. Test results of the three steel scaffolds are  $186.62 \text{ kN/mm}^2$ ,  $190.48 \text{ kN/mm}^2$ , and  $183.52 \text{ kN/mm}^2$ , respectively. Mean value of the three elastic moduli is  $186.87 \text{ kN/mm}^2$ , which is close to the nominal value of  $200.12 \text{ kN/mm}^2$ .







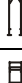
## 5. RESULTS AND DISCUSSION

### 5.1 One-bay Steel Scaffolds

Based on commonly used setups of one-bay steel scaffolds on a construction site, tests are conducted on five setups of one-bay steel scaffolds: two-story door-type scaffolds (2D), three-story door-type scaffolds (3D), combined setup of one-door, one-square, one-rectangle scaffolds (DSR), combined setup of one-door, one-square, two-rectangle scaffolds (DS2R), and combined setup of two-door, one-square, one-rectangle scaffolds (2DSR).

Two tests (A and B) are performed for each setup of one-bay steel scaffold applied by two loadings. Test results of one-bay steel scaffolds indicate that the failure modes of the five setups of steel scaffolds in both loadings are similar. The vertical displacements of all five setups of steel scaffolds under maximum load are less than 12.74 mm. Table 1 summarizes all of the test results.

Table 1. Test Results of One-bay Steel Scaffolds

Setup type		Figure	Height (cm)	Load, Displacement	Test value (kN); Displacement (mm)		
					Test A	Test B	Average
One-bay steel scaffolds	2D		375.00	2D (2DT)	200.94 (141.15)	199.76 (160.32)	200.35 (150.74)
				Displacement	8.30 (7.73)	8.59 (10.11)	8.45 (8.92)
	3D		545.00	3D (3DT)	201.68 (114.65)	197.49 (141.92)	199.59 (128.29)
				Displacement	11.68 (10.02)	11.84 (10.73)	11.76 (10.38)
	DSR		345.30	DSR (DSRT)	280.91 (151.57)	287.64 (148.62)	284.28 (150.10)
				Displacement	11.18 (8.13)	11.43 (7.78)	11.31 (7.96)
	DS2R		394.30	DS2R (DS2RT)	287.58 (137.25)	282.58 (132.38)	285.08 (134.82)
				Displacement	12.30 (9.27)	11.44 (8.34)	11.87 (8.81)
	2DSR		515.30	2DSR (2DSRT)	237.86 (96.50)	240.97 (109.44)	239.42 (102.97)
				Displacement	11.34 (11.50)	12.74 (11.38)	12.04 (11.44)
Notes:							
1. D: Door Scaffold; S: Square Scaffold; R: Rectangle Scaffold							
2. T: Second loading							

#### 5.1.1 Two-story door-type setup (2D)

Average maximum load of the first loadings is 200.35 kN and that of the second loadings is 150.74 kN, which is 75% ( $=150.74/200.35$ ) of that of the first loadings. Figure 12 shows the loads and vertical displacements of test A of one-bay, two-story door-type steel scaffolds (2D) under first loading and second loading, respectively. Figure 13(A) shows the failure modes of one-bay, two-story door-type steel scaffolds. According to figure 13(A), deformation occurs mainly on the in-plane of the back row at failure.

#### 5.1.2 Three-story door-type setup (3D)

Average maximum load of the first loadings is 199.59 kN and that of the second loadings is 128.29 kN, which is 64% ( $=128.29/199.59$ ) of that of the first loadings. Figure 13(B) shows the failure modes of the one-bay, three-story door-type steel scaffolds. According to this figure, the

deformation occurs mainly on the in-plane of the back row at failure. Maximum load of the one-bay, three-story door-type steel scaffolds (3D) closely resembles that of the one-bay, two-story door-type steel scaffolds (2D). This finding suggests that the effect of height (2D or 3D) on the load-carrying capacities of door-type steel scaffolds is negligible.

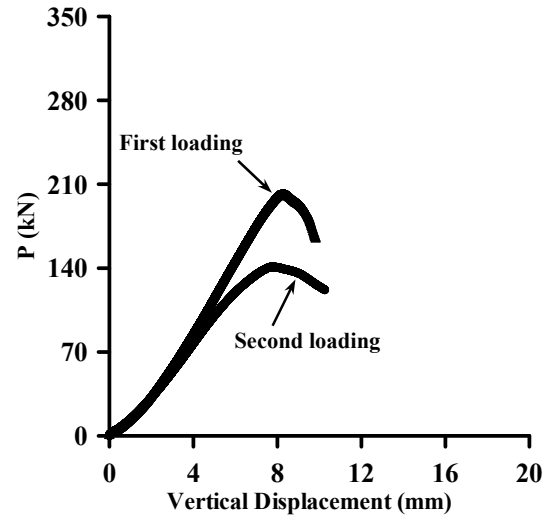
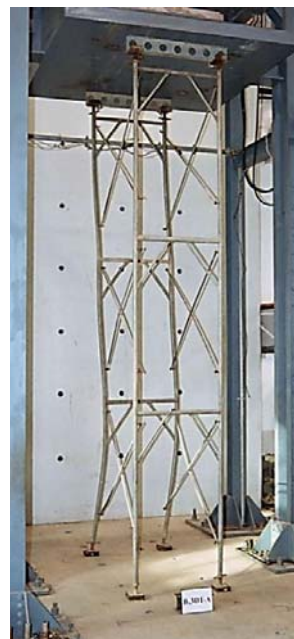


Figure 12. Loads and Vertical Displacements of One-bay, Two-story Door-type Steel Scaffolds (2D) in Test A



(A) 2D



(B) 3D

Figure 13. Failure Modes of One-bay, Two-story (2D) and Three-story (3D) Door-type Steel Scaffolds

### 5.1.3 Combined setup of one-door, one-square, one-rectangle (DSR)

Average maximum load of the first loadings is 284.28 kN, and that of the second loadings is 150.10 kN, which is 53% ( $=150.10/284.28$ ) of that of the first loadings. Figure 14(A) shows the failure modes of the DSR setup. According to this figure, the deformation occurs mainly on the in-plane of the back row door-type and square-type scaffolds at failure.

### 5.1.4 Combined setup of one-door, one-square, two-rectangle (DS2R)

Average maximum load of the first loadings is 285.08 kN, and that of the second loadings is 134.82 kN, which is 47% ( $=134.82/285.08$ ) of that of the first loadings. Figure 14(B) shows the failure modes of the DS2R setup. According to this figure, the deformation occurs mainly on the in-plane of the back row door-type and square-type scaffolds at failure.

Experimental results demonstrate that the load-carrying capacity of the DS2R setup is close to that of the DSR setup, indicating that the effect of adding one more rectangle steel scaffold on the top of the structure (DSR) on the load-carrying capacity is unapparent.

### 5.1.5 Combined setup of two-door, one-square, one-rectangle (2DSR)

Average maximum load of the first loadings is 239.42 kN, and that of the second loadings is 102.97 kN, which is 43% ( $=102.97/239.42$ ) of that of the first loadings. Figure 14(C) shows the failure modes of the 2DSR setup. According to this figure, deformation occurs mainly on the in-plane of the back row between the first and second door-type scaffolds at failure. This finding suggests that the structural stiffness of the door-type steel scaffold is smaller than that of the square-type and rectangle-type steel scaffolds.

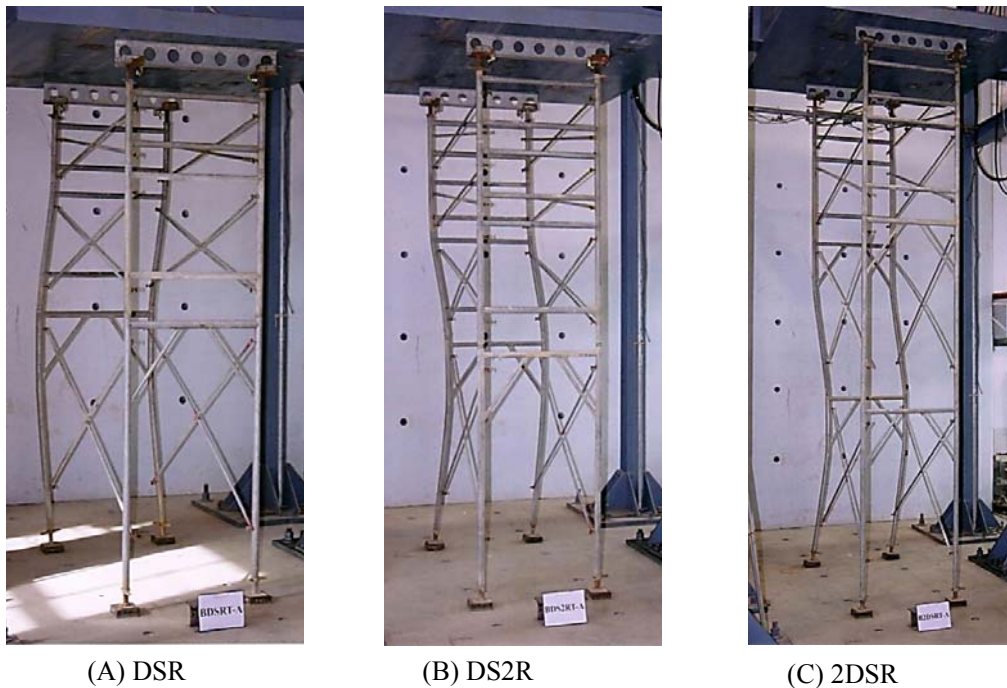


Figure 14. Failure Modes of One-bay DSR, DS2R and 2DSR Setups

According to the test results of one-bay steel scaffolds with different setups, the DS2R setup has the highest load-carrying capacity (285.08 kN), which is 1.42 ( $=285.08/200.35$ ) times higher than that of the 2D setup.



### 5.2.1 Two-bay, two-story door-type setup (2D-2B)

Average maximum load of the first loadings is 284.30 kN, and that of the second loadings is 151.77 kN, which is 53% ( $=151.77/284.30$ ) of that of the first loadings. Figure 15 shows the loads and the vertical displacements of test B of the 2D-2B setup under first and second loadings, respectively. According to Figure 16(A), deformation occurs mainly on the in-plane of the front set and middle set between the first story and the second story of steel scaffolds at failure.

Load-carrying capacity of the two-bay, two-story door-type steel scaffolds (2D-2B) is 1.42 ( $=284.30/200.35$ ) times of that of the one bay, two-story door-type steel scaffolds (2D). This finding suggests that the multi-bay setup can increase the load-carrying capacity.

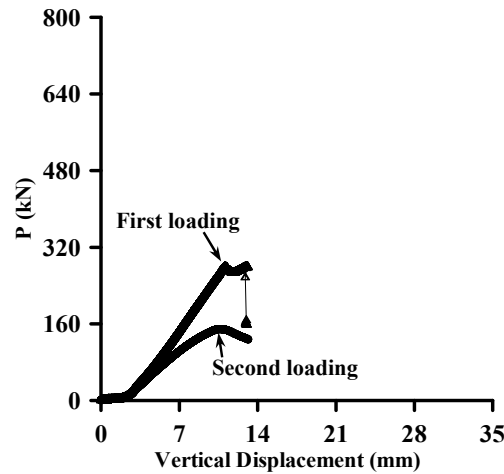


Figure 15. Loads and Vertical Displacements of Two-bay, Two-story Door-type Steel Scaffolds (2D-2B) in Test B

### 5.2.2 Interlaced setup of three-bay, two-story door-type (2D-3B)

Average maximum load of the first loadings is 418.15 kN, and that of the second loadings is 280.69 kN, which is 67% ( $=280.69/418.15$ ) of that of the first loadings. According to Figure 16(B), deformation occurs mainly on the in-plane of the last set between the first story and the second story of steel scaffolds at failure.

Load-carrying capacity of the three-bay, two-story door-type steel scaffolds (2D-3B) is 2.09 ( $=418.15/200.35$ ) times of that of the one bay, two-story door-type steel scaffolds (2D). This finding reveals that the interlaced multi-bay setup can increase the load-carrying capacity.

### 5.2.3 Interlaced setup of four-bay, two-story door-type (2D-4B)

Average maximum load of the first loadings is 460.37 kN and that of the second loadings is 264.73 kN, which is 58% ( $=264.73/460.37$ ) of that of the first loadings. According to Figure 16(C), deformation occurs mainly on the in-plane of the first and the third sets between the first story and the second story of steel scaffolds at failure.

Load-carrying capacity of the four-bay, two-story door-type steel scaffolds (2D-4B) is 2.30 ( $=460.37/200.35$ ) times of that of the one bay, two-story door-type steel scaffolds (2D). This finding suggests that the load-carrying capacity increases with the number of bays in interlaced setups.



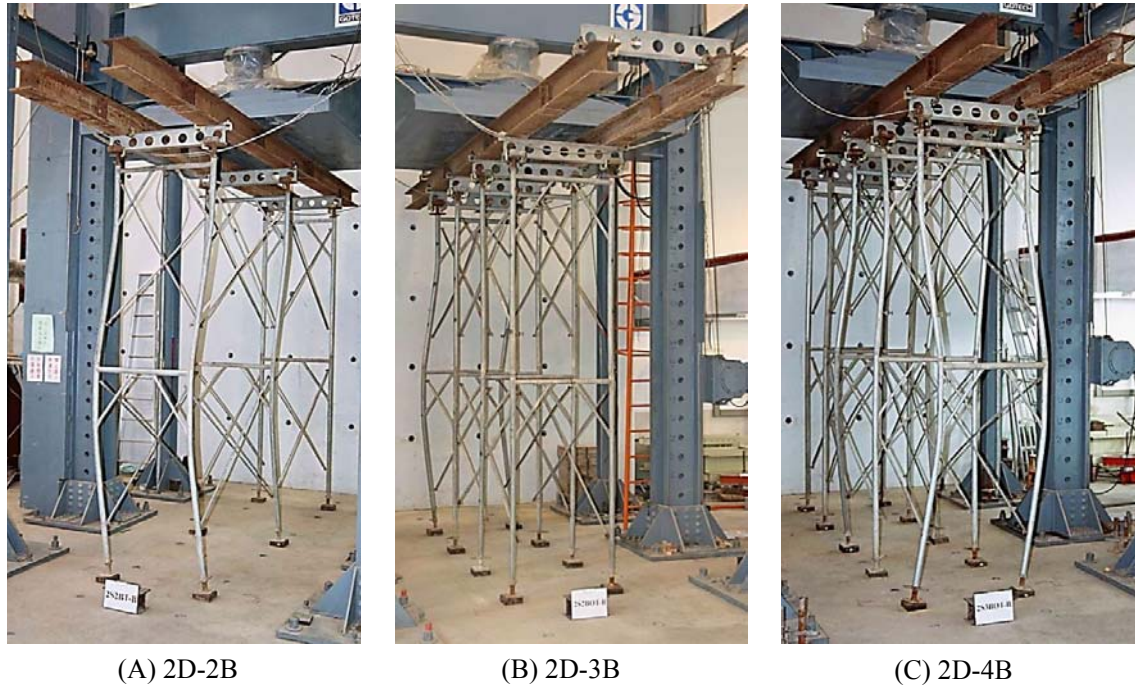


Figure 16. Failure Modes of 2D-2B, 2D-3B and 2D-4B Setups

#### 5.2.4 Two-bay, one-door, one-square, two-rectangle setup (DS2R-2B)

Average maximum load of the first loadings is 383.01 kN, and that of the second loadings is 228.13 kN, which is 60% ( $=228.13/383.01$ ) of that of the first loadings. According to Figure 17(A), deformation occurs mainly on the in-plane of the last and the middle sets between the first story and the second story of steel scaffolds at failure.

Load-carrying capacity of the DS2R-2B setup is 1.34 ( $=383.01/285.08$ ) times of that of the DS2R setup. This finding demonstrates that under the circumstances of the DS2R setup, the multi-bay setup can increase the load-carrying capacity.

#### 5.2.5 Interlaced setup of three-bay, one-door, one-square, two-rectangle (DS2R-3B)

Average maximum load of the first loadings is 529.21 kN and that of the second loadings is 298.48 kN, which is 56% ( $=298.48/529.21$ ) of that of the first loadings. According to Figure 17(B), deformation occurs mainly on the in-plane of the last two sets between the first story and the second story of steel scaffolds at failure.

Load-carrying capacity of the interlaced setup of DS2R-3B is 1.86 ( $=529.21/285.08$ ) times of that of the DS2R setup. This finding demonstrates that the interlaced multi-bay setup can increase the load-carrying capacity.

#### 5.2.6 Interlaced setup of four-bay, one-door, one-square, two-rectangle (DS2R-4B)

Average maximum load of the first loadings is 649.47 kN, and that of the second loadings is 285.49 kN, which is 44% ( $=285.49/649.47$ ) of that of the first loadings. According to Figure 17(C), deformation occurs mainly on the in-plane of the third, the fourth and the last sets between the first story and the second story of steel scaffolds at failure.

Load-carrying capacity of the interlaced setup of DS2R-4B is 2.28 ( $=649.47/285.08$ ) times of that of the DS2R setup. This finding suggests that the interlaced multi-bay setup can increase the load-carrying capacity. Moreover, a higher number of bays implies a higher load-carrying capacity.

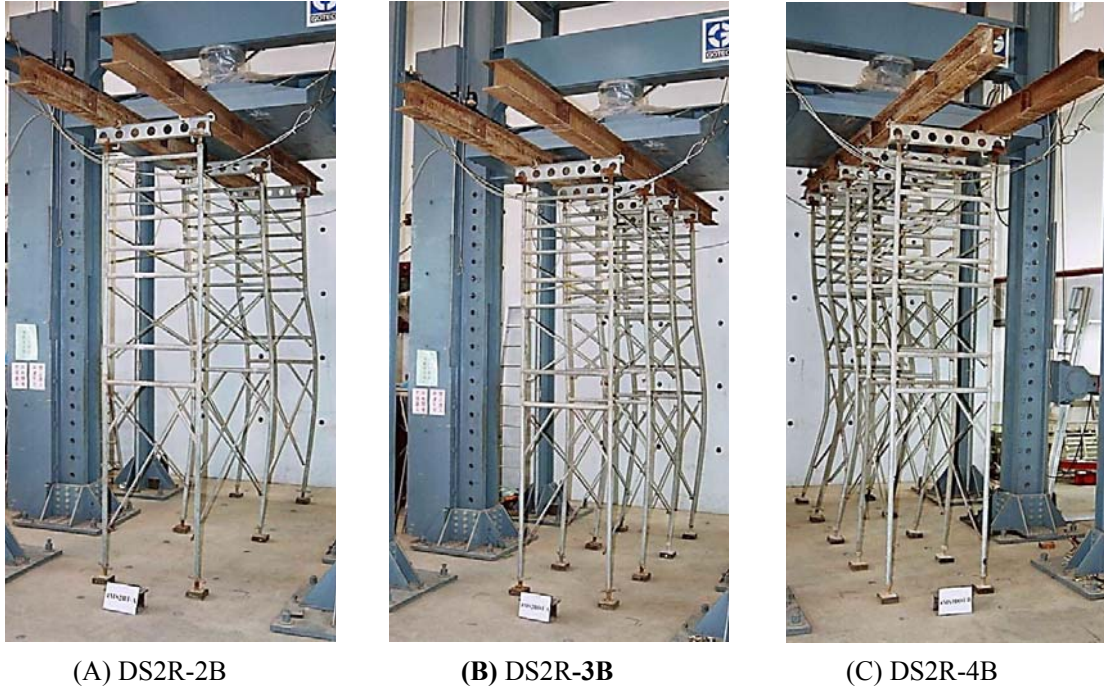


Figure 17. Failure Modes of DS2R-2B, DS2R-3B and DS2R-4B Setups

### 5.3 One-bay Steel Scaffolds with Defects

Tests are performed on four types of one-bay steel scaffolds with defects. Arrangements of these scaffolding structures are the same as those of one-bay steel scaffolds. The four types of tests are defined as two-story door-type scaffolds with defects (Df-2D), three-story door-type scaffolds with defects (Df-3D), combined setup of one-door, one-square, one-rectangle scaffolds with defects (Df-DSR), and combined setup of two-door, one-square, one-rectangle scaffolds with defects (Df-2DSR).

Since the test results on steel scaffolds with defects have larger errors than that of steel scaffolds without defects, the four tests (A, B, C and D) are generally performed by the one-bay steel scaffold with defects applied by two loadings. Test results of one-bay steel scaffolds with defects indicate that the failure modes of these four setups of steel scaffolds under both loadings closely resemble each other. Vertical displacements of all four types of steel scaffolds under maximum load are less than 11.02 mm. Table 3 summarizes all of the tests results.

Table 3. Test Results of One-bay Steel Scaffolds with Defects

Setup type	Figure	Height (cm)	Load, Displacement	Test value (kN); Displacement (mm)				
				Test A	Test B	Test C	Test D	Average
One-bay steel scaffolds with defects	2D	375.00	Df-2D (Df-2DRT)	142.81 (117.55)	100.08 (81.76)	174.65 (135.64)	142.53 (118.99)	140.02 (113.49)
			Displacement	7.97 (7.20)	9.93 (12.55)	7.01 (6.71)	5.85 (6.13)	7.69 (8.15)
	3D	545.00	Df-3D (Df-3DRT)	116.22 (89.97)	170.72 (128.58)	184.95 (142.87)	129.53 (98.33)	150.36 (114.94)
			Displacement	9.96 (15.79)	9.80 (8.69)	10.09 (8.90)	9.92 (11.24)	9.94 (11.16)
	DSR	345.30	Df-DSR (Df-DSRT)	280.36 (166.64)	271.33 (118.11)	249.61 (182.10)	214.13 (164.57)	253.86 (157.86)
			Displacement	10.76 (7.19)	11.02 (9.50)	10.40 (8.85)	10.65 (7.59)	10.71 (8.28)
	2DSR	515.30	Df-2DSR (Df-2DSRT)	179.86 (131.64)	205.98 (151.23)	206.93 (118.16)	---	197.59 (133.68)
			Displacement	9.64 (8.48)	9.90 (9.17)	10.30 (9.75)	---	9.95 (9.13)

Notes:  
1. D: Door Scaffold; S: Square Scaffold; R: Rectangle Scaffold  
2. Df: Defective; T: Second loading;  
3. ---: Not available

### 5.3.1 Two-story door-type setup with defects (Df-2D)

Average maximum load of the first loadings is 140.02 kN, and that of the second loadings is 113.49 kN, which is 81% ( $=113.49/140.02$ ) of that of the first loadings. Figure 18 shows the loads and the vertical displacements of test A of the Df-2D setup under first and second loadings, respectively. According to Figure 19(A), deformation occurs mainly on the in-plane of the front set between the first story and the second story of steel scaffolds at failure. Load-carrying capacity of the Df-2D setup is 70% ( $=140.02/200.35$ ) of that of the 2D setup.

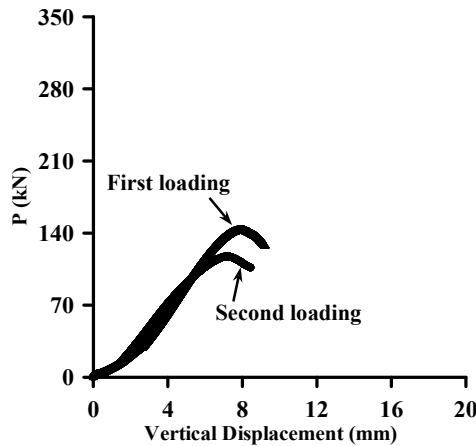


Figure 18. Loads and Vertical Displacements of One-bay, Two-story Door-type Steel Scaffolds with Defects (Df-2D) in Test A

### 5.3.2 Three-story door-type setup with defects (Df-3D)

Average maximum load of the first loadings is 150.36 kN, and that of the second loadings is 114.94 kN, which is 76% ( $=114.94/150.36$ ) of that of the first loadings. According to Figure 19(B), deformation occurs mainly on the in-plane of the back set of the first, the second and the third stories of steel scaffolds at failure. Load-carrying capacity of the Df-3D setup is 75% ( $=150.36/199.59$ ) of that of the 3D setup.





(A) Df-2D

(B) Df-3D

Figure 19. Failure Modes of One-bay Df-2D and Df-3D Setups with Defects

### 5.3.3 Combined setup of one-door, one-square, one-rectangle with defects (Df-DSR)

Average maximum load of the first loadings is 253.86 kN, and that of the second loadings is 157.86 kN, which is 62% ( $=157.86/253.86$ ) of that of the first loadings. According to Figure 20(A), deformation occurs mainly on the in-plane of the back set between the first story and the second story of steel scaffolds at failure. Load-carrying capacity of the Df-DSR setup is 89% ( $=253.86/284.28$ ) of that of the DSR setup.

### 5.3.4 Combined setup of two-door, one-square, one-rectangle with defects (Df-2DSR)

Three tests (A, B and C) are performed for this setup. Average maximum load of the first loadings is 197.59 kN, and that of the second loadings is 133.68 kN, which is 68% ( $=133.68/197.59$ ) of that of the first loadings. According to Figure 20(B), deformation occurs mainly on the in-plane of the back set between the first story and the second story of steel scaffolds at failure. Load-carrying capacity of the Df-2DSR setup is 83% ( $=197.59/239.42$ ) of that of the 2DSR setup.

## 6. COMPARISON OF LOAD-CARRYING CAPACITIES OF STEEL SCAFFOLDS

### 6.1 Comparison of Load-carrying Capacities between Steel Scaffolds with and without Defects

Figure 21 compares the test results of one-bay steel scaffolds with and without defects. According to Figure 21, the load-carrying capacities of steel scaffolds with defects reduce to 70~89 % of those of the steel scaffolds without defects. Basically, we recommend avoiding the use of defective materials to set up steel scaffolds on a construction site. However, if the steel scaffolds with defects are used on the construction site, the reduction of load-carrying capacity of the defective steel scaffolds should be considered when engineers design the scaffolding structure.

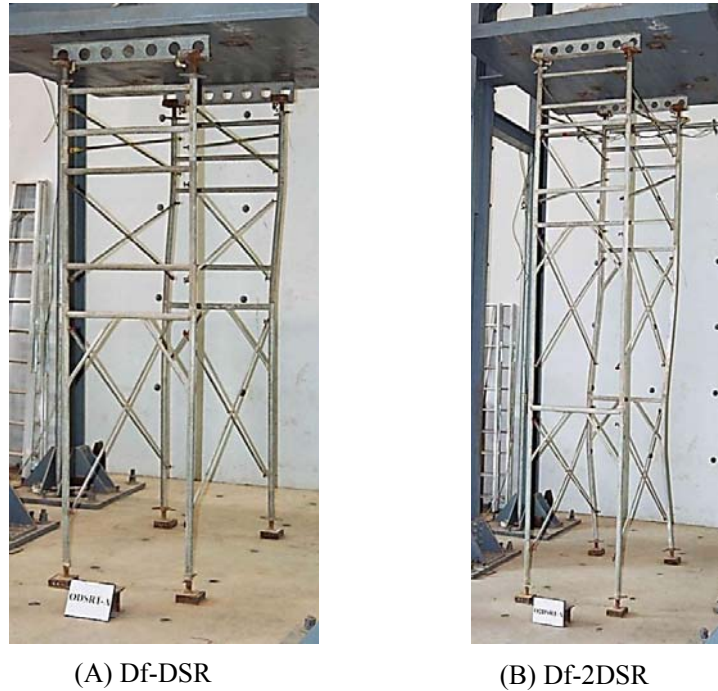


Figure 20. Failure Modes of One-bay Df-DSR and Df-2DSR Setups with Defects

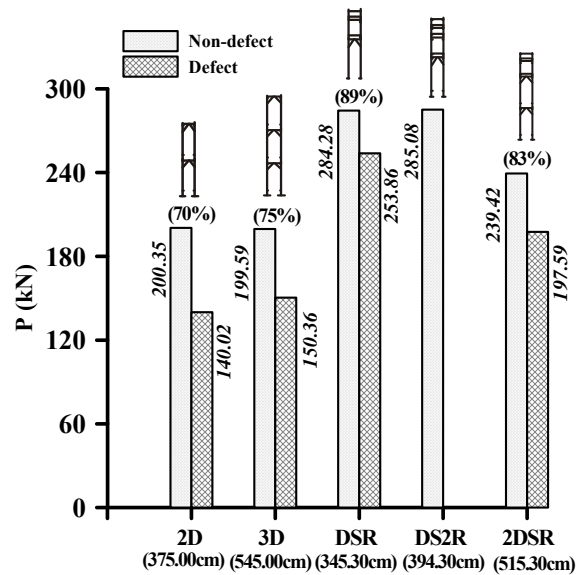


Figure 21. Comparison of Load-carrying Capacities of One-bay Steel Scaffolds with and without Defects in Different Setups

## 6.2 Multi-bay 2D Setup

Figure 22 compares the test results of two-story door-type steel scaffolds with one-bay and multi-bay setups at a height of 375.00 cm. According to this figure, load-carrying capacities of the multi-bay steel scaffolds increase with the number of bays. Additionally, the load-carrying capacity of the 2D-2B setup is 1.42 ( $=284.30/200.35$ ) times of that of the 2D setup, the 2D-3B setup is 2.09 ( $=418.15/200.35$ ) times of that of the 2D setup, and the 2D-4B setup is 2.30 ( $=460.37/200.35$ ) times of that of the 2D setup.

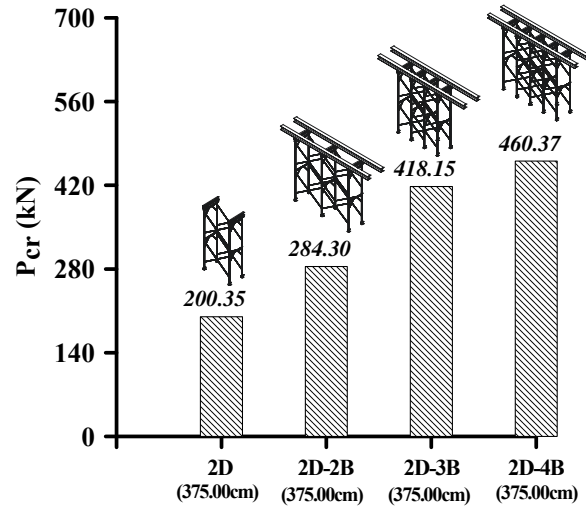


Figure 22. Comparison of Load-carrying Capacities of One-bay and Multi-bay Two-story Door-type Steel Scaffolds (2D)

Comparing the 2D-2B setup and the 2D-4B setup, which have the same overall length (366.00 cm) and width (91.50 cm), reveals that the load-carrying capacity of the 2D-4B setup is 1.62 ( $=460.37/284.30$ ) times of that of the 2D-2B setup. This is owing to that the 2D-4B setup has two more sets of steel scaffolds than those of the 2D-2B setup within the same length.

When the test results are divided by the number of sets, the load-carrying capacities of the set of the single-row steel scaffolds in 2D, 2D-2B, 2D-3B, and 2D-4B setups are 100.18 kN ( $=200.35/2$ ), 94.77 kN ( $=284.30/3$ ), 104.54 kN ( $=418.15/4$ ), and 92.07 kN ( $=460.37/5$ ), respectively. The average load-carrying capacity of a set of the four setups of single-row steel scaffolds is 97.89 kN ( $=(100.18+94.77+104.54+92.07)/4$ ). The data multiplied by the number of sets can provide a valuable reference for quickly estimating the load-carrying capacity of single-row, multi-bay, two-story door-type steel scaffolds.

### 6.3 Multi-bay DS2R Setup

Figure 23 compares the test results of one-door, one-square, two-rectangle steel scaffolds (DS2R) with one-bay and multi-bay setups at a height of 394.30 cm. According to Figure 23, load-carrying capacities of the multi-bay DS2R steel scaffolds increase with the number of bays. Additionally, the load-carrying capacity of the two-bay DS2R setup (DS2R-2B) is 1.34 ( $=383.01/285.08$ ) times of that of the one-bay DS2R setup, the three-bay DS2R setup (DS2R-3B) is 1.86 ( $=529.21/285.08$ ) times of that of the one-bay DS2R setup, and the four-bay DS2R setup (DS2R-4B) is 2.28 ( $=649.47/285.08$ ) times of that of the one-bay DS2R setup.

Comparing the DS2R-2B setup and DS2R-4B setup which have the same overall length (366.00 cm) and width (91.50 cm) reveals that the load-carrying capacity of the DS2R-4B setup is 1.70 ( $=649.47/383.01$ ) times of that of the DS2R-2B setup. This is owing to that the DS2R-4B setup has two more sets of steel scaffolds than those of the DS2R-2B setup within the same length.

When the test results are divided by the number of sets, the load-carrying capacities of the set of the single-row steel scaffolds in DS2R, DS2R-2B, DS2R-3B, and DS2R-4B setups are 142.54 kN ( $=285.08/2$ ), 127.67 kN ( $=383.01/3$ ), 132.30 kN ( $=529.21/4$ ), and 129.89 kN ( $=649.47/5$ ), respectively. The average load-carrying capacity of a set of the four setups of single-row steel

scaffolds is 133.10 kN  $(=(142.54+127.67+132.30+129.89)/4)$ . This load-carrying capacity multiplied by the number of sets provides a valuable reference for efforts to fast estimate the load-carrying capacity of single-row, multi-bay, one-door, one-square, two-rectangle steel scaffolds.

Although the height (394.30 cm) of the DS2R setup described in this section is higher than that (375.00 cm) of the 2D setup described in the previous one, the average load-carrying capacity of a set of the DS2R setup (133.10 kN) is higher than that of a set of the 2D setup (97.89 kN). This finding demonstrates that the load-carrying capacity of the combined setup of steel scaffolds is higher than that of two-story door-type steel scaffolds. Moreover, the rectangle and the square steel scaffolds can increase the load-carrying capacity of the steel scaffolds.

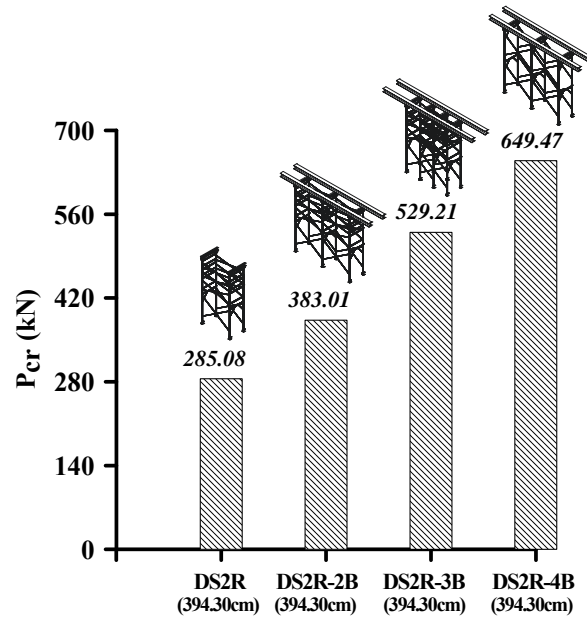



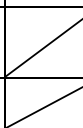
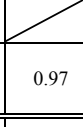


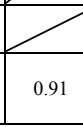
Figure 23. Comparison of Load-carrying Capacities of One-bay and Multi-bay DS2R Setups

#### 6.4 Estimate Load-carrying Capacities of Single-row, Multi-set Scaffolds based on those of Single-row, One-set Scaffolds

For convenience, when designing the strength of steel scaffolds, the designer can estimate the load-carrying capacities of single-row, multi-set steel scaffolds based on those of single-row, one-set steel scaffolds. Notably, the load-carrying capacities of one-set steel scaffolds for these two setups (2D and DS2R) can be obtained when the load-carrying capacities of the single-row, one-bay 2D setup (200.35 kN) and DS2R setup (285.08 kN) are divided by 2, respectively. Therefore, multiplying the load-carrying capacity of one-set steel scaffolds by the number of sets obtains the estimated load-carrying capacities of multi-set steel scaffolds for these two setups (Table 4).

Table 4 lists the estimated and real values of the load-carrying capacities of single-row, multi-set steel scaffolds in two setups (2D and DS2R). The average estimating factor of the 2D setup is 0.97, explaining why average load-carrying capacity of the 2D setup increases 97.17 kN  $(=100.18 \times 0.97)$  for each additional set. Additionally, average estimating factor of the DS2R setup is 0.91, explaining why average load-carrying capacity of the DS2R setup increases 129.71 kN  $(=142.54 \times 0.91)$  for each additional set.

Table 4. Estimated Value and Real Value of the Load-carrying Capacities of Single-row, Multi-set Steel Scaffolds

Setup type	Figure	Comparison	Load-carrying capacity (kN)						
			Single-row, one-bay	1 set	2 sets	3 sets	4 sets	5 sets	Average
2D		Estimated value (A)	---	100.18	200.35	300.53	400.70	500.88	
		Real value (B)	200.35	---	200.35	284.30	418.15	460.37	
		Estimating factor (B)/(A)	---	---	---	0.95	1.04	0.92	0.97
DS2R		Estimated value (C)	---	142.54	285.08	427.62	570.16	712.70	
		Real value (D)	285.08	---	285.08	383.01	529.21	649.47	
		Estimating factor (D)/(C)	---	---	---	0.90	0.93	0.91	0.91
Notes: 1. D: Door Scaffold, S: Square Scaffold, R: Rectangle Scaffold 2. ---: Not available									

On a construction site, the designer can quickly estimate the load-carrying capacities of single-row, multi-set (or multi-bay) steel scaffolds for various setups. Additionally, load-carrying capacities of steel scaffolds with different stories can be calculated by determining the analytical parameters of the steel scaffolds used in this study through numerical analyses in future research. However, the estimating factors must be verified with a large number of tests. This study only provides preliminary findings as a reference for designers to quickly estimate the load-carrying capacities of single-row, multi-set steel scaffolds.

## 7. LOWER BOUND OF LOAD-CARRYING CAPACITY OF REUSABLE SCAFFOLDS

This study also investigates the load-carrying capacity reduction of the reusable steel scaffolds in the worst condition on the construction site. After the first loading, the steel scaffolds are reset and a second loading is applied. Test results of the second loading can be regarded as the worst condition of the reusable steel scaffolds on the construction site, which can be compared with those of the first loading. Moreover, the load-carrying capacities of the reusable steel scaffolds in the worst condition can also be compared with those of the steel scaffolds with defects.

Figure 24 compares the load-carrying capacities of the reusable steel scaffolds subtracting one to three-fold standard deviations. According to this figure, the average ratio of dividing the load-carrying capacities of the second loading by those of the first loading is  $\mu=0.63$ , with a standard deviation of  $\sigma=0.13$ . Additionally, according to Figure 21, the ratio of load-carrying capacity of the steel scaffolds with defects to those without defects is 70~89 %, which is higher than that of the reusable steel scaffolds in the worst condition (63%). This finding demonstrates that the strength of the steel scaffolds with defects is still reusable.

Figure 24 also shows various situations with different standard deviations. Subtracting one-fold standard deviation from the average ratio of the reusable steel scaffolds ( $\mu-\sigma$ ) yields 0.50. Moreover, subtracting two-fold standard deviations ( $\mu-2\sigma$ ) yields 0.37. Also, subtracting three-fold standard deviations ( $\mu-3\sigma$ ) yields 0.24. Above results can be regarded as the strength reduction factors ( $\phi$ ) of the reusable steel scaffolds. The designer can select proper strength

reduction factors ( $\phi$ ) of reusable scaffolds based on project fund and safety requirements. These factors can provide a valuable reference for determining the strength reduction of the reusable steel scaffolds.

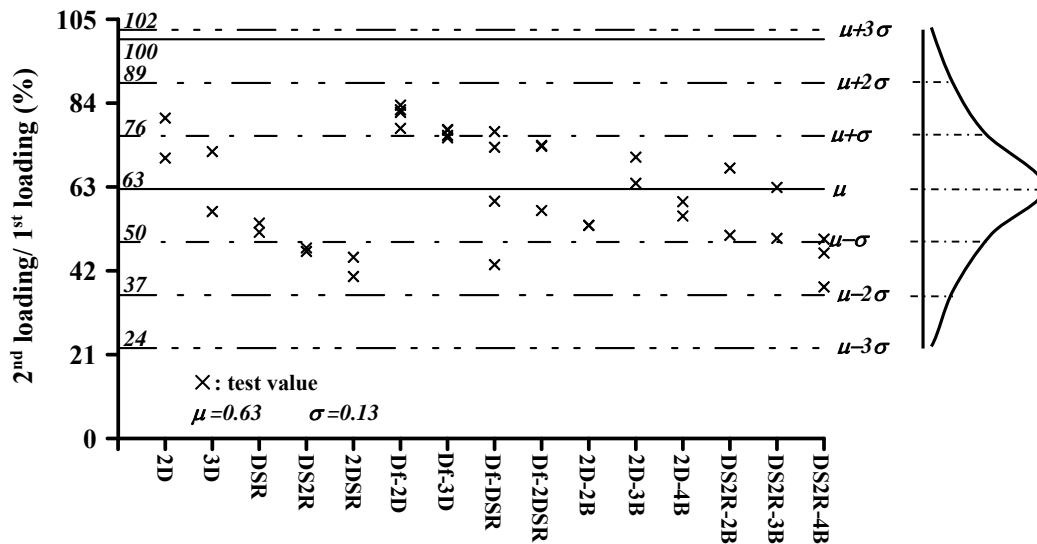


Figure 24. Comparison of Load-carrying Capacities of Reusable Steel Scaffolds Subtracting and Adding One to Three-fold Standard Deviations

## 8. VERTICAL DISPLACEMENTS OF STEEL SCAFFOLDS AT FAILURE

In various tests on the single-row, one-bay steel scaffolds both with and without defects, the vertical displacements of all of the scaffolding structures at maximum load are less than 12.74 mm. In tests on the single-row, multi-bay 2D setup and the multi-bay DS2R setup, the vertical displacements of all of the scaffolding structures at maximum load are less than 20.35 mm. Above test results can serve as a valuable reference for contractors in designing the isolated reinforced concrete beams if the construction accuracy must be considered.

## 9. CONCLUSIONS

This study explored the structural behaviors of single-row steel scaffolds with various setups to determine the load-carrying capacities and failure modes of these scaffolding structures. Experimental results indicate that the load-carrying capacities of one-bay, three-story door-type steel scaffolds (3D) are close to those of two-story door-type steel scaffolds (2D). Additionally, deformation occurs mainly in the in-plane direction of the steel scaffolds at failure. Load-carrying capacity of the 2D-2B setup is 1.42 times of that of the 2D setup. Also, load-carrying capacities of the 2D-3B and 2D-4B setups are 2.09 times and 2.30 times of that of the 2D setup, respectively. Moreover, although with the same overall length, load-carrying capacity of the 2D-4B setup is 1.62 times of that of the 2D-2B setup. This finding demonstrates that increasing the number of bays can increase the load-carrying capacity of door-type steel scaffolds.

Load-carrying capacity of the two-bay DS2R setup (DS2R-2B) is 1.34 times of that of the one-bay DS2R setup. Also, load-carrying capacities of the three-bay DS2R setup (DS2R-3B) and four-bay DS2R setup (DS2R-4B) are 1.86 times and 2.28 times of that of the one-bay DS2R setup, respectively. This finding demonstrates that increasing the number of bays can increase the

load-carrying capacity of these steel scaffolds. Additionally, load-carrying capacity of the 2D setup and the DS2R setup increases 97.17 kN and 129.71 kN on average for each additional set, respectively. Designers can quickly estimate the load-carrying capacities of multi-set steel scaffolds by multiplying the load-carrying capacity of one-set steel scaffolds by the number of sets.

In this study, test results of the second loading are regarded as the worst condition of the reusable steel scaffolds on the a construction site. The average ratio of dividing the load-carrying capacities of the second loading by those of the first loading is  $\mu=0.63$ , with a standard deviation of  $\sigma=0.13$ . Additionally, subtracting one to three -fold standard deviation from the average ratio of the reusable steel scaffolds [i.e.,  $(\mu-\sigma)$ ,  $(\mu-2\sigma)$ ,  $(\mu-3\sigma)$ ] yields the strength reduction factors ( $\square$ ) of the reusable steel scaffolds, 0.50, 0.37, and 0.24, respectively. Designers can select appropriate strength reduction factors of reusable scaffolds, based on the design requirements.

Test results of steel scaffolds with defects indicate that the ratio of load-carrying capacity of the steel scaffolds with defects to those without defects is higher than that of the steel scaffolds using the second loading condition to those using the first loading condition. This finding demonstrates that the steel scaffolds with defects are not yet in the worst quality condition on the construction site. Additionally, when under a maximum load, the vertical displacements of all setups of multi-bay steel scaffolds are less than 20.35 mm. If the construction accuracy of the isolated reinforced concrete beams must be considered, the data can serve as a valuable reference for allowable deformation.

## ACKNOWLEDGEMENTS

The authors would like to thank the National Science Council, Taiwan, for financially supporting this research under Contract No. NSC 102-2221-E-224-044. Pin-Huei Construction & Engineering Co., Ltd. and Ruentex Engineering & Construction Co., Ltd. are appreciated for providing the testing materials. Mr. Jhih-Wei Guo is commended for his assistance in conducting the tests.

## REFERENCES

- [1] Chan, S.L. and Peng, J.L., "Performance-based Design of Steel Scaffolding Systems by Stability Analysis", Invited Lecture, International Conference on Structural Stability and Dynamics, 7-9 Dec. 2000, Organised by National Taiwan University, proceedings edited by Yang, Y.B., Leu, L.J. and Hsieh, S.H., pp. 205-210.
- [2] Chan, S.L., Chu, A.Y.T. and Albermani, F.G., "Stability and Simulation-based Design of Steel Scaffolding without Using the Effective Length Method", Structural Stability and Dynamics, 2003, Vol. 3, No. 4, pp. 443-460.
- [3] Huang, Y.L., Kao, Y.G. and Rosowsky, D.V., "Load-carrying Capacities and Failure Modes of Scaffolding Shoring Systems, Part II: Analytical model and its closed-form Solution", Structural Engineering and Mechanics, 2000, Vol. 10, No. 1, pp. 53-66.
- [4] Liu, H.B., Chen, Z.H., Wang, X.D. and Zhou, T., "Theoretical Analysis and Experimental Research on Stability Behavior of Structural Steel Tube and Coupler Falsework with X-Bracing", Advanced Steel Construction, 2010a, Vol. 6, No. 4, pp. 949-962.
- [5] Liu, H., Zhao, Q., Wang, X., Zhou, T., Wang, D., Liu, J. and Chen, Z., "Experimental and Analytical Studies on the Stability of Structural Steel Tube and Couple Scaffolds without X-bracing", Engineering Structures, 2010b, Vol. 32, pp. 1003-1015.



- [6] Peng, J.L., Pan, A.D., Rosowsky, D.V., Chen, W.F., Yen, T. and Chan, S.L., "High Clearance Scaffold Systems during Construction – I. Structural Modelling and Modes of Failure", *Engineering Structures*, 1996a, Vol. 18, No. 3, pp. 247-257.
- [7] Peng, J.L., Rosowsky, D.V., Pan, A.D., Chen, W.F., Chan, S.L. and Yen, T., "High Clearance Scaffold Systems during Construction - II. Structural Analysis and Development of Design Guidelines", *Engineering Structures*, 1996b, Vol. 18, No. 3, pp. 258-267.
- [8] Peng, J.L., Pan, A.D.E., Chen, W.F., Yen, T. and Chan, S.L., "Structural Modeling and Analysis of Modular Falsework Systems", *Journal of Structural Engineering*, ASCE, 1997, Vol. 123, No. 9, pp. 1245-1251.
- [9] Peng, J.L., Pan, A.D.E. and Chan, S.L., "Simplified Models for Analysis and Design of Modular Falsework", *Journal of Constructional Steel Research*, 1998, Vol. 48, No. 2/3, pp. 189-209.
- [10] Peng, J.L., Pan, A.D.E. and Chen, W.F., "Approximate Analysis Method for Modular Tubular Falsework", *Journal of Structural Engineering*, ASCE, 2001, Vol. 127, No. 3, pp. 256-263.
- [11] Peng, J.L., Chan, S.L. and Wu, C.L., "Effects of Geometrical Shape and Incremental Loads on Scaffold Systems", *Journal of Constructional Steel Research*, 2007, Volume 63, Issue 4, pp. 448-459.
- [12] Peng, J.L., Wang, P.L., Huang, Y.H. and Tsai, T.C., "Experimental Studies of Load Capacities of Double-Layer Shoring Systems", *Advanced Steel Construction*, 2010, Vol. 6, No. 2, pp. 698-721.
- [13] Peng, J.L., Yen, T., Kuo, C.C. and Chan, S.L., "Analytical and Experimental Bearing Capacities of System Scaffolds", *Journal of Zhejiang University SCIENCE A*, 2009, Vol. 10, No. 1, pp. 82-92.
- [14] Weesner, L.B. and Jones, H.L., "Experimental and Analytical Capacity of Frame Scaffolding", *Engineering Structures*, 2001, Vol. 23, No. 6, pp. 592-599.
- [15] Yu, W.K., Chung, K.F. and Chan, S.L., "Structural Instability of Multi-storey Door-type Modular Steel Scaffolds", *Engineering Structures*, 2004, Vol. 26, pp. 867-881.
- [16] Zhang, H., Chandrangsu, T. and Rasmussen, K.J.R., "Probabilistic Study of the Strength of Steel Scaffold Systems", *Structural Safety*, 2010, Vol. 32, pp. 393-401.
- [17] Zhang, H., Rasmussen, K.J.R. and Ellingwood, B.R., "Reliability Assessment of Steel Scaffold Shoring Structure for Concrete Formwork", *Engineering Structures*, 2012, Vol. 36, pp. 81-89.



# EVALUATION FOR EARTHQUAKE-RESISTANT CAPABILITY OF UN-LANDING STEEL ARCH

Qinghua Han<sup>1,2</sup>, Yan Lu<sup>1,2\*</sup> and QiuHong Zhao<sup>1,2</sup>

<sup>1</sup>*School of Civil Engineering, Tianjin University, Tianjin 300072, China;*

<sup>2</sup>*Key Laboratory of Coast Structure Safety (Tianjin University), Ministry of Education, Tianjin 300072, China*

*\*(Corresponding author: E-mail: yanlu86@tju.edu.cn)*

*Received: 31 October 2013; Revised: 5 September 2014; Accepted: 29 September 2014*

**ABSTRACT:** This paper presents research results on the earthquake-resistant capability of the un-landing steel arch. A shaking table test of an un-landing solid-web steel arch was carried out to present the seismic behavior. During the shaking table test, the acceleration response at the arch-top is largest. The maximum displacement response and the maximum stress at the quarter point of the arch is larger than other test points. The added braces could effectively help decreasing the displacement and deformation of the un-landing steel arch. The seismic response under the Tianjin wave is the largest while that under the Loma Prieta wave is the least, since the predominant frequency of the Tianjin wave is closest to the fundamental frequency of the model. Then IDA approach is applied in the un-landing steel arch. A single IDA curve is plotted, which fits the test result. By the IM-based rule, the capacity point of the structure is acquired. Finally, the earthquake-resistant capability of the un-landing latticed steel tubular arch is evaluated by the multi-record IDA study from a real project. A suite of records by having mean, 16%, 84% fractiles is summarized.

**Keywords:** Un-landing steel arch, earthquake-resistant capability, shaking table test, IDA approach, capacity point

## 1. INTRODUCTION

Earthquake may cause serious damage and even collapse of the spatial structures, and it is necessary to study the earthquake-resistant capability of spatial structures such as steel arch. In order to meet the requirement of the use space, many steel arches are the un-landing steel arches. The ends of the steel arch are supported on the steel column or other structures. An un-landing solid-web steel arch was adopted in the Xianglujiao light-rail station in Dalian, which had a span of 23.2m and a rise-to-span ratio varying from 0.08 to 0.12 (Figure 1(a)). The ends of I-type steel arch were supported on the I-type steel column. An un-landing latticed steel tubular arch was adopted in the Beidaihe railway station canopy with a span of 68.6m (Figure1(b)). The ends of latticed steel tubular arch were supported on the latticed steel column.

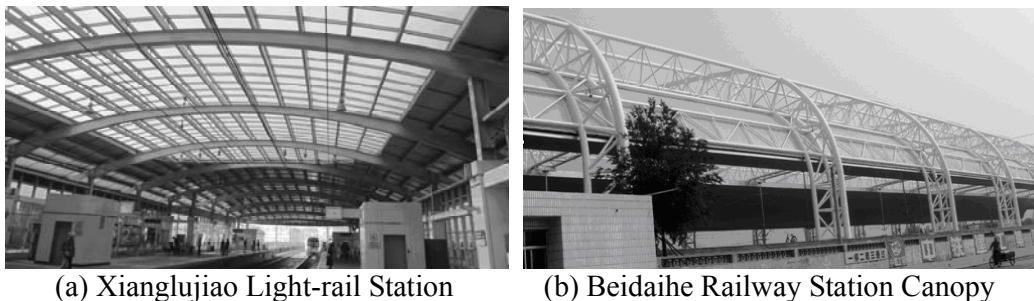


Figure 1. Project Photos

A shaking table test is a direct way to study the earthquake response of structures, and shaking table tests were conducted on various spatial structures before. The model-frequency behavior, earthquake response, failure mechanism, failure mode and energy dissipation mechanism were investigated[1-6]. All of this will help to provide the test support for the research theory about structural seismic performance.



Studies have been conducted on the stability and buckling of steel arches, and design rules have been proposed for both the in-plane buckling [14-15] and the out-of-plane buckling [16-17]. Steel arches with sufficient lateral bracing would fail due to the plastic collapse instead of the in-plane or out-of-plane buckling [18]. Therefore, 4 braces were applied along the arch with equal distance in order to avoid the out-of-plane buckling, and both columns were fixed at the bottom [19]. The braces were welded to the test model on one end, and sliding against a bracing frame on the other end (Figure 3). According to the Chinese code [20], an additional mass of 25.8 kg was attached to the test model, which represented the dead load and half of the live load applied on the arch-frame structure. Each mass block was 2.87 kg. Accelerometers, displacement sensors and strain gauges were used to monitor the response of the test model, and the location of the 4 displacement sensors (named U1, U2, U3, U4), 4 accelerometers (named A1, A2, A3, A4) and 7 strain gauges (named S1, S2, S3, S4, S5, S6, S7) are shown in Figure 4 below. Due to symmetry, most of the strain gauges were installed on the right half of the test model, while there were only 2 gauges installed on the left half as checkpoints.

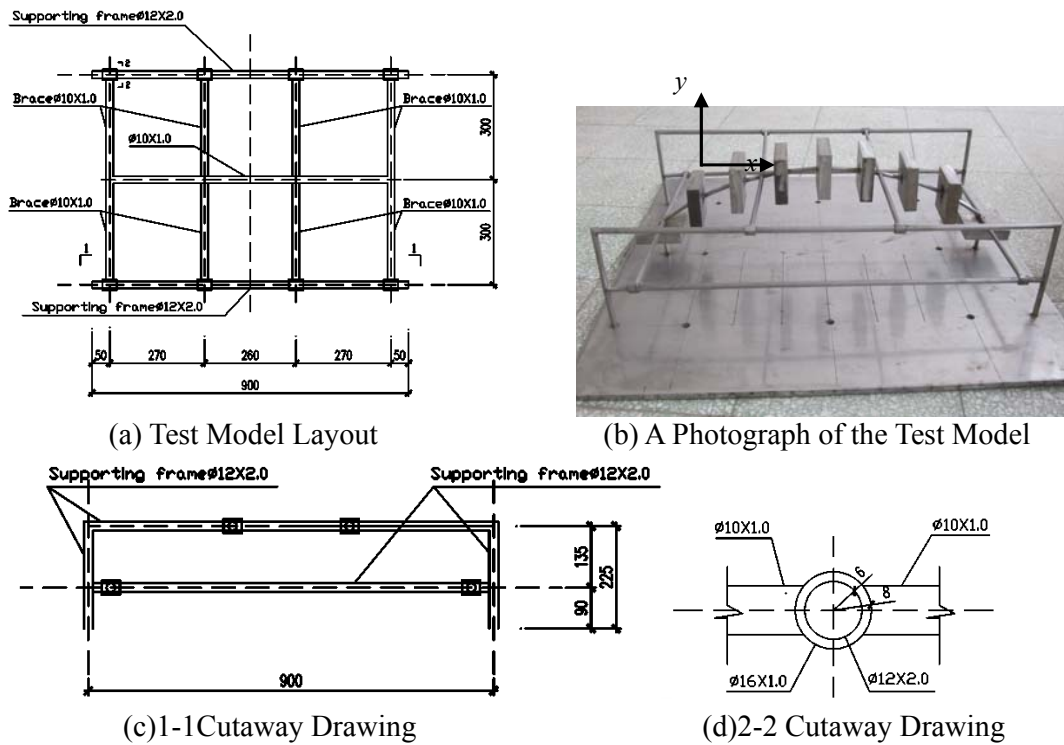


Figure 3. Brace and Supporting Frame Layout

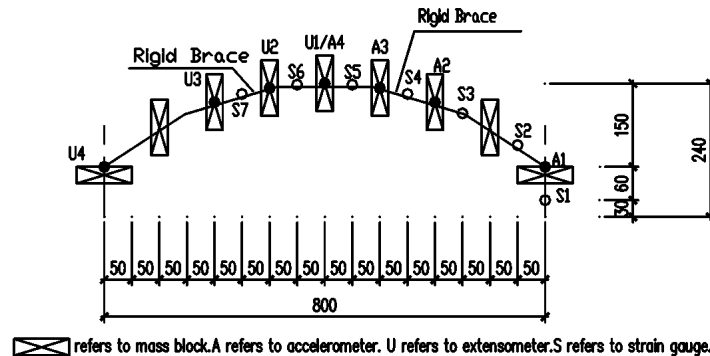


Figure 4. Sensor Placement

### 3.2. Ground Motion Record and Loading Plan

According to the shaking table test method about steel structure[21-23], three earthquake records were selected as input for the shaking table test, in order to evaluate the seismic performance of the test model under different levels of the seismic excitations, including the Tianjin earthquake (1976, NS), the Taft earthquake (1952, NS), and the Loma Prieta earthquake (1989, NS). White noise of 30s was applied before each test. The ground motion record was compacted 10 times according to the natural frequency of the test model. After the Fourier transform, the main frequency is 10-12Hz for the Tianjin wave, 12-18Hz for the Taft wave, and 15-18Hz for the Loma Prieta wave. The loading plan is shown in Table 1.

Table 1. Loading Plan of the Shaking Table Test

Process	Case #	Input Record	PGA (g)
Process 1	1	White noise	0.1
	2	Tianjin wave	0.07
	3	Taft wave	0.07
	4	Loma Prieta wave	0.07
	5	Tianjin wave	0.14
	6	Taft wave	0.14
	7	Loma Prieta wave	0.14
Process 2	8	White noise	0.1
	9	Tianjin wave	0.22
	10	Taft wave	0.22
	11	Loma Prieta wave	0.22
Process 3	12	White noise	0.1
	13	Tianjin wave	0.40
	14	Taft wave	0.40
	15	Loma Prieta wave	0.40
Process 4	16	White noise	0.1
	17	Tianjin wave	0.62
	18	Taft wave	0.62
	19	Loma Prieta wave	0.62
Process 5	20	White noise	0.1
	21	Tianjin wave	0.8
	22	Tianjin wave	1.0
	23	Tianjin wave	1.2
	24	Tianjin wave	1.5

### 3.3. System Response

#### 3.3.1 Self-vibration Characteristic

Firstly, the model was scanned by the white noise before the ground motion was input. The three natural frequencies were tested. The first-order frequency of the test model was 12.25Hz, which is close to the main frequency of Tianjin wave. And the damping ratio was about 0.012. From Figure 5, the natural frequency shows a decrease trend and fall by 1%-7%. The results show that internal damage grows for the model after the earthquake.

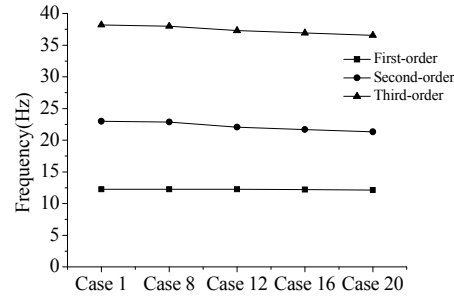


Figure 5. The Influence of Different Seismic Wave on the Natural Frequencies

### 3.3.2 Acceleration Response

As the acceleration amplitude of the ground motion input increases, the acceleration amplification factor  $\beta$  ( $\beta$ =the peak acceleration of a test point/peak acceleration of the test table) increases at first and then decreases. This phenomenon reflects that there is internal damage in the model after the earthquake, which makes the structural stiffness decline (Figure 6). It is clear that the acceleration response at the arch-top (A4) is largest.

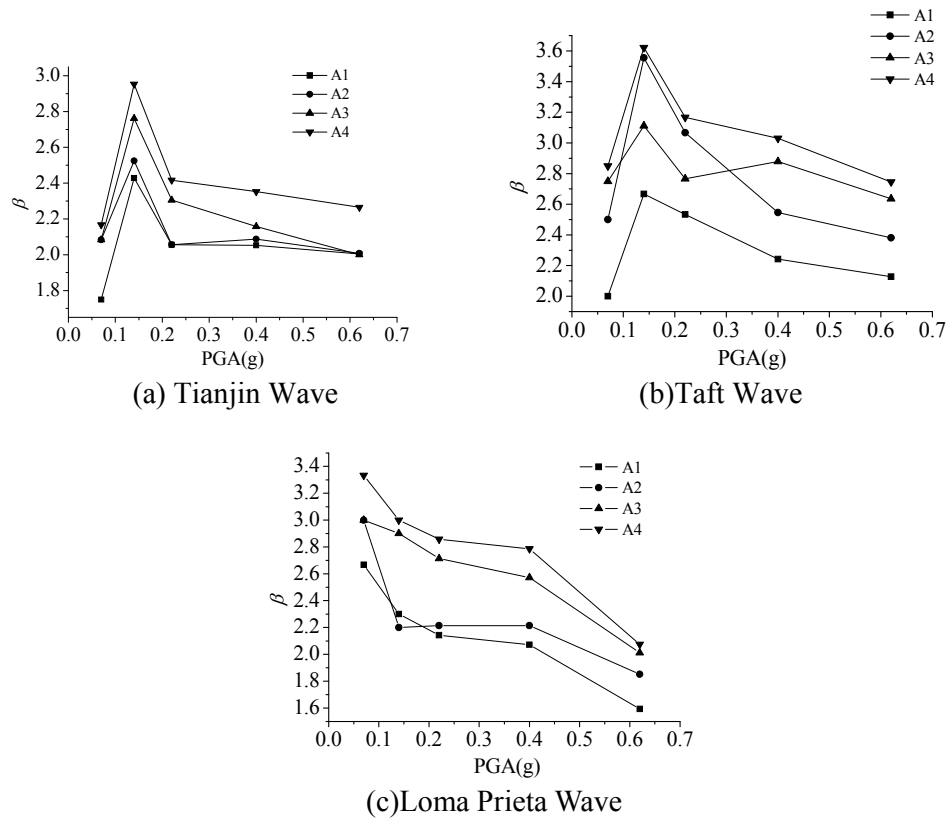


Figure 6. Influence of Different PGA on  $\beta$

### 3.3.3 Displacement Response and Stress Results

The maximum displacement response  $U_{\max}$  at the quarter point of the arch is larger than other test points, as shown in Figure 7. Figure 8 shows that the maximum stress  $\sigma_{\max}$  at the quarter point of the arch (S4, S7) is larger than the  $\sigma_{\max}$  at the arch-top and at the arch-column connection. All these results reflect that the added braces could effectively help decreasing the displacement and deformation of the arch-frame. When  $\text{PGA} \leq 0.62\text{g}$ , the maximum stress  $\sigma_{\max}$  under the Tianjin wave is the largest while  $\sigma_{\max}$  under the Loma Prieta wave is the least, since the predominant frequency of the Tianjin wave is closest to the fundamental frequency of the model.

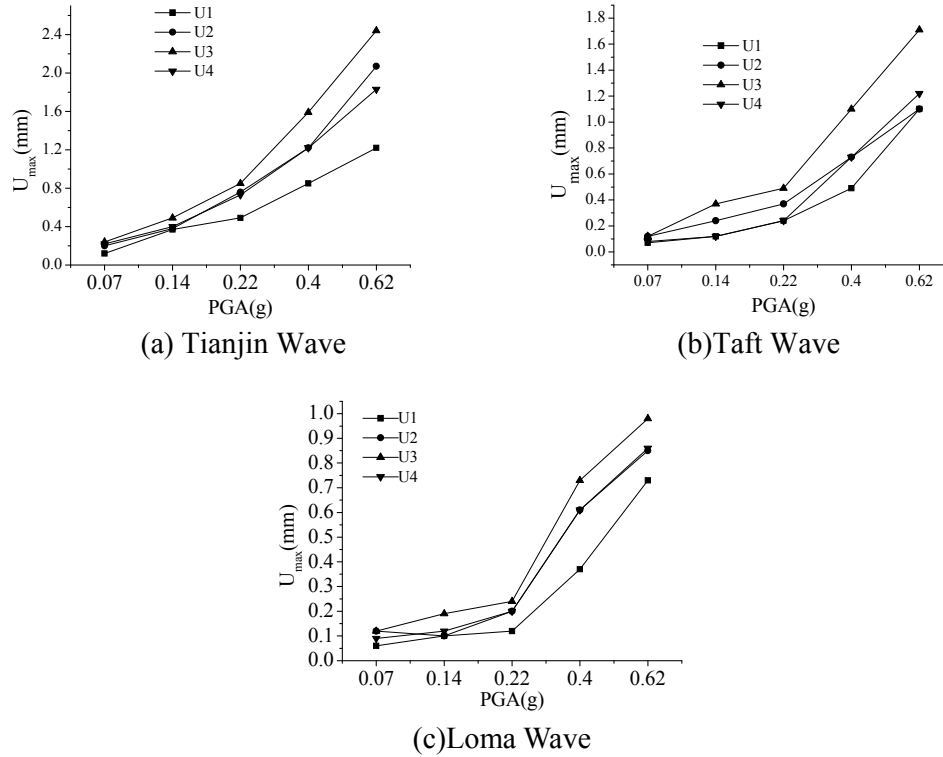
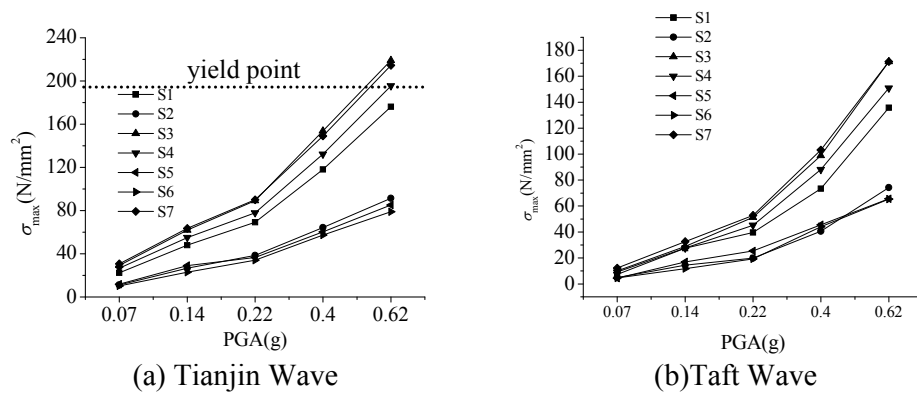


Figure 7. Displacement Response of the Test Points



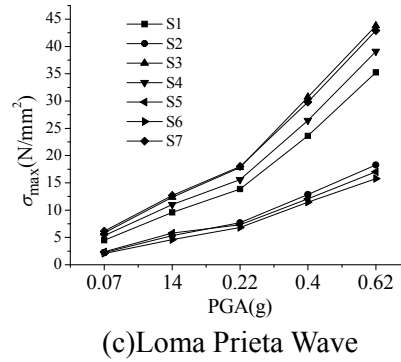


Figure 8. Maximum Stress of Different Test Points

### 3.3.4 Test Analyses

After Process 4 of the shaking table test, PGA of the Tianjin wave continued to increase in order to study the development of plastic deformation and the failure mechanism of the arch-frame. When PGA of the ground motion records was smaller than 0.40g, the behavior of the model was mainly elastic. When PGA of the ground motion records was 0.62g, the maximum stress in the model was 214.5N/mm<sup>2</sup> and larger than  $f_y$ (Figure 8(a)). then plastic zone started to form in the test model. When PGA of the ground motion record was 0.80g, the plastic zone started to spread. Finally, when PGA=1.2g, the arch top deformed along the X direction(Figure 9(a)). The test model was in-plane antisymmetric deformation(Figure 9(b)). The braces reduced the lateral deformation of the model. The test model lost the bearing capacity.

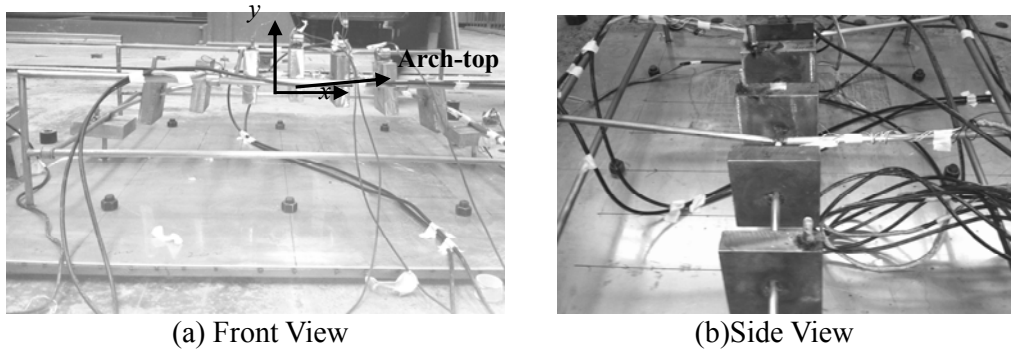


Figure 9. Failure Mode of the Test Model

### 3.4. Incremental Dynamic Analysis

Performance levels or limit-states are important ingredients of PBEE (Performance-Based Earthquake Engineering), and the IDA curve contains the necessary information to assess them. The material model was elastic perfectly-plastic with the elastic modulus and yield strength acquired from the coupon tests. The model was constructed with beam element Beam188, and the additional mass was modeled with mass element Mass21. The material nonlinear effects as well as geometrically nonlinear effects have been considered to simulate the realistic behavior of the arch as accurately as possible. By restraining the nodes displacement of Z direction may simulate the lateral braces. The structural model is shown in Figure 10. The first-order frequency is 13.7Hz by ANSYS, which is close to the value by the shaking table test(12.25Hz).

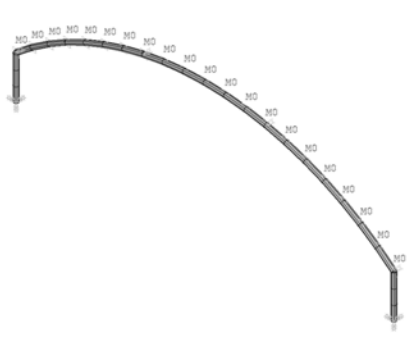


Figure 10. Numerical Analysis Model

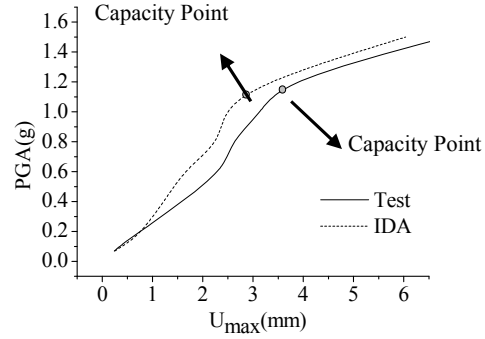


Figure 11. Maximum Displacement vs. PGA Curve

When a statement or a rule is satisfied, the structure reaches a limit-state. There are DM-based rule and IM-based rule. First comes the DM-based rule, which is generated from a statement of the format: “If  $DM \geq C_{DM}$  then the limit-state is exceeded”. DM is a damage indicator. Different spatial structures have different structure response. Hence, it is difficult to rule the  $C_{DM}$ . The IM-based rule is a rule is generated by a statement of the form: “If  $IM \geq C_{IM}$  then the limit-state is exceeded”. The IM-based rule can refer to the 20% tangent slope approach ruled by FEMA[24]. In effect it is that the last point on the curve with a tangent slope equal to 20% of the elastic slope is defined to be the capacity point. Taking the maximum displacement of U3 for example (Figure 11), the IDA results are slightly smaller than the test results. According to the IM-based rule, when the structure comes to the capacity point, PGA is 1.20g by both the test and IDA approach. It is also shown that the IDA curves can assess the earthquake-resistant capability of the spatial structures.

#### 4. EVALUATION OF EARTHQUAKE-RESISTANT CAPABILITY OF THE UN-LANDING LATTICED STEEL TUBULAR ARCH

##### 4.1 Project Introduction

The earthquake-resistant capability of an un-landing latticed steel tubular arch was evaluated using the IDA approach from a real project described in Figure 1(b). The project is a railway platform canopy, which consists of thirteen 68.6m-span transverse latticed steel tubular arch and three longitudinal steel-tube trusses, as shown in Figure 12. The space between each arch is 22m and the overall canopy length is 270m. The height of the truss column is 6.8m. One un-landing latticed steel tubular arch was analyzed by ANSYS. The truss type is triangular truss as shown in Figure 13, and the member section is steel tube shown in Table 2. Material of the steel tubes is Q235B. The chords were simulated by Beam188. The web members were simulated by Link8. By restraining the nodes displacement of Z direction may simulate the longitudinal steel-tube trusses.

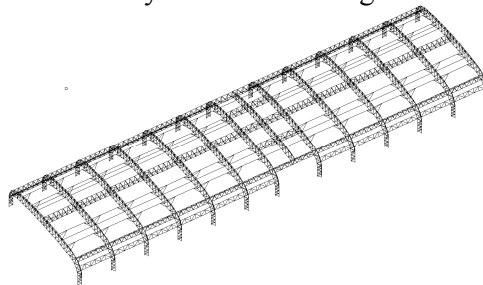


Figure 12. A Railway Platform Canopy



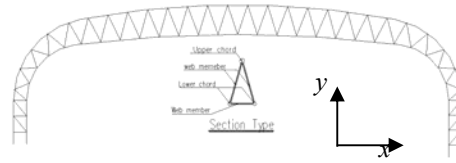


Figure 13. Configuration of An Un-landing Latticed Steel Tubular Arch

Table 2. Section Type of the Un-landing Latticed Steel Tubular Arch

Member	Section Type
Upper chord of the truss-arch	$\Phi 550 \times 14$
Lower chord of the truss-arch	$\Phi 426 \times 14$
Web member of the truss-arch	$\Phi 114 \times 6$ , $\Phi 168 \times 8$ and $\Phi 273 \times 8$
Upper chord of the truss-column	$\Phi 550 \times 18$
Lower chord of the truss-column	$\Phi 426 \times 18$
Web member of the truss-column	$\Phi 114 \times 6$ , $\Phi 168 \times 8$ and $\Phi 273 \times 8$

#### 4.2 Selection of the Ground Motion Record

15 ground motion records for duration of 20s were selected as the input ground motion in Table 3 from PEER Strong Motion Database. The PGA has been increased 8~10 times and the step is 0.3~0.5g.

Table 3. The Suite of 15 Ground Motion Records

No.	Event	Moment magnitude	Station
1	Cape Mendocino 1992/04/25	7.1	89324 Rio Dell Overpass - FF(CDMG)
2	Cape Mendocino 1992/04/25	7.1	89486 Fortuna - Fortuna Blvd(CDMG)
3	Duzce, Turkey 1999/11/12	7.1	1058 Lamont
4	Duzce, Turkey 1999/11/12	7.1	362 Lamont 362(LAMONT)
5	Duzce, Turkey 1999/11/12	7.1	531 Lamont 531(LAMONT)
6	Duzce, Turkey 1999/11/12	7.1	1060 Lamont
7	Tabas, Iran 1978/09/16	7.4	70 Boshrooyeh
8	Landers 1992/06/28	7.3	12149 Desert Hot Springs(CDMG)
9	Loma Prieta 1989/10/18	6.9	57217 Coyote Lake Dam(CDMG)
10	Northridge 1994/01/17	6.7	127 Lake Hughes #9(USGS)
11	Northridge 1994/01/17	6.7	90017 LA - Wonderland Ave(USC)
12	Chi-Chi, Taiwan 1999/09/20	7.6	WGK(CWB)
13	Kocaeli, Turkey 1999/08/17	7.4	Arcelik(KOERI)
14	Imperial Valley 1940/05/19	7.0	117 El Centro Array #9(USGS)
15	Tianjin	6.9	Station NO. 02001 Tianjin Hospital

### 4.3 Multi-Record IDA Study

Vertical ground motion records and horizontal ground motion records in the EW direction of the selected ground motions were used as input for the IDA study. Such a study, correspondingly produces sets of IDA curves, can be plotted on the same graph. (Figure 14(a) and Figure 14(b)). By the IM-based rule, the capacity point can be obtained. As we are able to summarize a suite of records by having, for example, mean, 16%, 84% fractiles, which are practically coincident with the mean, mean-sigma and mean+sigma values. These values can accurately characterize the distribution of the seismic demand and capacity of the structure for frequent or rare earthquakes. According to the capacity point, the critical displacements under the vertical ground motion records ( $Y_{\max}$ ) and horizontal ground motion records ( $X_{\max}$ ) are acquired respectively. The critical vertical displacements of the 16%, 50% and 84% fractiles are 0.32m, 0.37m, 0.44m, respectively, which corresponds to 1/235, 1/200, 1/170 of the structure span. The critical horizontal displacements of the 16%, 50% and 84% fractiles are 0.15m, 0.17m, 0.19m, respectively, which corresponds to 2.2%, 2.5%, 2.8% of the column height.

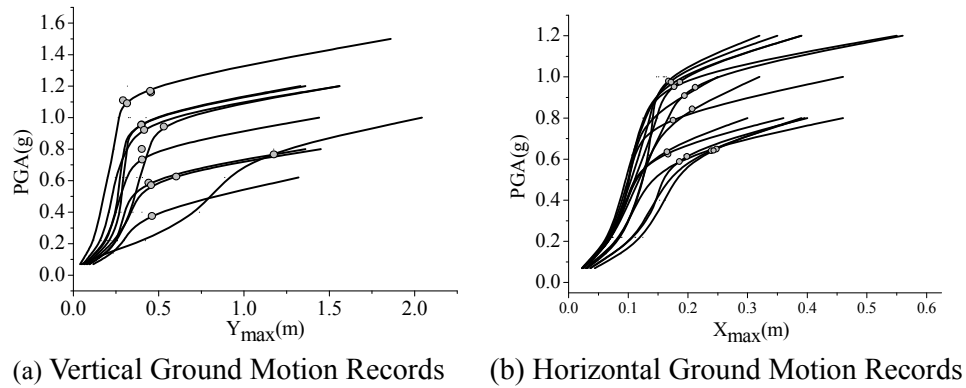


Figure 14. Critical Displacement vs. PGA

## 5. CONCLUSIONS

This paper focuses on the earthquake-resistant capability of un-landing steel arch. A shaking table test of an un-landing solid-web steel arch was carried out to present the seismic behavior. By the IM-based rule, the capacity point is acquired of the test model from the IDA curve. Finally, the earthquake-resistant capability of an un-landing latticed steel tubular arch from a real project is evaluated. The major findings from this study are listed below.

- 1) During the shaking table test, as the acceleration amplitude of the ground motion input increases, the internal damage in the model is cumulative after the earthquake. The acceleration response at the arch-top is largest.
- 2) The maximum displacement response and the maximum stress at the quarter point of the arch are larger than other test points. All these results reflect that the added braces could effectively help decreasing the displacement and deformation of the un-landing steel arch. The seismic response under the Tianjin wave is the largest while that under the Loma Prieta wave is the least, since the predominant frequency of the Tianjin wave is closest to the fundamental frequency of the model.
- 3) IDA approach is applied in the un-landing steel arch. A single IDA curve is plotted, which fits the test result. By the IM-based rule, the capacity point of the structure is acquired.

4) The earthquake-resistant capability of the un-landing latticed steel tubular arch is evaluated by the multi-record IDA study from a real project. Summarizing a suite of records by having mean, 16%, 84% fractiles, the critical vertical displacements of the 16%, 50% and 84% fractiles are 0.32m, 0.37m, 0.44m, respectively, which corresponds to 1/235, 1/200, 1/170 of the structure span. The critical horizontal displacements of the 16%, 50% and 84% fractiles are 0.15m, 0.17m, 0.19m, respectively, which corresponds to 2.2%, 2.5%, 2.8% of the column height.

## ACKNOWLEDGEMENTS

This research project is supported by the National Natural Science Foundation of China (No. 51078259 and No. 51308386) and Research Fund for the Doctoral Program of Higher Education of China (No.20130032110044). Support from the funding agency above is gratefully acknowledged.

## REFERENCES

- [1] Tanami, T. and Hangai, Y., "Dynamic Experiments and Earthquake Observation of Reticulated Single-layer Domes", International Symposium on Practical Aspects in the Computation of Shell and Spatial Structures, Belgium, 1987, pp.221-230.
- [2] Tanami, T. and Hangai, Y., "Shaking Table Tests for the Dynamic Behaviors of Reticulated Single-layer Dome by Use of a Spring Model", International Colloquium on Space Structures for Sports Buildings, China, 1987, pp.101-111.
- [3] Li, G.Q., Shen, Z.Y., Ding, X. and et al, "Shaking Table Experimental Study on R2 Steel Roof Model of Shanghai Pudong International Airport Terminal Subjected to Three Dimensional Earthquakes", Journal of Building Structure, 1999, Vol.34, No.14, pp.18-27.
- [4] Fan, F. and Shen, S.Z., "Study on the Shaking Table Experiment and the Vibration Reducing Experiment of Single Layer Reticulated Shells", Journal of Harbin University Civil Engineering Architecture, 2000, Vol.33, No.3, pp.18-22.
- [5] Xing, J.H., Liu, X.D., Fan, F. and et al, "Shaking Table Experiment Research on Seismic Behavior of Single-layer Latticed Cylindrical Shell", Journal of Building Structure, 2004, Vol.25, No.6, pp.1-8.
- [6] Liu, J.S., Qiu, T. and He, M.W., "Shaking Table Experiment Study on Performance of Long-span Steel Transfer Trusses", World Earthquake Engineering, 2006, Vol.22, No.4, pp.145-149.
- [7] Vamvatsikos, D., "Seismic Performance, Capacity and Reliability of Structures as seen through Incremental Dynamic Analysis", Stanford University, Stanford, CA, 2002.
- [8] Vamvatsikos, D. and Fragiadakis, M., "Incremental Dynamic Analysis for Estimating Seismic Performance Sensitivity and Uncertainty", Earthquake Engineering and Structural Dynamics, 2010, Vol.34, No.13, pp.141-163.
- [9] Vamvatsikos, D. and Cornell, C.A., "Applied Incremental Dynamic Analysis", Earthquake Spectra, 2004, Vol.20, No.2, pp.523-553.
- [10] Vamvatsikos, D. and Cornell, C.A., "Developing Efficient Scalar and Vector Intensity Measures for IDA Capacity Estimation by Incorporating Elastic Spectral Shape Information", Earthquake Engineering and Structural Dynamics, 2005, Vol.34, No.13, pp.1573-1600.
- [11] Vamvatsikos, D. and Cornell, C.A., "Direct Estimation of the Seismic Demand and Capacity of Oscillators with Multi-linear Static Pushovers through IDA", Earthquake Engineering and Structural Dynamics, 2006, Vol.35, No.9, pp.1097-1117.
- [12] Vamvatsikos, D. and Cornell, C.A., "Incremental Dynamic Analysis", Earthquake Engineering and Structural Dynamics, 2002, Vol.31, No.3, pp.491-514.

- [13] Yang, D.B., Zhang, Y.G. and Wu, J.Z., “Application of Incremental Dynamic Analysis in the Collapse Evaluation of Single-layer Latticed Dome”, *Spatial Structure*, 2010, Vol.16, No.3, pp. 91-96.
- [14] Pi, Y.L. and Trahair, N.S., “In-plane Buckling and Design of Steel Arches”, *Journal of Structure Engineering*, ASCE, 1999, Vol.125, No.110, pp.1291-1298.
- [15] Pi, Y.L. and Bradford, M.A., “In-plane Strength and Design of Fixed Steel I-section Arches”, *Engineering Structure*, 2004, Vol.26, No3, pp.291-301.
- [16] Sakimoto, T. and Komatsu, S., “Ultimate Strength Formula for Steel Arches”, *Journal of Structure Engineering*, ASCE, 1983, 109, pp.613-27.
- [17] Pi, Y.L. and Trahair, N.S. “Out-of-plane Inelastic Buckling and Strength of Steel Arches”, *Journal of Structure Engineering*, ASCE, 1998, Vol.124, No.2, pp.174-83.
- [18] Spoorenberg, R.C., Snijder, H.H. and Hoenderkamp C.D. “A Theoretical Method for Calculating the Collapse Load of Steel Circular Arches”, *Engineering Structure*, 2012, Vol.38, No.2, pp.89-103.
- [19] Lu, Y., “Theoretical Analyses and Experimental Research on Collapse Mechanism of Large-span Arched Frame”, Tianjin University, Tianjin, China, 2012.
- [20] “Load Code for the Design of Building Structures” (GB50009-2001, 2006 edition), China, 2006.
- [21] Wang, L., “Seismic Response Analyses of Long-span Rigid-frame Bridge and the Shaking Table Model Test”, Beijing Jiaotong University, Beijing, China, 2010.
- [22] Huang, H.H., “Design and Application Technology of the Shaking Table Test”, Beijing, China, Seismological Press, 2008.
- [23] Li, Z.X., “Theory and Technology of Structure Test”, Tianjin, China, Tianjin University Press, 2006.
- [24] FEMA, “Recommended Seismic Design Criteria for New Steel Moment-frame Buildings” Report No. FEMA-350, SAC Joint Venture, Federal Emergency Management Agency, Washington, DC, 2000.

# NOVEL NON-LINEAR ELASTIC STRUCTURAL ANALYSIS WITH GENERALISED TRANSVERSE ELEMENT LOADS USING A REFINED FINITE ELEMENT

C.K. Iu<sup>\*,1</sup> and M.A. Bradford<sup>2</sup>

<sup>1</sup> *School of Civil Engineering and Built Environment  
Queensland University of Technology  
QUT Brisbane, QLD, Australia*

<sup>2</sup> *Centre for Infrastructure Engineering and Safety  
School of Civil and Environmental Engineering  
The University of New South Wales  
UNSW Sydney, NSW, Australia*

*\*(Corresponding author: E-mail: jerry.iu@qut.edu.au / iu.jerryu@gmail.com)*

*Received: 4 May 2014; Revised: 16 June 2014; Accepted: 8 July 2014*

**ABSTRACT:** In the finite element modelling of structural frames, external loads usually act along the elements rather than at the nodes only. Conventionally, when an element is subjected to these general transverse element loads, they are usually converted to nodal forces acting at the ends of the elements by either lumping or consistent load approaches. For a first- and second-order elastic analysis, the accurate displacement solutions of element load effect along an element can be simulated using neither lumping nor consistent load methods alone. It can be therefore regarded as a unique load method to account for the element load nonlinearly. In the second-order regime, the numerous prescribed stiffness matrices must indispensably be used for the plethora of specific transverse element loading patterns encountered. In order to circumvent this shortcoming, this paper shows that the principle of superposition can be applied to derive the generalized stiffness formulation for element load effect, so that the form of the stiffness matrix remains unchanged with respect to the specific loading patterns, but with only the magnitude of the loading (element load coefficients) being needed to be adjusted in the stiffness formulation, and subsequently the non-linear effect on element loadings can be commensurate by updating the magnitude of element load coefficients through the non-linear solution procedures. In principle, the element loading distribution is converted into a single loading magnitude at mid-span in order to provide the initial perturbation for triggering the member bowing effect due to its transverse element loads. This approach in turn sacrifices the effect of element loading distribution except at mid-span. Therefore, it can be foreseen that the load-deflection behaviour may not be as accurate as those at mid-span, but its discrepancy is still trivial as proved. This novelty allows for a very useful generalised stiffness formulation for a single higher-order element with arbitrary transverse loading patterns to be formulated. Moreover, another significance of this paper is placed on shifting the nodal solution (system analysis) to both nodal and element solution (sophisticated element formulation). For the conventional finite element method, such as cubic element, all accurate solutions can be only found at node. It means no accurate and reliable structural safety can be ensured within element, and as a result, it hinders the engineering applications.

**Keywords:** Elastic instability, Finite element, Transverse element load effect, Higher-order element formulation, Nodal solution, Element solution

## 1. INTRODUCTION

General load cases for framed structures, such as permanent loads, live loads and wind loads, usually involve patterns of loading which act transversely along the elements of the frame. It is usual in the finite element modelling to convert these loads to nodal loads, and to discretise the member into several elements, with the transverse loads taken account of as nodal forces in order to capture the first- and second-order structural response accurately in terms of nodal solution. However, when using one element for a member, it in turn means no accurate first-order (element load effect) and second-order (member bowing effect triggered by transverse element load) solutions is available except at the element nodes, as long as the assumed finite element function of an element excludes the condition of force equilibrium, such as cubic function. This paper is therefore concerned with the development of a numerical technique for incorporating transverse

element loading in a sophisticated element formulation to replicate the accurate first- and second-order solutions along itself, when subjected to transverse element loads, and with the reducing of the difficulties encountered with the multiplicity of possible loading patterns and regimes to being represented by the stiffness formulation of a single element.

Kondoh *et al.* [1] presented a simplified procedure for the finite deformation analysis of space frames using one beam element to model each member, which involved the non-linear coupling of bending and stretching. Unfortunately, a few of elements were required for a single member in some reported examples for the accurate solutions by using the higher-order element approach. To this end, Chan and Zhou [2][3] developed a PEP finite element to simulate the second order effect on a member with an initial geometric imperfection. Izzuddin [4] subsequently formulated a fourth-order displacement-based finite element for structures under thermal loads, while Liew *et al.* [5] made use of a stability function formulation in their stiffness matrices so that geometric non-linearity in a member could be incorporated. Recently, Iu and Bradford [6][7][8] have developed the higher-order element using higher-order element, which showed the great applications of second-order inelastic framed structures.

Despite the advocacy of using a second-order analysis with a higher-order element approach, it seems a sophisticated element of this type which accounts for element loading has not been presented in the open literature, and either consistent or lumped load methods are used in lieu of incorporating transverse loading into the element formulation. The main drawback of using lumped and consistent loads is its inaccuracy, since it takes the form of a first- and second-order element loading response at node (nodal solution) by virtue of the system analysis; especially, the assumed finite element function does not satisfy the force condition. Because of this, most reported research has accounted for the coupling effect at the system level by merely dividing a member into a few elements to replicate the behaviour of a member by the accurate solutions at nodes of a few elements.

In order to account for the element load effect within a single element, Zhou and Chan [9][10] presented a second-order analysis that is capable of modelling the effects of element loads in the element stiffness formulation, in lieu of by a system analysis. However, each element loading pattern or regime requires a specific element stiffness matrix, which is limiting its applications because of the usual multiplicity of loading scenarios met in practice. To overcome this difficulty, a proficient and generalised element formulation is developed in this paper which facilitates the modelling of second-order loading effects covering a wide range of transverse loading regimes, which is founded on the principle of superposition of simple loading cases within a second-order analysis framework. The complex loading regimes are formed from these specific simple or fundamental loading cases, each of which is characterised by one representative bending moment coefficient. Consequently, the complex loading regime is defined in the stiffness coefficient by the combination of these moment coefficients only prior to present non-linear analysis. It means the magnitude of stiffness matrix representing the specific complex loading regime in lieu of stiffness matrix itself, which is updated with the recourse to the non-linear solution procedures for non-linear member bowing effect due to that complex element loading. Meanwhile, the principle of superposition is no longer effective in the course of non-linear solution procedures which is merely applied for deriving that non-linear stiffness formulation afore non-linear analysis. As such, the method is a trade-off between simplicity in the formulation and accuracy in describing the member buckling due to element load effect by virtue of the generalized element stiffness matrix. The ranges of the validity of the proposed non-linear analysis which incorporates element loading are illustrated through several examples chosen to illustrate its feasibility, versatility and accuracy.

## 2. ASSUMPTIONS

The following assumptions are made in the formulation:

- The beam is prismatic and slender, with the Euler-Bernoulli hypothesis being valid;
- Warping deformations, shear deformations and the Wagner effect are neglected, so that lateral buckling is not considered;
- The loads increase and decrease incrementally and proportionally;
- The loading is conservative, with both nodal and element loading being admissible; and
- The strains are small but large displacements are included.

The transverse loading is not restricted as can occur in conventional finite element formulations, insofar as the lumped and consistent nodal approaches are not merely used to treat the transverse element load.

## 3. DISPLACEMENT FUNCTION FOR HIGHER-ORDER BEAM-COLUMN ELEMENT

The vector of deformations along an element are taken as  $\mathbf{u} = \{u, v, w, \phi\}^T$ , which comprise the deformations  $u$  in the longitudinal  $x$ -direction,  $v$  in the  $y$ -direction,  $w$  in the  $z$ -direction and the twist  $\phi$  about the  $x$ -axis. Because the displacement functions for the element representation herein are referred to a co-rotational coordinate, the dependent variables for the transverse displacement  $v$  and  $w$  are replaced by the nodal rotations  $\theta_z$  and  $\theta_y$  about the  $z$  and  $y$ -axes, respectively. These rotations are the dependent variables which define the transverse displacements in the element stiffness formulation which follows.

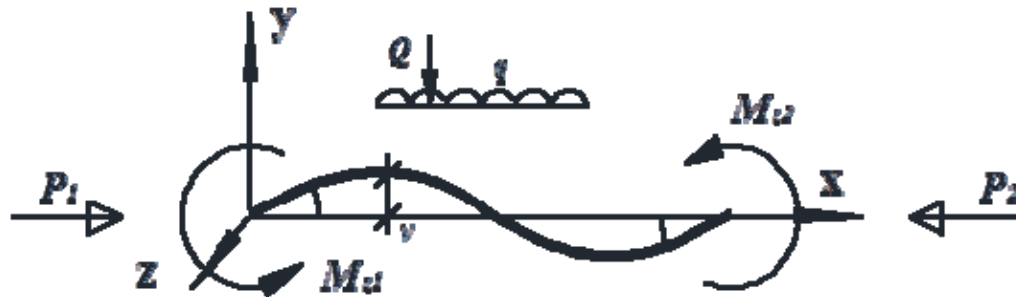


Figure 1. Equilibrium of Beam-column Element about z-axis under Element Loadings

External transverse element loads on an element generate additional non-linear effects that are manifested in the second-order element solution. To this end, the effect of transverse loading in the element is taken into account in the magnitude of element stiffness formulation, in which a relationship between the deflections and the loading under transverse element loads is modelled accurately and adequately using a single element. As a result, apart from satisfying the primary kinematic boundary conditions, the displacement function proposed which includes the general transverse element distributed loading  $q$  and concentrated loading  $Q$  shown in Figure 1 can be derived by satisfying the secondary statical boundary of force equilibrium. Without loss of generality, the mid-span moment  $M_0$  obtained by superimposing the loading effects using elementary force statics, is used in the equilibrium condition for moments about the  $z$ - and  $y$ -axes; this superposition being valid prior to the commencement of the non-linear analysis. Further, the second-order moments  $Pv$  and  $Pw$  due to the member P- $\delta$  effects are also introduced into the equilibrium equation when equilibrium is formulated along the element instead of at the end nodes of the element. It is therefore helpful to incorporate the member bowing and element load effects

into the element stiffness formulation based on a single element, whose higher-order elastic displacement function is derived in the following.

Linear functions are assumed for the axial deformation and twist; pure axial deformation and twist are assumed as being independent of the element load effect, so that

$$u = (1 - \xi)u_1 + \xi u_2 \quad \text{and} \quad \phi = (1 - \xi)\theta_{x1} + \xi\theta_{x2}, \quad (1)$$

in which  $u = u_1$  at  $x = 0$ ,  $u = u_2$  at  $x = L$  are the axial nodal deformations,  $\phi = \theta_{x1}$  at  $x = 0$ ,  $\phi = \theta_{x2}$  at  $x = L$  are the twist nodal deformations, and where  $\xi = x/L$ . In order to include the member bowing effect and transverse element loading in a single element, the kinematic boundary conditions about the  $y$ -direction are

$$v = \begin{cases} 0 & x = 0 \\ 0 & x = L \end{cases} \quad \text{and} \quad \frac{\partial v}{\partial x} = \begin{cases} \theta_{z1} & x = 0 \\ \theta_{z2} & x = L, \end{cases} \quad (2)$$

while the equation of bending given by

$$EI_z \frac{\partial^2 v}{\partial x^2} = Pv - M_{z1}(1 - \xi) + M_{z2}\xi + M_0 \quad (3)$$

which produces

$$EI_z \frac{\partial^2 v}{\partial x^2} = Pv + \frac{M_{z2} - M_{z1}}{2} + M_0 \quad \text{at} \quad \xi = 1/2, \quad (4)$$

leads to the deflection

$$v = \left[ \xi - \frac{4(24 + \omega)\xi^2}{48 + \omega} + \frac{(48 + 5\omega)\xi^3}{48 + \omega} - \frac{2\omega\xi^4}{48 + \omega} \right] L\theta_{z1} + \left[ \frac{-(48 - \omega)\xi^2}{48 + \omega} + \frac{3(16 - \omega)\xi^3}{48 + \omega} + \frac{2\omega\xi^4}{48 + \omega} \right] L\theta_{z2} \\ - \frac{\bar{M}_0 L}{(48 + \omega)} [\xi^2 - 2\xi^3 + \xi^4] \quad (5)$$

or

$$v = N_1 L\theta_{z1} + N_2 L\theta_{z2} + N_q L\bar{M}_0, \quad (6)$$

in which

$$\omega = \frac{PL^2}{EI} \quad (7)$$

is a dimensionless axial load parameter and  $N_1$ ,  $N_2$  and  $N_q$  are displacement functions with respect to the first and second node rotations, and element loads, respectively. The equivalent mid-span moment  $\bar{M}_0$  for a variety of element loads is given in Appendix 1, which represents the amount of the equivalent mid-span moment produced by various element loads and derived analytically from a force equilibrium equation. The transverse displacement  $v$  in the  $z$  direction can be similarly defined.



An elementary verification of the functions in Eqs. 5 and 6 can be established for a fixed beam under a point load applied at mid-span, for which  $\theta_1$  and  $\theta_2$  are zero and using  $a = L/2$  by Eqs. 72 or 73 in Appendix 1 reduces to the exact theoretical solution for the mid-span deflection of  $QL^3/192EI$  ( $x = L/2$ ). Similarly for a uniformly distributed load instead of a point load at mid-span, the displacement function produces the exact mid-span deflection of  $qL^4/384EI$  using Eq. 76 in Appendix 1. Further theoretical verifications of displacement function for more general load distributions are discussed in Section 6.

It should be noted that the higher-order displacement function  $N_q$  in Eq. 5 is independent of the loading regime along the element. The different element load solutions for different loading regimes is merely incorporated into the equivalent moment  $\bar{M}_0$  with respect to mid-span given in Appendix 1 which does not depend on the independent variable  $x$ , but on the magnitude of the loading and the point of application of the load with respect to the mid-span location. This significantly implies that the different element loading regimes vary with the magnitudes of stiffness matrix in lieu of stiffness matrix itself, and so only the fundamental load cases listed in Appendix 1 are needed to customize complex loading regimes in the second-order analysis. The distribution of complex loading regimes is therefore condensed into the magnitude of stiffness matrix in terms of equivalent moment  $\bar{M}_0$  at mid-span, for which provides the initial perturbation for triggering the member bowing effect due to its transverse element loads.

#### 4. STIFFNESS FORMULATION FOR HIGHER-ORDER BEAM-COLUMN ELEMENT

The internal strain energy  $U$  caused by the axial strain  $\varepsilon_x$  and twist strain  $\gamma_x$  in the element continuum is considered in order to formulate the stiffness matrices in the present second order elastic beam-column element. It is routinely given by

$$U = \frac{1}{2} \int_{Vol} (E\varepsilon_x^2 + G\gamma_x^2) d(Vol), \quad (8)$$

which can be expressed as [6]

$$U = \frac{1}{2} EA \int_L \left( \frac{du}{dx} \right)^2 dx + \frac{1}{2} P \int_L \left( \frac{dv}{dx} \right)^2 dx + \frac{1}{2} P \int_L \left( \frac{dw}{dx} \right)^2 dx \\ + \frac{1}{2} EI_z \int_L \left( \frac{d^2 v}{dx^2} \right)^2 dx + \frac{1}{2} EI_y \int_L \left( \frac{d^2 w}{dx^2} \right)^2 dx + \frac{1}{2} GJ \int_L \left( \frac{d\phi}{dx} \right)^2 dx \quad (9)$$

in which  $EA$  is the axial rigidity,  $EI_y$  and  $EI_z$  the flexural rigidities about the  $y$  and  $z$ -axes respectively,  $GJ$  the torsional rigidity,  $P$  the axial force; and  $E$  is the elastic modulus and  $G$  the shear modulus.

In this study, external loads are produced by nodal force vectors  $\mathbf{f}_k$  and element load vectors  $\Phi_k$ , so that the external work done  $V$  comprises of two components. The first of these is the work done by the nodal forces  $\mathbf{f}_k$  in moving through nodal displacements  $\mathbf{u}_k$ , while the second is the work done by the transverse element load  $\Phi_k$  moving through the assumed transverse displacement field associated with the element displacement function vector  $\mathbf{N}$  over the element length, in which  $\mathbf{u}_k = \langle u, \theta_{z1}, \theta_{z2}, \theta_x, \theta_{y1}, \theta_{y2} \rangle^T$  with  $u = u_1 - u_2$  and  $\theta_x = \phi_1 - \phi_2$ . The principle of superposition can be

applied to simplify the effect of the element load  $\Phi_k$  on the external work  $V$ , for which in accordance with the assumption of conservative loading the work done  $V$  caused by the element load vector  $\Phi_k$  moving through the element deflections represented by  $\mathbf{N}$  is independent of the axial load  $P$  (and thus axial load parameter  $\omega$ ) throughout; hence setting  $\omega = 0$  gives

$$V = \int_L \mathbf{u}_k^T \mathbf{N}^T \Phi_k \, dx + \mathbf{u}_k^T \mathbf{f}_k. \quad (10)$$

The elastic force-displacement relationship is derived from the total potential energy  $\Pi$  of the general beam-column element subjected to both nodal and element loads. For second-order analysis, the total potential is the sum of the internal strain energy in Eq. 9 and external work done in Eq. 10, giving

$$\begin{aligned} \Pi = & \frac{EA}{2} \int_L \left( \frac{du}{dx} \right)^2 dx + \frac{P}{2} \int_L \left( \frac{dv}{dx} \right)^2 dx + \frac{P}{2} \int_L \left( \frac{dw}{dx} \right)^2 dx + \frac{EI_z}{2} \int_L \left( \frac{d^2 v}{dx^2} \right)^2 dx \\ & + \frac{EI_y}{2} \int_L \left( \frac{d^2 w}{dx^2} \right)^2 dx + \frac{GJ}{2} \int_L \left( \frac{d\phi}{dx} \right)^2 dx - \int_L \mathbf{u}_k^T \mathbf{N}^T \Phi_k \, dx - \mathbf{u}_k^T \mathbf{f}_k. \end{aligned} \quad (11)$$

The strain energy functional in Eq. 9 depends not only on the variables  $\mathbf{u}_k$  but also on the axial load parameter  $\omega$ . Hence from Castigliano's first theorem of strain energy, the secant stiffness matrix is obtained from

$$\mathbf{K}_s = \frac{\partial U}{\partial \mathbf{u}_k} + \frac{\partial U}{\partial \omega} \cdot \frac{\partial \omega}{\partial \mathbf{u}_k}. \quad (12)$$

This then leads to

$$M_{\alpha 1} = \frac{\partial U}{\partial \theta_{\alpha 1}} = \frac{EI_\alpha}{L} (C_1 \theta_{\alpha 1} + C_2 \theta_{\alpha 2} + C_q \bar{M}_0), \quad (13)$$

in which

$$C_1 = \frac{9216 + 3456\omega/5 + 68\omega^2/5 + 8\omega^3/105}{(48 + \omega)^2} \quad (14)$$

$$C_2 = \frac{4608 + 576\omega/5 + 2\omega^2 + \omega^3/42}{(48 + \omega)^2} \quad (15)$$

$$C_q = \frac{\omega^2}{210(48 + \omega)^2} \quad (16)$$

and to

$$M_{\alpha 2} = \frac{\partial U}{\partial \theta_{\alpha 2}} = \frac{EI_\alpha}{L} (C_1 \theta_{\alpha 1} + C_2 \theta_{\alpha 2} - C_q \bar{M}_0), \quad (17)$$

in which  $(\cdot)_\alpha = (\cdot)_y$  or  $(\cdot)_z$  as appropriate. Eq. 12 also leads to

$$P = P_1 - P_2 = \frac{\partial U}{\partial e} + \frac{\partial U}{\partial \omega} \cdot \frac{\partial \omega}{\partial e} \quad (18)$$

$$= EA \left[ \frac{e}{L} + \sum_{\alpha=y,z} (C_b + b_{q1}(\theta_{\alpha1} - \theta_{\alpha2})\bar{M}_0 + b_{q2}\bar{M}_0^2) \right]$$

in which  $e = u = u_1 - u_2$ ,  $P_i$  is the axial load at  $i$ -th node and

$$C_b = b_1(\theta_{\alpha1} + \theta_{\alpha2})^2 + b_2(\theta_{\alpha1} - \theta_{\alpha2})^2 \quad (19)$$

$$b_1 = \frac{6(48)^2/5 + 18(48)\omega/5 + 126\omega^2/35 + \omega^3/40}{(48 + \omega)^3} \quad (20)$$

$$b_2 = \frac{2(48)^2 + 14(48)\omega/5 + 66\omega^2/35 + 11\omega^3/840}{(48 + \omega)^3} \quad (21)$$

$$b_{q1} = \frac{16\omega}{35(48 + \omega)^3} \quad (22)$$

$$b_{q2} = -\frac{12/35 + \omega/105}{(48 + \omega)^3}. \quad (23)$$

It can be seen the internal strain energy  $U$  is load-dependent, so that coupling of the external element load and the element deformations is inherent in the present non-linear stiffness formulation of Eqs. 13 to 18.

Again, it is noteworthy that despite there being a vast range of possible element loading pattern, the line integration with respect to  $x$  in Eq. 11 is essentially unchanged against a plethora of transverse element loads, because the use of principle of superposition prior to non-linear procedures separates the element load effect from deformations along an element  $N_q$ . As a result, the element load effect merely depends on the magnitude of the term  $\bar{M}_0$  associated with the particular loading pattern, as given in Appendix 1. This salient feature provides a crucial insight into the generalized stiffness matrix of an element for a member regardless of a diverse element load cases instead of the magnitude of the term  $\bar{M}_0$  being formulated in the non-linear stiffness formulation. The nonlinearity of element load effect can be traced through the magnitude of element load  $\bar{M}_0$  through incremental load factor  $\Delta\lambda_i$  in the nonlinear solution procedures. This feature avoids the need for tedious and numerous stiffness matrices under a plethora of general element loading patterns, leading to a simple, versatile and generalized stiffness formulation. The secant stiffness coefficients  $C_q$ ,  $b_{q1}$  and  $b_{q2}$  which account for the element loading therefore vary between different loading patterns by altering the magnitude  $\bar{M}_0$  only.

The coefficient  $C_q$  induces the second-order moment due to the coupling of both the lateral element loads and the axial loads, whereas  $b_{q1}$  and  $b_{q2}$  quantify the axial force effect from this coupling. However, when there is no axial force and so  $\omega = 0$ ,  $b_{q1}$  and  $b_{q2}$  are 0 and  $-12/3,870,720 \approx -3.1 \times 10^{-6}$  respectively. The last term  $b_{q2}\bar{M}_0^2$  may still be of certain contribution to axial resistance  $P$  due to

element load that in turn represents elongation caused by element load because of the squaring of  $\overline{M}_0$ . It should be emphasized that in most previous research on non-linear analysis, the coupling effect between the lateral load and the element stiffness has been neglected in non-linear finite element formulations.

The large deformations and the inclusion of the axial force parameter  $\omega$  into the element formulation herald a potential situation for which convergence may be somewhat difficult. In addition, the member axial force term  $\omega$  involves the bowing functions  $b_1$  and  $b_2$ , which in turn are functions of  $\omega$ . Hence, Eq. 18 can be written in the form

$$\Omega(\omega) = \frac{\omega I}{AL^2} - \frac{e}{L} - \sum_{\alpha=y,z} \left[ b_1(\theta_{\alpha 1} + \theta_{\alpha 2})^2 + b_2(\theta_{\alpha 1} - \theta_{\alpha 2})^2 + b_{q1}(\theta_{\alpha 1} - \theta_{\alpha 2})\overline{M}_0 + b_{q2}\overline{M}_0^2 \right] \quad (24)$$

in which  $\omega$  is the only unknown. The iterative procedure for which an equilibrium condition is sought, as also mentioned by Chan and Zhou [3] and Kassimali [11], proceeds by letting  $\omega_i$  be an approximate solution of this equation  $\Omega(\omega)$ , which can measure the equilibrium condition within the element formulation. The first order Taylor expansion of this equation  $\Omega(\omega)$  is

$$\Omega(\omega_i + \Delta\omega_i) = \Omega(\omega_i) + \Omega'(\omega_i)\Delta\omega_i, \quad (25)$$

in which  $(\cdot)' = d(\cdot)/d\omega$ . Further, from Eq. 24

$$\Omega'(\omega) = H = \frac{I}{AL^2} - \sum_{\alpha=y,z} \left[ b'_1(\theta_{\alpha 1} + \theta_{\alpha 2})^2 + b'_2(\theta_{\alpha 1} - \theta_{\alpha 2})^2 + b'_{q1}(\theta_{\alpha 1} - \theta_{\alpha 2})\overline{M}_0 + b'_{q2}\overline{M}_0^2 \right] \quad (26)$$

in which the expression for  $H$  also forms a part of the stiffness coefficients in the tangent stiffness matrix given subsequently, and also  $H$ ,  $b'_{q1}$  and  $b'_{q2}$  are also given in Appendix 2. It is interesting to note that the bowing function  $b_1$  is stationary with respect to  $\omega$ . An updated value of  $\omega$  is thus obtained from

$$\omega_{i+1} = \omega_i + \Delta\omega_i = \omega_i - \frac{\Omega(\omega_i)}{H}. \quad (27)$$

The tangent stiffness matrix is obtained by taking the second derivative of the total potential functional in Eq. 11 with respect to the variables  $\mathbf{u}_k$  and axial load parameter  $\omega$ . When the work done  $V$  is linear, this differentiation results in

$$\mathbf{K}_t = \frac{\partial^2 \Pi}{\partial \mathbf{u}_j \partial \mathbf{u}_k} = \frac{\partial}{\partial \mathbf{u}_j} \left( \frac{\partial U}{\partial \mathbf{u}_k} \right) + \frac{\partial}{\partial \mathbf{u}_k} \left( \frac{\partial U}{\partial \omega} \cdot \frac{\partial \omega}{\partial \mathbf{u}_j} \right). \quad (28)$$

The tangent stiffness matrix of the beam-column element incorporating the response of the element load derived in this way is

$$\mathbf{K}_t = \frac{EI}{L} \begin{bmatrix} \frac{1}{L^2 H} & \frac{G_{y1}}{LH} & \frac{G_{z1}}{LH} & 0 & \frac{G_{y2}}{LH} & \frac{G_{z2}}{LH} \\ \xi_y \left( C_1 + \frac{G_{y1}^2}{H} \right) & \frac{G_{y1} G_{z1}}{H} & 0 & \xi_y \left( C_2 + \frac{G_{y1} G_{y2}}{H} \right) & \frac{G_{y1} G_{z2}}{H} \\ \xi_z \left( C_1 + \frac{G_{z1}^2}{H} \right) & 0 & \frac{G_{z1} G_{y2}}{H} & \xi_z \left( C_2 + \frac{G_{z1} G_{z2}}{H} \right) \\ \text{symmetric} & \eta & 0 & 0 \\ \xi_y \left( C_1 + \frac{G_{y2}^2}{H} \right) & \frac{G_{y2} G_{z2}}{H} \\ \xi_z \left( C_1 + \frac{G_{z2}^2}{H} \right) \end{bmatrix} \quad (29)$$

in which  $\eta$  is torsional rigidity of  $(GJ+Pr^2)/EI$  and it relates the incremental deformation to the corresponding external loads applied to an element in the member coordinates, in which  $K_{ij}$ ,  $G_{\alpha i}$  and  $H$  are given in Appendix 2,  $I$  is the relevant second moment of area about which bowing is considered and  $\xi_\alpha = I_\alpha/I$  ( $\alpha = y$  or  $z$ ).

The tangent stiffness matrix needed for assembly and transformations in global coordinates  $\mathbf{K}_T$  is

$$\mathbf{K}_T = \sum_{\text{elements}} \mathbf{L} \mathbf{K}_e \mathbf{L}^T = \sum_{\text{elements}} \mathbf{L} (\mathbf{T}^T \mathbf{K}_t \mathbf{T} + \mathbf{M}_\sigma) \mathbf{L}^T, \quad (30)$$

in which  $\mathbf{T}$  is the transformation matrix relating the member forces to the element forces in local coordinates,  $\mathbf{L}$  is the transformation matrix from the local coordinates to the global coordinates and  $\mathbf{M}_\sigma$  is a stability matrix to allow for the work done by rigid body motions or the change of geometry of the structures as also shown in [12]. Because of the nature of the non-linearity in Eq. 11, an incremental-iterative solution procedure is needed to trace the non-linear equilibrium path, including the non-linearity due to transverse element load effect.

## 5. ILLUSTRATION OF ELEMENT LOAD EFFECT

Figure 2 illustrates the theoretical principle of load lumping numerical procedures using the conventional finite element. A transverse element point load  $\Delta Q$  is firstly applied at mid-span at a node between two elements, as in Figure 2(a). The deflection of the beam is such that its load-deflection response satisfies the tangent stiffness relationship; there is no axial deformation at the support as indicated in Figure 2(b) because there is no axial component initially in the tangent stiffness in the context of the conventional finite element method. In Figure 2(c), the secant stiffness determines the member resistance in accordance with the deformations of the finite elements (transverse deflections only); the axial force  $P$  results from the extension of the element due to deflection alone which attempts to balance the external point load  $\Delta Q$  by its vertical component due to the slightly deflected geometry; and thereby the unbalanced axial force appears in the next iteration. In the second iteration in Figure 2(d), the axial deformation  $e$  (longitudinal movement) at the roller end is computed from the tangent stiffness relationship corresponding to the unbalanced axial force  $P$  component. In Figure 2(e), the unbalanced axial force from the first iteration caused by the axial member force  $P$  is cancelled by axial resistance from the secant stiffness relationship in accordance with the axial deformation  $e$ ; equilibrium is achieved only if the convergence criterion is satisfied. In summary, the conventional finite element using lumping load method requires at least two elements and iterations to achieve equilibrium for this simple

beam so as to include the element load response. Equilibrium can only be achieved through global system analysis, and so the element load response is solved at the global level using the conventional finite element method.

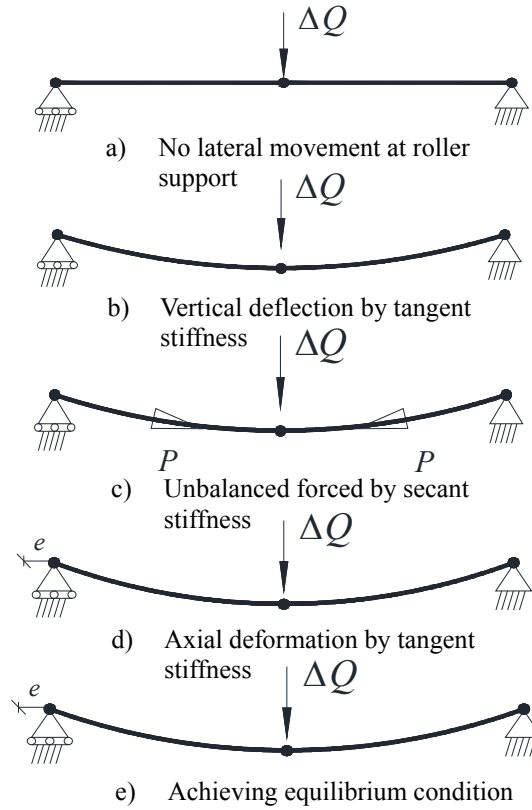


Figure 2. Numerical Procedures using the Conventional Finite Element Method

According to the present element load approach, once the transverse element point load  $\Delta Q$  is applied at the mid-span of the single element used to model a simply-supported beam (Figure 3(a)), the axial deformation  $e$  is computed from the tangent stiffness equation (Figure 3(b)). Despite there being no axial external load or unbalanced force component at the first iteration, the terms involving the coupling between the rotations  $\theta$  and the axial deformation  $e$  in the tangent stiffness matrix  $\mathbf{K}_T$  in Eq. 29 allow for the axial deformations of the element to be computed according to vertical component of point load  $\Delta Q$ . Subsequently, the axial member force  $P$  (Figure 3(c)) in Eq. 18 is self-equilibrated which is determined from the secant stiffness formulation  $\mathbf{K}_S$  in Eqs. 13 to 18 and which encompasses the axial effect through  $e/L$ , the flexural effect through  $\theta$  as well as the element load effect through  $\bar{M}_0$  and thereby maintains equilibrium at the element level; hence no unbalanced force is induced for the next iteration. Therefore, one iteration is theoretically adequate to achieve equilibrium for this simple beam subjected to element load, and it leads to efficient numerical convergence.

For simply speaking, the conventional finite element method accounting for the element load effect is reliant of the system analysis, whereas the present approach for the element load effect resorts to the sophisticated element stiffness formulation within element level, into which the element load in terms of  $\bar{M}_0$  is incorporated.

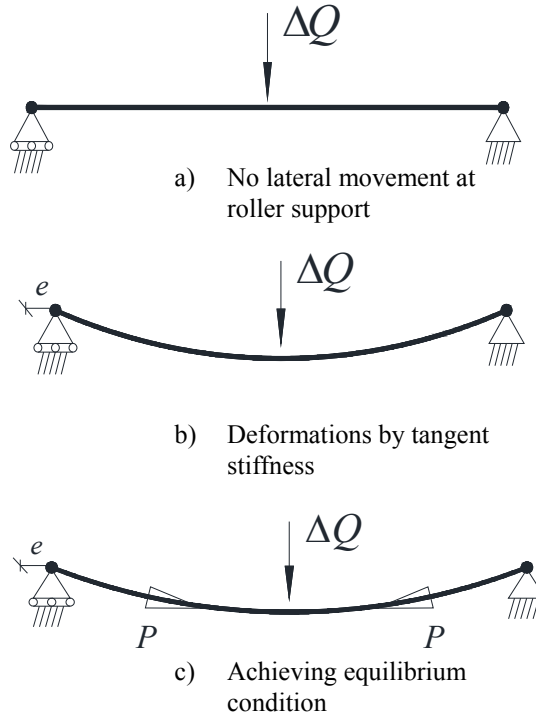


Figure 3. Numerical Procedures using the Present Approach

## 6. NUMERICAL VERIFICATIONS

This section firstly validates the displacement function for an element, for which the deflections obtained with the first-order effects of transverse load are compared with exact analytical results from the linear elastic method. A simple beam subjected to various regimes of transverse load using second-order analysis with or without axial load is then investigated. Following this, two small-scale elastic framed structures are investigated using the second-order procedure; one is a right-angled frame and the other a two-storey frame under uniform loading in which P-Δ effects take place. In these validation studies, a single element is used for each member of the framed structures in order to study the element solution.

### 6.1 Deflections of a Prismatic Beam

#### 6.1.1 Propped cantilever subjected to a point load

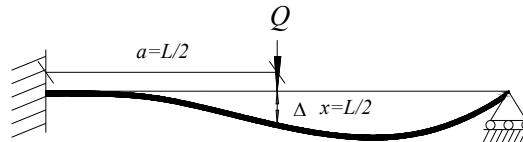


Figure 4. A propped Cantilever subjected to a Mid-span Point Load

Figure 4 shows a propped cantilever subjected to a concentrated load  $Q$  at mid-span, for which the theoretical mid-span deflection is  $\Delta = -(7/768)(QL^3/EI)$ , of which is derived from the linear elastic analytical method (e.g. unit load method).

Using the consistent load method with a cubic element, the consistent load with respect to a released freedom, as well as the corresponding rotation, is

$$\frac{4EI\theta_2}{L} = \frac{QL}{8}; \quad \theta_2 = \frac{QL^2}{32EI}, \quad (31)$$

and using

$$v = \left(1 - \frac{3x^2}{L^2} + \frac{2x^3}{L^3}\right)v_1 + \left(x - \frac{2x^2}{L} + \frac{x^3}{L^2}\right)\theta_1 + \left(\frac{3x^2}{L^2} - \frac{2x^3}{L^3}\right)v_2 + \left(-\frac{x^2}{L} + \frac{x^3}{L^2}\right)\theta_2 \quad (32)$$

at  $x = L/2$  produces

$$v|_{x=L/2} = \frac{QL^2}{32EI} \left(-\frac{L}{8}\right) = -\frac{QL^3}{256EI}, \quad (33)$$

which is 57% different from the exact result. Using the higher-order element of this paper with the element load, when the axial force parameter  $\omega = 0$ , the functions  $N_1$  and  $N_2$  in Eqs. 5 and 6 are the same as those of a cubic element. The function  $N_q$  can calibrate its element solution due to element load from cubic element, and using Eqs. 52 or 53 in  $N_q$  (Appendix 1). Eq. 5 produces

$$v|_{x=L/2} = -\frac{QL^3}{256EI} - \frac{(4QL^2/EI)L}{48} \left[ \left(\frac{1}{2}\right)^2 - 2\left(\frac{1}{2}\right)^3 + \left(\frac{1}{2}\right)^4 \right] = -\frac{7QL^3}{768EI}, \quad (34)$$

which is the same as the exact result. It can therefore be seen that the higher-order element load component  $N_q$  produces the exact solution, but using a cubic interpolation polynomial yield an answer that differs 57% from the exact one.

### 6.1.2. Simply supported beam subject to a point load

Figure 5 shows a beam subjected to a concentrated load at either a third point or at mid-span. For a load at mid-span (Figure 5(a)), the theoretical deflection is  $\Delta = -(1/48)(QL^3/EI)$ . The consistent load and nodal end rotations are obtained from

$$\frac{EI}{L} \begin{bmatrix} 4 & 2 \\ 2 & 4 \end{bmatrix} \begin{Bmatrix} \theta_1 \\ \theta_2 \end{Bmatrix} = \begin{Bmatrix} -QL/8 \\ QL/8 \end{Bmatrix}; \quad \begin{Bmatrix} \theta_1 \\ \theta_2 \end{Bmatrix} = \begin{Bmatrix} -3QL^2/48EI \\ 3QL^2/48EI \end{Bmatrix} \quad (35)$$

and using a cubic element, Eq. 32 produces

$$v|_{x=L/2} = -\frac{3QL^2}{48EI} \left(\frac{L}{8}\right) + \frac{3QL^2}{48EI} \left(-\frac{L}{8}\right) = -\frac{QL^3}{64EI}, \quad (36)$$

which is 25% different from the correct result. However, using Eqs. 52 or 53 in  $N_q$  (Appendix 1). Eq. 5 produces

$$v|_{x=L/2} = -\frac{QL^3}{64EI} - \frac{(4QL^2/EI)L}{48} \left[ \left(\frac{1}{2}\right)^2 - 2\left(\frac{1}{2}\right)^3 + \left(\frac{1}{2}\right)^4 \right] = -\frac{QL^3}{48EI}, \quad (37)$$



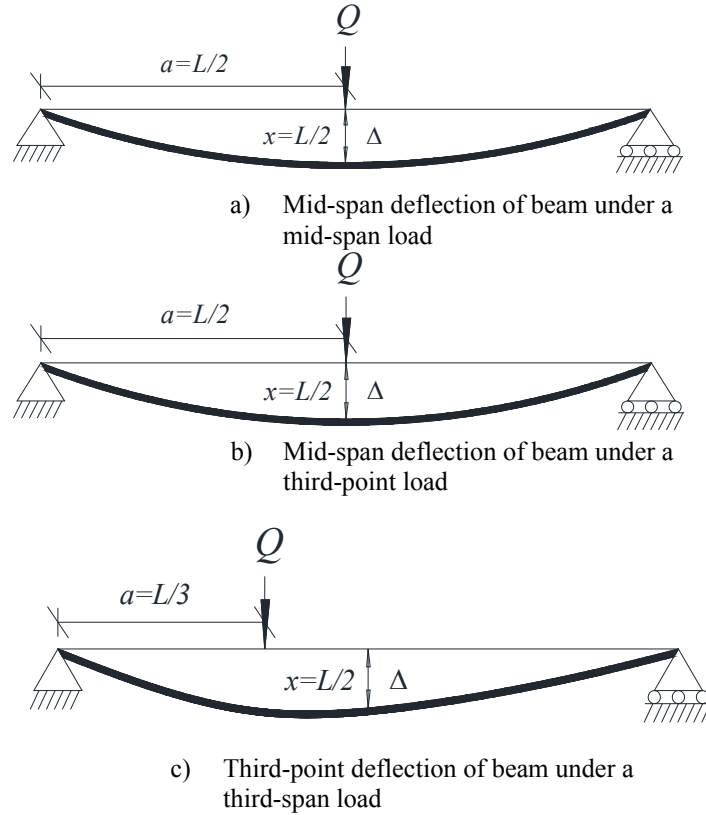


Figure 5. Simply-supported Beam subjected to a Point Load at Different Locations

which is the same as the theoretical result. For a third-point load (Figure 5(b)), the consistent load and nodal end rotations are obtained from

$$\frac{EI}{L} \begin{bmatrix} 4 & 2 \\ 2 & 4 \end{bmatrix} \begin{Bmatrix} \theta_1 \\ \theta_2 \end{Bmatrix} = \begin{Bmatrix} -4QL/27 \\ 2QL/27 \end{Bmatrix}; \quad \begin{Bmatrix} \theta_1 \\ \theta_2 \end{Bmatrix} = \begin{Bmatrix} -5QL^2/81EI \\ 4QL^2/81EI \end{Bmatrix} \quad (38)$$

and so for the consistent load method using a cubic element (Eq. 32)

$$v|_{x=L/2} = -\frac{5QL^2}{81EI} \left( \frac{L}{8} \right) + \frac{4QL^2}{81EI} \left( -\frac{L}{8} \right) = -\frac{QL^3}{72EI}, \quad (39)$$

which differs by 22% from the exact result  $\Delta = -(23/1296)(QL^3/EI)$ . Using the present element load method with a higher-order element, it is not necessary to derive a new displacement function, but instead using  $a = L/3$  in Eq. 52 in Appendix 1 gives  $\bar{M}_0 = 8QL^2/3EI$  and so, from Eq. 5

$$v|_{x=L/2} = -\frac{QL^3}{72EI} - \frac{(8QL^2/3EI)L}{48} \left[ \left( \frac{1}{2} \right)^2 - 2 \left( \frac{1}{2} \right)^3 + \left( \frac{1}{2} \right)^4 \right] = -\frac{22.5QL^3}{1296EI}, \quad (40)$$

which is only 2% less than the exact solution and clearly much closer than the cubic displacement function. For third-point loading (Figure 5 (c)), the third-point deflection using a cubic element (with Eq. 38 for the rotations) is

$$v|_{x=L/3} = -\frac{5QL^2}{81EI} \left( \frac{4L}{27} \right) + \frac{4QL^2}{81EI} \left( -\frac{2L}{27} \right) = -\frac{28QL^3}{2187EI}, \quad (41)$$

which is 22% different from the exact result  $\Delta = -(36/2187)(QL^3/EI)$ . For the higher-order element with the element load effect,  $\bar{M}_0$  is the same but the new location  $x = L/3$  is used for  $N_q$ , giving

$$v|_{x=L/3} = -\frac{28QL^3}{2187EI} - \frac{(8QL^2/3EI)L}{48} \left[ \left( \frac{1}{3} \right)^2 - 2 \left( \frac{1}{3} \right)^3 + \left( \frac{1}{3} \right)^4 \right] = -\frac{34QL^3}{2187EI}, \quad (42)$$

which is 5.6% different from the exact result.

### 6.1.3. Simply supported beam with trapezoidal loading

A simply supported beam with distributed loading in two trapezoidal patterns is shown in Figure 6; this example being chosen to demonstrate the use of superposition. For the case in Figure 6(a) where the trapezoidal loading is rectangular, the consistent load and nodal rotations are

$$\frac{EI}{L} \begin{bmatrix} 4 & 2 \\ 2 & 4 \end{bmatrix} \begin{Bmatrix} \theta_1 \\ \theta_2 \end{Bmatrix} = \begin{Bmatrix} -13qL^2/324 \\ 13qL^2/324 \end{Bmatrix}; \quad \begin{Bmatrix} \theta_1 \\ \theta_2 \end{Bmatrix} = \begin{Bmatrix} -13qL^3/648EI \\ 13qL^3/648EI \end{Bmatrix} \quad (43)$$

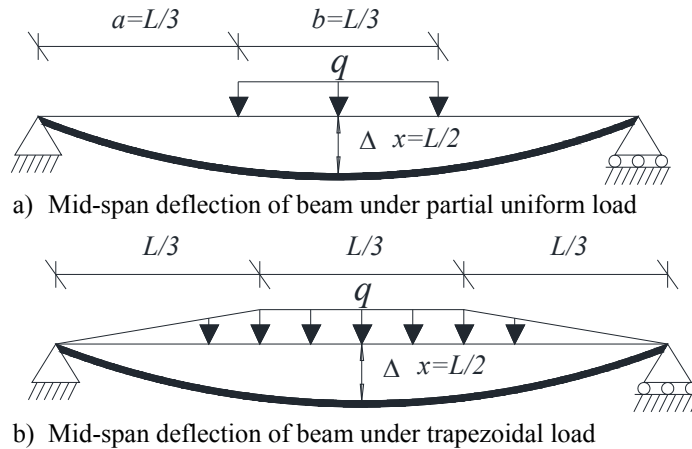


Figure 6. Simply-supported Beam subjected to various Trapezoidal Loads

and so the mid-span deflection using a cubic element is

$$v|_{x=L/2} = -\frac{13qL^3}{648EI} \left( \frac{L}{8} \right) + \frac{13qL^3}{648EI} \left( -\frac{L}{8} \right) = -\frac{13qL^4}{2592EI}, \quad (44)$$

which is 24% different from the exact result  $\Delta = -(205/31,104)(qL^4/EI)$ . The equivalent mid-span moment of Eq. 58 in Appendix 1 when  $a = L/3$  and  $b = 2L/3$  is  $\bar{M}_0 = 10qL^3/9EI$ , producing

$$v|_{x=L/2} = -\frac{13qL^4}{2592EI} - \frac{(10qL^3/9EI)L}{48} \left[ \left(\frac{1}{2}\right)^2 - 2\left(\frac{1}{2}\right)^3 + \left(\frac{1}{2}\right)^4 \right] = -\frac{201qL^4}{31,104EI}, \quad (45)$$

for the higher-order element, which is within 1.95% of the exact result. A typical floor loading pattern is obtained by adding two triangular distributed loading portions to the uniform distribution in Figure 6(a), to produce the pattern in Figure 6(b). For this, the consistent load and associated end rotations are

$$\frac{EI}{L} \begin{bmatrix} 4 & 2 \\ 2 & 4 \end{bmatrix} \begin{Bmatrix} \theta_1 \\ \theta_2 \end{Bmatrix} = \begin{Bmatrix} -11qL^2/162 \\ 11qL^2/162 \end{Bmatrix}; \quad \begin{Bmatrix} \theta_1 \\ \theta_2 \end{Bmatrix} = \begin{Bmatrix} -11qL^3/324EI \\ 11qL^3/324EI \end{Bmatrix} \quad (46)$$

for which the mid-span deflection using a cubic element is

$$v|_{x=L/2} = -\frac{11qL^3}{324EI} \left(\frac{L}{8}\right) + \frac{11qL^3}{324EI} \left(-\frac{L}{8}\right) = -\frac{11qL^4}{1296EI}, \quad (47)$$

which is 22% different from the exact result  $\Delta = -(1681/155,520)(qL^4/EI)$ . On the other hand, the value of  $\bar{M}_0$  for the higher-order element can be obtained by adding Eqs. 58, 63 and 68 in Appendix 1, giving

$$\bar{M}_0 = \frac{8qL^3}{27EI} + \frac{10qL^3}{9EI} + \frac{8qL^3}{27EI} = \frac{46qL^3}{27EI}; \quad (48)$$

And Eq. 5 produces

$$v|_{x=L/2} = -\frac{11qL^4}{1296EI} - \frac{(46qL^3/27EI)L}{(48+q)} \left[ \left(\frac{1}{2}\right)^2 - 2\left(\frac{1}{2}\right)^3 + \left(\frac{1}{2}\right)^4 \right] = -\frac{1665qL^4}{155,520EI}, \quad (49)$$

which is within 0.95% of the exact result.

In conclusion, the present higher-order element can improve the accuracy of first-order element solution in terms of deflection subjected to the diverse kind of loading patterns remarkably compared to the cubic element. Further, the solutions at other locations seem to be as somewhat less accurate as the solution at mid-span, but these solutions are still regarded as a good agreement with the exact solutions.

## 6.2 Numerical Results for Beam-column Deflections with Varied Locations

The previous study indicated the accuracy and versatility for an elastic beam under a variety of element loading regimes, whose behaviour is first-order. The present example illustrates the deflections with varied locations of a beam-column element under different element loads with and without second-order effects considered. The profound implication of this example is to extend the capability of element solution to the higher degree of accuracy in the field of displacement with recourse to the present analysis with element load effect. On the contrary, one conventional cubic element by virtue of the consistent load method is deficient at evaluating the element solution. Actually, the consistent load method is incapable of predicting the second-order element solution when regardless of equilibrium condition in the assumed finite element function. To this end, this

example is targeted for demonstration of the present element load method that is valid for the second-order element solution using only one element.

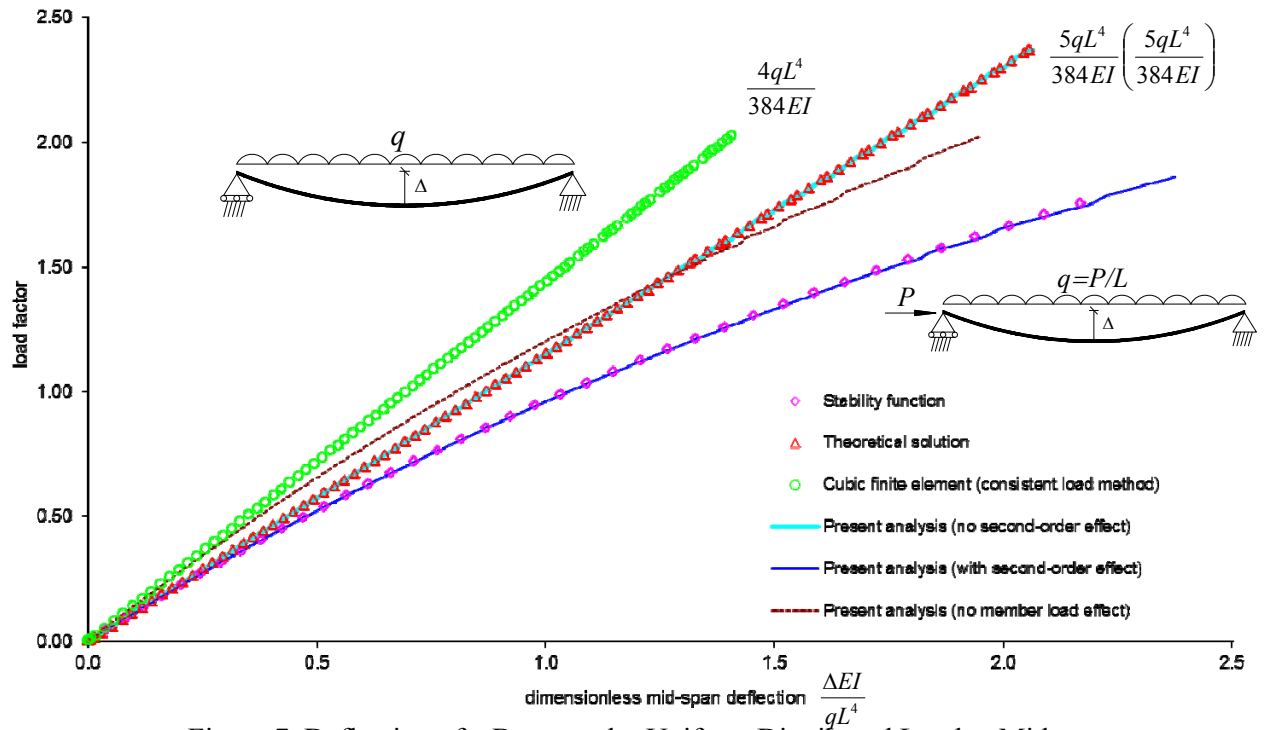


Figure 7. Deflection of a Beam under Uniform Distributed Load at Mid-span

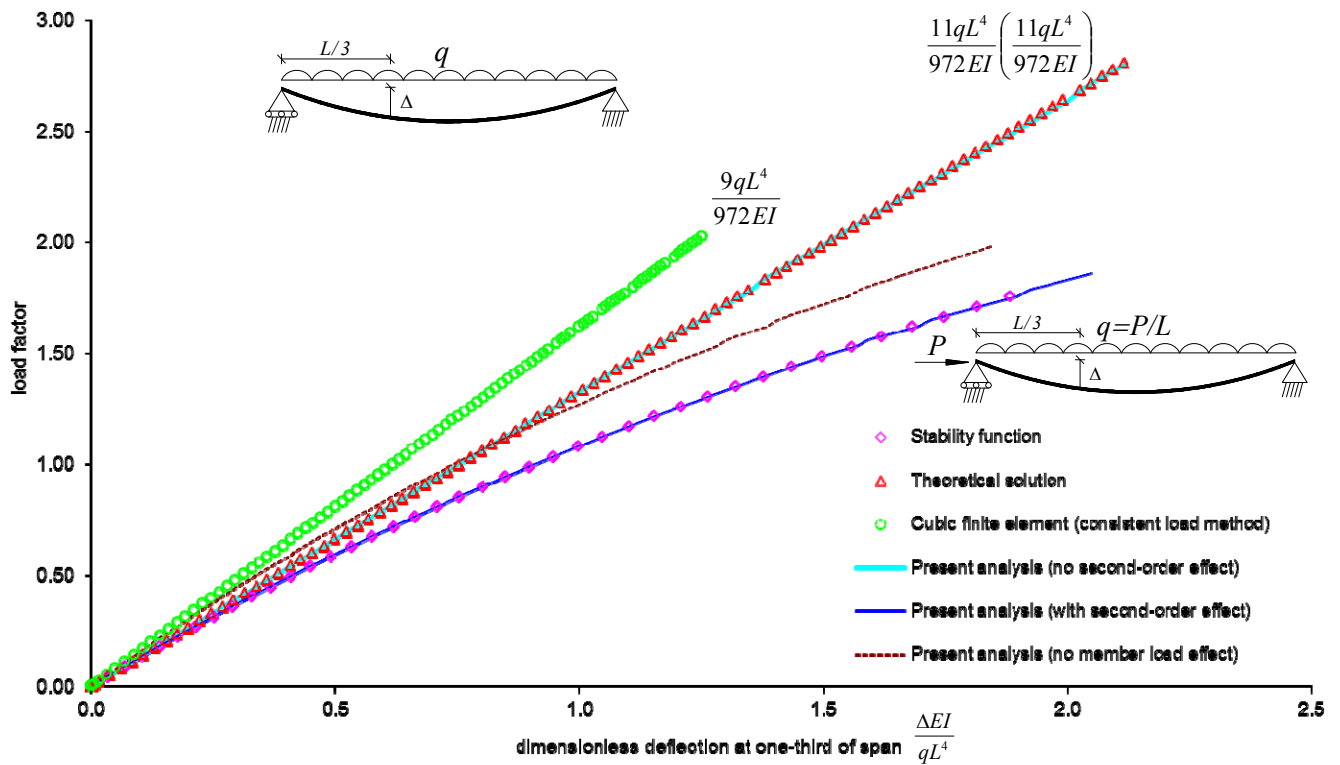


Figure 8. Deflection of a Beam under Uniform Distributed Load at One-third of Span

Figures 7 and 8 show a simply supported beam subjected to a uniformly distributed load  $q$  ( $5kN/m$ ), and they respectively plot the normalised beam deflection at mid-span and one-third of span  $EI\Delta/qL^4$  against the load factor  $\lambda$  whose incremental value complies with various load method. The proposed method is able to produce numerically the accurate deflections at mid-span and one-third of span as depicted in Figures 7 and 8, respectively, whose values are plotted in the figures inside the parenthesis correspondingly, in which the values from cubic element and exact solution from simple beam theory (first-order) are also indicated. On the other hand, one cubic element using consistent load is unable to replicate the first-order theoretical solution as shown in Figures 7 and 8. In regard to second-order element solution, the present element load method is able to predict the same deflection solution as obtained using the stability functions (second-order), in which coupling between the transverse element load and axial compression is incorporated.

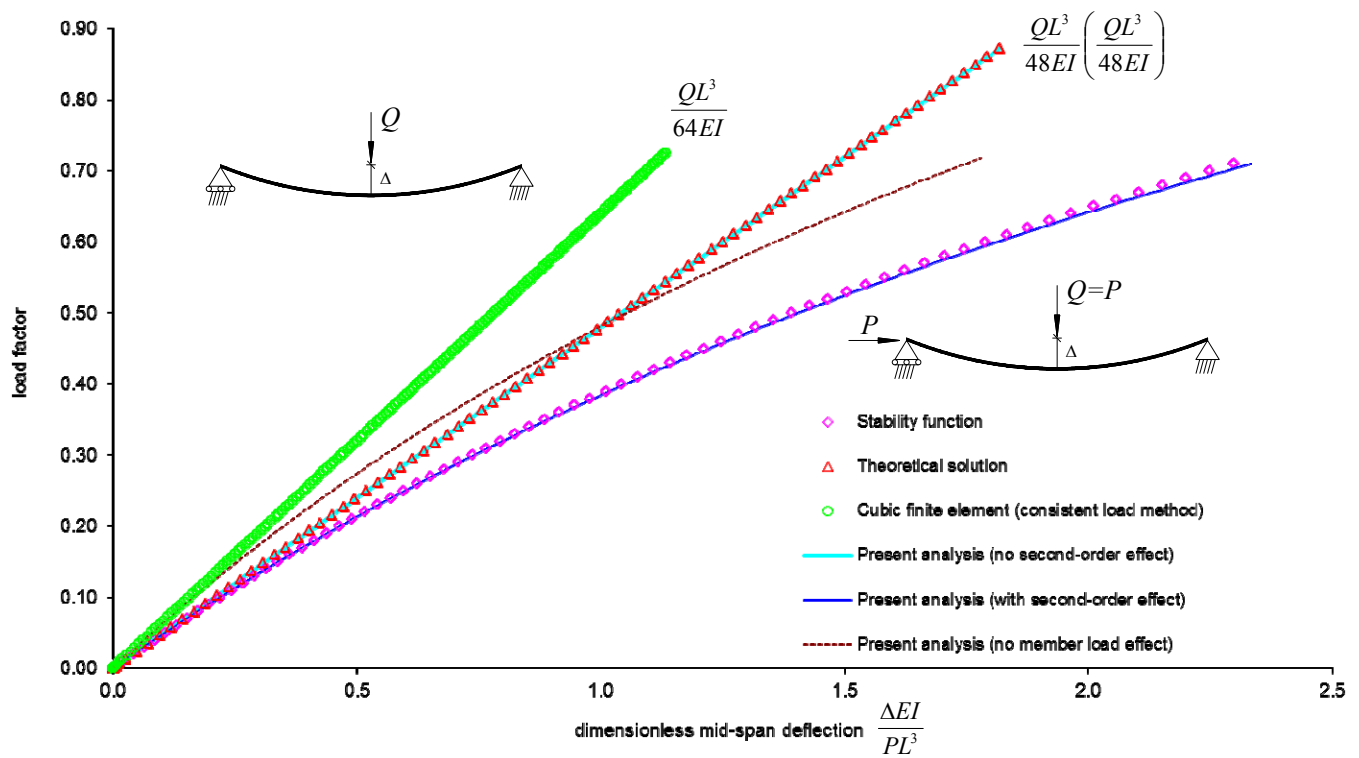


Figure 9. Deflection of a Beam under a Single Point Load at Mid-span

A counterpart analysis with a concentrated load  $Q$  ( $10kN$ ) at mid-span and one-third of span is presented in Figures 9 and 10, respectively, with the normalised beam deflection  $EI\Delta/QL^3$  plotted against the load factor  $\lambda$ . Similarly, the disparity between cubic element with the consistent load method and theoretical solution are notably present, as indicated in Figures 9 and 10. Their disparity of first-order mid-span deflection is exactly 25% as also stated in the Section 6.1.2. On the contrary, the first-order deflections at mid-span and one-third of span from the present analysis, which display inside parenthesis in Figures 9 and 10, respectively, are both close to the exact solutions.

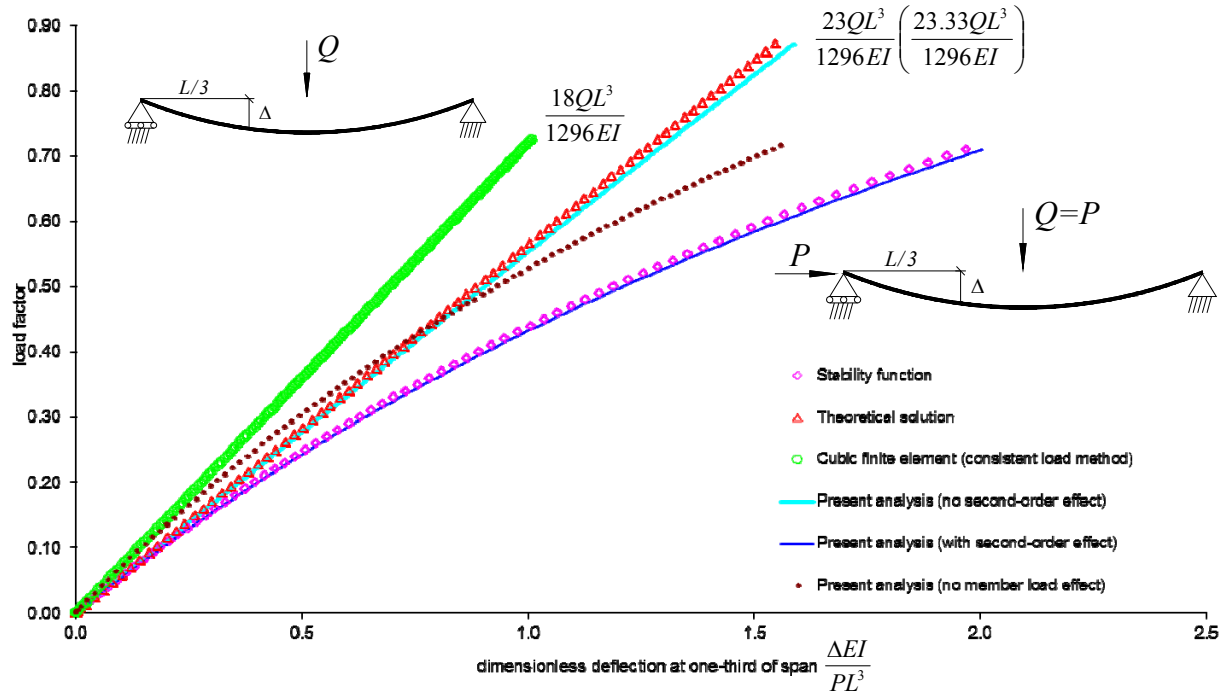


Figure 10. Deflection of a Beam under a Single Point Load at One-third of Span

A beam with two point loads  $Q$  ( $10kN$ ) located at quarter points is shown in Figures 11 and 12 for the load-deflection solution at mid-span and a quarter of span in order to demonstrate the principle of superposition adopted in the numerical formulation. The normalised deflections  $EI\Delta/QL^3$  at mid-span and a quarter of span against load factor  $\lambda$  from present analysis is respectively plotted in the Figures 11 and 12 are shown to be in good agreement with the exact solution for first-order analysis except the cubic element using consistent load method. Their first-order deflections from the present analysis are shown inside the parenthesis in the corresponding figures. The axial force introduces second-order behaviour into the element solution, and its solution is the same as that determined from the stability functions. Therefore, the present approach with the element load effect can successfully demonstrate its accuracy of the first-order element load effect as well as second-order coupling effect.

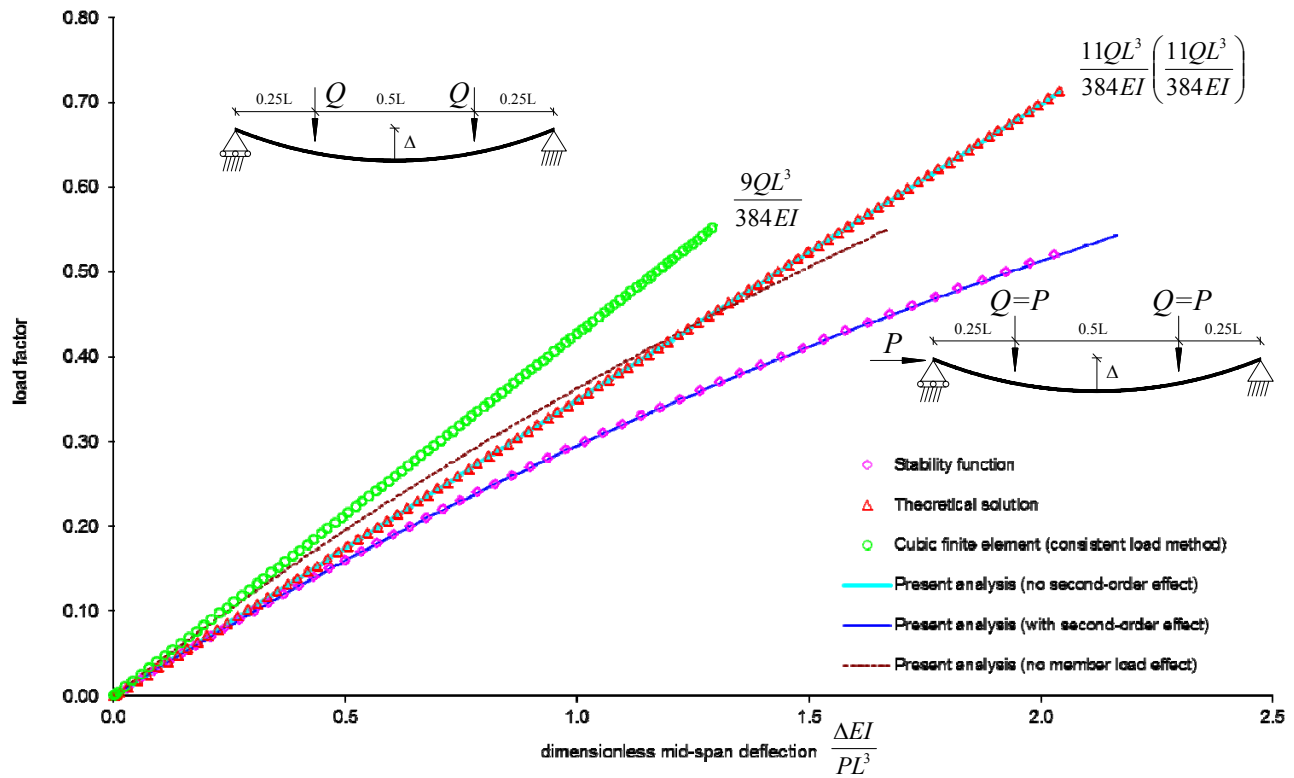


Figure11. Deflection of a Beam under Two Point Loads at Mid-span

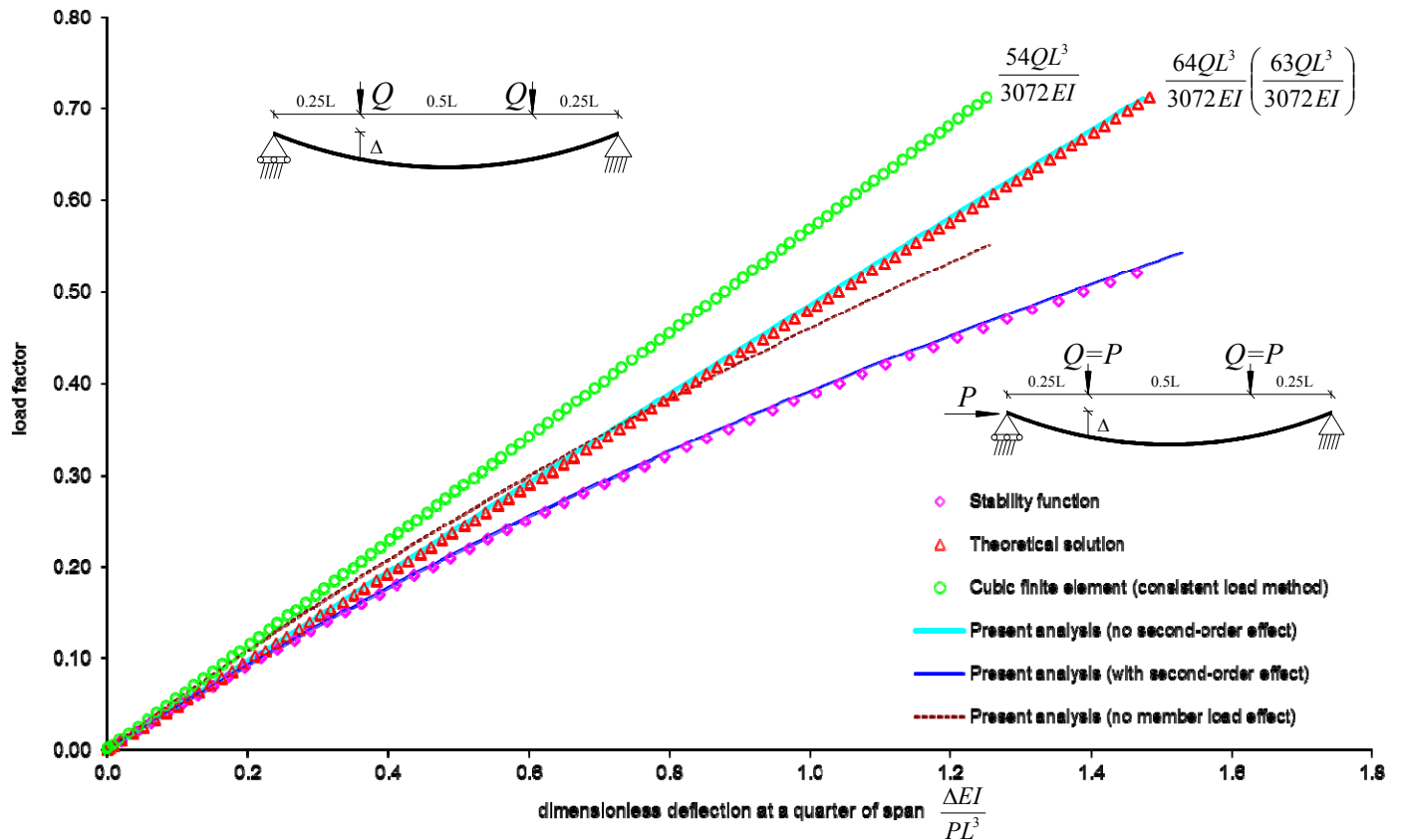


Figure12. Deflection of a Beam under Two Point Loads at a Quarter of Span

It should be remarked that, according to the present analysis with element load effect, the discrepancy between the deflections at mid-span and other locations are very insignificant as similarly demonstrated in the previous example that the first-order deflections were studied. It can be concluded that, despite the sacrifice of load distribution effect at other locations but mid-span, the present analysis with element load effect can still produce accurate element solution in terms of displacements along an entire element. Therefore, the present analysis with element load effect is very capable of analysing the whole element solution of either a bending beam or a typical buckling member.

Further, this example can demonstrate that a single present higher-order element function with element load effect can generalize and replace the plethora of stability functions with different element loads, in which the present element load method is same but changing the magnitude of the equivalent mid-span moment coefficient  $\bar{M}_0$  only in a robust manner. In summary, the stability functions with a plethora of element load scenarios can be transformed into a single present generalized element load method without loss of accuracy along an element itself.

### 6.3 Postbuckling of Right-angled Frame

Roorda [13] and Koiter [14] provided the first experimental and analytical results respectively for the right-angled frame shown in Figure 13, with the analytical formulation accounting for member bowing and for postbuckling. This structure was later studied by Argyris and Dunne [15] and Chan and Zhou [2]. The right-angled frame in Figure 13 with pin supports was analysed herein with a member point load  $P$  at an eccentricity of  $e = 254$  mm (10 inch), applied directly to the beam without resolving it as an eccentric moment and point loads at the element nodes. The cross-section, geometry and material properties of the frame are given in Figure 13, which also plots the joint rotation  $\theta$  against the dimensionless load  $P/P_E$ , where  $P_E$  is the Euler load. The proposed non-linear modelling using only one element produces results which are in close coincidence with those of Chan and Zhou [2], as well as approaching the postbuckling response of the perfect frame ( $e = 0$ ) given by Koiter. This example validates that the present approach is capable of accounting for the element load effect including member bowing and postbuckling of a simple framed structure in which load transformation is needed between member and global coordinates. It should be noted that the present analysis produces slightly larger joint rotations than those obtained by Iu and Bradford [6] which utilise lumped loading, as the axial load due to element load effect produced in the beam due to its restraint induces a further minor second-order element load effect.



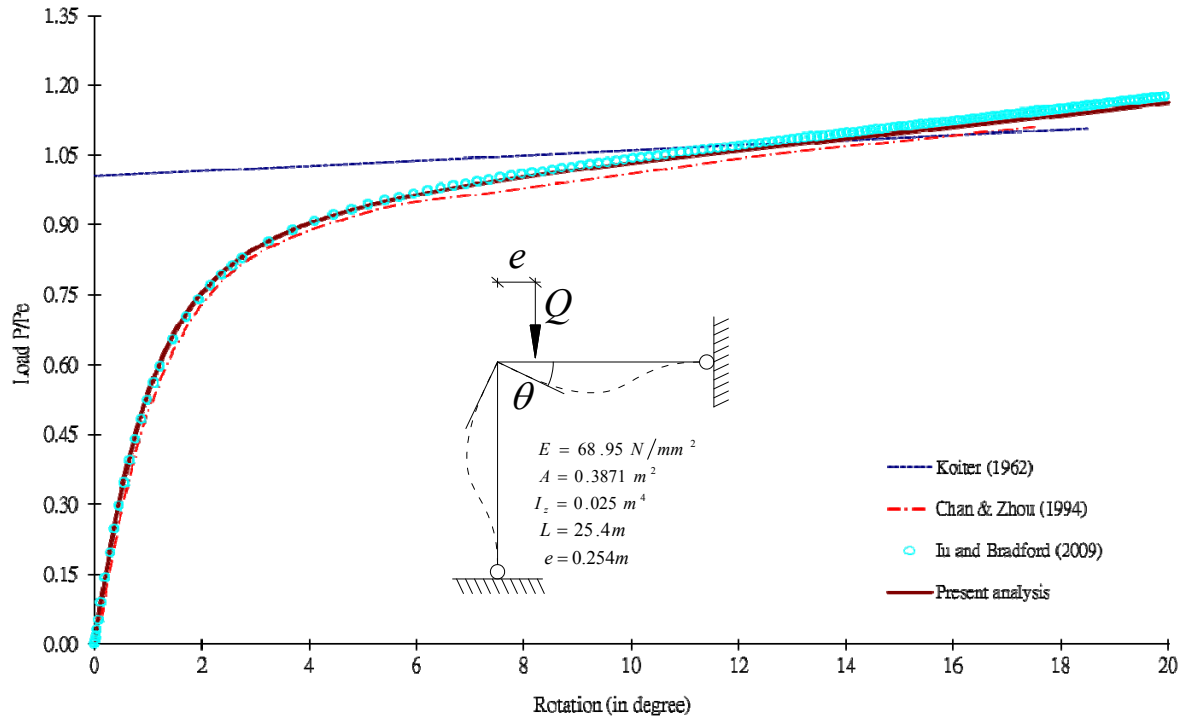


Figure 13. Load-deformation Response of Right-angle Frame

#### 6.4 Two-storey Rigid Sway Frame

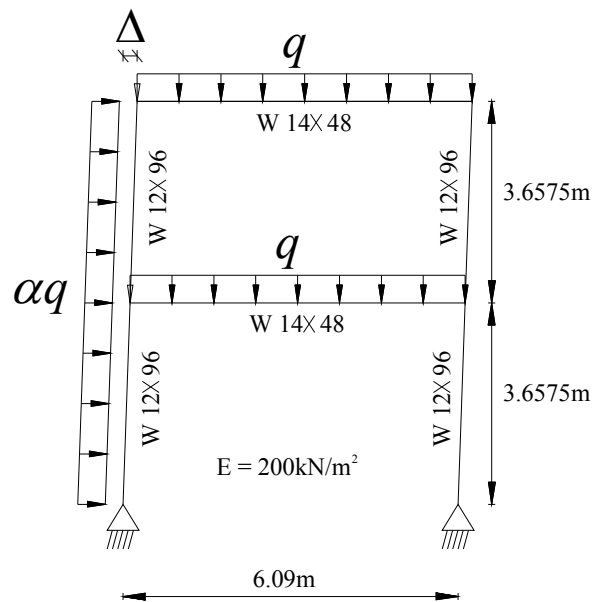


Figure 14. Geometry of Two-storey Building Frame

Applied forces in practical engineering frames such as wind load, imposed live load and dead load commonly act along the elements, and these loads contributed to sway effect in rigid frames [16]. The present element load method is important, therefore, to be able to use an element permitting element load effects in second-order frame analysis. The two-storey frame shown in Figure 14 has been studied; this frame was also analysed by Zhou and Chan [9] and its geometry, cross-sections and material properties are given in Figure 15. The frame is subjected to uniformly distributed gravity loading  $q$  on both beams and to a lateral (wind) loading  $\alpha q$ , where  $\alpha$  is taken as  $10^{-3}$ ,  $10^{-2}$  and  $10^{-1}$ .

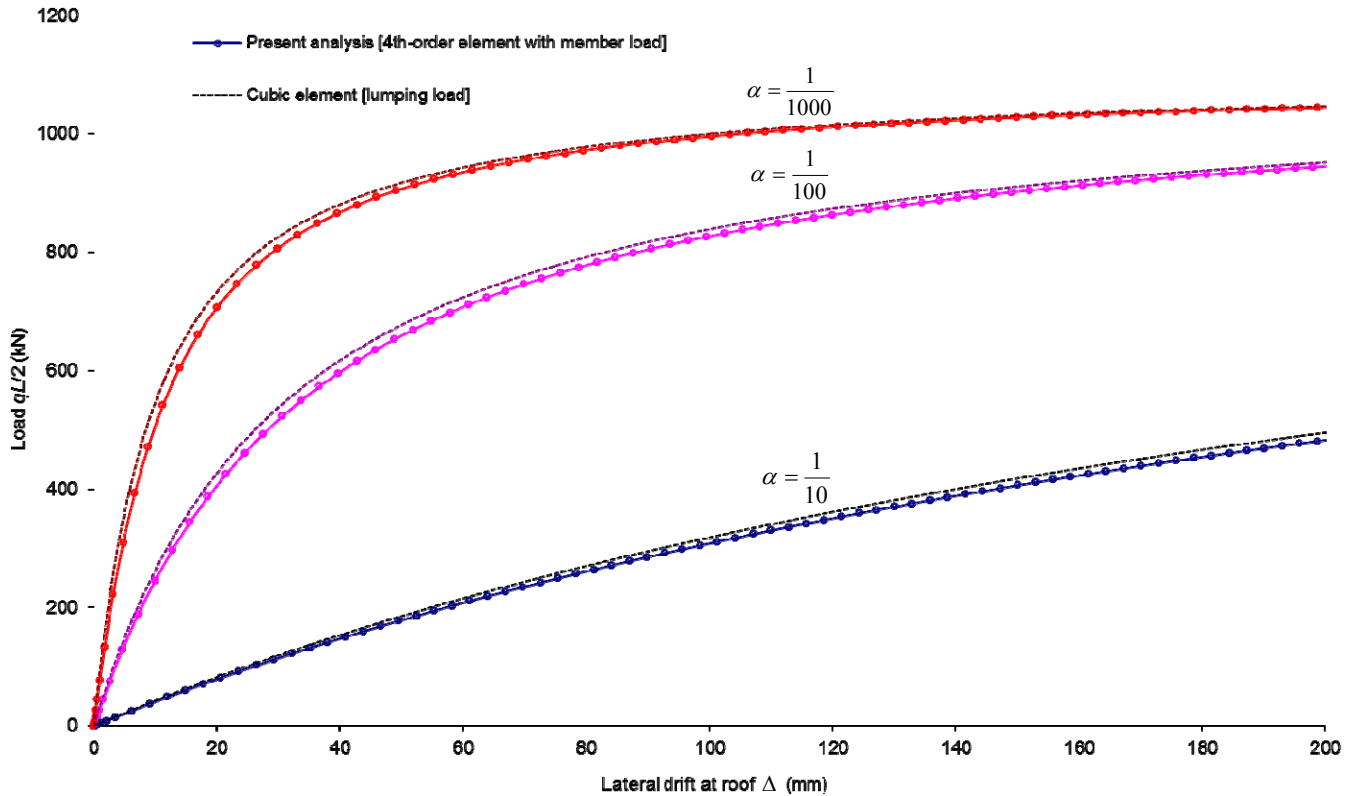


Figure 15. Lateral Drift  $\Delta$  and Load Factor Relationship for Two Storey Frame

Figure 15 shows the sway behaviour in terms of the lateral drift of the roof of the building, which is affected by both  $P-\delta$  and  $P-\Delta$  responses. The lateral force parameter  $\alpha$  has a large influence on the frame behaviour, with the structural responses being different for the three values of  $\alpha$  considered. It can be seen, however, that the discrepancies between the results using the lumped loads and the present element load approach for each value of  $\alpha$  are not overly large. This is because the most significant contribution to the  $P-\Delta$  sway effect is the lateral force rather than nodal moments that are neglected in the lumping load method, so that the lumping load method retains the important lateral force effects and its effect especially for low axial forces is very minor. With larger loads the discrepancy increases owing to the coupling effect between the element load effect and the element stiffness, as in Section 6.2.

## 7. DISCUSSION AND CONCLUDING REMARKS

This paper presents a profound impact on shifting the nodal solution (robust system analysis) to both nodal and element solution (sophisticated element formulation) and opens a door to study the element solution using an element itself, when element load directly acting on an element is ubiquitous. For the traditional numerical approach, a whole domain must be divided into sub-domain, and the approximate function aims at reproduce the accurate solution for this sub-domain, unfortunately, restrictive to the nodal solution through the system analysis. Therefore, the present analysis provides an alternative but unique means to study first- and second-order element solution effectively without element discretization.

This paper possesses another important implication of superimposition principle being imposed in the derivation of element stiffness formulation that the numerous number of general element loading scenarios can be simply and succinctly unified from a few of standard individual load cases afore non-linear analysis, during which the element loading distribution of any kinds is converted into the standard loading magnitude at mid-span. Meanwhile, this magnitude of element load coefficient, such as  $\overline{M}_0$ , updates in the course of the non-linear solution procedures for the sake of tracing second-order element solution. As a result, despite trading off the element load distribution for that the element stiffness with element load effect is unnecessarily reformulated for a diverse kind of element load cases, the present numerical analysis is therefore versatile and adaptive to a structure under diverse element loading types and scenarios without loss of accuracy considerably.

In addition, in contrast to the numerous stability functions with a plethora element load scenarios, the present higher-order element functions is basically same but adjusting the equivalent mid-span moment  $\overline{M}_0$  for the corresponding element load cases, but results in an accurate solution as the stability functions as elaborated in Section 6.2. In contrast to the conventional finite element being irrelevant to element loads, such as the cubic element or other advanced finite elements in the open literature, in which all element load effect taking into account at nodes through the system analysis without considering the element solutions, the present higher-order element can accurately evaluate the first- and second-order elastic element solution by element itself when subjected to element loads. In short, the present higher-order element function with element load effect can generalize and replace the numerous stability functions with a plethora of element load scenarios and its load combinations in a simple, efficient, effective, versatile and robust manner.

In conclusion, based on all above mentioned benign features and advances, the present second-order elastic analysis with element; load solution is adequately articulated as being an accurate (solution), simple (formulation), versatile (applications and non-linear behaviour), efficacious (computational speed) and effective (numerical modelling and computational storage) approach, which is favourable to the practical applications for the general steel structures subjected to the multiplicity of random loading cases; especially the reliable structural safety and adequacy of an element (member) can be assured.

## ACKNOWLEDGMENT

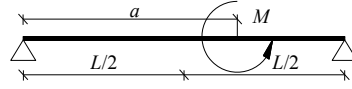
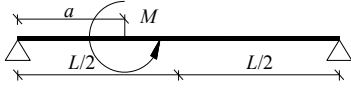
The work in this paper was supported by the Australian Research Council through a Federation Fellowship awarded to the second author. Further, the gratitude is given to the School of Civil Engineering and Built Environment of QUT in support to the first author.

## REFERENCES

- [1] Kondoh, K., Tanaka, K. and Atluri, S.N., "An Explicit Expression for the Tangent-stiffness of a Finitely Deformed 3-D Beam and its use in the Analysis of Space Frames", *Computers and Structures* 2006, Vol. 24, No. 2, pp. 253-271.
- [2] Chan, S.L. and Zhou, Z.H., "Pointwise Equilibrating Polynomial Element for Nonlinear Analysis of Frames", *Journal of Structural Engineering*, ASCE 1994, Vol. 120, No. 6, pp. 1703-1717.
- [3] Chan, S.L. and Zhou, Z.H., "Second-order Elastic Analysis of Frames using Single Imperfect Element per Member", *Journal of Structural Engineering*, ASCE 1995, Vol. 121, No. 6, pp. 939-945.
- [4] Izzuddin, B.A., "Quartic Formulation for Elastic Beam-columns subject to Thermal Effects", *Journal of Engineering Mechanics*, ASCE 1996, Vol. 122, No. 9, pp. 861-871.
- [5] Liew, J.Y.R., Chen, H., Shanmugam, N.E. and Chen, W.F., "Improved Nonlinear Plastic Analysis of Space Frame Structures", *Engineering Structures* 2000, Vol. 22, pp. 1324-1338.
- [6] Iu, C.K. and Bradford, M.A., "Second-order Elastic Analysis of Steel Structures using a Single Element per Member", *Engineering Structures* 2010, Vol. 32, pp. 2606-2616.
- [7] Iu, C.K. and Bradford, M.A., "Higher-order Non-linear Analysis of Steel Structures Part I: Elastic Second-order Formulation", *International Journal of Advanced Steel Construction* 2012, Vol. 8, No. 2, pp. 168-182.
- [8] Iu, C.K. and Bradford, M.A., "Higher-order Non-linear Analysis of Steel Structures Part II: Refined Plastic Hinge Formulation", *International Journal of Advanced Steel Construction* 2012, Vol. 8, No. 2, pp. 183-198.
- [9] Zhou, Z.H. and Chan, S.L., "Refined Second-order Analysis of Frames with Members under Lateral and Axial Loads", *Journal of Structural Engineering*, ASCE 1996, Vol. 122, No. 5, pp. 548-554.
- [10] Zhou, Z.H. and Chan, S.L., "Second-order Analysis of Slender Steel Frames under Distributed Axial and Member Loads", *Journal of Structural Engineering*, ASCE 1997, Vol. 123, No. 9, pp. 1187-1193.
- [11] Kassimali, A., "Large Deformation Analysis of Elastic-plastic Frames", *Journal of Structural Engineering*, ASCE 1983, Vol. 109, No. 8, pp. 1869-1886.
- [12] Meek, J.L. and Tan, H.S., "Geometrically Nonlinear Analysis of Space Frames by an Incremental Iterative Technique", *Computer Methods in Applied Mechanics and Engineering* 1984, Vol. 47, pp. 261-282.
- [13] Roorda, J., "Stability of Structures with Small Imperfections", *Journal of the Engineering Mechanics Division*, ASCE 1965, Vol. 91, No. 1, pp. 87-106.
- [14] Koiter, W.T., "Post-buckling Analysis of a Simple Two-bar Frame", *Recent Progress in Applied Mechanics* (Broberg *et al.* eds), John Wiley & Sons, New York, 1967, pp. 337-354.
- [15] Argyris, J.H. and Dunne, P.C., "On the Application of the Natural Mode Technique to Small Strain Large Displacement Problems", *Proceedings of World Congress on Finite Element Methods in Structural Mechanics*, Bournemouth, UK, 1975.
- [16] Trahair, N.S., Bradford, M.A., Nethercot, D.A. and Gardner, L., "The Behaviour and Design of Steel Structures to EC3", 4<sup>th</sup> edn., Taylor & Francis, London, 2008.

## Appendix 1. Equivalent Mid-Span Moment $\bar{M}_0$

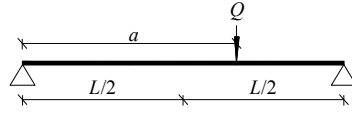
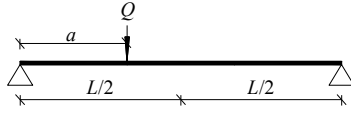
### 1. Concentrated moment



$$\bar{M}_0 = -\frac{L}{EI} \times 8M \quad (a \leq L/2) \quad (50)$$

$$\bar{M}_0 = \frac{L}{EI} \times 8M \quad (a \geq L/2) \quad (51)$$

### 2. Point load



$$\bar{M}_0 = \frac{L}{EI} \times 8Qa \quad (a \leq L/2) \quad (52)$$

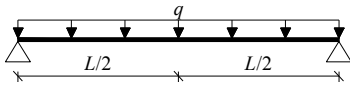
$$\bar{M}_0 = \frac{L}{EI} \times 8Q(L-a) \quad (a \geq L/2) \quad (53)$$

### 3. General $n$ point loads

$$\bar{M}_0 = \frac{L}{EI} \sum_{i=1}^j 8Q_i \alpha_i \quad (a_j \leq L/2) \quad (54)$$

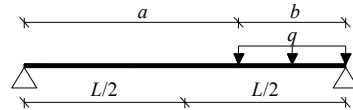
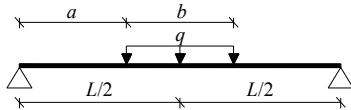
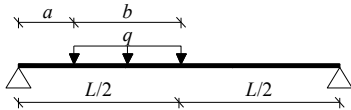
$$\bar{M}_0 = \frac{L}{EI} \sum_{i=j+1}^n 8Q_i (L - \alpha_i) \quad (a_j \geq L/2) \quad (55)$$

### 4. Uniformly distributed load over entire length



$$\bar{M}_0 = \frac{L}{EI} \times 2qL^2 \quad (56)$$

### 5. Uniformly distributed load over partial length



$$\bar{M}_0 = \frac{L}{EI} \times 8qb \left( a + \frac{b}{2} \right) \quad (a+b \leq L/2) \quad (57)$$

$$\bar{M}_0 = \frac{L}{EI} \times 8q \left[ b \left( L - \left( a + \frac{b}{2} \right) \right) - \left( \frac{L}{2} - a \right)^2 \right] \quad (a \leq L/2 \leq a+b) \quad (58)$$

$$\bar{M}_0 = \frac{L}{EI} \times 8qb \left( L - \left( a + \frac{b}{2} \right) \right) \quad (a \geq L/2) \quad (59)$$

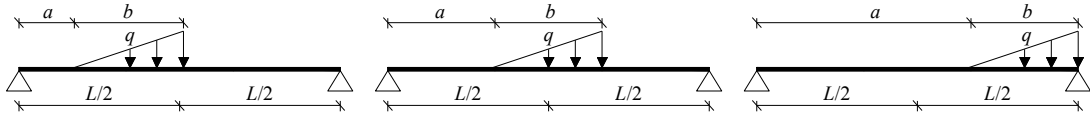
## 6. General $n$ uniform loads

$$\bar{M}_0 = \frac{L}{EI} \times 8 \sum_{i=1}^{j-1} q_i b_i \left( a_i + \frac{b_i}{2} \right) \quad (a+b \leq L/2) \quad (60)$$

$$\bar{M}_0 = \frac{L}{EI} \times 8q_j \left[ b_j \left( L - \left( a_j + \frac{b_j}{2} \right) \right) - \left( \frac{L}{2} - a_j \right)^2 \right] \quad (a \leq L/2 \leq a+b) \quad (61)$$

$$\bar{M}_0 = \frac{L}{EI} \times 8 \sum_{i=j+1}^n q_i b_i \left( L - \left( a_i + \frac{b_i}{2} \right) \right) \quad (a \geq L/2) \quad (62)$$

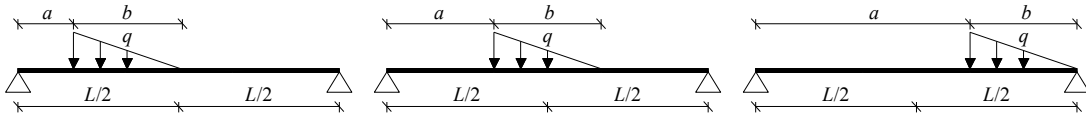
## 7. Hydrostatic loading



$$\bar{M}_0 = \frac{L}{EI} \times 4qb \left( a + \frac{2b}{3} \right) \quad (a+b \leq L/2) \quad (63)$$

$$\bar{M}_0 = \frac{L}{EI} \times 8q \left[ \frac{b}{2} \left( L - \left( a + \frac{2b}{3} \right) \right) - \frac{(L/2 - a)^3}{3b} \right] \quad (a \leq L/2 \leq a+b) \quad (64)$$

$$\bar{M}_0 = \frac{L}{EI} \times 4qb \left( L - \left( a + \frac{2b}{3} \right) \right) \quad (a \geq L/2) \quad (65)$$



$$\bar{M}_0 = \frac{L}{EI} \times 4qb \left( a + \frac{b}{3} \right) \quad (a+b \leq L/2) \quad (66)$$

$$\bar{M}_0 = \frac{L}{EI} \times 8q \left[ \frac{b}{2} \left( a + \frac{b}{3} \right) - \frac{(L/2 - a)^2 (L/2 - a + b)}{3b} \right] \quad (a \leq L/2 \leq a+b) \quad (67)$$

$$\bar{M}_0 = \frac{L}{EI} \times 4qb \left( L - \left( a + \frac{b}{3} \right) \right) \quad (a \geq L/2) \quad (68)$$

## Appendix 2. Stiffness Terms

The terms  $G_{\alpha i}$  ( $\alpha = y$  or  $z$ ,  $i = 1$  or  $2$ ) in Eq. 26 are:

$$\begin{aligned} \frac{\partial M_{\alpha 1}}{\partial \omega} &= \frac{EI_{\alpha}}{L} \left\{ \left[ \frac{12(48)^2/5 + 36(48)\omega/5 + 252\omega^2/35 + \omega^3/20}{(48 + \omega)^3} \right] (\theta_{\alpha 1} + \theta_{\alpha 2}) \right. \\ &\quad + \left[ \frac{4(48)^2 + 28(48)\omega/5 + 132\omega^2/35 + 11\omega^3/420}{(48 + \omega)^3} \right] (\theta_{\alpha 1} - \theta_{\alpha 2}) \\ &\quad \left. + \left[ \frac{16\omega}{35(48 + \omega)^3} \bar{M}_0 \right] \right\} \end{aligned} \quad (69)$$

$$\begin{aligned} &= \frac{EI_{\alpha}}{L} \{ 2b_1(\theta_{\alpha 1} + \theta_{\alpha 2}) + 2b_2(\theta_{\alpha 1} - \theta_{\alpha 2}) + b_{w1}\bar{M}_0 \} = \left( \frac{EI_{\alpha}}{L} \right) G_{\alpha 1} \\ \frac{\partial M_{\alpha 2}}{\partial \omega} &= \frac{EI_{\alpha}}{L} \left\{ \left[ \frac{12(48)^2/5 + 36(48)\omega/5 + 252\omega^2/35 + \omega^3/20}{(48 + \omega)^3} \right] (\theta_{\alpha 1} + \theta_{\alpha 2}) \right. \\ &\quad - \left[ \frac{4(48)^2 + 28(48)\omega/5 + 132\omega^2/35 + 11\omega^3/420}{(48 + \omega)^3} \right] (\theta_{\alpha 1} - \theta_{\alpha 2}) \\ &\quad \left. - \left[ \frac{16q}{35(48 + \omega)^3} \right] \bar{M}_0 \right\} \end{aligned} \quad (70)$$

$$= \frac{EI_{\alpha}}{L} \{ 2b_1(\theta_{\alpha 1} + \theta_{\alpha 2}) - 2b_2(\theta_{\alpha 1} - \theta_{\alpha 2}) - b_{w1}\bar{M}_0 \} = \left( \frac{EI_{\alpha}}{L} \right) G_{\alpha 2}$$

$$\frac{\partial \omega}{\partial e} = \frac{1/L}{I/AL^2 - \sum_{\alpha=y,z} [b'_2(\theta_{\alpha 1} - \theta_{\alpha 2})^2 + b'_{w1}(\theta_{\alpha 1} - \theta_{\alpha 2})\bar{M}_0 + b'_{w2}\bar{M}_0^2]} = \frac{1}{HL} \quad (71)$$

$$\frac{\partial \omega}{\partial \theta_{\alpha 1}} = \frac{2b_1(\theta_{\alpha 1} + \theta_{\alpha 2}) + 2b_2(\theta_{\alpha 1} - \theta_{\alpha 2}) + b_{w1}\bar{M}_0}{I/AL^2 - \sum_{\alpha=y,z} [b'_2(\theta_{\alpha 1} - \theta_{\alpha 2})^2 + b'_{w1}(\theta_{\alpha 1} - \theta_{\alpha 2})\bar{M}_0 + b'_{w2}\bar{M}_0^2]} = \frac{G_{\alpha 1}}{H} \quad (72)$$

$$\frac{\partial \omega}{\partial \theta_{\alpha 2}} = \frac{2b_1(\theta_{\alpha 1} + \theta_{\alpha 2}) - 2b_2(\theta_{\alpha 1} - \theta_{\alpha 2}) - b_{w1}\bar{M}_0}{I/AL^2 - \sum_{\alpha=y,z} [b'_2(\theta_{\alpha 1} - \theta_{\alpha 2})^2 + b'_{w1}(\theta_{\alpha 1} - \theta_{\alpha 2})\bar{M}_0 + b'_{w2}\bar{M}_0^2]} = \frac{G_{\alpha 2}}{H} \quad (73)$$

in which

$$b'_2 = \left[ \frac{-16(48)^2/5 - 64(48)\omega/35}{(48 + \omega)^4} \right] \quad (74)$$

$$b'_{w1} = \left[ \frac{16(48) - 32\omega}{35(48 + \omega)^4} \right] \quad (75)$$

$$b'_{w2} = \left[ \frac{4/7 + 2q/105}{(48 + q)^4} \right]. \quad (76)$$